Department of Mechanical Engineering

Visualisation of Articular Cartilage Microstructure

Christopher David Rowles

This thesis presented for the Degree of
Doctor of Philosophy
of
Curtin University

December 2016

Declaration

To the best of my knowledge and belief this thesis contains no material previously published by any other person except where due acknowledgment has been made.

This thesis contains no material which has been accepted for the award of any other degree or diploma in any university.

The research presented and reported in this thesis was conducted in compliance with the National Health and Medical Research Council Australian code for the care and use of animals for scientific purposes 8th edition (2013).

This thesis did not use any live animals and no animal was purchased for this work. All biological samples were salvaged from waste animal parts used in relation to other projects at the University of Western Australia prior to 2011.

The research study received animal ethics approval from the University of Western Australia Animal Ethics Committee, Approval Number #07/100/565.

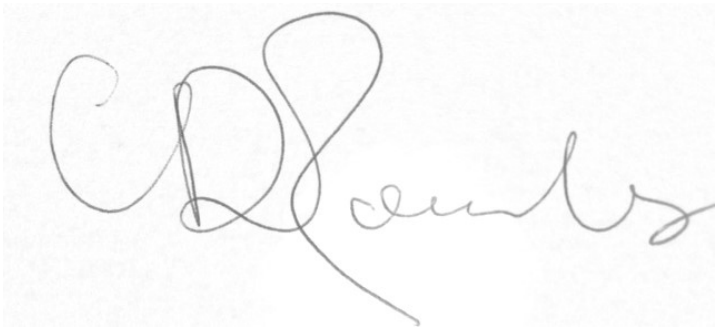

Signature: ……

Christopher David Rowles

Date: 21 December 2016……...

Statement of Contributors

The software developed in this thesis used Matlab functions supplied by Dr Peter Kovesi at the University of Western Australia ("UWA") MATLAB functions were the starting point for the develop software. Initially this provided 1D phase congruency and phase symmetry codes. This package formed the basis of the image processing modifications. Additional software was developed as an extension to the original system as 2D and 3D routines which were developed by me with Dr Peter Kovesi acting in a consulting role.

The modified package was tested and operation verified by Pieter Luitjens and Ben Richardson as part of their final year Engineering projects at the University of Western Australia. Both students were under my supervision and direction during their projects. The resultant code was shared with Dr Kovesi. The final versions of the directional 2D and 3D filters and those that included integrated monogenic filters were sent to Dr Kovesi and are included into the software distribution available from his web site.

Various confocal images used in the quality assurance testing of this thesis were supplied by Dr Jian Ping Wu, Department of Mechanical Engineering, University of Western Australia and Curtin University. These images were published by Dr Jian Ping Wu and used to verify processed images from the developed software. The resultant processed images were compared to the original data as verification that the image processing was successful.

The collection of porcine (pig) cartilage, early ovine (sheep) cartilage samples and subsequent confocal images and relaxation data was assisted by the following forth year UWA mechanical engineering students: Alex Hayes, Tom Ferguson, Tom Kierath, Daniel Spagnolo, Christopher Bird and Michael Smith. I directly supervised these students as part of their final year Engineering projects.

ImageJ was used as the Visualisation software for image display. The Matlab code was converted to use ImageJ as the preferred image processing environment for production software.

No live animals were specifically euthanased for any specimens used in this thesis. All animal samples were collected under the supervision and usage protocols of the Large Animal Facility at UWA from the waste materials of animals used for some other research, for which ethics approval had already been granted. I want to thank the researchers at UWA for the provision of these unused tissue samples from their animals.

Abstract

The structure and function of articular cartilage in articulated joints is critical to the continued operation of the joint. Dysfunction of the cartilage leads to arthritic degeneration which affects 14.7% of the Australian population. Cartilage dysfunction increases to over 40% of those aged 65 years and over. Over the lifespan of an average Australian, one in two will suffer from the symptoms of osteoarthritis. Cartilage has two common forms: a hard glass like substance known a hyaline cartilage; and a spongy fibrous substance known as fibrous cartilage. The aim of this thesis is to develop methods to examine cartilage at a microscopic level to eventually alleviate the human suffering associated with cartilage disorders.

Imaging Cartilage and Image Processing

The outcome of this work was to develop image processing techniques for the visualisation of articular cartilage using *in vivo* approved imaging stains. The main purpose is to get clearer images for hyaline cartilage with minimal staining protocols, along with the ability to segment the image into its component objects. This process is to assist in the categorisation and measurement of these component parts, which then gives the ability to recognise and measure early signs of cartilage wear (as shown by fibre bundle loss).

The purpose of the improved measurement of cartilage components is to aid in the early detection of osteoarthritis and other degenerative conditions that affect the general population, particularly the aging population. As a requirement for non-invasive surgery, *in vivo* imaging is preferred, since biopsy permanently damages cartilage. The imaging technique uses only wide acting biologically safe staining of samples, such as fluorescein (“FITC”). Issues arising from the use of fluorescein include the rise of background noise (reduced image quality) associated with small cartilage fibres (collagen II), which reduces the clarity of fibres contained within the extra cellular matrix (“ECM”) that comprises the hyaline cartilage. Due to the similarity in the refractive indices of collagen and the ECM that makes up the hyaline cartilage, imaging of the collagen component is difficult to perform.

Development of Image Processing Software

Examination of the two-dimensional image frames (or stacks) that are vertically aligned above one another thus forming into three dimensional images stacks showed that the quality of the images would be enhanced by image processing, both for noise reduction and feature detection. Such software has not used for biological images, as these images are less structured than photographic images. It was felt that computer vision could provide a basis for image processing. The image processing techniques used are described within this thesis. Phase symmetry and phase congruency image processing techniques showed early promise as a solution for image segmentation and for the identification of specific objects in imaging processing.

The image processing technique was developed from code provided by Dr Peter Kovesi to de-noise and process line features within each two-dimensional ("2D") image, for automated vision recognition. These images are similar to the three-dimensional ("3D") image contained within an 2D image stack collected using confocal microscopy and resulting in a process that was developed to analyse the 3D stack as a single entity.

This work was developed for automated vision systems that analyse 2D images, to detect and segment objects into recognisable forms that robots could identify. The code was then successfully extended to 3D images. During the reconstruction in 3D, the objects under study had strong axial (z axis) properties were attenuated relative to objects within the normal planes (x axis and y axis). This led to poor reconstruction of a true 3D object and does not lend itself to 3D segregation, cleaning nor de-noising the component image structures.

The biological imaging is formed from within the specimen with the objects of interest making up the entire imaging region, whereas vision images are formed external to the observer and the objects look part of the scene. It is interesting to note that the information surrounds the viewer, rather than is information presented as disjoint views well separated from the viewer.

A true 3D approach to signal filtering has eliminated most of the short-comings of the 2D system. This approach will permit the various cartilage components to be separated from one another, with the ability to use artificially coloured objects for new images, that are clearer and more easily separated the component parts of the image, thus showing the spatial relationship between each other. This unbalanced axial view could have been compensated to allow for the non-isotropic microscope resolution but space equalisation gave better interactive views.

Several different approaches were investigated for extending the phase symmetry algorithm approach to 3D. Monogenic filters were found to provide the best results and the lowest computation time. It was found that image compression due to non-isotropic confocal microscope resolution could be compensated by scaling the distance vectors used to construct the filter set. Intensity based image normalisation prior to image processing was found to improve the performance of the phase symmetry algorithm. The monogenic filters were developed from a scale space model of the image.

The main issue with biological images at the scale studied (1 to 10 microns in size) is that these images are not readily recognisable as 3D objects in the same way as a building or room interior are recognised. The image processing software was developed without pre-assumptions of the objects detected or the presence of defining features such as sharp edges or corners.

The phase symmetry method was found to provide excellent results segmenting chondrocyte cells and good results segmenting collagen fibres and isolating larger fibre bundles from more dispersed fine single fibres. 3D volume views created using ImageJ show that the 3D algorithm provided useful data. The 3D algorithm was successfully able to segment collagen fibres surrounding the chondrocyte cells, which the 2D algorithm was unable to do.

The system was tested and verified by processing existing images collected by Dr Jian-Ping Wu as part of her research into articular cartilage and tendons. The processed images showed more detail than unprocessed images without the introduction of artefacts. This process was then successfully used on other biological confocal images, and computed axial tomography ("CAT") scans of bone structures and MRI images.

In developing these imaging techniques, it was determined that a single unifying imaging and visualisation system was preferable. To make this system more user friendly, I decided to rewrite all the Matlab function implementation as ImageJ filters, which are an industry standard freeware for displaying and editing images. This will ease the use of the system for interactive processing and make it more freely available to users outside of Curtin University.

Small Scale Studies of Articular Cartilage

During this work, several small-scale pilot studies were undertaken to examine the effectiveness of the image processing upon the measurement of the mechanical properties of ovine and porcine cartilage.

The purpose of the pilot studies was to test various hypotheses that relate to topological variation of sheep articular cartilage to the mechanical loading of the cartilage. These hypotheses were tested using cartilage from donor animals of diverse ages as samples became available to see if the mechanical properties of the cartilage changed with age as well as topological site. The studies were extended to pig samples when they became available. The studies showed that topological variation in mechanical properties of cartilage. Subsequent analysis showed that most of the variation could be attributed to age and superficial zone thickness.

The study showed that pig cartilage was more consistent in its properties than sheep cartilage, which had larger variation. Also, the study showed that the cartilage compressed under postnatal loading. The thickness of superficial layer cartilage reached a maximum just prior to birth, and then decreased in thickness thereafter. The mechanical properties of the cartilage were found to shadow the thickness of the superficial zone cartilage. Most of the findings were statistically significant, but sometimes lacked sufficient sample sizes to reduce the sampling error associated with specific readings. This study has however, given some understanding of the environmental factors that affect cartilage growth and development in young animals.

The measurements of the strength of the developing cartilage were dependent upon age and thickness of the sample. Cartilage stiffness mirrored the thickness of the superficial layer of the cartilage samples. The statistical variation can be explained by the sample thickness. The study showed that the superficial layer thickness increased up to the time the animal was borne and then decreased with age and weight loading placed upon the cartilage tissue. The mechanical properties likewise varied with age and thickness of the cartilage sample.

Acknowledgements

I want to express my gratitude to Professor Brett Kirk and Dr Jian-Ping Wu for their patience and guidance in the development of this study.

I want to thank my Curtin thesis committee Professor Brett Kirk, Professor Tilak Chandratilleke and Dr Chris Ford for their guidance throughout this study.

I would also like to acknowledge the financial support offered by Curtin University in the form of a postgraduate research scholarship.

I would like to express my thanks to my research team for their input into this study and Intan for proof reading this script.

I wish to acknowledge that I have written this thesis in Standard English with United Kingdom (Australian) spelling. I have attempted to remove US spelling despite Microsoft Word's attempt to use odd and funny spellings for common English words.

Dedication

I dedicate this work to my wife Eileen and daughters Siobhan and Alexandra Rowles for their support in editing this work and their encouragement to leave full time employment and return as a student during the course of this study.

Table of Contents

List of Figures

List of Tables

List of Microscope Images

List of Abbreviations

Abbreviation	Meaning
2D	Two Dimensional
3D	Three Dimensional
AC	Articular Cartilage
ALC	Anterior Lateral Condyle
AMC	Anterior Medial Condyle
CLC	Central Lateral Condyle
CMC	Central Medial Condyle
Curtin	Curtin University
ECM	Extra cellular Matrix
FFT	Fast Fourier Transform
FITC	Fluorescein Isothiocyanate
GAG	Glycosaminoglycan
GUI	Graphical User Interface
HA	Hyaluronic Acid
LVDT	Linear Variable Differential Transformer
LFC	Lateral Femoral Condyle
LT	Lateral Trochlea
LSCA	Laser Scanning Confocal Arthroscope
LSCM	Laser Scanning Confocal Microscope
MFC	Medial Femoral Condyle
MT	Medial Trochlear
NA	Numerical Aperture
OA	Osteoarthritis
PBS	Phosphate Buffered Saline (0.9%)
PDSF	Point Spread Function
PLC	Posterior Lateral Condyle
PMC	Posterior Medial Condyle
PSF	Point Spread Function
SEM	Scanning Electron Microscope

Abbreviation	Meaning
TEM	Transmission Electron Microscope
TPM	Two Photon Microscopy
UWA	University of Western Australia

Chapter 1 Introduction

The motivation for developing image processing techniques for the analysis of articular cartilage was to characterise the distribution of chondrocytes and (collagen) fibres using non-invasive sampling techniques and clinically viable stains. Traditionally a destructive biopsy is used to collect samples for examination, which results in a major lesion that is equivalent to severe osteoarthritic damage. A non-invasive method was desirable and this thesis presents the techniques on which to base non-invasive procedures.

High resolution images using clinically viable fluorescent stains are not easy to obtain, as the size of the fibres is just below the resolution of confocal optical techniques, using lenses with numerical apertures of around 1.4. Two photon or second harmonic techniques provide good quality images but at the potential expense of destructive sampling. This is because of the high light radiation levels experienced by the sample during the imaging processes. Furthermore, the visualisation has limitations when the reconstruction is based upon 2D slices that are stacked one on top of another to give a 3D representation of the sample. The movement of fibres between layers of the collected image stacks was unclear and, did not make a good representation of the sample.

Although modern confocal techniques can improve image collection, these techniques are often time consuming, difficult to set up and destroy the sample by exposing it to high levels of excitation energy photons. Two photon confocal techniques can use auto-fluorescence of collagen fibres to give clearer images of the collagen structure. Together with selective staining, two photon techniques can show the fibres in relation to other biological structures, such as cells. This study attempts to resolve the 3D images into collagen fibres and separate cells. The confocal images are compared for accuracy with scanning transmission electron microscope and transmission electron microscope images.

The computer analysis methods described in this study develops techniques published by Dr Peter Kovesi (Kovesi 1999 and Kovesi 2004) using phase symmetry and phase congruency to identify, segment and label objects within a well-defined and structured 2D image. These techniques were extended to process 2D biological images that do not have well defined corner features. They were then further developed to process 3D images, forming the basis of this study. Traditional corner detection methods such as Harris corner strength had difficulties identifying corners correctly.

This thesis aims to develop techniques that will enable fast and accurate visualisation of structures present within articular cartilage microscopy images subject to commonly available clinically viable stains such as fluorescein (FITC). Additionally, it will explore the possibility of *in vivo* micro examination of articular cartilage using confocal arthroscopy. The process will also segregate objects within the image, permitting the development of preprogramed analysis methods for tracking fibre length, orientation, and distribution. This study uses fluorescein as it is a clinically viable stain that is safe to use with *in vitro* samples. Fluorescein is attracted to the bound water physically surrounding cellular bodies within the specimen, and generates background noise due to the volume of free water in the samples. Fluorescence does not stain the proteoglycan components of the extra cellular matrix, which appear as noise specks throughout the image. Objects are distinguished by considering various image properties to segregate and isolate individual features within the image and reduce the background noise.

The visualisation method used ImageJ as a 3D viewer to display 3D data stacks as a single block that can be manipulated by the user and obtain desirable viewports into the data structure. Pre-processing of image slices is helpful in obtaining optical balance throughout the sample and aids in the segregation of objects within the image, so that the same object has similar optical density. The original voxels (3D pixels) were reshaped from rectangular prisms to cubes towards the end of this work using sub-voxel extraction and linear interpolation, giving much clearer definition of vertical changes.

ImageJ also permits reprocessing of images. Where ImageJ has a wide variety of data smoothing routines incorporated into its structure, some of the processing initially performed by developed Matlab functions have been omitted in favour of the ImageJ processing. The additional Matlab functions have been rewritten in Java to operate as filters under ImageJ and these will be released as ImageJ plugins and filters, following submission of this thesis.

1.1 Background

In this study, articular cartilage was imaged using a laser scanning confocal microscope to assess the health, viability and structure of the sample examined. It was discovered that the quality of such images varied, depending upon*:*

- Age of sample;
- The state of the sample (i.e. fresh or preserved by freezing);
- Species of sample;
- Stain used to image sample; and
- Setup of the confocal microscope.

The aim of this study was to produce clear and consistent images from a clinically viable stained specimen using image processing to reduce noise and segregate the objects within the image. Once the image can be routinely produced, the differences between samples can be measured and categorised. The resultant images could then be used to assess the clinical health and viability of cartilage, in the early assessment of osteoarthritis.

In this study a wide-ranging stain was used to preserve the clinical viability of the staining technique used with live cartilage. The stain chosen was fluorescein because it illuminates a wide variety of cellular structures and has a broad-spectrum fluorescence response to 477 nm incident (excitation) illumination. Optical filtering is used to remove the excitation light wavelengths from the output (fluorescent) response, so that the synthesised image is due to fluorescence only. This eliminates light refraction on the excitation side of the microscope and improves the Gaussian response on the fluorescent output side.

The wide response of the fluorescein stain allows a range of structures to be illuminated concurrently and thus capture a bright field fluorescence normally associated with light microscopy. Many stains adhere to specific structures within the tissue, but not to other structures. This can cause feature omission from the fluorescent image and generate an incomplete picture of the specimen under study. Since this study began, multi-photon studies have been used to isolate collagen using auto-fluorescence and staining to identify other specific structures of interest. The purpose of this study is, however, to use simple staining techniques to give a near complete picture of the specimen.

1.2 Synovial Joints

The knee and shoulder joints are examples of two of the six different types of diarthrodial joints (Tortora and Derrickson, 2006) which provide a wide range of motion (Mow *et al.,* 1992). Under normal conditions these joints are an efficient weight bearing system, capable of providing nearly frictionless performance with little, if any, wear for the lifespan of the individual (Mow *et al*., 1984, Saladin, 2003).

All diarthrodial joints have been determined to contain a common set of basic components, these being the capsule, synovial membrane (or synovium) and articular cartilage (Davies, 1945, Mow *et al*., 1992, Saladin, 2003). The capsule is a tough, inelastic, avascular, white fibrous tissue (Mow *et al.,* 1992) which, while able to resist disease, has low powers of repair (Davies, 1945). It is lined with a thin, elastic membrane which has a rich supply of pain fibres and blood, good powers of repair, and phagocytic properties which enable absorption of waste material and harmful microorganisms (Davies, 1945). This metabolically-active tissue, known as the synovial membrane, or synovium, secretes synovial fluid and provides nutrients to the avascular cartilage within the joint (Mow *et al.,* 1992). The thin layer of hydrated soft tissue covering the articulating ends of the bone in a joint is called articular cartilage (Saladin, 2003, Julkunen *et al*., 2008c).

The function of articular cartilage is to absorb shock (Niederauer *et al.,* 2004), transmit loads between the opposing joint surfaces, distribute stresses over the subchondral bones and provide low-friction articulation (Franz *et al*., 2001, Krishnan *et al*., 2004, Niederauer *et al*., 2004) while minimising the degenerative effects of friction and wear (Stachowiak *et al*., 1994), allowing long-term, heavy use of the joints (Clark, 1999).

The synovial membrane (synovium) and articular cartilage form a joint cavity which contains the synovial fluid. The basic structure of these joints, shown in Figure 1-1 below, remains consistent throughout the literature and will therefore be used for this study. In the animal models, the knee joint is termed a stifle; however, as it is used as an analogue for the human knee joint, the term knee joint and stifle are used interchangeably.

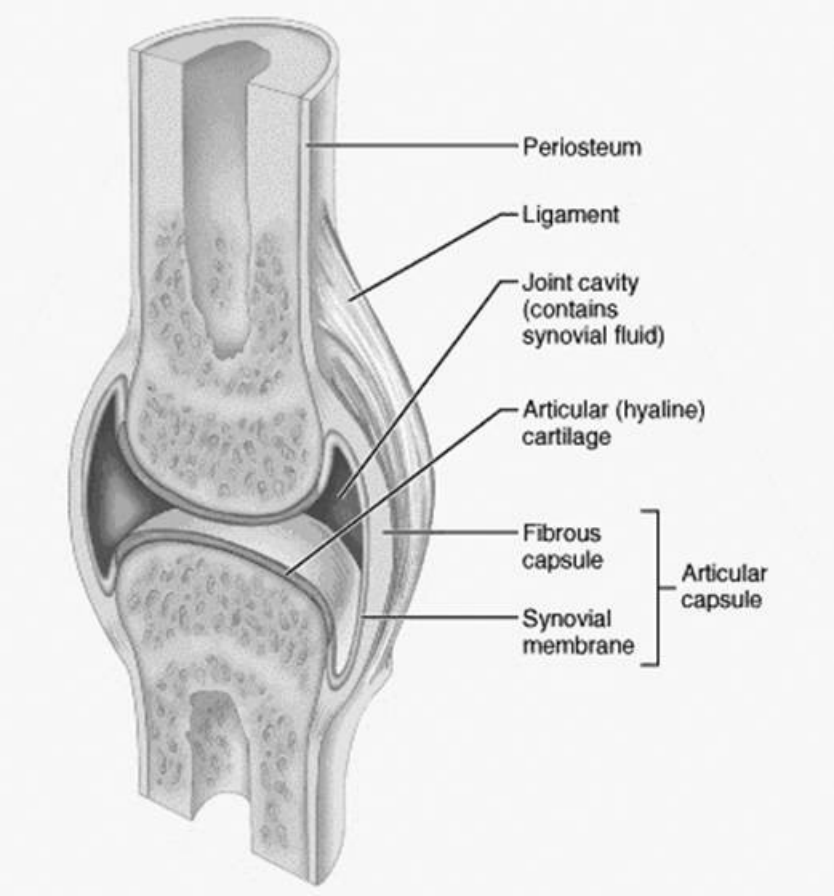

Figure 1-1: Anatomy of the synovial joint. **(After Klein 2007)**

It has been demonstrated that diarthrodial joints are subject to a large range of loading conditions (Mow *et al.,* 1992), and under normal conditions the articular cartilage suffers little wear and tear (Klein *et al*., 2007, Stachowiak *et al*., 1994). Large joints, such as the knee and hip, may sustain loads up to ten times body weight during activities such as walking. It has been reported that the joints commonly bear loads several times the body weight when held static (Mow *et al.,* 1992). In dynamic situations, loading can be as high as 18 megapascals (Mow *et al*., 1992, Arokoski *et al*., 2000). Failure of any of these weight bearing components can therefore be debilitating.

The synovial fluid nourishes the articular cartilage (Saladin, 2003) and possesses lubricating properties that, together with the articular cartilage itself, work to provide an almost frictionless surface for the joint during loading (Stachowiak *et al*., 1994, Saladin, 2003). Several mechanisms for this joint lubrication have been proposed (Krishnan *et al.,* 2004). It has been established that the flow properties of this lubrication are non-Newtonian (not having a single constant value of viscosity) (O'Neill and Stachowiak, 1992). These flow properties appear to be required for fluid film lubrication, the type of lubrication thought to be utilised by diarthrodial joints during locomotion (O'Kelly *et al*., 1978, Stachowiak *et al*., 1994, Clark *et al*., 1999). Synovial fluid is also thought to contain a molecule for boundary film lubrication (Mow *et al.,* 1992), although to the author's knowledge this has not been confirmed. While the method of lubrication is important to the function of synovial joints (Crockett *et al.,* 2007) it is irrelevant to this study and will not be explored further.

1.3 Articular Cartilage

This subsection describes the makeup of articular cartilage.

Articular cartilage ("AC") is a load bearing elastic tissue that grows on the exterior surface of articulating bones in synovial joints such as the knee, jaw, or shoulder. These joints are covered by a near frictionless surface that allows for joint movement and acts to cushion the transmission of forces across the joint (Mow et al 1992). AC's low coefficient of friction and high load bearing capabilities make it ideally suited to its role in the body to transmit and distribute mechanical loads with near frictionless motion (Mow V, Gu W, and Chen F 2005) and (Klein et al 2007).

Sheep and pig articular cartilage was chosen, due to the long history of their study by my colleagues in the research group and its ready availability. This study allowed the recent images to be compared to an existing catalogue of similar images taken over a considerable time. It also allowed early images from this study to be reprocessed, to ensure that the image processing was still valid and it also minimised any artefact generation. This study starts with a background discussion on the nature and structure of articular cartilage, including the histology of damaged cartilage found in osteoarthritic cartilage.

1.3.1 Articular Cartilage Structure

The nearly frictionless surface in synovial joints is known as articular cartilage and its mechanical properties are characterised by a complex internal matrix of collagen fibres, proteoglycans, and chondrocytes (Stockwell 1979) and (Quin T and Morel V 2007). Electrostatic repulsion between negatively charged proteoglycans creates a swelling pressure that resists compressive forces acting on the cartilage. Conversely, collagen fibres form a depth-dependent network that restricts the movement of proteoglycans and hence, resists swelling pressure (Mow et al 1992). It is the action of the collagen fibre network that provides the cartilage with tensile properties (Mow VC and Guo XE 2002).

The orientation of fibres in the cartilage is depth dependent, being classified into four distinct regions:

- The superficial layer, where collagen fibres run parallel to the cartilage surface;
- The intermediate articular cartilage, a hard, glasslike, and semi-transparent organic tissue found in synovial joints such as the knee, rotator cuff joints in the hip and mandible joint in the jaw (Klein et al 2007);
- The deep cartilage layer where the chondrocytes are vertically aligned and constrained by long vertical collagen fibres; and
- The calcified zone where the cartilage bonds with the underlying bone.

The main function of articular cartilage is to transmit loads through the joint whilst also allowing joint movement. In its healthy condition, AC provides a near-frictionless surface. The mechanical properties of the AC relate to the hydraulic properties of the proteoglycan components in compression, as modified by the presence of interwoven collagen matrix. These collagen fibres have little individual compressive strength but massive tensile strength.

In articular cartilage, collagen fibres consist mainly of type II collagen, with smaller amounts of types I and III collagen, and elastin fibres (Bo He, Wu JP, Xu J, Day RE and Kirk TB 2013), as well as traces of type IX and XI collagen (Teshima R et al 1995). Each fibre is formed from an interwoven mesh of smaller fibrils, similar in form to a rope-like fibre network, which result from the interconnection of types IX, XI, and II collagen.

Tropocollagen molecules are the basic building blocks for the collagen fibrils. These molecules consist of three linked polypeptide helices (Figure 1-2) and are approximately 300nm in length and 1.4nm in diameter (Kühn and Glanville, 1980). The tropocollagen molecules aggregate together, forming collagen fibrils. Multiple collagen fibrils combine using cross-linked bonds to form collagen fibres.

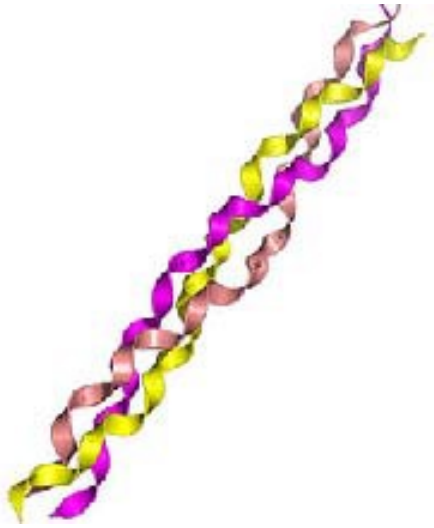

Figure 1-2: Polypeptide helices forming tropocollagen molecule
(http://www.3dchem.com/imagesofmolecules/Collagen1.jpg)

It is the strong covalent bonds that form between fibrils that account for the high tensile strength of collagen fibres (Clarke 1971) (Mow et al 1992). Fibrils are typically around 0.1µm in diameter (Figure 1-3), while the larger fibres, can be anywhere over 100µm thick (Clarke 1971). In particular, the diameter of fibrils and fibres has been shown to be dependent on age, depth, species and layer (Stockwell 1979), (Jadin K et al 2007), where collagen fibres are randomly orientated, and the deep and calcified layers where fibres are orientated radial to the cartilage surface (see Figure 1-3) (Broom N and Poole C 1983) (Alford J and Cole B 2005) (Clarke 1971) (Eyre 2002). The way the distribution of fibre orientation relates to the mechanical properties of articular cartilage is largely unknown, and remains an area of significant research (Wu 2005).

Cartilage is a hard, glass like substance with a refractive index of 1.51, which happens to be the refractive index of its component ground fibres. This makes imaging difficult without staining or using other imaging techniques.

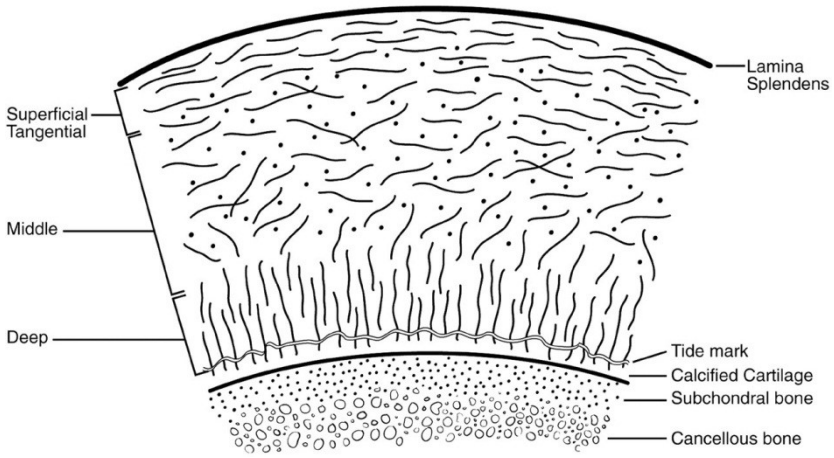

Figure 1-3: Articular cartilage layered structure (after Stockwell 1979)

All specimens were stained for five minutes using 0.05% fluorescein in a buffered phosphate saline to ensure a mildly alkaline environment for staining. The most superficial surface was presented to the confocal microscope, which meant that the tangential fibres within the laminar splendens (“LS”) and middle zones were visible to a depth of 70 to 100 microns, whilst the radial fibres deep within the sample were beyond the range of the instrument. The deep fibres are much harder to reconstruct as they present as very tiny bright spots disconnected to other features within the sample, making them harder to reconstruct accurately.

Chondrocytes are the only cellular bodies within the articular cartilage matrix. Chondrocytes manufacture the essential building blocks required to synthesise collagen (proto collagen) and proteoglycans. The type and structure of the collagen fibres directly impact the mechanical properties of the cartilage (Stockwell 1979) and (Mow V, Gu W, and Chen F 2005). The components of the articular cartilage matrix are continuously, albeit slowly, recycled; any disturbance to normal cellular processes can have a significant impact on the health of the tissue (Mow et al 1992).

Chondrocytes often appear grouped together as two or three cells. These groupings were evident in young actively growing cartilage but become distorted within the superficial layer, as entrapped chondrocytes enclosed within lacunae in mature cartilage. Cartilage growth is determined by the function of chondrocytes and the removal of old cartilage is governed by the production and action of an enzyme (proteinase) which removes proteoglycans and cartilage from the body. The decay of these cellular processes over the lifetime of the cartilage is a suspected cause of arthritis (Jones C et al 2007).

The actual structure of articular cartilage can be represented in a balloon and string model (Figure 1-4) as proposed by Broom, in which the string represents collagen fibres and balloons represent the proteoglycans. Here the balloons (proteoglycans) support the loaded cartilage structure, while the strings (collagen fibres) hold the integrity of the overall cartilage structure and regulate the flow of the proteoglycan within the extra cellular matrix ("ECM") that forms the framework of the articular cartilage structure.

Studies have shown that the size, shape, and distribution of chondrocytes vary with respect to the depth of the tissue (Stockwell 1979), (Jadin K et al 2007). Chondrocytes appear as circular disks parallel to the cartilage surface within the superficial layer; they become almost spherical towards the intermediate and middle layers, and are aligned in radial columns within the deep layer (Stockwell 1979).

The shape, size, and distribution of chondrocytes throughout the matrix have been shown to be characteristic of different stages of cartilage development and states of health (Stockwell 1979). Chondrocytes become entrapped within the ECM in a lacuna or lake of proteoglycan bounded by collagen fibres. The chondrocytes become squashed and irregular in shape, and in this form, produce both the collagen and proteoglycan basic building blocks for the rest of their existence. It is the local production of these collagen building blocks, known as tropocollagen that causes growth in the collagen fibres in their immediate vicinity. The chondrocytes are no longer free to move throughout the ECM and cluster in groups of two or three cells near the cartilage surface.

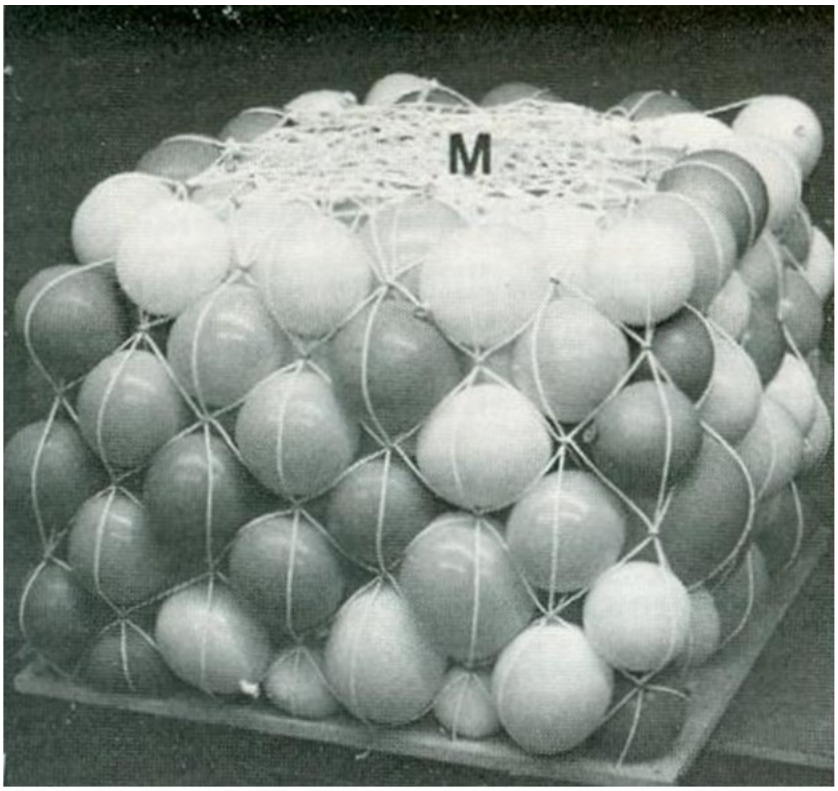

Figure 1-4: A balloon and string model of articular cartilage. The string represents the collagen fibres and the balloons represent the proteoglycans within the articular cartilage (from Broom ND 1988)

Articular cartilage is made up of three main components: a network of collagen fibre bundles; proteoglycan that are huge macromolecules that give adequate response to compressive loads on the cartilage ECM; and many chondrocyte cells. The balance of the ECM is water and synovial fluids

The collagen fibres in AC have a tensile strength similar to that of steel and greatly influence the mechanical properties of the AC (Wu 2005). There are three main types of collagen fibres present in AC; collagen I, II and III. Collagen I fibres form large thick fibre bundles with a typical diameter in the range of 2-10 microns. Collagen II fibres tend to clump together in fibrous regions and have typical diameters in the range of 0.02-0.08 microns. Collagen III fibres form a sparse fibre network similar to collagen I and have typical diameters in the range of 0.5-1.5 microns.

In addition to collagen fibres, AC also has elastin fibres in its composition. The ground substance is comprised primarily of proteoglycans and water, influencing the compressive response of the AC (Mow V, Gu W, and Chen F 2005). Repair and maintenance of the collagen fibre network and proteoglycans in the AC is the function of the chondrocyte cells.

The outer most layer of the AC (the Laminar Splendens) is attached to the remaining cartilage structure, although it is easily removed or peeled from the main structure. Since forces are applied directly to the superficial layer of the AC, it is the health of this layer that ultimately determines how well loads are distributed, and hence, the overall health and mechanical properties of the cartilage (Wu J P and Hezog W 2002) and (Korhonen R et al. 2003). Many previous studies have overlooked the relative importance of the LS and, still, the acceptance of the existence of the LS has been questioned by other researchers. During this study, the LS has been detected (and successfully removed) from all ovine, porcine, bovine cartilage samples.

The deterioration of the Laminar Splendens ("LS") is usually the early signs of AC wear. As the outer layer degrades, the underlying hyaline cartilage also wears, which ultimately results in fully blown osteoarthritis. The nature of the importance of the LS has been reported in the literature (Poole 2003) and may hold the key to successful cartilage transplantation and regrowth (Teshima R, Ono M, Yamashita Y, Hirakawa H, Nawata K and Morio Y 2004).

Studies of early cartilage development in sheep showed that the LS reached a maximum thickness just prior to birth in the new born sheep and that the depth of the LS decreased due to environmental loading experienced in highly loaded regions of the femoral condyle due to normal mobility following birth. During this compression, the fibre density in the superficial layer increased to give rise to a region of fibres parallel to the articulating surface, observed in all sheep specimens throughout this study.

Chondrocytes change shape from spherical cells in young cartilage (and in deep level cartilage) to compressed ellipses in the LS as the cartilage ages, to form the layer of fibres bundled parallel to the articulating surface. The number of chondrocytes also decreases with the maturity of the LS, leaving the superficial layer depleted of spherical cells as shown in Figure 1-3. Chondrocytes are located in an enclosed lake (lacuna) which forms as the cartilage matures. These lacunae prevent the chondrocytes from moving within the ECM and the collagen fibres that form around the chondrocytes entrap them making physical communication between neighbouring lacunae impossible. The chondrocytes are unable to reproduce and replace themselves and hence appear deformed with respect to chondrocytes in young cartilage or deep zones of the mature cartilage.

Studies have shown that the degeneration of articular cartilage due to osteoarthritis is closely linked to the deterioration of collagen fibres in the superficial layer of the AC (Broom N and Poole C 1983). More recently the overall health of the cartilage has been shown to be dependent upon the presence of intact proteoglycans. These are mega molecules with mass weights in the millions atomic weight units. It has been shown that the proteoglycans give rise to biphasic compression behaviour and that the volume of proteoglycan increases rapidly after birth. The growth in type II collagen increases from 75% of the dry mass of the ECM to 90% shortly after birth. The type II collagen binds tightly to the proteoglycan molecules via sulphate ions. This study noted the emergence of biphasic behaviour and the mass of collagen II.

Degradation of proteoglycan, due to attack by enzymes designed to remove old structures from the cartilage, also affect the mechanical compressibility and functioning of the cartilage. These structures are not resolvable directly into separate objects using confocal microscopy due to their small, but they do absorb histological stain and add to the background noise associated with the imaging, due to the increase in the number of collagen type II fibres.

Much of the research in osteoarthritis has been focused on the collagen fibre network or the microscopic construction of collagen, and has ignored the mesh that forms the fibres (Wu JP, Kirk TB and Zheng MH 2008). This is partly due to limitations in microscopy techniques and the inability to accurately visualise the 3D internal structure of collagen fibres.

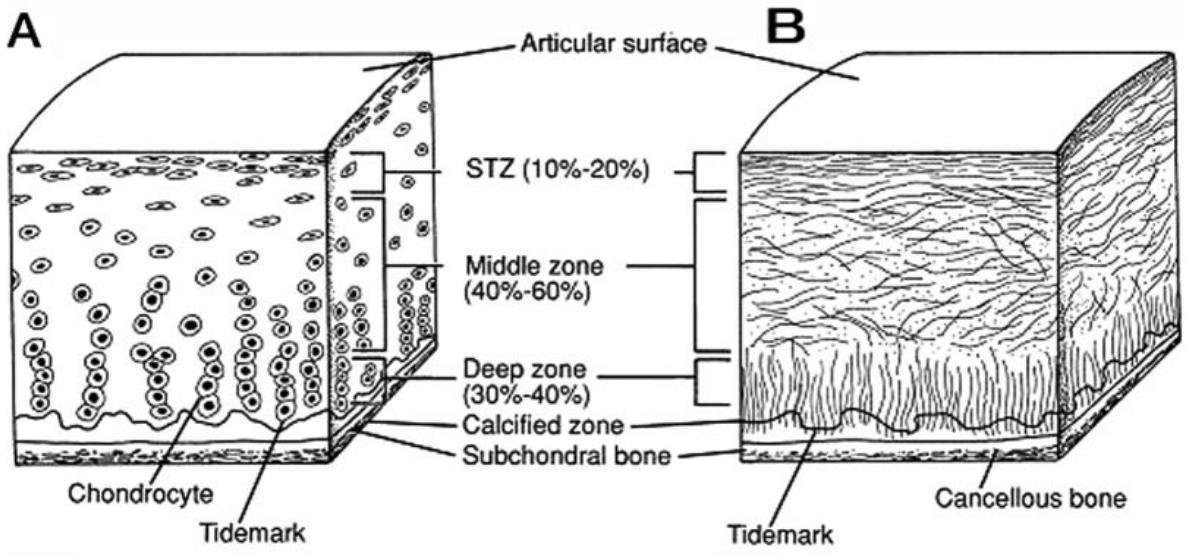

Figure 1-5: Cross-sectional diagram of healthy cartilage: A - cellular organisational zone; B - collagen fibre architecture (American Academy of Orthopaedic Surgeons, 1994)

AC can be divided up into four distinct zones:

- The Calcified Zone, also known as the end plate;
- the Radial Zone, also known as the middle zone;
- the Superficial Transitional Zone; and
- the Superficial Zone, including the articular surface Lamina Splendens.

It is noted that there is a lack of chondrocytes in the superficial and transitional layers and that the chondrocytes within these layers appear vertically deformed or squashed. The cells are sparse and isolated from each other, when compared to the spherical chondrocytes in the middle and deep zones.

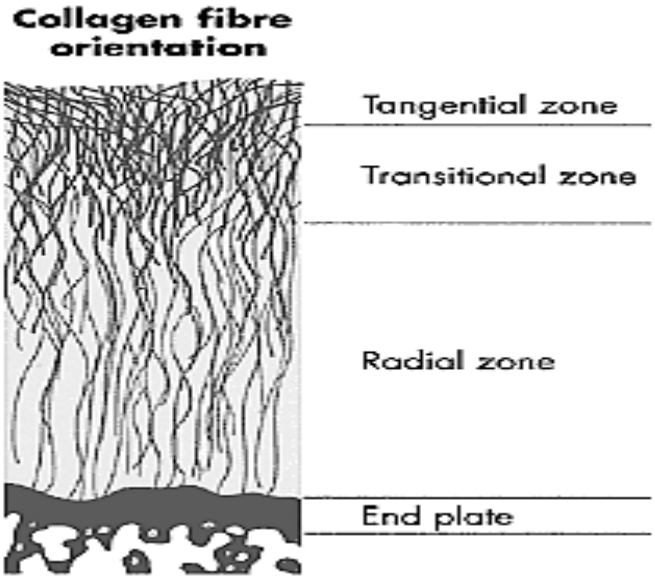

Figure 1-6: Layer structure of collagen fibres in articular cartilage (Stockwell, 1979)

One of the main distinguishing factors between the different zones is the orientation of the collagen (Figures 1-5 and 1-6). In the Calcified and Radial Zones, the collagen fibres are seen to run radially, perpendicular to the articulating cartilage surface. In the Superficial Zone, the collagen fibres run parallel to the articulating surface. In the Transitional Zone, the collagen fibres are changing between these two orientations. This is of key importance in the confocal microscope images. At the top of the image, the collagen fibres run parallel to the articulating cartilage surface. Further down in the image, the collagen fibres start to change orientation, dropping down vertically, as the observed cross sectional area decreases, making the fluorescent collagen fibres appear as single point light sources.

Collagen is a triple hex structure that resists stretching. The protein strands take up the initial strain, but once straightened out, the protein strands do not continue to stretch, but rather provide stiffness to the structures they support.

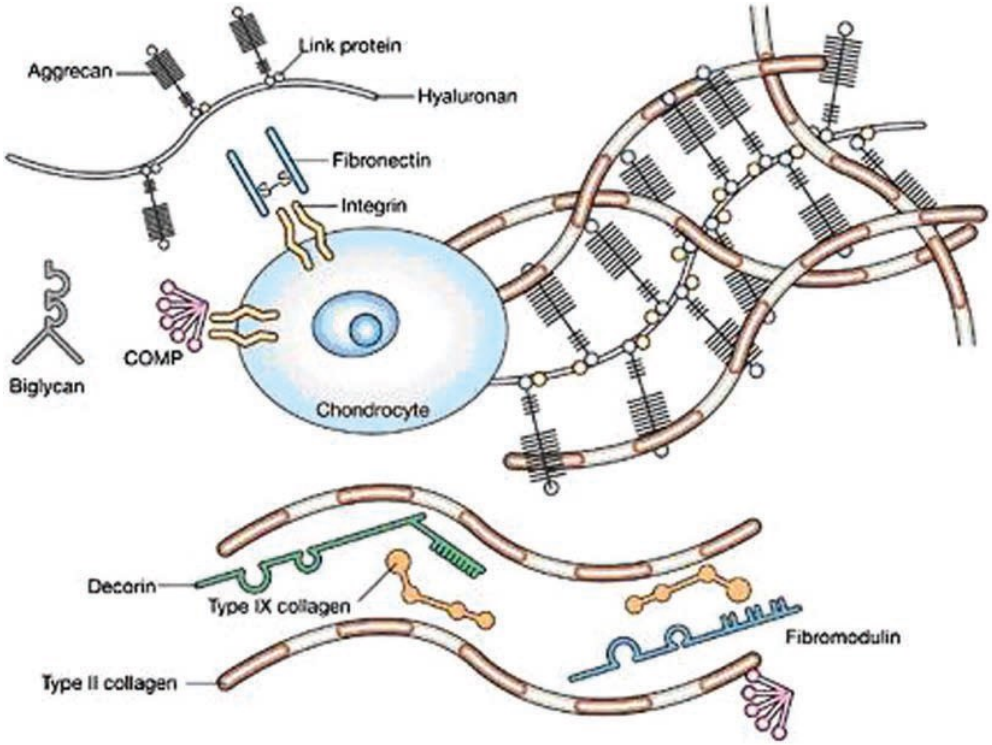

Figure 1-7: Extracellular matrix of articular cartilage. (Chen FH, Rousche KT and Tuan RS 2006)

The make-up of the proteoglycan structure is mostly Aggrecan, assembled on Hyaluronan backbones. These are then attached to collagen II fibres by means of chondroitin sulphate or keratin sulphate closer to the starting end of the Hyaluronan chains. These Aggrecan structures (also known as glycosaminoglycan “GAG”) form massive macromolecules. These GAGs often have atomic weights in the region of millions of atom weight units. With aging, Aggrenase breaks the Hyaluronan chains, making the GAGs less effective in supporting the compressive loads experienced by the cartilage. This remodelling and degradation of the large molecule groups leads to the depletion of proteoglycan and the loss of cartilage strength.

1.3.2 Fibrous Components Collagen and Elastin

In normal articular cartilage, tissue fluid represents between 65% and 80% of the total weight. (Mow VC, Wenbo Z and Ratcliffe A 1991). Collagens and proteoglycans account for the remaining dry weight. Several other classes of molecules can be found in smaller amounts in the ECM; these include lipids, phospholipids, non-collagenous proteins, and glycoproteins.

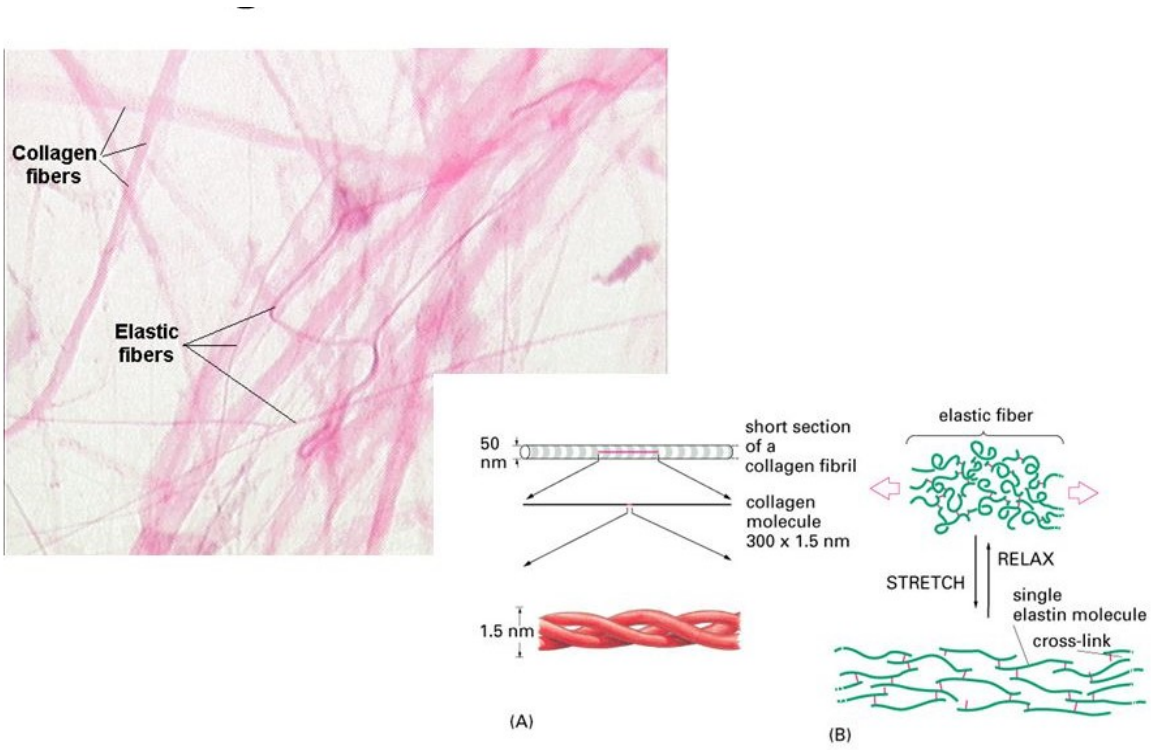

Figure 1-8: Collagen and Elastin fibres coexist within cartilage (Pearson Education 2012)

Collagen is the most abundant structural macromolecule in ECM, and it makes up about 60% of the dry weight of cartilage. Type II collagen represents 90% to 95% of the collagen in ECM and forms fibrils and fibres intertwined with proteoglycan aggregates as shown in Figure 1-6 and Figure 1-7. Collagen types I, IV, V, VI, IX, and XI are also present but contribute only a minor proportion of the total collagen present. The minor collagens help to form and stabilize the type II collagen fibril network.

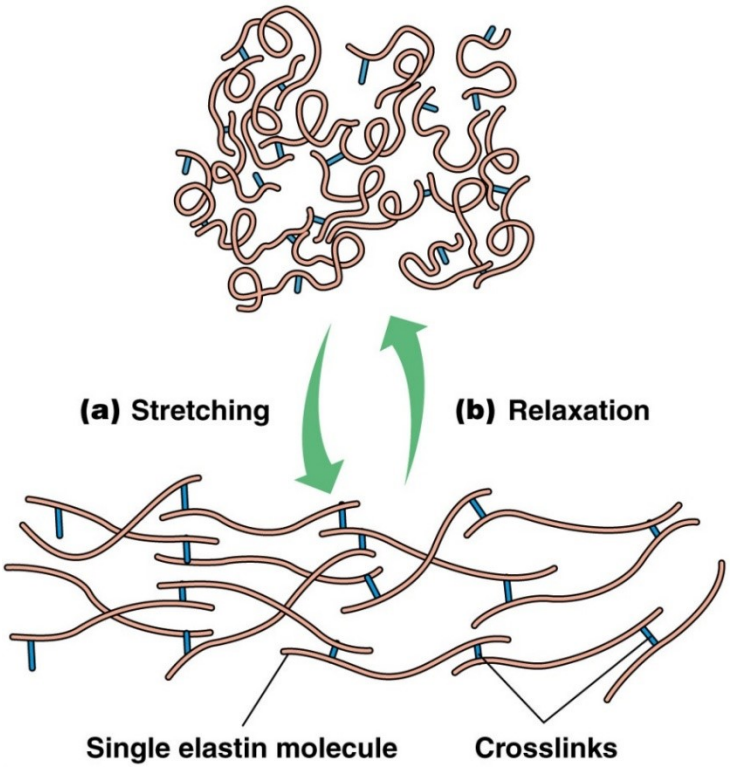

Figure 1-9: Elastin under tension and relaxation (Pearson Education Inc, 2012)

There are at least 15 distinct collagen types composed of at least 29 polypeptide chains. All members of the collagen family contain a region consisting of three polypeptide chains (α-chains) wound into a triple helix (Figure 1-11). The amino acid composition of polypeptide chains is primarily glycine and proline, with hydroxyproline providing stability via hydrogen bonds along the length of the molecule. The triple helix structure of the polypeptide chains provides articular cartilage with important shear and tensile properties, which help to stabilize the matrix. (Maroudas 1979).

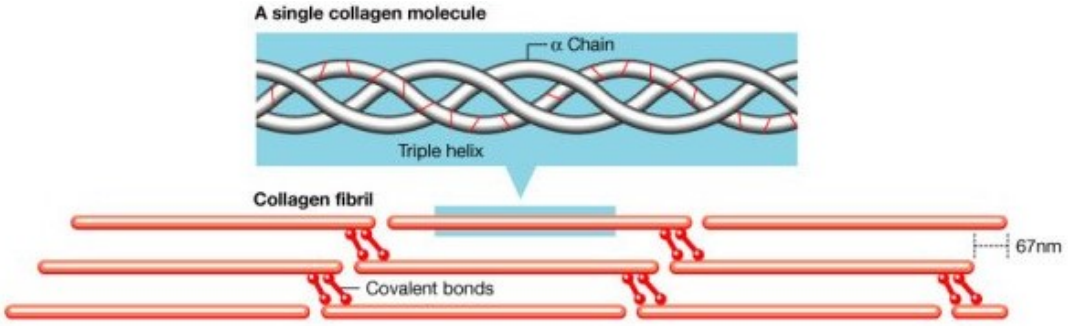

Figure 1-10: Collagen fibres resist tension and remain intact under compression (Mow 1992)

In its various forms, collagen accounts for approximately two thirds of the dry weight of AC. It has been previously reported that collagen type II is the predominant form found in AC (Eyre, 2001), along with traces of types IX and XI (Mow *et al*., 1992, Eyre, 2001). Type I and type III collagen are reported to also be present in the most superficial layer of AC (Teshima *et al*., 2004). Type III has been identified throughout the AC using new techniques (Eyre, 2001). Type I has also been found throughout AC, with its presence increasing with the age of the AC (Sasano *et al*., 1996).

The purpose of the various types of collagen has been thoroughly examined. For example, Sandberg *et al.* and Aigner *et al.* supposed that collagen type I and III may be residue from the perichondrium during the prenatal period (Teshima *et al*., 2004), while Eyre (2001) has stated that it is possible that type III, along with type II, is made by chondrocytes in response to matrix damage, similar to the function of type III in type I based collagen.

Quantitative analysis indicates that every type IX molecule is covalently cross-linked to a type II fibre; thus type IX may play a pivotal role in providing interfibrillar stabilisation between type II fibres (Mow *et al*., 1992). As no definite evidence, has been produced to either prove or disprove these theories, their effect on the properties and structure of AC is unknown.

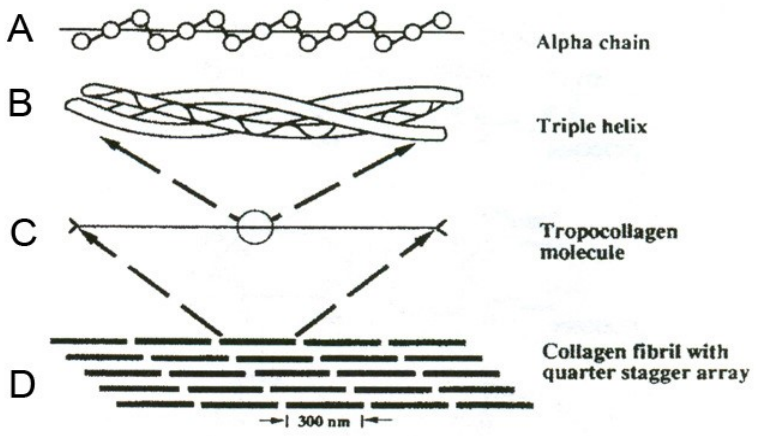

Figure 1-11: Components of a collage fibre. A – An individual α-chain, B – right hand coil of α-chains, C - tropocollagen molecule, D – formation of a collagen fibril (adapted from Mow *et al.* 1992)

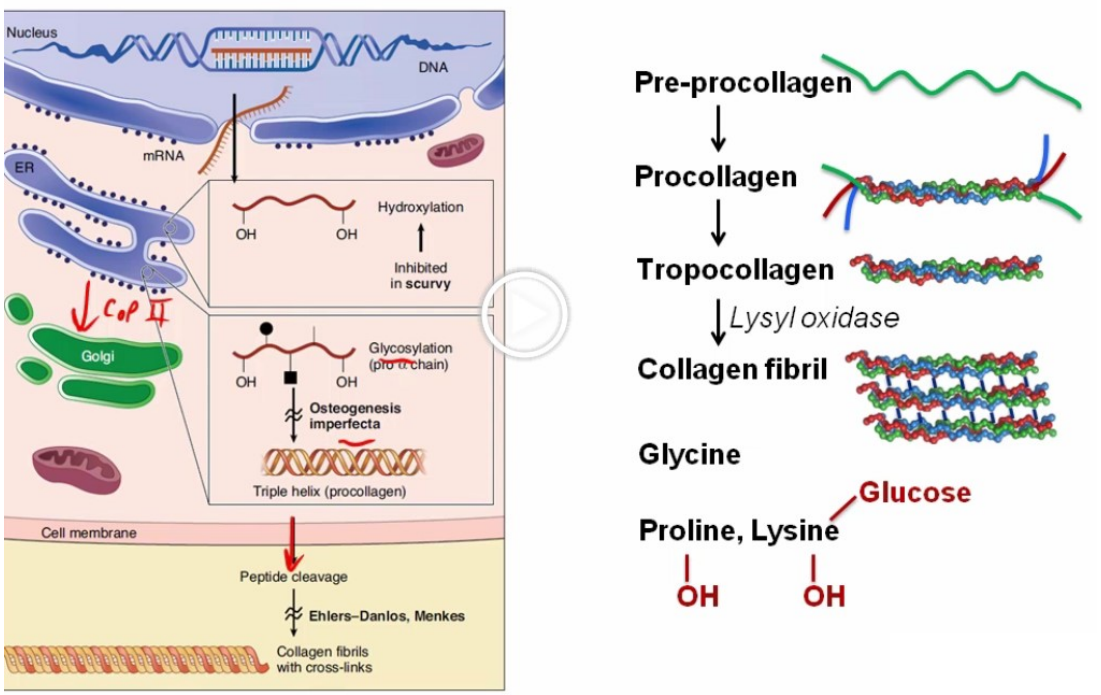

Figure 1-12: Collagen fibril formation from tropocollagen (Pearson Education 2012)

Advances in the science of understanding gene expression, have led to the discovery of the structure of individual collagen fibres (Shoulders and Raines, 2009). The basic tropocollagen structural unit is composed of three collagen polypeptide chains (α chains) coiled into left-handed helixes which, are further coiled about each other into right handed triple helixes, as shown in Figure 1-11 and 1-12 (Mow *et al*., 1992)(Shoulders and Raines, 2009). Each α-chain is composed of glycine, proline and either another amino acid or hydroxyproline (Mow *et al*., 1992). By varying the polypeptide composition (α-chain) of the tropocollagen molecule, different collagen fibres, such as those found in AC, are created (Mow *et al*., 1992). Polymerisation of these rod-like tropocollagen molecules occurs outside of the cells to form larger collagen fibrils. Intramolecular and intermolecular covalent cross-links form between the α-chains and collagen molecules (Mow *et al*., 1992). These cross-links function to maintain the cohesiveness of the collagen network and provide the high tensile stiffness and strength for the tissue (Bank *et al*., 1998, Quinn and Morel, 2007).

The high tensile stiffness of the collagen network is responsible for the resistance of cartilage to compression and fatigue (Bank *et al*., 1998). Under high load, cartilage acts as a non-compressive material, allowing a change in the shape of the matrix which is restricted by the collagen fibrils (Arokoski *et al*., 2000). Stronger orientation of collagen fibres in superficial and deep zones, compared with those in the middle, is responsible for greater stiffness of the network in these areas (Maroudas *et al*., 1980)

Elastin is another fibre found in the superficial layers of cartilage (Bo He, Wu JP, Chen H, Kirk TB and Xu 2013). Elastin provides an elastic structure that returns tissue to a rested ground state following tension forces (Figure 1-13). Elastin unravels and stretches with tension, but returns to its original state once the stress is released. Elastin and collagen coexist in many body tissues such as skin tissue, tendon (Bo He, Wu JP, Xu J, Day RE and Kirk TB 2013), blood vessels and heart muscle. In aging tissue both elastin and collagen are broken down and are depleted

1.3.3 Proteoglycans

Proteoglycans are heavily glycosylated protein monomers. In articular cartilage, proteoglycans represent the second-largest group of macromolecules in the ECM and account for 10% to 15% of the wet weight. Proteoglycans consist of a protein core with one or more linear glycosaminoglycan chains covalently attached. These chains may be composed of more than 100 mono-saccharides; they extend out from the protein core, remaining separated from one another because of charge repulsion (Figure 1-13). Articular cartilage contains a variety of proteoglycans that are essential for normal function, including aggrecan, decorin, biglycan, and fibromodulin. (Buckwater JA, Rosenburg LA and Hunziker EB 1990); and (Grodzinsky 2011).

Proteoglycans are large organic molecules contained within the extra cellular matrix. The molecules consist of a protein core with attached glycosaminoglycan chains (Mow et al., 1992). These glycosaminoglycan chains bind to hyaluronic acid to form aggrecans.

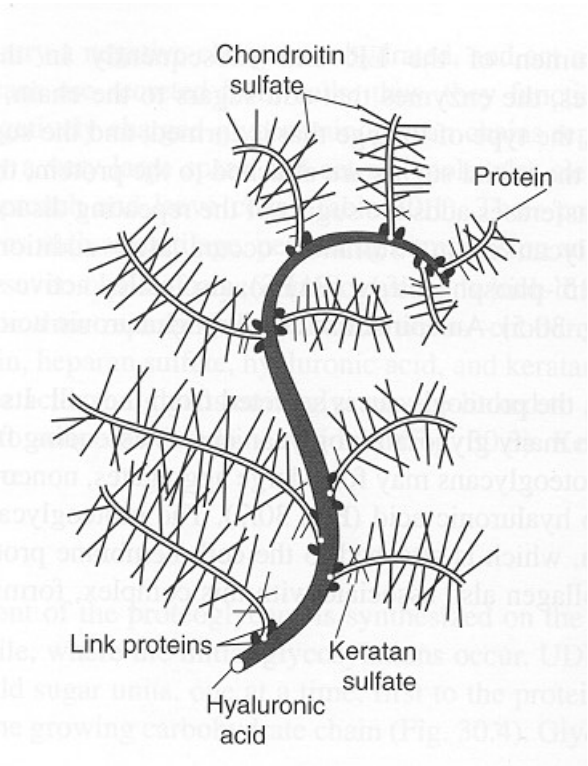

Figure 1-13: Proteoglycan structure in ECM (Grodzinsky 2011)

Proteoglycans are the primary component responsible for the compressive strength of AC. Aggrecans contained within proteoglycan molecules produce repulsive forces between each other due to their proximity and similar charge. The resultant swelling of the matrix resists compression within the tissue (Mow et al., 2005). The density of proteoglycans has been found to vary with the middle zones of AC containing more of these molecules than the upper layers (Mow et al., 2005). The depth dependent response of AC to compression can be accounted for by the variation in proteoglycan concentration within the tissue (Klein et al., 2007). Stiffer regions of AC have been found to correspond to areas of increased proteoglycan concentration (Klein et al., 2007).

The largest in size and the most abundant by weight is aggrecan, a proteoglycan that possesses more than 100 chondroitin sulphate and keratin sulphate chains. Aggrecan is characterised by its ability to interact with hyaluronan (HA) to form large proteoglycan aggregates via a link protein.

There is a strong structure-function relationship between the collagenous structure of the extra cellular matrix and the proteoglycan content which influences the mechanical properties of AC (Grodzinsky 2011). Proteoglycans bind strongly to type II collagen and weakly to type I collagen. The proteoglycan content is higher in regions rich in type II collagen compared to regions comprised primarily of type I collagen (Montes et al. 1988).

The structural arrangement of collagen fibres in AC plays a crucial role in the expulsion of fluids, both water and proteoglycan, from the bulk tissue (Nimni et al.1988). A densely-packed matrix provides resistance to fluid flow thereby allowing AC to better resist compressive loads. AC can be viewed as a fibre-reinforced composite material in which the collagen framework provides tensile and shear stiffness, while the proteoglycan constituent provides compressive strength (Mow et al. 1992). The integrity and porosity of the collagen framework plays an important role in the mechanical properties.

Evidence suggests negatively-charged compounds in proteoglycan react with positively-charged groups along the collagen fibrils (Mow *et al.*, 1992). This could account for the increased proteoglycan content in the deeper regions of the AC, where the collagen type II content is thought be greater (Montes and Junqueira, 1988).

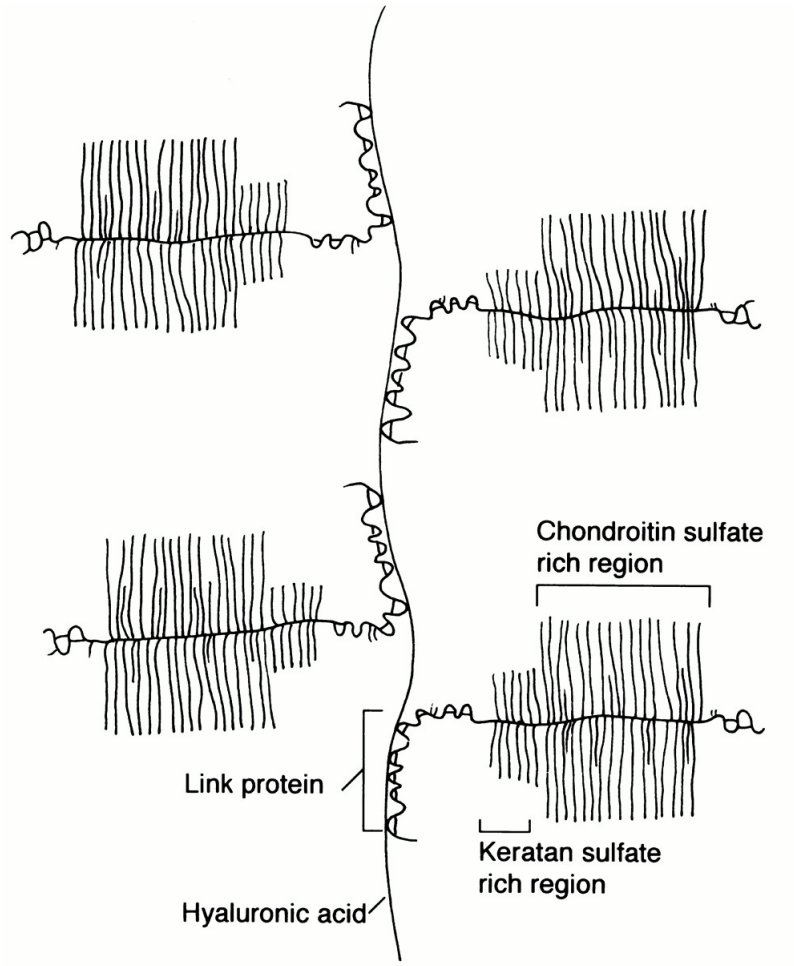

Figure 1-14: Sketch of proteoglycan structure within the ECM (Grodzinsky 2011)

Aggrecan occupies the ground space of the cartilage ECM between the fibres and provides AC with its osmotic properties, which are critical to its ability to resist compressive loads (Figure 1-14 and Figure 1-15). Aggrecan chains form negatively charged ions that repel each other and thus provide resistance to compression within the ECM (Grodzinsky 2011).

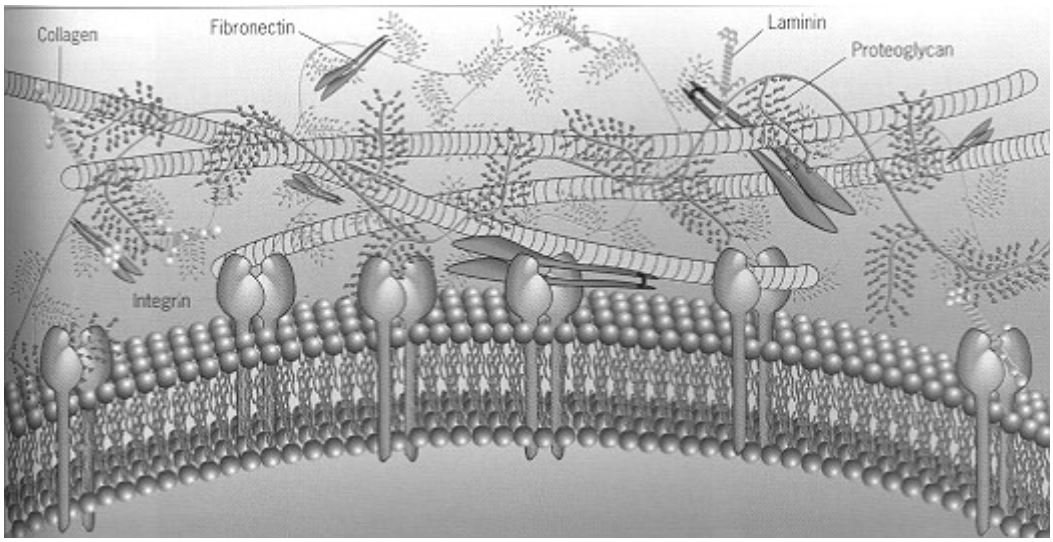

Figure 1-15: ECM showing component structures surrounding a chondrocyte
(Chen FH, Rousche KT and Tuan RS 2006)

The non-aggregating proteoglycans are characterised by their ability to interact with collagen. Although decorin, biglycan, and fibromodulin are much smaller than aggrecan, they may be present in similar molar quantities. Although these molecules are closely related in protein structure, they differ in glycosaminoglycan composition and function. These components have distinct characteristics, notably:

- Decorin and biglycan possess 1 and 2 dermatan sulphate chains, respectively;
- Fibromodulin possesses several keratin sulphate chains;
- Decorin and fibromodulin interact with the type II collagen fibrils in the matrix and play a role in the generation of fibres and their interactions;
- Biglycan is predominately found in the immediate surroundings of the chondrocytes, where they may interact with collagen VI. (Chen FH, Rousche KT and Tuan RS 2006).

1.3.4 Chondrocytes

Chondrocytes are often called cartilage cells (Figure 1-12). These cells secrete the non-cellular matrix of cartilage. As the extra cellular matrix forms, the chondrocytes become trapped in a pool of proteoglycan (also known as lacuna) and a web of collagen and elastin fibres. They often appear as single, paired or three isolated cells grouped together, encased within a small lake of material within the ECM.

In young AC, chondrocytes are spherical in shape. As the cartilage ages, deep level chondrocytes maintain their spherical shapes, however, chondrocytes within the superficial layers become elongated and distorted in the vertical direction, adopting a flattened or squashed ovoid appearance.

The chondrocyte is the resident cell type in articular cartilage. Chondrocytes are highly specialised, metabolically active cells that play a unique role in the development, maintenance, and repair of the ECM. Chondrocytes originate from mesenchymal stem cells and constitute about 2% of the total volume of AC (Alford J and Cole B 2005). Chondrocytes vary in shape, number, and size, depending on the anatomical regions of the AC. Chondrocytes in the superficial zone are flatter and smaller, having a greater density than that of chondrocytes deeper in the matrix. The chondrocyte trapped within its own matrix microenvironment is prevented from migration to adjacent areas of AC by collagen fibres. Each superficial zone chondrocyte establishes a specialised microenvironment and is responsible for the turnover of the ECM in its immediate vicinity

The chondrocytes are contained in cavities in the matrix, called cartilage lacunae. Around the lacunae, the matrix is arranged in concentric lines, as if it had been formed in successive portions around the cartilage cells. This constitutes the so-called capsule of the space. Each lacuna is occupied by a single cell, but during the division of the cells it may contain two or three cells. Lacunae are found between narrow sheets of calcified matrix that are known as lamellae.

Rarely do chondrocytes form cell-to-cell contacts for direct signal transduction and communication between cells. They do, however, respond to a variety of stimuli, including growth factors, mechanical loads, piezoelectric forces, and hydrostatic pressures (Buckwater JA, Rosenburg LA and Hunziker EB 1990). Chondrocytes have limited potential for replication and hence have a limited intrinsic healing capacity for cartilage outside of their immediate vicinity. Chondrocyte survival depends on an optimal chemical and mechanical environment.

1.3.5 Water

Water is the most abundant component of articular cartilage, contributing up to 80% of its wet weight. Approximately 30% of this water is associated with the intra-fibrillar space within the collagen, although a small percentage is contained in the intracellular space. The remainder is contained in the pore space of the matrix. Inorganic ions such as sodium, calcium, chloride, and potassium are dissolved in the tissue water.

The relative water concentration decreases from about 80% in the superficial zone to 65% in the deep zone. The flow of water through the AC and across the articular surface is thought to transport and distribute nutrients to chondrocytes, as well as providing lubrication. Much of the water appears to exist within the proteoglycan gel.

Frictional resistance against flow through the matrix is very high, resulting in a low permeability of the tissue. It is the combination of the frictional resistance to water flow and the pressurisation of water within the matrix that forms the basic mechanisms by which articular cartilage derives its ability to withstand significant mechanical loads (Fox AJS, Bedi A and Rodeo SA 2009).

1.4 Degraded Cartilage

Age determines the composition of the ECM as well as the organisation of chondrocytes and their response to external factors such as cytokines. With increasing age, there are zonal changes in the distribution of chondrocytes; however, the total number of chondrocytes remains unchanged.

In very young animals including humans, the early bone structures are normally composed of cartilage, which is mineralised over time with the uptake of calcium carbonate and calcium phosphate. These bone structures are very flexible and do not have the same mechanical properties of mature mineralised bone. Likewise, it was observed that the early cartilage structures in hyaline cartilage are more flexible (or less mechanically stiff) than aged cartilage. The cartilage becomes less pliable with the growth of collagen fibres.

Chondrocytes begin to dissipate in the superficial region, whereas the deeper layers have an increased number of cells. With increasing age, there is a decrease in the hydration of the matrix, with a corresponding increase in compressive stiffness (Figure 1-17). This may have implications for the underlying subchondral bone, which may see increased forces as the cartilage loses its ability to undergo reversible deformation.

Figure 1-16: Normal vs damaged cartilage (from Molecular Probes®))

The size of proteoglycan aggregates within the ECM decreases with age. This occurs because of a decrease in the available binding sites of the hyaluronic acid (HA) chain or as the result of damage to link proteins and their glycosaminoglycan chains (Grodzinsky 2011). Aggregation may also affect pore size distribution and solute permeability. There is also an increased ratio of keratin sulphate to chondroitin sulphate. The concentration of hyaluronic acid increases with age due to the gradual accumulation of partially degraded hyaluronic acid rather than increased synthesis. (Ateshian GA, Warden WH Kim JJ et al 1997)

Degradation of the AC leads to the replacement of the frictionless articulating surface with a rough section of bone giving rise to osteoarthritis (Figure 1-18).

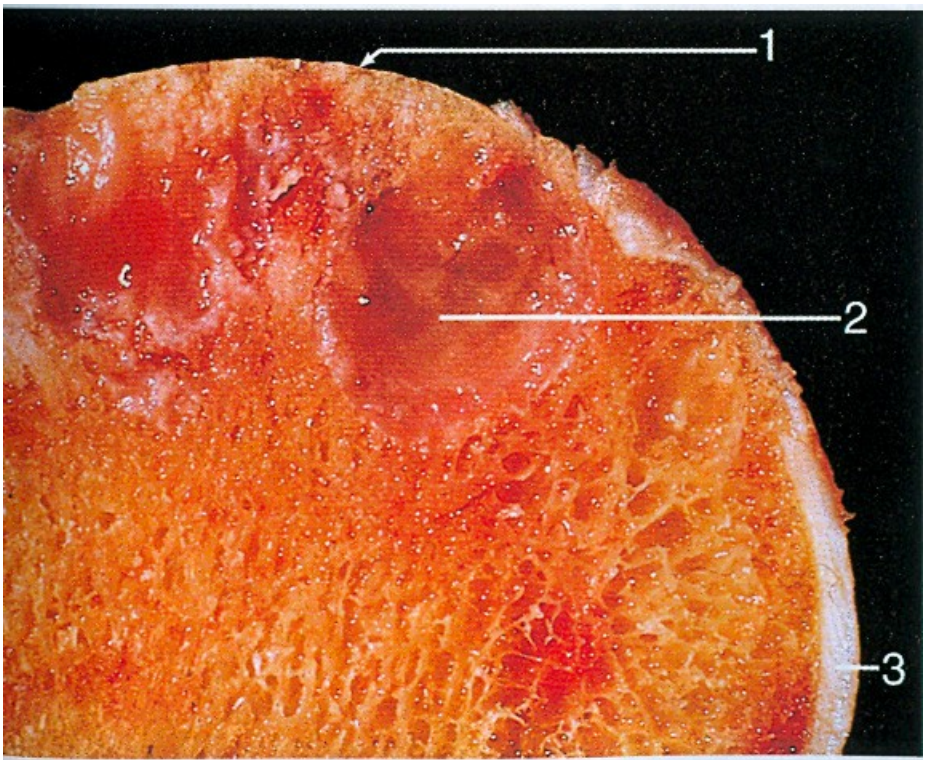

Figure 1-17: Cross section of femoral head showing (1) a region where the AC has been entirely worn away, exposing the bone which acts as an articulating surface; (2) degenerative cyst within the subchondral bone; and (3) residual normal cartilage (Robins et al. 2005)

1.5 Osteoarthritis

One of the main motivations for studying articular cartilage is to develop a better understanding of cartilage diseases such as osteoarthritis. Osteoarthritis, the most common form of arthritis is a debilitating disease affecting the normal use of synovial joints. Statistics from the Australian Bureau of Statistics in 2013, relating to osteoarthritis include:

- Musculoskeletal conditions, of which arthritis and osteoporosis are the most common, are one of the major causes of chronic pain and disability in Australia;
- The 2011-12 National Health Survey found that 14.8% Australians (around 3.3 million) had arthritis, with prevalence higher amongst women (17.7%) than men (11.8%);
- Of persons with arthritis, 55.9% had osteoarthritis and 13.6% had rheumatoid arthritis;
- Approximately 13.4% of the Australian population suffers from arthritis, with a further 27% diagnosed with symptoms of arthritis; and
- An estimate of the expectation of individuals suffering from osteoarthritis over their entire life span is as high as 1 in 2.

Osteoarthritis has been closely linked with the deterioration of articular cartilage in synovial joints, beginning with the superficial (uppermost) layer (Broom N and Poole C 1983) and (Robbins S, Abbas N, Kumar V and Cotran R 2005).

Articular cartilage affected by osteoarthritis is characterised by:

- Abnormal collagen fibre orientations;
- Breaks in collagen fibres;
- Reduced density of collagen fibres;
- Different ratio of collagen fibre types;
- Clumping of chondrocytes; and
- Deformation of chondrocytes (elliptical shape as opposed to spherical).

The knee is the largest and strongest joint in your body (Figure 1-15). It is made up of the lower end of the femur (thighbone), the upper end of the tibia (shinbone), and the patella (kneecap). The ends of the three bones where they touch are covered with articular cartilage, a smooth, slippery substance that protects and cushions the bones as you bend and straighten the knee. This is the joint that was studied.

Two wedge-shaped pieces of cartilage called meniscus act as "shock absorbers" between your thighbone and shinbone. They are tough and rubbery to help cushion the joint and keep it stable (Figure 1-18).

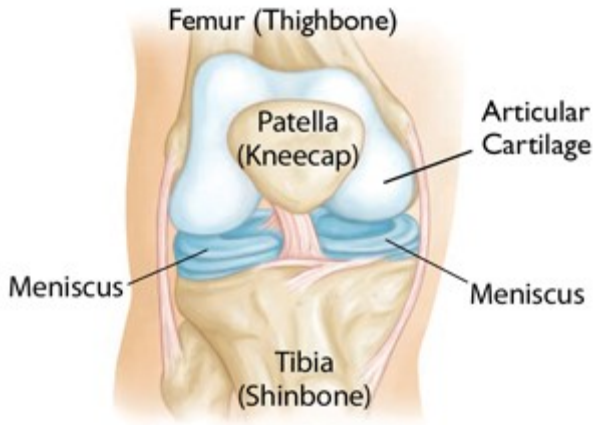

Figure 1-18: Normal human knee joint (from Molecular Probes®)

The knee joint is surrounded by a thin lining called the synovial membrane. This membrane releases a fluid that lubricates the AC and reduces friction.

Osteoarthritis is the most common form of arthritis in the knee. It is a degenerative, "wear-and-tear" type of arthritis that occurs most often in people 50 years of age and older, but may also occur in younger people.

In osteoarthritis, the cartilage in the knee joint gradually wears away. As the cartilage wears away, it becomes frayed and rough, and the protective space between the bones decreases. This can result in bone rubbing on bone, and produce painful bone spurs.

Osteoarthritis develops slowly and the pain it causes worsens over time due to the direct contact and rubbing of bone on bone as the AC layers are depleted.

Medical imaging tests for osteoarthritis (American Academy of Orthopaedic Surgeons, AAOS 2010) include:

- **X-rays.** These imaging tests create detailed pictures of dense structures, like bone. They can help distinguish among various forms of arthritis. For example, X-rays of an arthritic knee may show a narrowing of the joint space (Figure 1-20), changes in the bone and the formation of bone spurs (osteophytes).
- **Other tests.** Magnetic resonance imaging (MRI) scan, a computed tomography (CT) scan, or a bone scan may be needed to determine the condition of the bone and soft tissues of the knee.
- **Arthroscopic Examination.** An arthroscopy examination of the AC surface may give definitive evidence of articular cartilage health. The arthroscope is inserted into the knee capsule via two ports cut through the skin. One port provides saline under pressure to expand the knee joint so that the arthroscope can examine the articulating surfaces of the knee through the other port. The procedure is performed under a local anaesthetic. This is less invasive procedure than a punch biopsy.

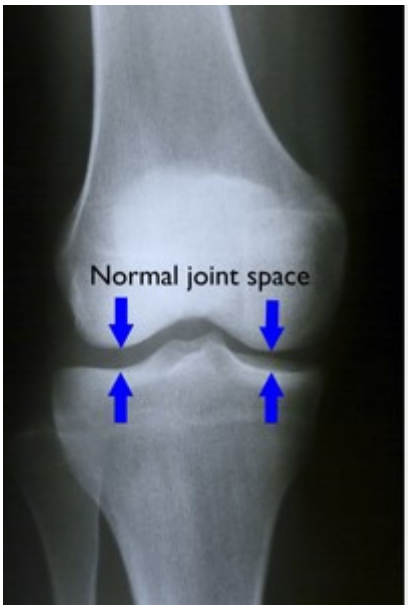

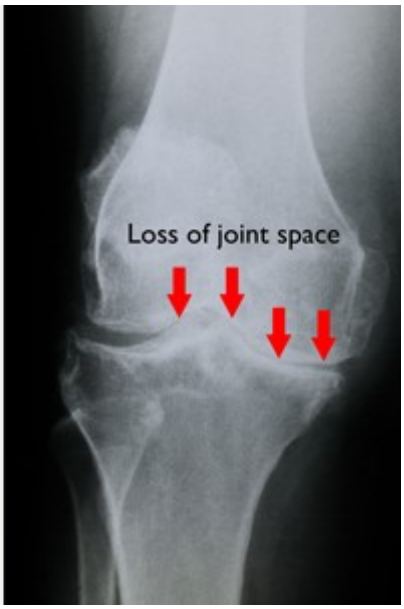

Figure 1-19 X-ray of a normal knee joint **Figure 1-20 Osteoarthritic knee joint**

Osteoarthritis is characterised by the progressive degradation of the articular cartilage of synovial joints. The disease begins as damage to the superficial zone of the articular cartilage, which when compromised no longer provides a low friction surface and protection to the underlying type II collagen. As the disease advances the entire thickness of the cartilage is worn away and painful bone to bone contact occurs. Reliable treatment for osteoarthritis does not exist and various experimental treatments depend upon the stage of the disease. Joint replacement surgery is used when extensive damage has occurred and the bone surfaces have been significantly deformed. However, if the bone surface is intact and isolated cartilage exists, cartilage repair techniques can be applied. These repair techniques aim to regenerate the natural cartilage to replace the original surface

1.6 Cartilage Repair

Osteoarthritis surgery had its origins in ancient Greece, where it was observed that damaged articular cartilage never heals (Widuchowski W, Widuchowski J and Trzaska T 2007). Surgery is therefore required to repair damaged AC and restore function in partial or full thickness defects (Tam HK, Srivastava A, Colwell CW and D'Lima DD 2007). Current treatment methods consist of osteotomy to correct joint misalignment and arthroscopic lavage to temporarily alleviate symptoms. Alternative treatments include abrasion arthroscopy, subchondral drilling, and micro-fracture techniques. There are currently multiple treatments available for the repair of articular cartilage damage. Unfortunately, these options only provide temporary relief and do not guarantee long term repair (Zheng M H, Willers C, Kirilak L, Yates P, Xu J, Wood D and Shimmin A 2007). In extreme cases, joint replacement by surgical intervention is preferred to provide longer term relief (Figure 1-21).

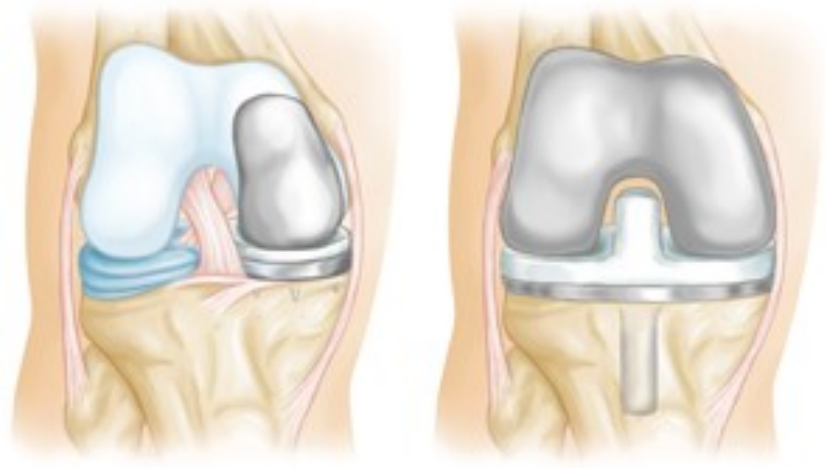

Figure 1-21: Model of partial (left) and full (right) knee replacement (Molecular Probes®)

The articular cartilage surface can be damaged by trauma such as a sports injury. Normal use, including running, will not wear out the cartilage unless it has been previously injured or if the meniscus cartilage has been removed. Bone misalignment or being overweight can also contribute to damage. The diseases osteoarthritis and inflammatory arthritis can directly damage the cartilage surfaces as well.

Damaged articular cartilage will not heal of its own accord. Over time, the cartilage breaks down and the underlying bone reacts. As the bone stiffens and develops bone spurs (osteophytes) the joints become inflamed and swollen, which further damages the cartilage, leading to pain, swelling or loss of motion. This is traumatic osteoarthritis.

Knee osteoarthritis is the most common form of arthritis, affecting millions of people around the world. If left untreated, it is usually a progressive degenerative disease in which the joint cartilage gradually wears away.

Articular cartilage damage is graded according to its severity.

- Grade 0: Normal healthy cartilage.
- Grade 1: The cartilage has a soft spot or blisters.
- Grade 2: Minor tears visible in the cartilage.
- Grade 3: Lesions have deep crevices (more than 50% of cartilage layer).
- Grade 4: Exposed underlying bone.

The contemporary treatment for damaged AC is Matrix-Induced Autologous Chondrocyte Implantation ("MACI"®). MACI therapy involves the harvesting of a patient's chondrocytes which are then cultured in a laboratory and seeded onto a type I/III collagen matrix prior to re-implantation back into the patient. The aim of the treatment is the regeneration of hyaline cartilage. The study examined a limited number of patients although reported a 75% success rate for the MACI procedure (Zheng M H, Willers C, Kirilak L, Yates P, Xu J, Wood D and Shimmin A 2007).

The superficial zone has been identified as an important element to regenerate AC. Should a procedure not produce a naturally functioning superficial zone, then the regenerate AC would exhibit severely decreased wear life (Mow et al 1992). It has been recently highlighted that little attention has been paid to engineering a depth dependent structure in the collagen scaffold as part of the restoration of full function to the tissue (Klein et al 2007)

A correlation between histological findings and clinical outcome based on the scores has not been established to date. However, the significance and consequently the validity of our findings are limited by the numbers of histology samples taken and the procedure does not demonstrate a definite trend. In a study of 25 patients, matrix induced autologous chondrocyte therapy ("MACT") displayed a confirmed objective and subjective clinical improvement over a period of up to 5 years after operation. MACT proved suitable to treat cartilage. (Behrens P, Bitter T, Kurz B and Russlies M 2006)

The MACT/MACI represents a very cost-intensive procedure and to date it is covered by private insurance, in individual cases only. Since 2001 MACI treatments have been on the decline as porcine based treatments became economically preferred. (Behrens P, Bitter T, Kurz B and Russlies M 2006)

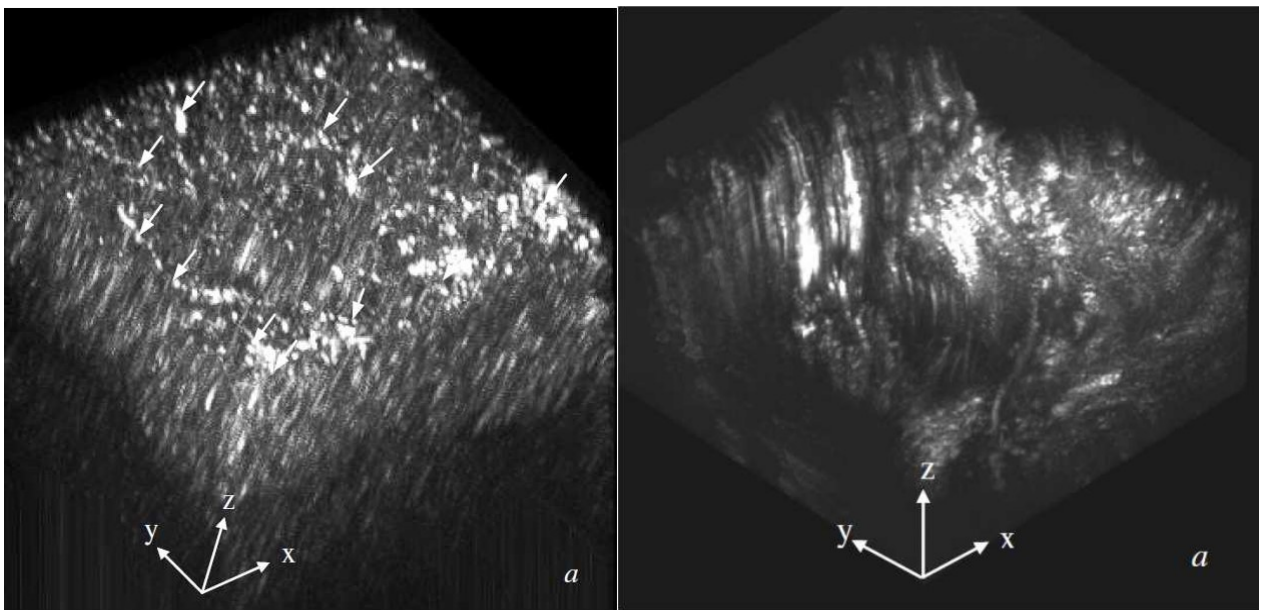

Figure 1-20 Confocal image of articular cartilage -Normal (left); and Damaged (right) **(Wu JP, Kirk TB and Zheng MH 2008)**

The main purpose of this study was the development of techniques to enhance *in vitro* staining of articular cartilage (Figure 1-22). Fluorescein, a readily available and viable stain, was selected to fit in with the confocal microscope on hand and to be non-toxic when applied to living tissue.

1.7 Cartilage Properties during Compression

Aggrecans within the AC matrix are responsible for its compressive properties. The similarly charged GAG chains attached to the protein backbone are in close proximity (static and compressed) and produce repulsive forces responsible for the swelling of the matrix which resists compression (Figure 1-23) (Korhonen et al. 2002; Mow et al. 2005) (Grodzinsky 2002). Articular cartilage displays depth-dependent and loading-dependent stiffness and displays creep behaviour and stress-relaxation behaviour characteristic of visco-elastic materials (Schinagl et al. 1997; Kerin et al. 1998; Wong et al. 2000; Wang et al. 2003). As AC is compressed, a non-uniform strain field is created throughout the tissue in which the superficial zone deforms more than the deeper layers

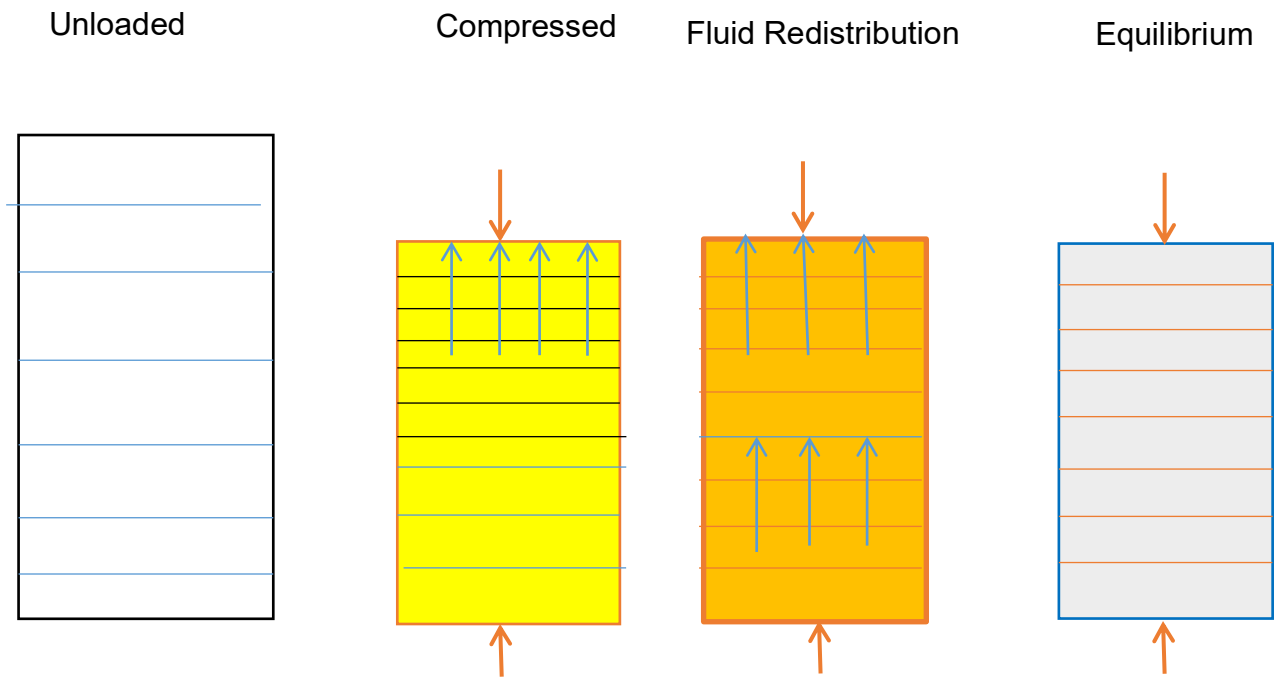

Figure 1-21: Compression of cartilage showing: normal state; compressed state; relaxation due to fluid movement; and equilibrium following creep (after Mow, 2005).

Different types of compression are achieved by the retention or removal of the compressive force, post initial compression. Stress/relaxation tests require the compressive force to be maintained for some time following initial compression. Creep testing requires the compression force to be increased to provide a constant pressure during the test.

The proteoglycans are initially held within the collagen matrix during compression by their viscous drag, as they flow through the tissue. As the tissue is held under constant compressive strain, fluid flows through the ECM to redistribute the strain field until a uniform strain throughout the tissue thickness is achieved "equilibrium" (Figure 1-23) (Mow et al. 2005). Therefore, the permeability of the cartilage matrix heavily influences the stress relaxation behaviour of the tissue. The mechanical properties of interest include compressive stiffness (as a function of compressive stress rate); relaxation stiffness due to redistribution of internal fluids; relaxation stiffness and equilibrium stiffness (following complete pressure redistribution or creep).

1.8 Compressive Methods

The compressive mechanical properties of AC can be assessed by unconfined, confined and indentation compression. These three compression modes have been extensively studied to produce numerous finite element models capable of predicting the compressive properties of cartilage (Schinagl et al. 1997; Jurvelin et al. 2000; Wong et al. 2000; Williamson et al. 2001; Korhonen et al. 2002a; Korhonen et al. 2003; Ficklin et al. 2007; Klein et al. 2007). It has been concluded that indentation compression results in a significantly higher Young's modulus than that determined by other compression regimes (Korhonen et al. 2002). Indentation compression regimes have been adapted for arthroscopic use to assess the mechanical properties of AC *in vivo* (Lyra et al. 1995). Brown reported that the use of handheld indentation probes cannot discriminate between healthy and osteoarthritic cartilage (Brown et al. 2007). Porous materials (0.5μm) are required for indentation and confined compression regimes to allow fluid flow under exterior load (Chen et al. 2001).

Previous studies have examined the topographical variation in mechanical properties (tensile properties included) across the entire knee joint rather than the site-specific variation which occurs along the femoral head (Jurvelin et al. 2000; Williamson et al. 2001; Williamson et al. 2003). In contrast to the studies of tensile properties, there are no conclusive studies investigating the development of compressive properties across the entirety of the femoral head (Williamson et al. 2001). It is of interest therefore to investigate the relationship between collagen fibre arrangement and the stiffness and equilibrium modulus across the femoral head.

Chapter 2 Imaging Cartilage

This section provides a brief overview on confocal microscopy and imaging articular cartilage.

2.1 Laser Scanning Confocal Microscopy

The basic concept of confocal microscopy was originally developed by Marvin Minsky in the mid-1950s (patented in 1957). Minsky's invention remained unnoticed, due to the lack of intense light sources necessary for imaging and the computer processing power required to handle large amounts of data. Following Minsky's work, M. David Egger and Mojmir Petran fabricated a multiple-beam confocal microscope in the late 1960s that utilised a spinning (Nipkow) disk for examining unstained brain sections and ganglion cells. Continuing in this arena, Egger further developed the first mechanically scanned confocal laser microscope, and published the first recognisable images of cells in 1973. During the late 1970s and the 1980s, advances in computer and laser technology, coupled to new algorithms for digital manipulation of images, led to a growing interest in confocal microscopy.

Fortuitously, shortly after Minsky's patent had expired, practical laser scanning confocal microscope designs were translated into working instruments. The first commercial instruments appeared in 1982. During the 1990s, advances in optics and electronics afforded more stable and powerful lasers, high-efficiency scanning mirror units, high-throughput fibre optics, better thin film dielectric coatings, and detectors having reduced noise characteristics. In addition, fluorochromes (unbound fluorophores) that were more carefully matched to laser excitation lines were beginning to be synthesised. The rapidly advancing computer processing speeds, enhanced displays, and large-volume storage technology emerging in the late 1990s resulted in a virtual explosion in the number of applications that could be targeted with laser scanning confocal microscopy.

Laser Scanning Confocal Microscopy ("LSCM") is an optical fluorescence imaging technique widely used for imaging biological specimens illustrated in Figure 2-1. The technique works by using a laser to excite a photosensitive stain (fluorophore) within a unit volume of the target specimen. The laser light is focused through a spatial filter and a pinhole, so that only light of the correct focal length illuminates the specimen, further increasing the resolution of the system by reducing the spread of laser light over several different focal lengths.

Laser light, being spatially coherent can be brought to a good focus by a microscope objective. The beam expander is used so that the full aperture of the objective lens is utilized. The pinhole spatial filter is not actually all that necessary, but is conventionally used with a beam expander to eliminate aberrations introduced by the first lens.

The laser light is focused through a spatial filter and a pinhole, so that only light focused at the correct focal length illuminates the specimen, further increasing the resolution of the system by reducing the spread of laser light over several different focal lengths. The laser beam passes through a beam splitter and the objective lens is focused onto the unit volume, causing the sample within the unit volume to fluoresce and emit light at a longer wavelength. The fluorescent light passes back through the objective lens and is separated from the laser light by the beam splitter (the beam splitter allows only light of the laser wavelength to pass). The fluorescent light then passes through a detector lens that focuses it onto the detector pinhole. The light emanating from different depths within the sample will not be in focus and subsequently rejected by the detector pinhole. A sensitive photomultiplier tube detects the intensity of the focused light passing through the pinhole filter and this signal corresponds to one voxel (3D pixel) within the image. By scanning the laser beam over the specimen, a single image section (2D image) is created. Altering the focal point creates optical sections at different depths, resulting in a series of 2D slices forming a 3D image.

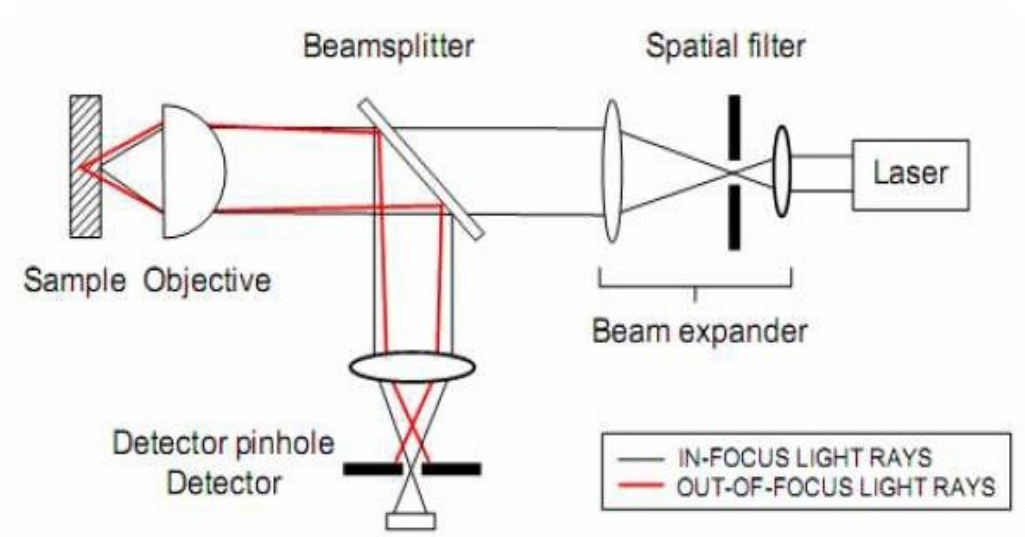

Figure 2-1 Basic principle of confocal microscopy. Light emanating from in front of or behind the focal plane is rejected by the detector pin hole.

LSCM has many advantages over other techniques, such as Electron Microscopy. Firstly, LSCM is a true 3D imaging technique. To create a 3D image using a technique such as Electron Microscopy, multiple thin sections of the specimen are required reconstruct the 3D object. This process is expensive, time-consuming and may lead to misleading results due to realignment of the sections and the resulting reconstruction. LSCM requires minimal sample preparation, reducing the cost and time taken to image the specimen, and reducing the disturbance to the specimen. For example, articular cartilage samples require dehydration in preparation for the vacuum environment required by electron microscopy. The high energies used by techniques such as Electron Microscopy or Stimulated Emission Depleted ("STED") microscopy dehydrate or burn the sample. This renders both techniques unsuitable for *in vivo* imaging.

Traditional optical microscopy is also unsuitable as collagen has a refractive index near one (thus the advantage of the fluorescence technique) and possesses insufficient resolution to make out more than the general texture of collagen fibres (Jeffery et al 1991).

The primary advantage of laser scanning confocal microscopy is the ability to serially produce thin (0.5 to 1.5 micrometre) optical sections through fluorescent specimens that have a thickness ranging up to 90 micrometres or more. The image series is collected by coordinating incremental changes in the microscope's fine focus mechanism (using a stepper motor) with sequential image acquisition at each step. Image information is restricted to a well-defined plane, rather than being complicated by signals arising from remote locations in the specimen. Contrast and definition are dramatically improved over wide-field techniques due to the reduction in background fluorescence and improved signal-to-noise ratio. Furthermore, optical sectioning eliminates artefacts that occur during physical sectioning and fluorescent staining of tissue specimens for traditional forms of microscopy. The non-invasive confocal optical sectioning technique enables the examination of both living and fixed specimens under a variety of conditions with enhanced clarity.

Figure 2-2: Commonly available objective lenses (from Molecular Probes®)

Objective lenses, as shown in Figure 2-2, are designed to assist in gaining the clearest image possible. For low magnification lenses with a long working distance, air is the preferred medium, to reduce aberration due to refraction along the light path between the sample and the lens (Figure 2-2). With higher magnification either a water immersion or oil immersion system is preferred. This helps to maintain the refractive index of the medium between the specimen and lens. Articular cartilage has a similar refractive index to the cover glass refractive index, which eliminates noise due to too much working light bypassing the lens Figure 2-3.

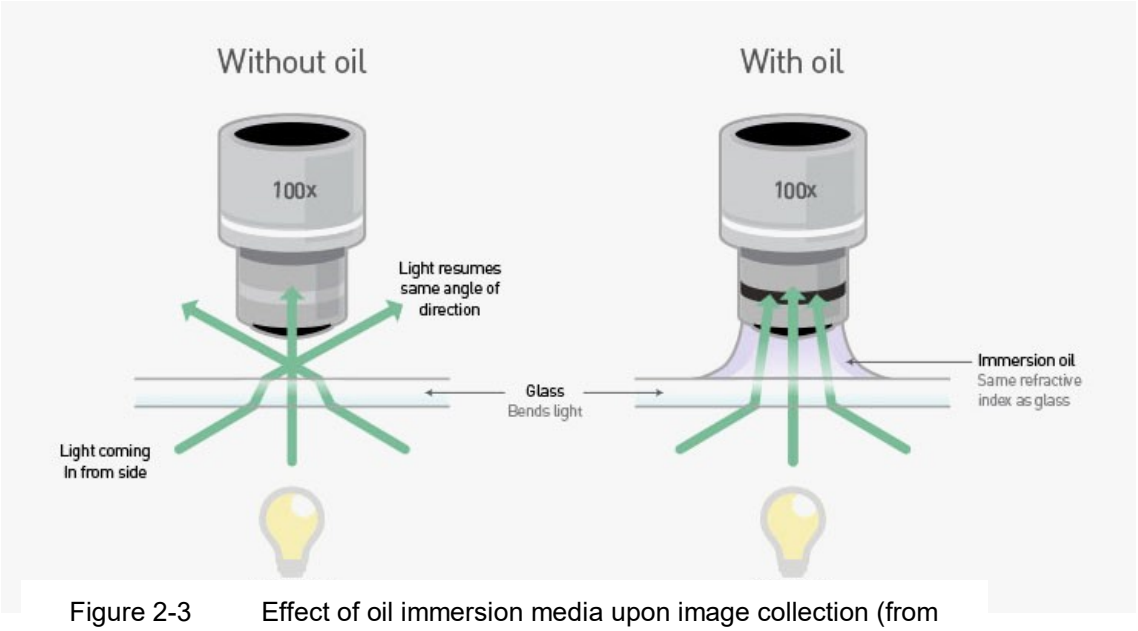

Figure 2-3 Effect of oil immersion media upon image collection (from Molecular Probes®)

The objective lens of a confocal microscope can be linked to an optic fibre endoscope, giving the confocal microscope the capability of an arthroscopic device for *in vivo* tissue examination. This also isolates the objective lens from the vibrations induced by the cooling fan on the microscope. The ease of use, non-destructive nature, and cost effectiveness of LSCM therefore makes it a useful study tool and makes an endoscopic LSCM a worthwhile contender for an osteoarthritis early detection system.

Numerical aperture “NA” shown in Figure 2-4 stands for numerical aperture and its value partly depends on the refractive index of the material that is between the objective and the glass coverslip mounting the sample (Figure 2-4). In general, objectives with higher NA give better resolution. Higher NA objectives often have higher magnification but require the use of some sort of immersion medium. Immersion medium is used to alter the refractive index of the space between the objective and the glass coverslip so that it is closer to the refractive index of the glass coverslip itself. This minimises refraction and loss of light, giving a better image.

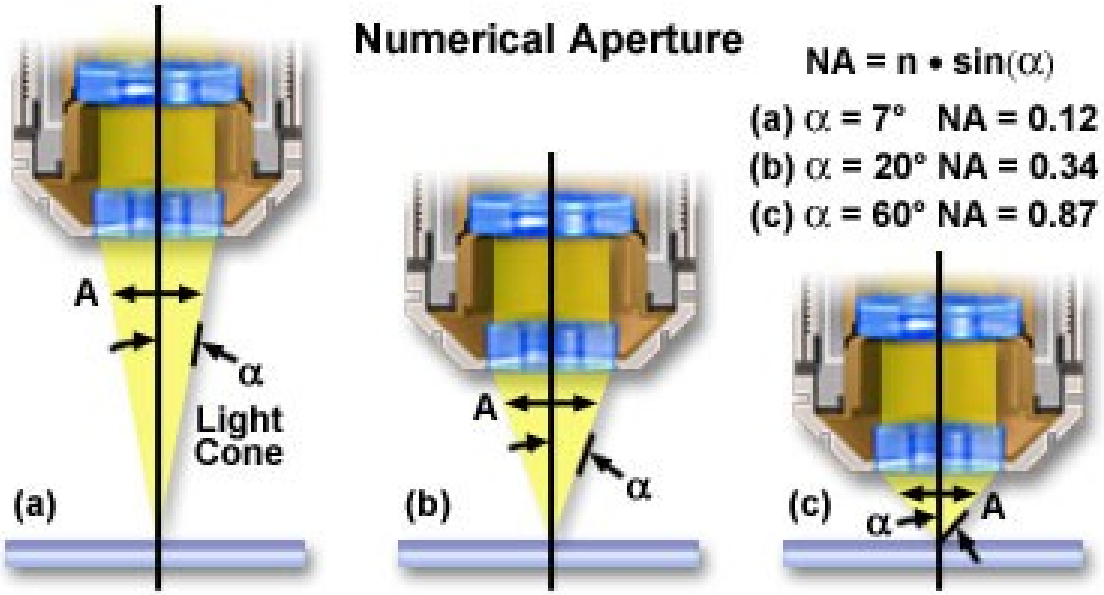

Figure 2-4: Effect of Numerical Aperture and working distance (from Molecular Probes®)

Considering Snell’s law, the numerical aperture (NA) equals refractive index (n) of the medium times the half angle (α) of the cone of light that enters or leaves the lens. The smaller the values of NA give rise to larger a working distance (Figure 2-5).

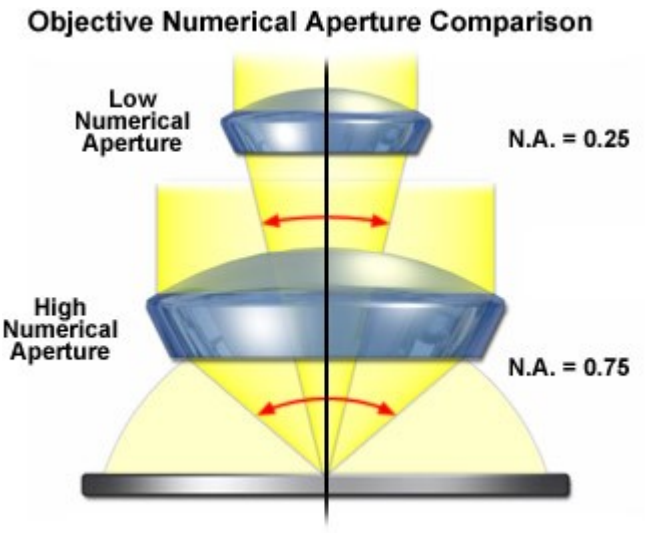

Figure 2-5: Comparison in width of field between high & low NA objective lenses (from Molecular Probes®)

$$NA = n \sin \alpha$$

For articular cartilage, the refractive index (n) is 1.51, and the maximum value of alpha (α) is 90°, which gives the maximum NA value of 1.51.

In practice, alpha (α) must be smaller than 90°, which is the minimum light path through the lens and gives maximum realistic value for NA to be 1.45 (Figures 2-6 and 2-7).

Air lenses are preferred to oil or water inversion lenses due to the ease of use. However, at higher numerical aperture lenses, oil immersion reduces the likelihood of aberration and hence for larger magnification objective, oil immersion lenses are preferred.

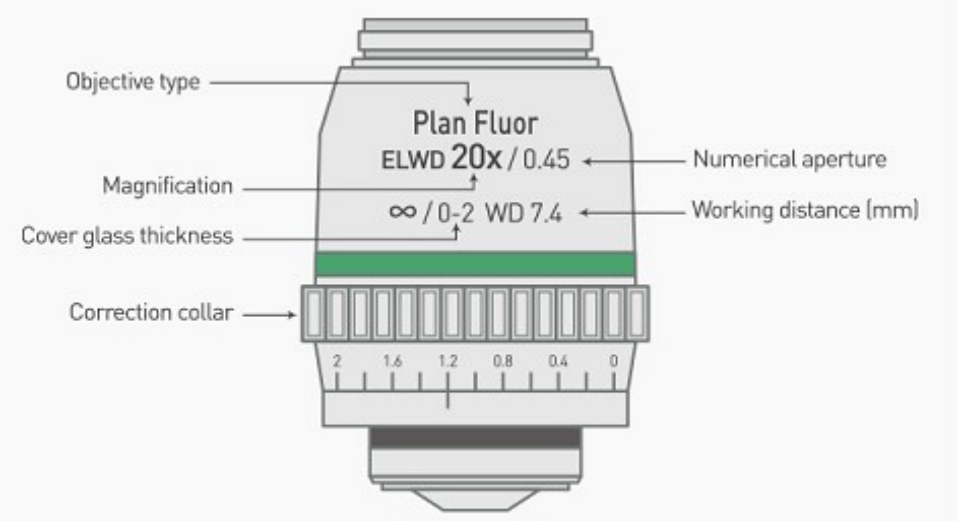

Figure 2-6: Low NA value objective lens (from Molecular Probes®)

Figure 2-7: High NA value objective lens (from Molecular Probes®)

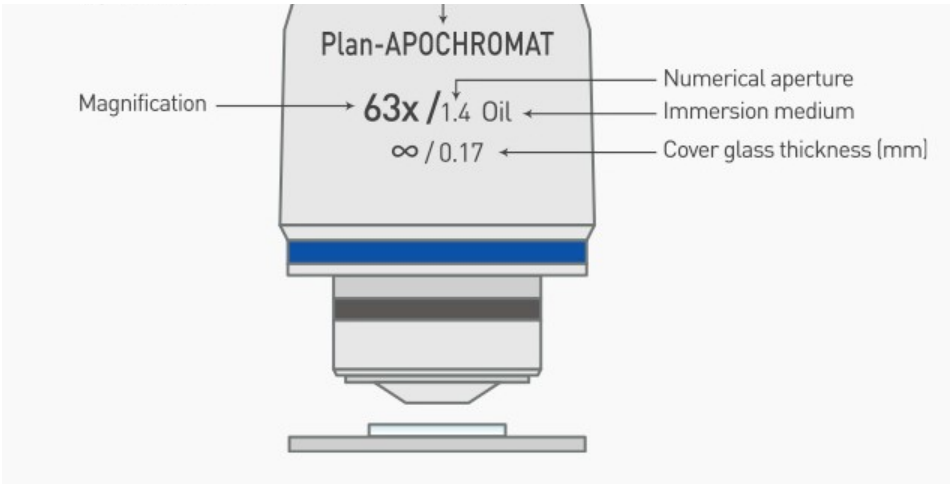

2.2 Laser Scanning Confocal Microscopy in Practice

Most the imaging work was performed on an Optiscan F900e confocal microscope, fitted with a 60X oil immersion lens or a Leica confocal microscope fitted with a 63X oil immersion lens. Both lenses had a numerical aperture of 1.4. With these lenses, the confocal microscopes have a lateral resolution of 0.23 microns and an axial resolution of 0.73 microns. Typical 3D images created by the confocal microscope consisted of 30 to 90 slices of 512 x 512-pixel image sections, corresponding to a sample area of 65 x 65 microns, with a depth of 15-30 microns. An image of this size takes 45 minutes to construct. Larger images were obtained using the Leica confocal microscope fitted with a 63X oil immersion lens giving an image resolution of 1024 by 1024 pixels.

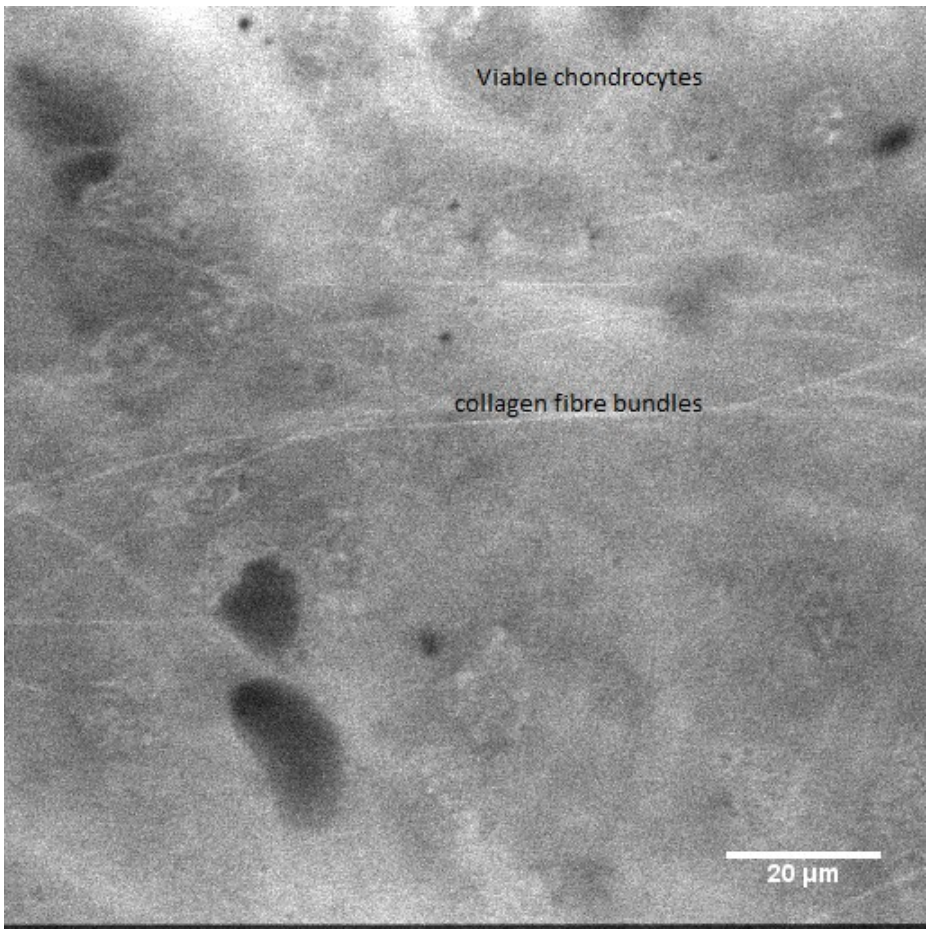

Image 2-1: Sheep cartilage showing collagen fibres

Fluorescein Isothiocyanate ("FITC") was used in this study as this dye allows for *in vivo* imaging of AC. Dr Wu investigated a number of other dyes including the Rhodamine range, Picro-Sirius Red, Texas Red and Immuno-cytochemical staining. Dr Wu concluded that these dyes damage the articular cartilage and are therefore unsuitable for use in a clinical environment (Wu 2005).

Furthermore, some dyes do not adhere to various structures within the sample and these produced incomplete fluorescent responses. Testing of various stains showed that FITC adhered to most objects within the sample set, provided that the sample was not dehydrated. FITC adheres to the water molecules that surround the collagen strands within the sample and it achieves the best response when the sample is fresh. Testing also showed that biochemical fixing of the sample with paraformaldehyde gave better results as the fixative was not auto fluorescent as the more commonly used fixative agent, glutaraldehyde.

Two typical images of a sheep's cartilage (Images 2-1 & 2-2) created by the Optiscan microscope are shown. These images and layers on either side of each will be used in this thesis to demonstrate the effect of the various techniques of imaging and the visualisation of cartilage.

The collagen fibres in Image 2-1 appear as bright features as the FITC dye attaches itself to the water molecules that are bound to the proteoglycans attached to the collagen fibres. The large bright lines present are collagen or collagen III fibres. The bright areas correspond to regions of dense collagen II fibres

Image 2-2 demonstrates the power of the LSCM in determining the histology of cells within the ECM. A LSCM image could be used to determine the nature and health of chondrocytes from *in vivo* examination of cartilage. The damage shown here is due to dehydration prior to the biopsy being imaged. The same image could have been collected from living cartilage, where the bright chondrocytes would be due to damage in situ.

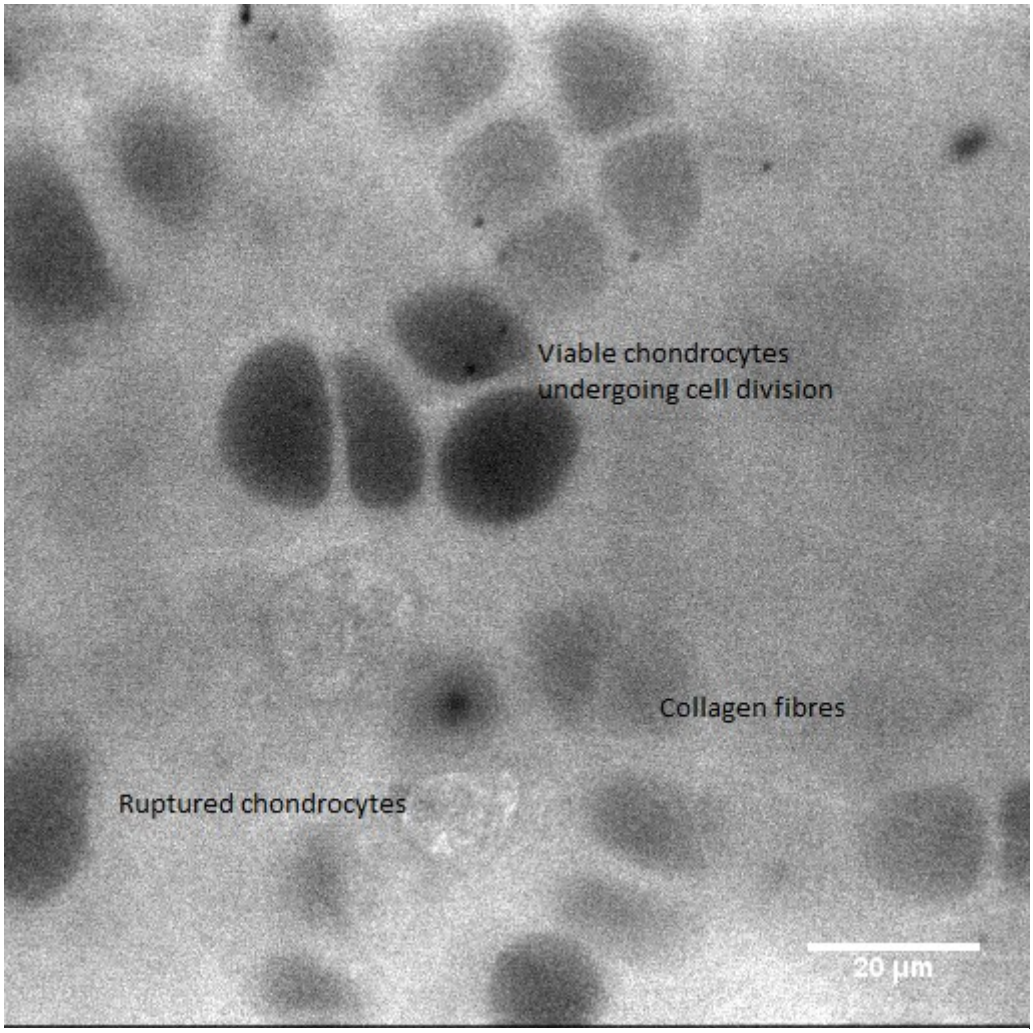

Image 2-2: Viable and damaged chondrocyte cells

The large dark regions in Image 2-2 are intact cells where the FITC dye cannot penetrate the cell wall and the bright circular objects are ruptured cells where the FITC has entered the damaged cell wall and stained the internal cell organs.

Table 2.1 below summarises the key characteristics of the different types of collagen present in articular cartilage.

Table 2-1: Overview of collagen types by appearance

Fibre Type	Size (microns)	Appearance
Collagen I	2-10	Bright individual or branched lines
Collagen II	0.02-0.08	Large bright regions
Collagen III	0.5-1.5	Sparse thin lines
Elastin	2-10	Not visible with FITC

Image 2-3: 3D volume rendition of confocal image stack

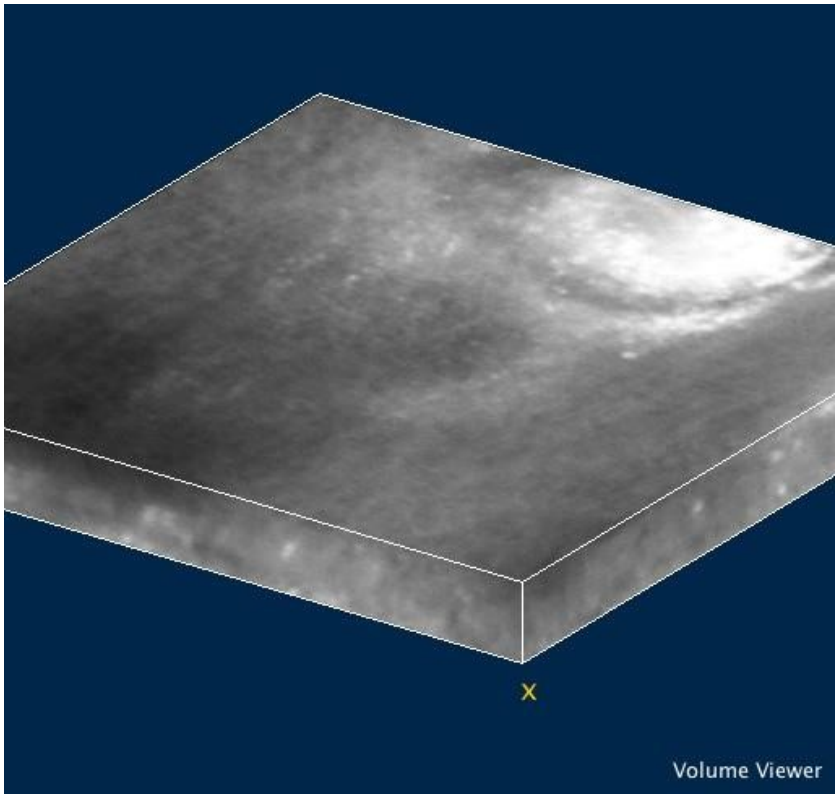

Image 2-4 is a single slice from the volume rendered cartilage sample. Image 2-3 is a 3D volume rendition is made up of 50 single 2D images.

Most chondrocytes appear as large dark dots, as the chondrocyte cell membrane is impervious to FITC. However, as the sample degrades, the chondrocyte cell membranes sometimes rupture and allow the stain to enter the cell wall thereby staining organelles within the chondrocyte. Subsequently the staining dye gets into the cell, resulting in the organelles within the chondrocyte appearing as a white dot in the confocal microscope image 2-4.

Consequently, when searching for chondrocytes in confocal microscope images of degraded samples, both white and dark dots need enhancing for further clarification and identification.

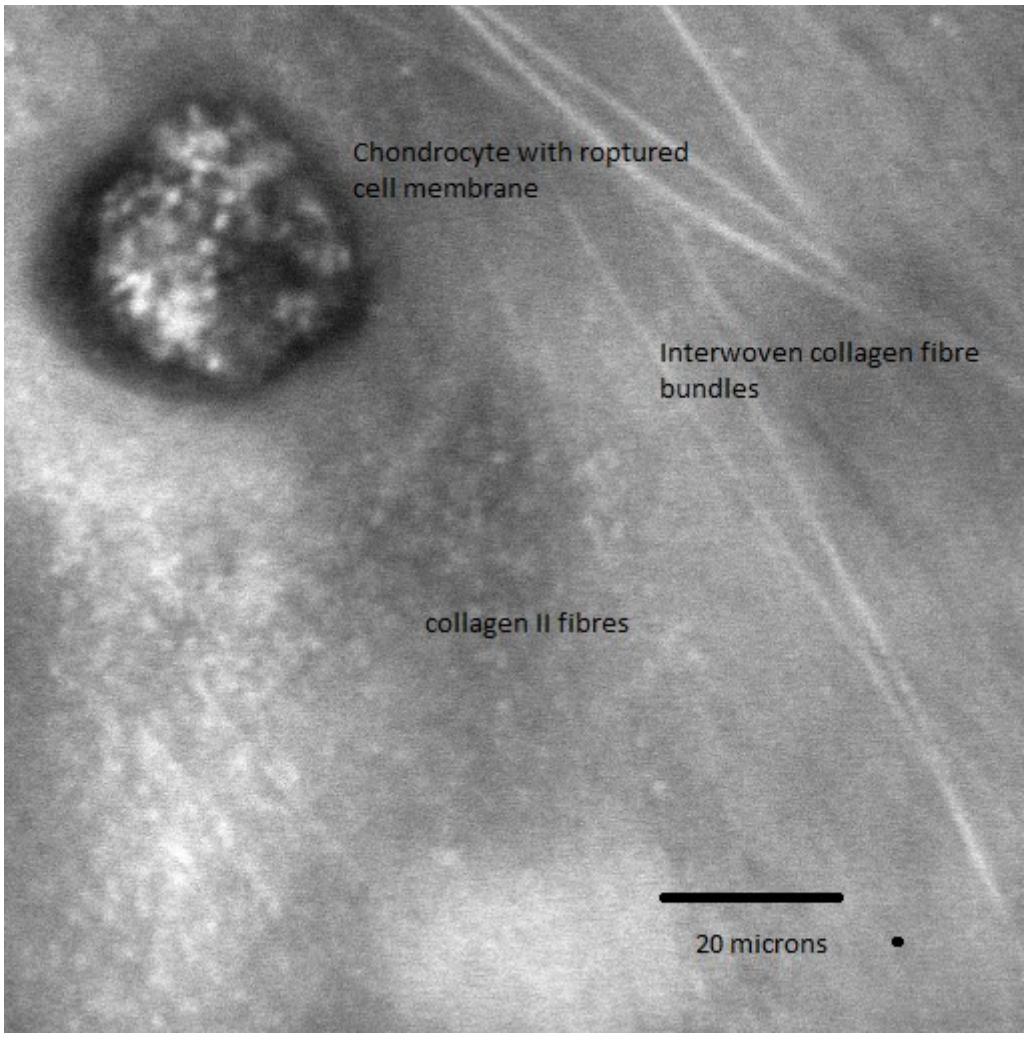

Image 2-4 : 2D slice of confocal image stack

In Image 2-4 the dispersion of the fluorescent stain creates a noisy response, which renders only the surface of the 3D visualisation visible. The thin bright objects located in the top right corner are collagen fibres, the dark circular object in the top left is a ruptured chondrocyte (broken membrane with the nuclear organelles showing as white dots within the surrounding dark cell membrane), and the bright shading in the bottom centre is the top of an intact chondrocyte.

Features within the sample are characterised by unusually dark or bright responses within the image. Collagen fibres have a bright response; while chondrocytes with ruptured cellular membranes appear as dark ellipses. The intact cellular membranes protect the interior of the cell from the stain. Ruptured or non-viable cell membranes allow stain to penetrate the cell due to breaks during sample preparation or degradation. The stain that penetrates the cell acts upon the internal structures by absorption causing the stain to fluoresce. However, in their current form, the collagen and chondrocyte detail is limited to the interpretation of various noisy patterns in the response. Thus, their 3D structure is not easily visualised. It was these limitations that provided the motivation to develop 3D phase symmetry.

2.3 Image Intensity: Function of Optical Depth

The specimen is excited with a coherent light source and objects within the specimen respond by emitting a light response with a longer wavelength back to the detector. The x and y position of the excitation beam, which is colocalised with the output beam, is recorded along with the output light intensity. These points when plotted form a scanned image in which the intensity of the fluorescent light is proportional to the type and concentration of excited material encountered. In general, most specimens need to be stained (by the addition of a photoactive substance) in a way that responds favourably to the excitation by laser light. These substances are called fluorophores and adhere to the internal structures of the specimen. Under ideal circumstances, such as multiphoton LSCM, the specimen will be auto-fluorescent, that is, the specimen will fluoresce without additional staining.

Fluorescence is the optical emission from molecules that have been excited to higher energy levels by absorption of electromagnetic radiation. The main advantage of fluorescence detection compared to absorption measurements is the greater sensitivity achievable, because the fluorescence signal has in principle a zero background. Analytical applications include quantitative measurements of molecules in situ within a specimen. The uptake of excitation photons and consequent release of fluorescent photons is shown in Figure 2-8.

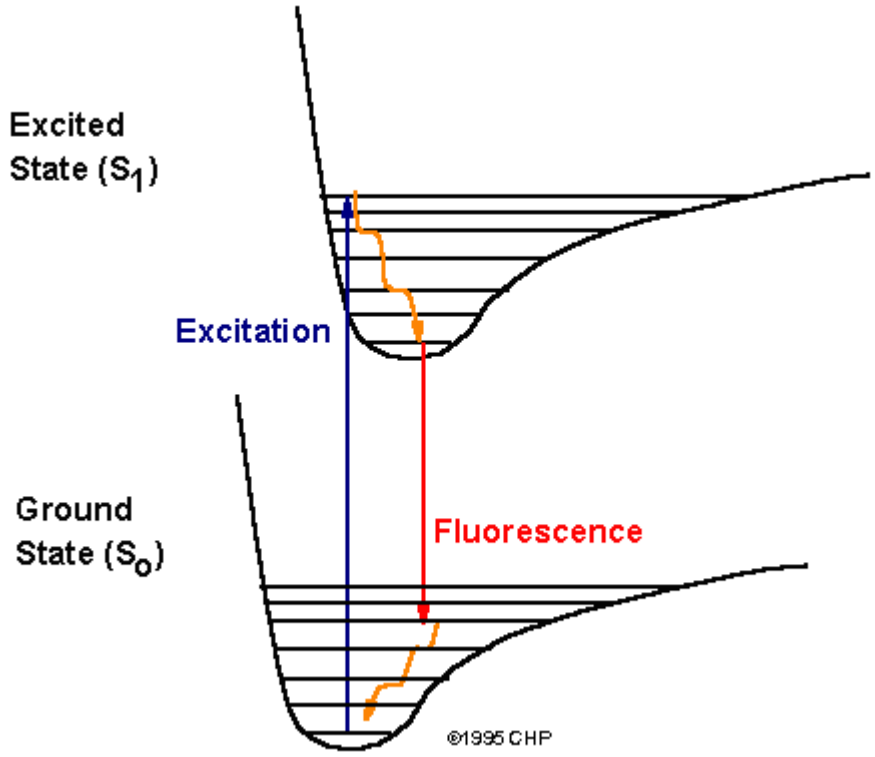

Figure 2-8: Fluorescence response to excitation radiation.

Note that in Figure 2-8, the length of the emission/excitation path is proportional to the wavelength of the photon exciting the ground state to an excited state and its subsequent release of the excited photon.

Figure 2-8 shows the capture of an excitation photon; the subsequent loss of thermal energy followed by the emission of a fluorescent photon in returning to the ground state. The excitation wavelength is shorter than the fluorescent photon wavelength and, using a dichromatic filter, the excitation energy can be removed from the returning emitted light to give a fluorescent image. This emitted light forms the principal of a fluorescent image. Non-active elements within the sample do not undergo fluorescence, which means that it is possible to segment the objects within the image by tracking the fluorescent response as a function of the location of the excitation light. The image formed is a scanned image or a bright field image, depending upon the nature of the microscope used. When the excitation beam width is very narrow with respect to the sample, the individual fluorescent responses are gathered to give a scanned image.

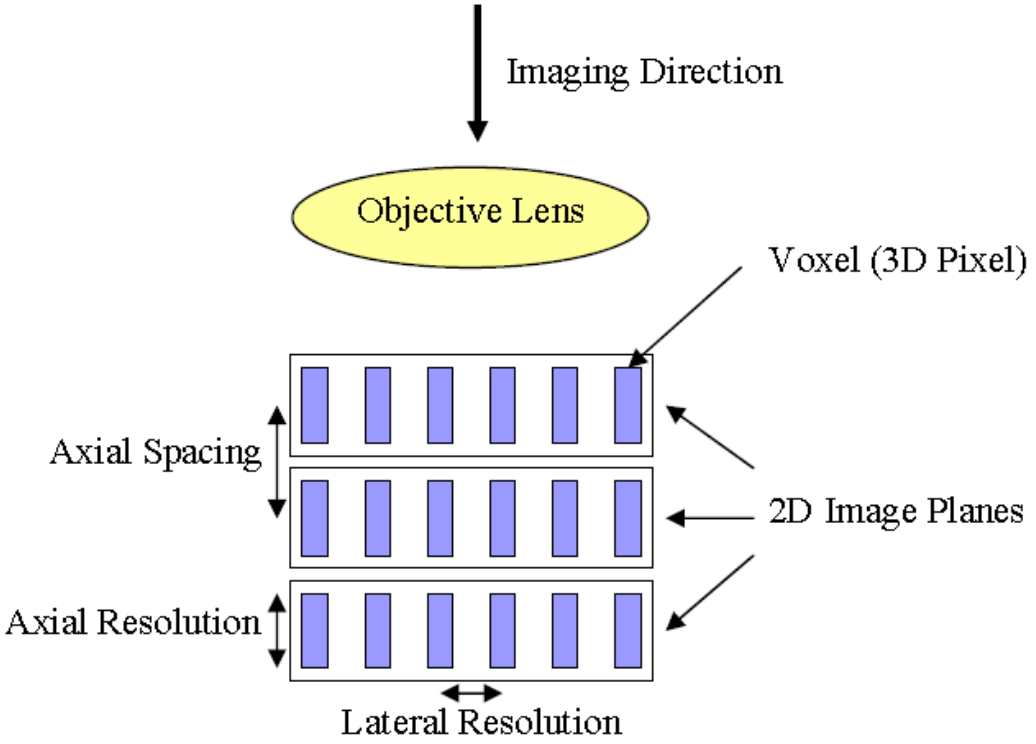

Figure 2-9: Formation of 3D scanned image

The scanned image has two fundamental sizes of resolution: the sideways or lateral resolution (x and y directions); and the axial resolution (z direction) as shown in Figure 2-9. Additionally, due to z direction motion, there is an axial spacing which may not match the axial resolution. Typically, the axial resolution and the axial spacing should be the same to give a good sampling rate for the image. When axial spacing is greater than axial resolution the image is left with un-sampled bands (under sampled). When the axial spacing is less than the axial resolution oversampling occurs and, there is duplication at the upper and lower edges of the image.

In practice, a fluorescent stain is required and it is added to the specimen under a reproducible protocol. In this study, fluorescein was chosen as the stain and each specimen was treated for five minutes by immersion in 0.05% FITC solution dissolved 9% phosphate buffered saline. The specimen was then washed with 9% phosphate buffered saline to remove excess stain, until the wash solution was clear with no sign of yellow colouration. The specimen was then subjected to laser radiation with a wavelength of 488 nm and a filter was used to block emitted light with wavelengths below 500 nm.

The fluorophores concentration was dependent upon the concentration of the stain binding to the bound water molecules within the specimen. For cartilage, the water binds to the surface of cell membranes as well as the water bound to the collagen fibres to produce the fluorescent images. The emission spectrum contained wavelengths from 500nm upwards. Shorter wavelengths, including the excitation frequency wavelengths, were blocked using an optical filter block to eliminate non-excited wavelengths from increasing the illumination response.

The input (excitation) laser is focused upon the section of specimen under observation (of known x, y and z co-ordinates). The laser excites the voxel in question and causes atoms within the eradiated region to absorb energy thereby putting the electrons into an unstable excited state. After a short time, the electrons lose energy and finally drop back to a ground state by emitting photons of lower energy than the wavelength of the excitation laser light. This emitted light is filtered to remove any excitation radiation and collected as the output signal of a photo multiplier tube detector.

Due to scattering, photons are emitted in all directions, and only a small proportion of the total photons emitted by the fluorescent stain re-enter the microscope lens to be captured by the detector. Both excitation light and emission light are scattered by opaque objects within the specimen and refracted by the rest of the specimen in a Gaussian distribution pattern. An optical filter is placed in the pathway of the emitted light to ensure the elimination of any excitation wavelengths from the emission spectrum.

The intensity of both the excitation beam and the emitted light beam varies with the focused depth within the specimen. Light focused and captured from the upper surface is stronger than light captured from lower planes within the specimen. However, due to the pinhole within the light pathway, all collected and excitation photons will be in focus. The resultant scanned images form a stack of in-focus planes slices, each associated with a particular focal length of the light path. When these planes are plotted, they form a 3D image of the specimen. In extreme cases, this can lead to intensity banding within the synthesised 3D structure.

In 2010, stack adjustments for contrast was added to ImageJ by Jan Michalek, who conjectured that

> *"fluorescent images captured by a confocal laser scanning microscope ("CLSM") from deep layers of a specimen are often darker than images from the top layers due to absorption and scattering of both excitation and fluorescent light. These effects cause problems in subsequent analysis of biological objects"*

(Michalek J, Capek M, Mao XW and Kubinova L 2010). His software plugin filter to ImageJ implements an algorithm for brightness matching of CLSM image stacks, based on aligning distribution functions of image pairs. A modified form of brightness compensation was added to my basic image processing.

Images acquired by confocal laser scanning microscopy should map regions corresponding to the same concentration of fluorophores in the specimen (light intensity of emitted light) to the same greyscale levels. Artificial colour mapped greyscales can be produced by simultaneous excitation and detection of the sample using a different set of excitation wavelength and block filters. They are collected on different detector channels and assigned greyscales in collected points. Often these are then displayed as red, green, and blue greyscale images. Due to multiple distortion effects, CLSM images suffer from irregular brightness variations, e.g., darkening of image edges and lightening of the centre. A spatially varying greyscale map complicates 3D image reconstruction during post-processing since measures of similarity assume a spatially independent greyscale map. ImageJ presents a fast correction method based on estimating a spatially variable illumination gain, and multiplying acquired CLSM images by the inverse of the estimated gain.

In practice, the ImageJ plugin had difficulties in estimating the illumination gain. A Matlab routine was created to remove spikey noise using a median filter, whereby the voxels immediately surrounding the voxel of interest are ordered in ascending order and the median value is used as the current voxel. This is replicated over the entire stack space of the confocal image (in either 2D for single planes or 3D for a larger stack sized samples). This spikey noise was overcome by using median filtering to generate histograms between the adjacent planes to correct image brightness for the overall 3D structure. Each plane was scaled by the intensity of the median illumination found within the histogram distribution to remap the brightness of objects that pass through more than one z plane in the image stack.

Image intensity smoothing and sub-voxel smoothing is shown in the following section 3.1.2.

2.4 Other Imaging Techniques

Other imaging techniques have been used to examine AC. These include transmission electron microscopy and scanned transmission electron microscopy. These dehydrate and shrink the sample unless cryogenic techniques are used to freeze the sample. The lack of specific staining makes identification of fibre bundles difficult, as electron microscopy uses the density (atomic mass) of the specimen to determine the sample composition. Electron microscopes are not very accurate in the separation of molecules under the atomic masses of 20. This means that objects composed of nitrogen, carbon, oxygen, and hydrogen do not image compared to heavier materials. The power required for clear images is often beyond the tolerance to resist damage to the biological samples.

The image collection in this study has been restricted to confocal imaging.

Chapter 3 Image Processing

This chapter covers the basic 2D signal (image) processing mathematics and the rationale for performing pixel (or 3D voxel) equalisation and smoothing operations.

3.1 Noise in Digital Images

Noise is the unwanted error within a captured image and results in poor feature textures and image definition. Scanning microscope images have some inherent noise due to the nature of signal capture from the photo multiplier tubes, the recording of the signal strength and the recording of the signal position (x, y co-ordinates). Light entering the microscope from outside of the view plane is kept to a minimum. By operating the instrument in the dark (light off), extra light from the microscope environment is prevented from entering the microscope objective. Manufacturers provide hardware assistance to reduce the noise level by averaging multiple frame scans to compile a single averaged composite frame; and by averaging single line outputs over a nominated number of single line scans. These hardware signal smoothing processes helps reduce noise at the cost of additional collection time on the instrument. If, however, noise persists, it can be reduced by further digital processing of the image including 2D and 3D filters to segregate and enhance features of interest. The filters are normally of limited extent, to smooth the gradient (pixel to pixel signal strength) and to assist in collecting clearer images.

The quality of the captured image is also affected by the axial collection of data. All light enters through one surface, moves through the specimen to the focal point and excites a fluorescent response that travels back along the excitation light path to a photomultiplier collector. Due to scattering within the sample and the extra distance travelled at larger depth, the intensity of the light is reduced. This intensity of the emitted light signal needs to be compensated to ensure identification of objects within the sample.

Digital signal processing can improve the quality of the digital image to correct for contrast, noise levels, edge detection and image clarity for display purposes.

3.1.1 Physical Noise Generation due to Sample Staining

When applied to articular cartilage, Fluorescein Isothiocyanate (FITC) disperses throughout the sample and specifically binds to collagen molecules. However, the exact amount of stain, its concentration, and the amount of time given to allow for dispersion and absorption, is a precarious balance that varies from sample to sample. Failure to reach this balance results in a combination of overstaining, under staining (where features are poorly resolved), or the uneven dispersion of stain throughout the sample (leading to areas of dark and low intensities spread across the corresponding image) (Wu, 2005).

According to Fick's Law, the movement of stain within a sample block is dependent on the transportation of the stain to the internal structures of the sample. Further, the exact distribution of the stain surrounding a given segment of collagen is unknown. Although, it would be reasonable to assume that the stain will have a high concentration immediately adjacent to the surface, with the concentration of stain decreasing with distance travelled away from the surface. This means that objects within the sample would stain at different time rates, leading to an uneven uptake of the stain on the surface of the object of interest, as well as the internal components of the sample, such as a chondrocyte or fibre bundles. Likewise, when the stain is washed in clean phosphate buffered saline ("PBS"), the stain at the surface is first removed to minimise the effects of overstaining the internal structures.

The surface of the AC sample has a strong signal but due to washing with PBS, the maximum signal strength is below the surface. The signal strength stays strong for some depth and then drops, due to uneven uptake of stain as the distance from the surface increases. This process shows the transport effects of the stain. The diffusion of liquid stain through a solid sample leads to uneven staining: overstaining at the surface and under staining deeper down. The under staining can be compensated, however, overstaining cannot as it appears as one bright undecipherable mass in the image.

For example, a collagen fibre would resolve as a blurred object, with stronger intensities corresponding to internal fibrils. In addition, there is no certainty that all focused light received from stain fluorescence is from a given depth within the sample. Hence, LSCM images will always be noisy, and it is the processed response to noise that will determine the accuracy of any resolved features. This is a fundamental limitation upon the use of stained samples and confocal microscopy. Thinner samples stain from both sides at once, but are more difficult to handle and prepare without mounting on a microscope slide. For *in vivo* or *in vitro* work, slide mounting is not possible. The sample thickness is uneven, which equates to staining from the outside surface only.

An artefact of staining the cell nucleus occurs because the nuclear membrane is impervious to FITC. This means that an intact membrane does not hold stain and appears as a dark region within the chondrocyte. However, when the nuclear membrane has been ruptured, stain is permitted to enter the damaged nuclear membrane to stain both the inside of the membrane and some of the nuclear organelles within the nucleus which then display as bright spots against a darker background. The side effect of this is that FITC can distinguish between viable and non-viable cells (i.e. healthy cells and nuclear membrane ruptured cells). This is clearly shown in Images 2-1 and 2-2.

3.1.2 Image Voxel Equalisation

The sample slice is constructed from a set of identical rectangular prisms that are assigned to a single intensity. These are viewed as a 3D scanned image. The length of the prism faces is different, with the longest length in the axial direction and shorter lengths in the transverse direction. When considering intensity differences, the difference between two adjacent image planes or slices in the axial direction is much larger than those in the radial directions. This gives rise to the image gradient being different in each of the x, y and z directions. Furthermore, the display of the image requires scaling in the axial direction to form a natural image. Scaling of the slices creates a larger data set and ensures that:

- No image scaling for viewing by ImageJ as the voxel sides are equal in length and thus the image does not require rescaling when viewed as a 3D entity; and
- The need to compensate the gradients when applying calculations for phase symmetry, phase congruency and monogenic filtering.

The derivation of mathematical compensation is dealt with later in this work, as the visualisation of 3D images required the scaling of the axial direction. ImageJ does not manage this well unless all three scales are similar (ideally identical). It was also found that continuity in objects spanning the z direction was more clearly imaged by scaling all axes to the same value. The phase congruency and phase symmetry calculations benefitted from the sub-voxel scaling of the image stacks.

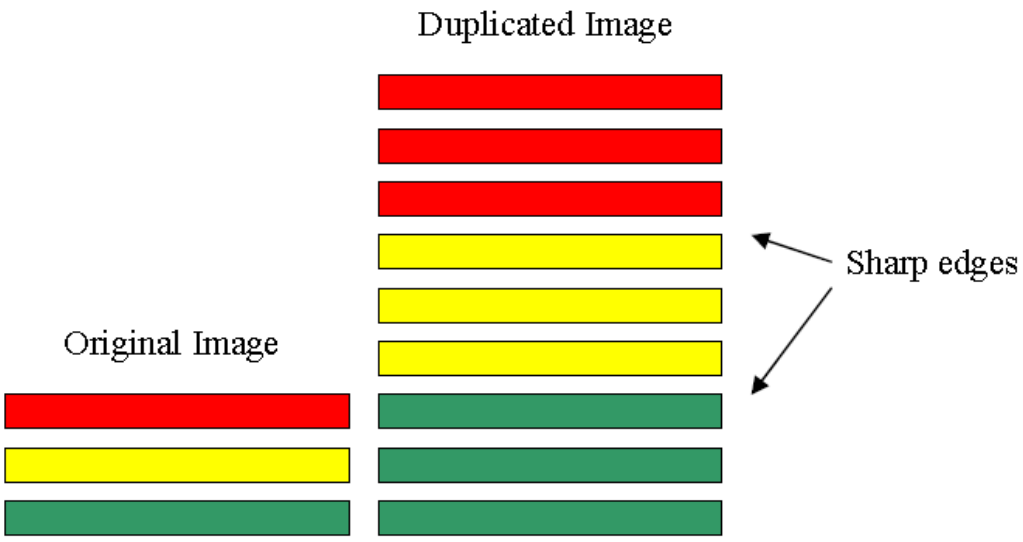

Figure 3-1: Image Equalisation. The compressed image is duplicated and the slice's edges use linear interpolation to give a smooth, sub-voxel transition between adjacent slices.

The image expansion that was implemented using linear interpolation provided clearer images than the non-scaled stack as shown in Figure 3-1. An expansion routine was developed to provide an isotropic image. Note that the increased number of stacks leaves the total image depth unchanged, by assigning sub-voxel values to the additional intermediate planes in the raw image. Another advantage of this expansion is that Gaussian de-noising also functions better as the voxel dimensions are now equal (i.e. the voxel is composed of cubic voxels rather than square prisms or rectangular voxels). Gaussian de-noising uses gradients to estimate the signal quality in each principal direction, and equal step sizes aids the process.

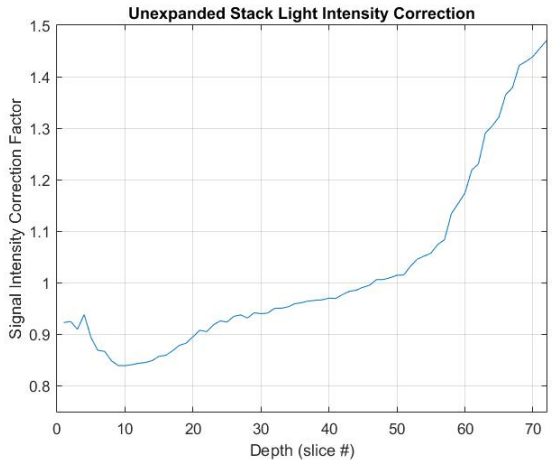

Figure 3-2: Raw Image Light Correction

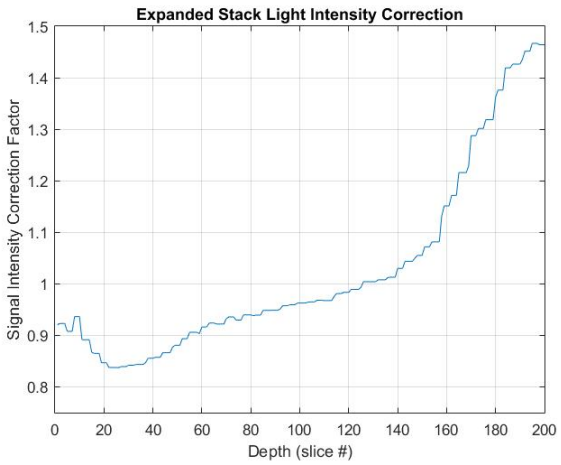

Figure 3-3: Expanded Light Correction

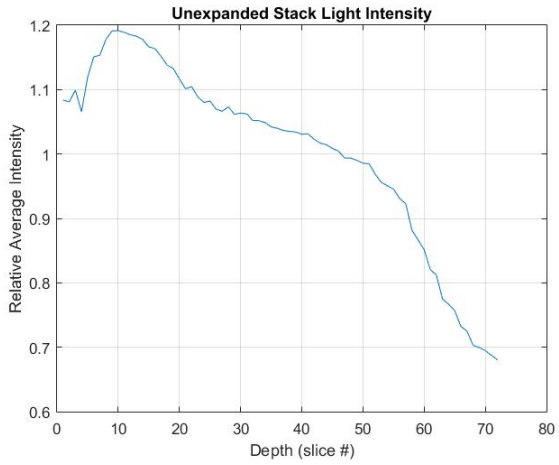

Figure 3-4: Raw Image Intensity

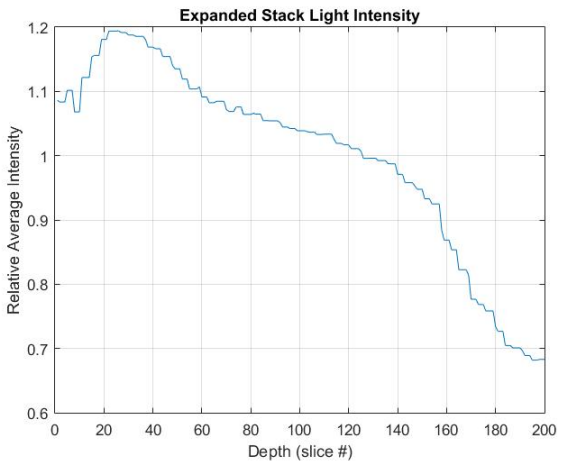

Figure 3-5: Expanded Image Intensity

Figure 3-2 shows the signal strength (image intensity) and correction factors required to balance the light intensity across the stack in an unexpanded image.

Figures 3-4 and 3-5 show the corresponding light intensity and correction factor applied to the raw image for the stack expanded to compensate for z-direction scale compression in the original stack. In this example the number slice elements was increased by a factor of 2.8 (i.e. from 73 slice elements to 201 slice elements) when the z increment was changed from 1.40 microns to 0.357 microns to match the x and y directions. This allowed ImageJ to display the 3D block directly without rescaling in the z direction, producing clearer and more realistic representations of the image viewed.

The shape of the features in Figures 3-2 and 3-3 are similar demonstrating that slice expansion has not altered the light intensity correction factors after expansion equalisation. The resultant 3D image has visibly less noise associated with the image.

Sub-voxel interpolation removes bands within the image due to under sampling of the image. Each stack is expanded by the same amount during the display process as the stacks do not consider vertical structures crossing slice boundaries. This gives rise to a displayed image that has bands of structure rather than a more uniform structural change from top to bottom.

As the study progressed, it was discovered that sub-voxel equalisation gave smoother images with less banding due to the excessive distance in the z direction. This was not an issue with 2D processing and became important only when 3D displays became more common. Sub-voxel equalisation allowed for smoother images with object's edges becoming clearer. Furthermore, voxel equalisation permitted interactive digital processing with the intermediate images being easily displayed by ImageJ without the need to rescale the z-direction and yet preserve the orientation and scale of these 3D images. Voxel equalisation along with intensity equalisation (see next section) has been adopted as standard practice prior to using other imaging techniques.

3.1.3 Image Intensity Smoothing

Noise is high frequency changes in pixel to pixel intensity. Unfortunately, image recognition (edge detection) is also derived from the high frequency sections of the image signal. Low frequency components relate to component segregation and lack detail of segmented shape due to interference with shape edges.

Most images will benefit from some high frequency smoothing whilst maintaining a clear low pass band filter to aid segmentation. Basically, 3D images contain noise within the vicinity of each voxel. Image 3-1 shows comparisons between the original images; the peak normalised image and the intensity normalised image, taken as sections across several slices rather than through the slices. The peak based output contains a number of dark banded lines due to abnormally high peak intensity values that has caused the peak normalisation method to overcompensate. The average intensity based method was successfully able to reject these high responses, giving smoother intensity distributions and reduced noise.

Figures 3-2 to Figure 3-5 display the normalisation coefficients for the average brightness algorithm for the image normalization from the values obtained in Image 3-1. There is a slight upward trend in coefficients with increasing depth, which is due to the images getting darker as depth increases. There are also several peaks and drops in the normalisation coefficients, which correspond to the average intensities of the image sections.

The phase symmetry and phase congruency methods are invariant to image parameters such as brightness; however, relative changes in brightness between image sections will impact the phase symmetry calculation. This is because the bright image slices between two darker sections represents a plane, which corresponds to a 3D phase symmetric feature. The image intensity also declines linearly with depth, as the light originating from deeper in the sample must pass through the overlaying material above it, where it is partially absorbed.

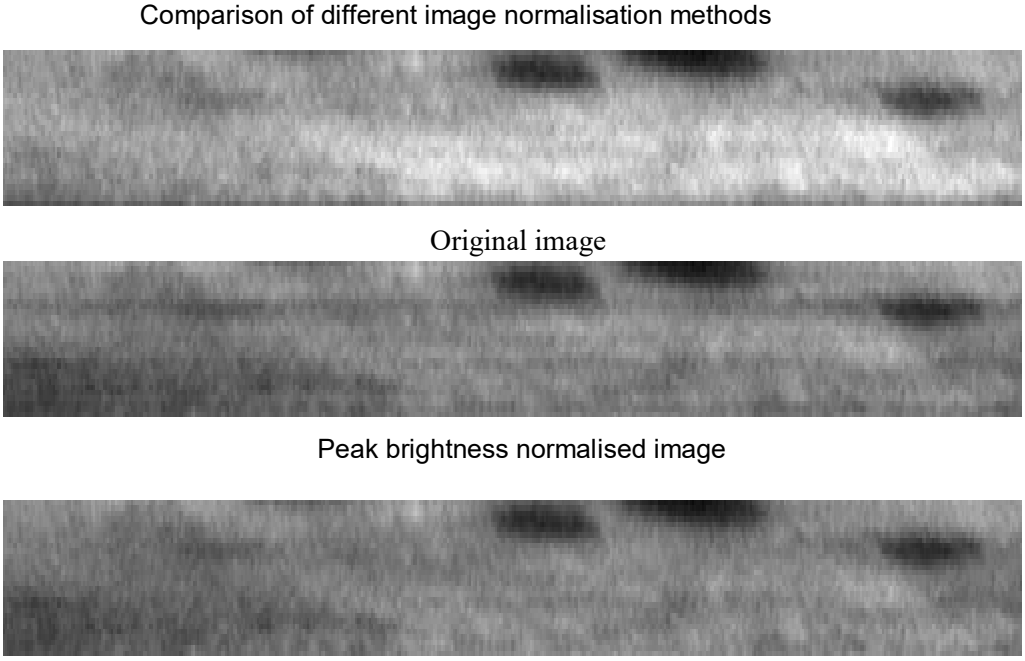

Image 3-1: Brightness equalisation over 25 stacks using peak and average normalisation

Additionally, uneven staining due to the dye tending to sit on the surface rather than penetrate the sample uniformly resulted in random bright regions near the top edges and bottom of the image. Images were normalised before being processed with a 3D Gaussian filter prior to the application of the phase symmetry and/or congruency routine(s).

The program initially used a simple peak intensity normalisation method, normalising the image greyscale values to have maximum and minimum values of 0 and 1 respectively. This method provided poor results, as image intensity varied widely over the image. Image 3-1 displays a typical confocal microscope image. There is a large bright area at the bottom of the image, and a darker region along the bottom left edge of the image. The peak intensity value in this case is not representative of the average image brightness. The use of a median filter removed single bright voxels from the image. A voxel is compared to its immediate surrounding voxels and replaced by the median value of the small sample. This eliminates bright spots in the image as high values are only passed when most voxels in the immediate region have a high signal.

To account for the wide range of intensity values in a typical image slice, a new average intensity based normalisation method was developed. In this approach, a normalisation factor was created for each image using Equation 3-1.

$$Normal = \frac{\sum image}{row \times columns \times slices} \quad (3\text{-}1)$$

The normalisation factors were then adjusted to have a mean value of 1, to not change the total 3D image intensity, using Equation 3.2. The median is taken from the intensity of the surrounding values:

$$N = \frac{Normal}{median_{slice\ i}} \quad (3\text{-}2)$$

Each normalisation factor was then applied to the corresponding image slide using Equation 3-3:

$$image(i) = \frac{slice(i)}{N} \quad (3\text{-}3)$$

This normalisation defined the image as a greyscale image. This normalisation scaled the brightness over the entire stack frame and dramatically improved the noise rejection of subsequent processing.

3.1.4 3D Image Smoothing

It is recognised that the intensity of an image is similar over very small distances. Image smoothing was carried out using a 3D Gaussian filter over 3 or 4 scales, which improved the performance of phase congruency and phase symmetry processes as well as edge detector software. Without localised smoothing, 3D versions of the Canny edge detectors performed unsatisfactorily. Likewise, Sobel, Susan, Prewitt, and Roberts edge detection methods performed poorly in 3D analysis despite the normalisation of the partial gradients in the z direction due to expansion and Gaussian smoothing.

For smoothing a 2D image, a Gaussian filter may be applied as the 5 x 5 kernel; the output is the centre element in the kernel as such:

$$B = \frac{1}{159}\begin{bmatrix} 2 & 4 & 5 & 4 & 2 \\ 4 & 9 & 12 & 9 & 4 \\ 5 & 12 & 15 & 12 & 5 \\ 4 & 9 & 12 & 9 & 4 \\ 2 & 4 & 5 & 4 & 2 \end{bmatrix}$$

For edge detection, the gradients in both the x and y directions must be estimated. The gradient kernel in the x direction is K_{GX} and the gradient kernel in the y direction K_{GY} by the so-called Sobel operator:

$$K_{GX} = \begin{bmatrix} -1 & 0 & 1 \\ -2 & 0 & 2 \\ -1 & 0 & 1 \end{bmatrix}$$

$$K_{GY} = \begin{bmatrix} 1 & 2 & 1 \\ 0 & 0 & 0 \\ -1 & -2 & -1 \end{bmatrix}$$

These kernel operators produce computed edge strengths G_X and G_Y, which when combined give the 2D gradient, $|G_X| \text{and } |G_Y| \quad so\ that\ |G| = \sqrt{{G_X}^2 + {G_Y}^2}$

and the direction of the edges, $\emptyset = \arctan\left(\frac{|G_Y|}{|G_X|}\right)$.

All edge detectors rely upon estimates of gradients in two directions to estimate and detect an edge within the image. In rudimentary form, these detectors use a 3 X 3 kernel in the x and y directions to estimate gradients ($\partial f/\partial x$) and ($\partial f/\partial y$). It is the gradient estimates that become unreliable under noisy conditions. Most of the 3 X 3 kernels have been extended to 5 X 5 or in the case of the Canny operator, even a 7 X 7 to get estimates of the second partial derivatives, and while these kernels function better than the 3 X 3 kernels, they are equally ineffective in noisy conditions. These detectors require the use of a Gaussian noise reduction process to give reasonable results.

The mathematical model of the 2D Gaussian filter is given by:

$$G_\sigma(x,y) = \frac{1}{2\pi\sigma^2}\, e^{-\frac{(x^2+y^2)}{2\sigma^2}} \qquad (3\text{-}4)$$

$$G_\sigma(x,y) = \left(\frac{1}{\sqrt{2\pi}\sigma^2}\, e^{-\frac{x^2}{2\sigma^2}}\right)\left(\frac{1}{\sqrt{2\pi}\sigma^2}\, e^{-\frac{y^2}{2\sigma^2}}\right) \qquad (3\text{-}5)$$

The 2D Gaussian can be expressed as the product of two functions: one function of x; and one function of y. In this case the two functions are identical 1D Gaussian with the variables separated. In practice this makes the formation of the convolution for the Gaussian simpler to compute.

Consider the 1D Gaussian filter. To find edges:

- First smooth the signal with the Gaussian wavelet (or kernel);
- Convolve the kernel and the 1D signal; and then
- Look for the differentiation of the convolved signal to find edges in the signal as follows:

f	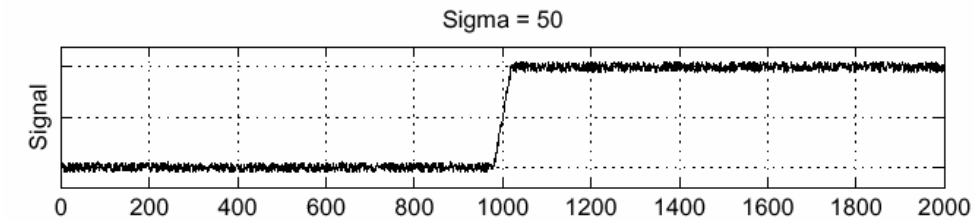
g	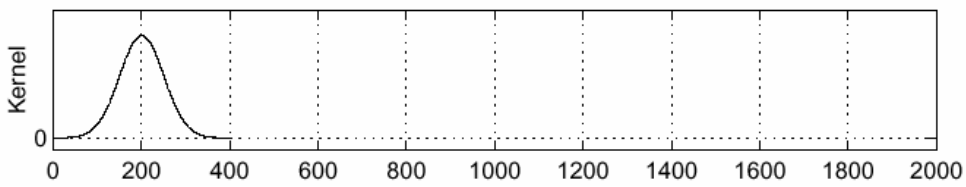

$f * g$	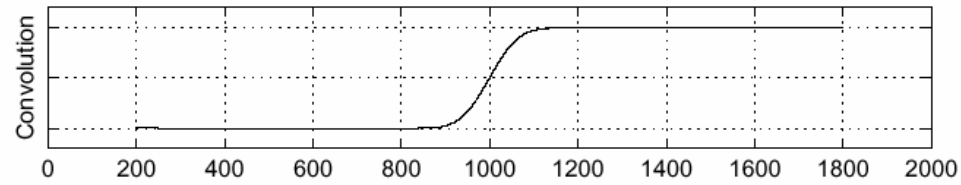
$\frac{d}{dx}(f * g)$	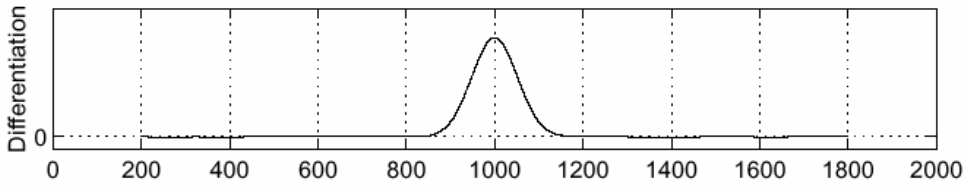

The edge is found from the peaks in $\frac{d}{d(x)}(f * g)$

f $\frac{d}{dx}\ g$ $f*\frac{d}{dx}\ g$	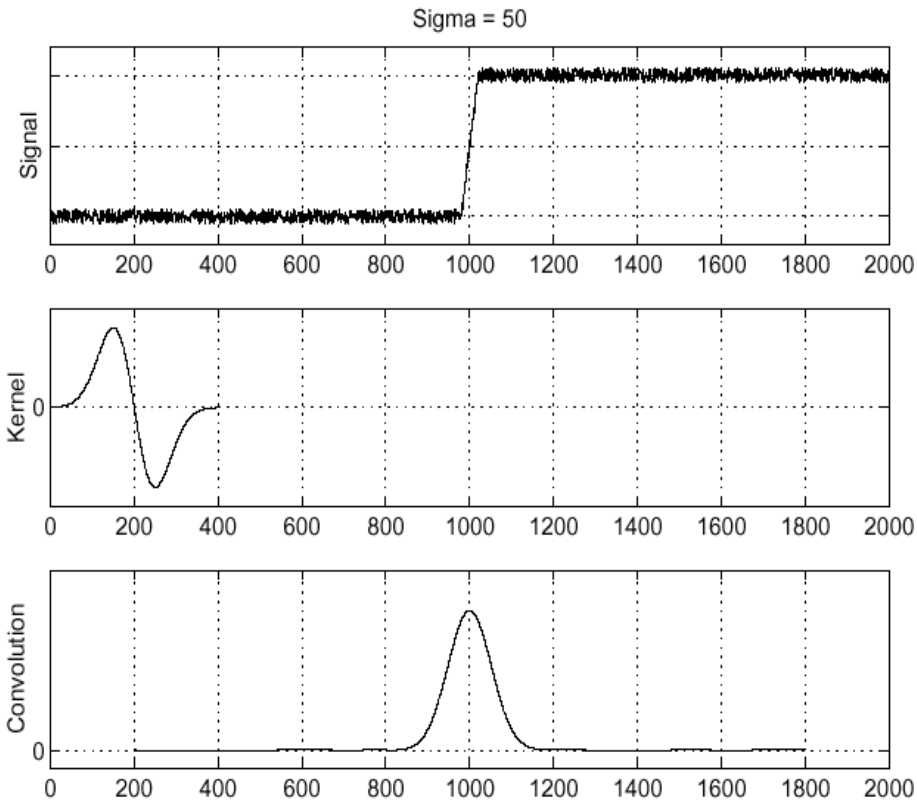

As differentiation is convolution and convolution is associative then:

$$\frac{d}{d(x)}(f * g) = f * \frac{d}{dx} g$$

This saves one operation for each 1D Gaussian filter.

Gaussian smoothing improves edge detection and eliminated noise. Gaussian filtering always follows voxel resizing and intensity equalisation. This corrects for the poorer resolution in the axial direction of the confocal images.

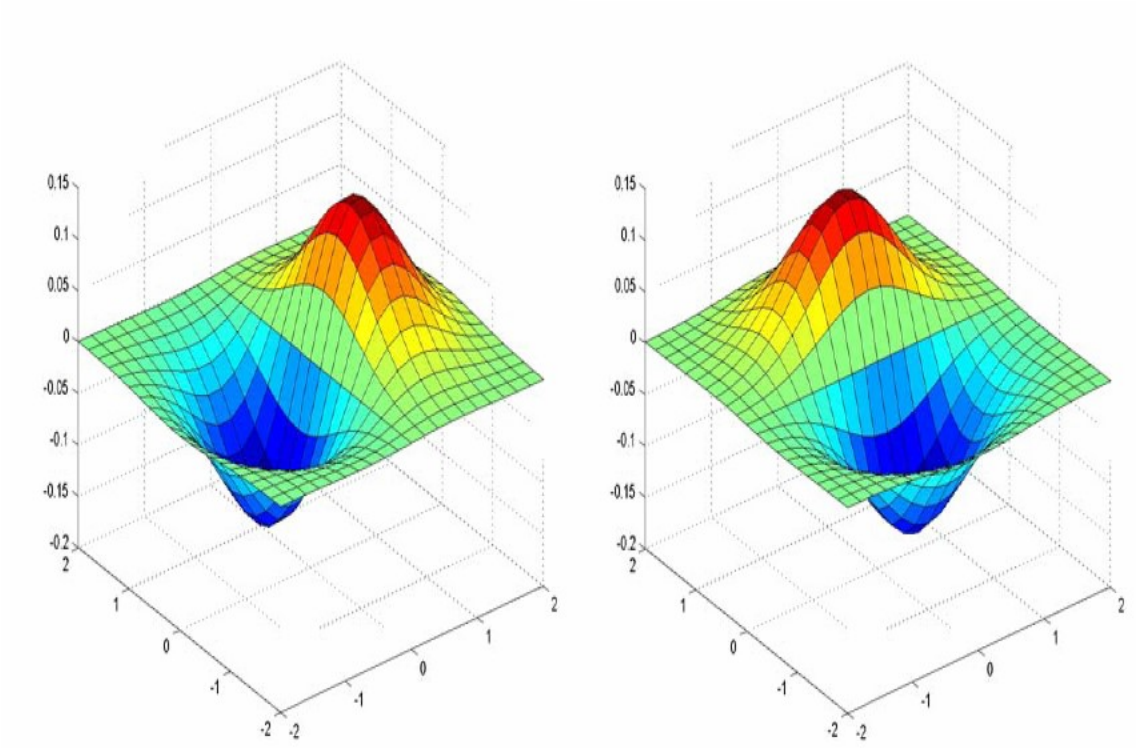

Figure 3-6: Derivative of Gaussian filter in *x* direction and in *y* direction

The 2D Gaussian filter was extended to 3D but the same principles apply, with the addition of an extra direction and subsequent additional angle. The 2D filter kernels are likewise extended to 3D kernels, to aid computational efficiency and yet maintain localisation.

$$G_\sigma(x, y, z) = \frac{1}{2\pi\sigma^2} e^{-\frac{(x^2+y^2+z^2)}{2\sigma^2}} \quad (3\text{-}6)$$

$$= \left(\frac{1}{\sqrt[3]{2\pi\sigma^2}} \, e^{-\frac{x^2}{2\sigma^2}} \right) \left(\frac{1}{\sqrt[3]{2\pi\sigma^2}} \, e^{-\frac{y^2}{2\sigma^2}} \right) \left(\frac{1}{\sqrt[3]{2\pi\sigma^2}} \, e^{-\frac{z^2}{2\sigma^2}} \right) \quad (3\text{-}7)$$

The various edge detectors use non-maximal suppression to ensure that only the maximum edge strength is stored in every location and thresholding to describe a continuous edge, should one exist. Several different methods have been used to evaluate edges. These were compared to phase congruency and phase symmetry methods described further on.

3.1.5 Image Processing using Fourier Transforms

The Fourier Transform ("FT") is a transformation technique widely used in signal analysis. The FT decomposes data into a series of sinusoid component waves, thus the transformed domain (also commonly known as the frequency domain).

The equation for the 1D FT is*:*

$$F(\xi) = \int_{-\infty}^{\infty} f(x) e^{\,-i\,2\pi\xi x} \, dx \quad (3\text{-}8)$$

Whilst the 1D FT is quite well known (Equation 3-8), the Fourier Transform also exists in higher dimensions. Equation 3-9 shows the multidimensional form of the equation.

$$F(\xi) = \int_{\mathcal{R}^n} f(x) e^{\,-i\,2\pi\xi x} \, dx \quad (3\text{-}9)$$

The 2D Fourier transform is widely used in image processing. Figure 3-7 illustrates the main features of the frequency domain representation of an image. Altering the frequency domain representation of an image causes a variety of common effects. Altering the zero-frequency point so that steady DC offset of the frequency domain representation of an image adjusts the overall brightness level of the image. Low pass filtering removes high frequencies that are present far from the origin. This operation corresponds to blurring the image. High pass filtering removes low frequency components near the origin, and removes large variations of brightness over the image, whilst leaving sharp features intact.

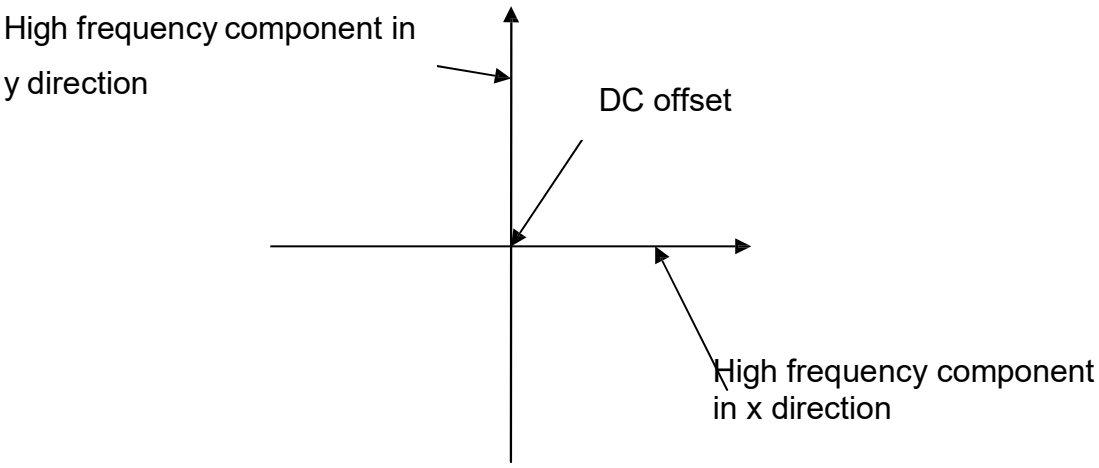

Figure 3-7: Illustration of 2D frequency domain

The symmetry present in the 1D FT is also present in higher dimensions. All information about the image is contained in the all positive quadrant, like the positive frequencies in the 1D case. The representation of the frequency domain is also variable. In 2D, the origin (zero frequency point) may be placed either in the centre of the image or the corners, depending on the definition. When the origin is centred within the image, applying the inverse FT to the output of the FT of the image results in a new image in which the noise level is reduced.

In other special filter designs, such as mean filtering, the idea of mean filtering is simply to replace each pixel value in an image with the mean (average) value of its neighbours, including itself. This has the effect of eliminating pixel values which are unrepresentative of their surroundings. Mean filtering is usually thought of as a convolution. Like other convolutions the mean filter is based around a kernel, which represents the shape and size of the neighbourhood to be sampled when calculating the mean.

Often a 3 × 3 square kernel is used to provide a limited range filter in the convolution integral, although larger kernels (e.g. 5 × 5 squares) can be used for more severe smoothing. (Note that a small kernel can be applied more than once to produce a similar but not identical effect as a single pass with a large kernel.) This is also true of other special filter designs that rely upon median, variance, maximum value, and minimum value rather than the mean.

Operations such as feature detection use convolution in image processing. Equation 3-10 gives the mathematical definition of convolution. The operation corresponds to multiplying the frequency domain representations of two images.

$$\boldsymbol{F}(\boldsymbol{f} * \boldsymbol{g}) = \boldsymbol{F}(\boldsymbol{f}) * \boldsymbol{F}(\boldsymbol{g}) \tag{3-10}$$

Such convolution operations are used in image processing for several different operations such as edge detection, smoothing and corner detection.

One of the two functions in Equation 3-10 is the original image and the other function is expressed as a limited kernel (or multiplier) arranged around a point of interest. The advantage of such an expression is the limited field over which it operates and hence the limited effect on the primary image.

3.1.6 Image Processing using Wavelet Transforms

This subsection defines operations that can be used to segregate images into component objects.

The Wavelet Transform is a counterpart to the Fourier Transform used in image processing. A signal is broken down into a set of localised waveforms or wavelets. Equation (3-8) gives the general form of the 1D wavelet transform. The resulting output is 'local frequency;' that is, the frequency components in the locality of the point. The extent of the wavelet is limited, such that the convolution of the wavelet with image signal drops to zero at the limit of its extent. In practice this means that the full convolution is performed over a limited size kernel surrounding the wave form to be processed. It is possible to localise filtering operations by manipulating the wavelet coefficients. The wavelets are not necessarily of sinusoidal shape and their shape is a derivative of the decomposition of a function using quadrature pairs of filters.

$$C(scale, position) = \int_{-\infty}^{\infty} f(t)\psi(scale, position, t)dt \tag{3-11}$$

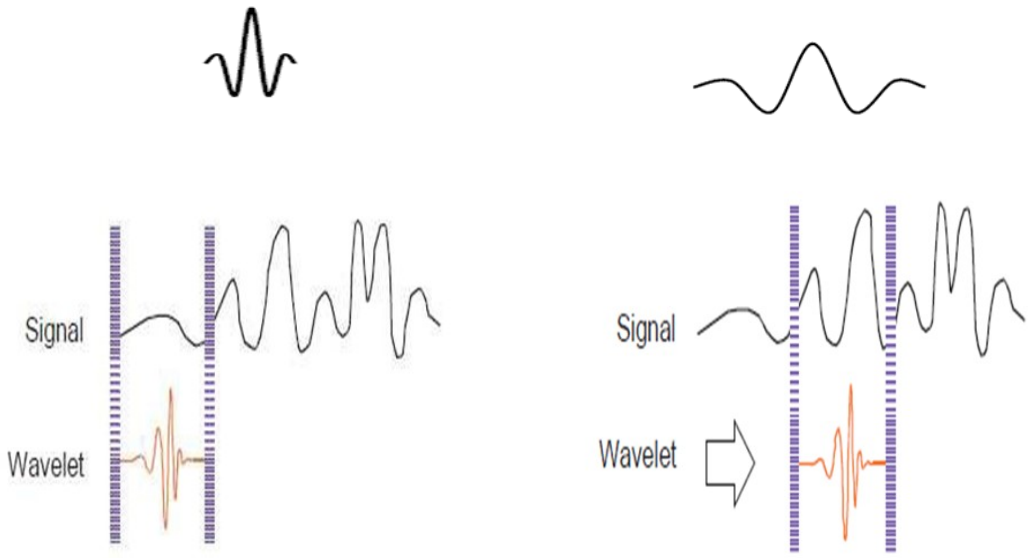

Figure 3-8: The wavelet transform of a function

Shifting the wavelet through each point of the signal and calculating the response generates the Wavelet Transform of a function for a particular scale. Varying the wavelet's spatial extent (scale) and repeating the process generates the wavelet transform of a signal.

Wavelet and wavelet transforms were used in this study as they localise the signals collected and reduce computational time required to perform the convolutions required for phase symmetry and phase congruency. The wavelet is defined in terms of a local kernel with a maximum extent determined by the number of phases used. Larger extent is calculated as larger scales over the same number of phases to affect longer wavelengths. The wavelets are the convolution filters described below, and much of this study has been devoted to implementing satisfactory filters in terms of both extent (range of operation) and shape. These are discussed below as evaluating filter design.

3.2 Two-Dimensional Edge Detectors

An image is treated as a two-dimensional signal which can be enhanced by applying standard signal processing techniques. Removing redundant data by transforming the image into a statistically uncorrelated data set, results in a new image (Priotr, 2004). According to Canning (1986) the most relevant data is in the neighbourhood of the edges, which are defined as where the grey scale values change significantly from one pixel to the next.

Image edge detection is the process of locating edges within an image. These edges can then be used to identify and segment the image into component parts.

3.2.1 Edge Detector Algorithms

An image processing system was developed for processing images into a set of line drawings, which are then used to generate an open wire frame 3D structure from the input photographs (Roberts, 1976) and (Mario & Maltoni, 1997). This process performs a 2-D spatial gradient convolution on the image to extract horizontal and vertical edges. The resultant lines were spliced together to result in edge detection. Two images are produced to define diagonals running top right to bottom left (G_x) and top left to bottom right (G_y). The two images are then combined into a single image $|G| = |G_x| + |G_y|$.

Extension to 3D detectors merely adds a third term G_z to the above equation.

The purpose of the edge detector is to accentuate regions of step change in the pixel to pixel signal intensity, which then modifies the output image, showing the edges within the original image. The processing required to compute edges is excessive and only detects areas of high spectral frequency that are subject to noise. Often with the noisy images used in this work, the Roberts cross edge detector failed to find as many edges as expected and failed to perform as well as the phase congruency edge detection.

Modifications to the Roberts detector have developed many other algorithms such as:

- Canny Edge Detector;
- Susan Detector;
- Sobel Operator; and
- Prewitt Edge Detector.

The Sobel operator performs a 2D special gradient measurement on images. This can be extended to 3D gradient measures for image stacks (or volumes). The method is extremely sensitive to noise and highlights the noise as edges using 3 x 3 x 3 kernels. Even using 5 x 5 x 5 kernels, the noise rejection impaired the performance of the Sobel Operator which required non-maximal suppression and two-valued thresholding to get reasonable results.

For this work, the Sobel Operator failed to produce reliable and fast edge detection. The Sobel method could find individual fibres outside of bundles and produced results that were not aligned along the fibre itself, but randomly along the edge (see 3D phase congruency results). Certainly, the 3D phase congruency method detected more edges and a more sensible selection of edges under noisy conditions. Moreover, traditional edge detectors also failed to produce consistent and reliable results.

The Sobel filter response indicated a fibril structure along the edges of collagen fibres, and hence, supports the existence of these features in the original image. It showed a gap along the centre of fibres which is due to the gradient being zero at those points. The response is blurred in a similar manner to 3D phase congruency and could be the result of axial features.

The Harris corner detector shows that there was a considerable amount of corner features along fibres, while the Canny edge detector merely shows the edges for the collagen fibres. Interestingly, the Canny edge detector is used commonly in image processing, but given the results, phase congruency provides far more useful information. Neither the Canny edge nor the Harris corner detectors provide any information on the internal structure of collagen fibres.

3.2.2 Scale and Wavelength / Frequency

For digital images, the frequency domain can be considered as the number of pixels separating points of interest. The maximum frequency is determined by the distance (frequency) between adjacent pixels (or voxels in 3D) images. An alternate measure for different frequencies is scale. This document uses the term scale to define frequency and wavelength measures. Hence a scale of 2 is half the frequency of scale 1 (or the wavelength is twice that of scale 1).

This concept can be extended to two and three dimensions, giving rise to the notion of scale space. The larger the scale, the less fine detail is visible from the image. The nature of the image remains unchanged; however, the boundaries of the points of interest blur as the scale increases. Likewise, the larger the scale, then the lower the frequency of the component waves within the Fourier transform.

3.2.3 The Fourier Transform

The Fourier Transform decomposes a signal into a weighted linear combination of complex exponentials. It is a function of frequency, and hence, the FT transforms a signal from the spatial domain into the frequency domain. In general, the Fourier transform is complex valued and is represented in terms of polar magnitude and phase. Magnitude describes how much of a particular given frequency component exists within the signal, and phase represents where that component exists. The frequency domain representation of a signal refers to the representation of magnitude with respect to orientation (phase data is ignored).

The continuous 2D FT of a signal, $f(x, y)$, is

$$f(x,y) = \iint_{1}^{\infty} e^{-i\omega t}\, dy\, dx \qquad (3- - 12)$$

Put simply, for an image, the 2D FT performs the 1D FT for every row, and to this result, performs the 1D Fourier transform for every column. Frequency magnitude is the radial distance away from the origin and the orientation is the polar angle from the horizontal axis. Magnitude along any given orientation refers to the frequency constituents along that orientation within the original signal.

Each feature within an image is characterised by a particular orientation and magnitude profile. In particular, magnitude profiles can vary widely for different features. Scaling the magnitude into bands or scales of frequency with equal bandwidth approximates every magnitude profile to a set profile. Different distributions of scale favour particular magnitude profiles and therefore it is impossible to equally account for all feature types. This is known as the issue of scale – a scale profile that favours 'broad' features in one image, may favour a completely different set of features in another image (Kovesi 1996).

In general, the faults in this approximation are widely accepted and usually overlooked. In comparison, localisation of the frequency domain with respect to orientation is reasonably independent of feature type. Orientation, therefore, is only localised to ensure that the phase congruency value at some point in the image is weighted, with respect to the locality of that point. In addition, spread filters are designed so that their total sum across the frequency domain provides even coverage of all orientations. Therefore, the distribution of spread filters is only specific to feature type in terms of the locality on which phase congruency is weighted.

3.2.4 Wavelet Filter Design

The major effort in the development of the software suite is the design and testing of wavelet filters. Wavelets are convolution functions that have limited extent and hence limited computational time required to perform the convolution operation. A full wave function has maximal extent and requires much longer computational effort to compute convolution functions. Sections 3-2-4 to 3-2-6 outline the filter design theory and discuss the effectiveness of the design. All filters were implemented and tested for performance in terms of adequacy and computational speed.

The performance of the wavelets generating suitable convolution integrals with the image signal was assessed to provide fast and accurate feature detection. These convoluted integrals are used by both phase congruency and phase symmetry feature detection. They are also used to segment the image by equally spaced band-passed filters in the frequency domain.

3.2.5 Log-Gabor Filters

Log-Gabor filters are constructed in the frequency domain as pairs of log-Gaussian filters place in quadrature. For a 1D filter, a single log-Gabor filter is characterised by two log-Gaussian functions placed symmetrically about the origin in the real axis. This is known as the even symmetric filter. The Hilbert transform of this filter, represented by two log-Gaussian functions placed anti-symmetrically about the origin in the imaginary axis, is known as the odd symmetric filter. A pair of quadrature log-Gabor filters then can be visually illustrated by the following Figures (3-10, 3-11 & 3-12) for some scale of frequency.

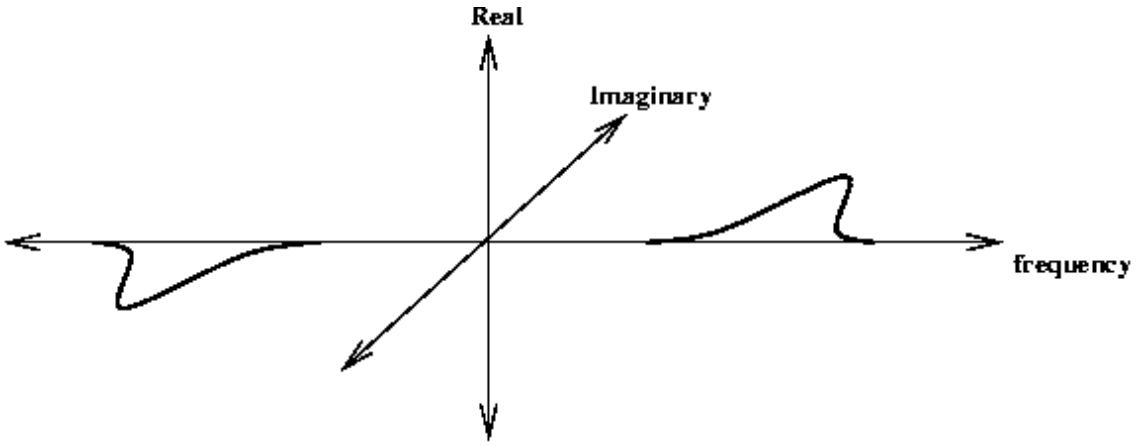

Figure 3-9: Odd symmetric log Gabor filter

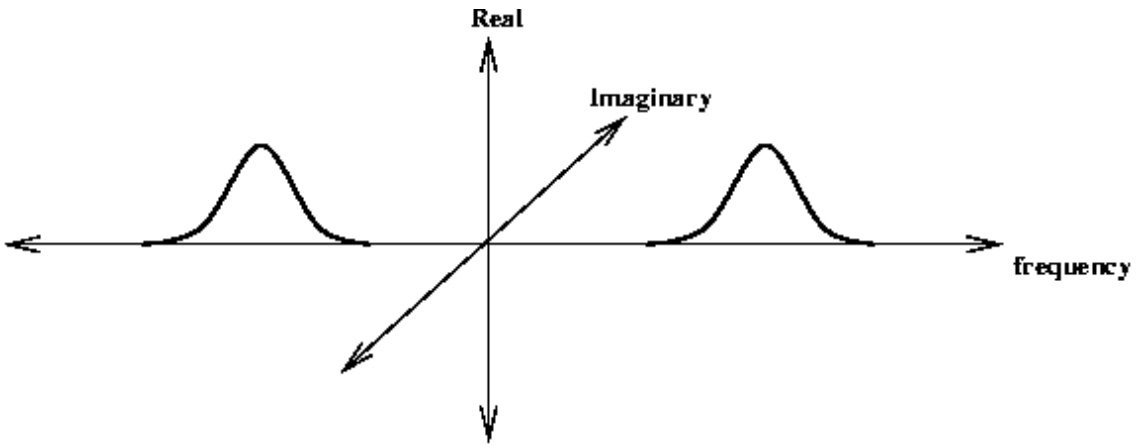

Figure 3-10: Even symmetric log Gabor filter

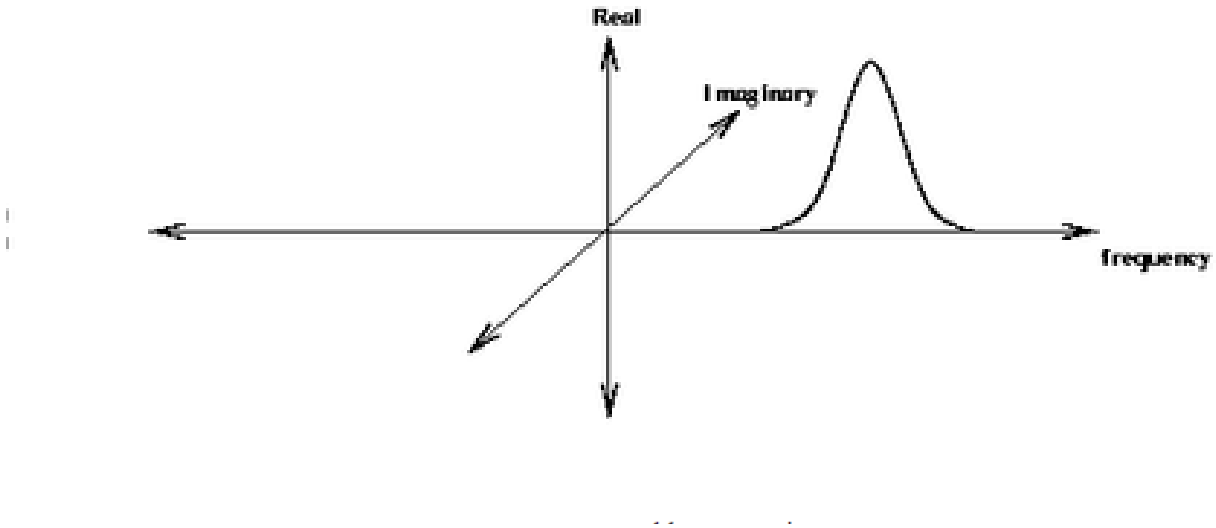

Figure 3-12: Local phase pattern at a point of symmetry (left) and asymmetry (right)

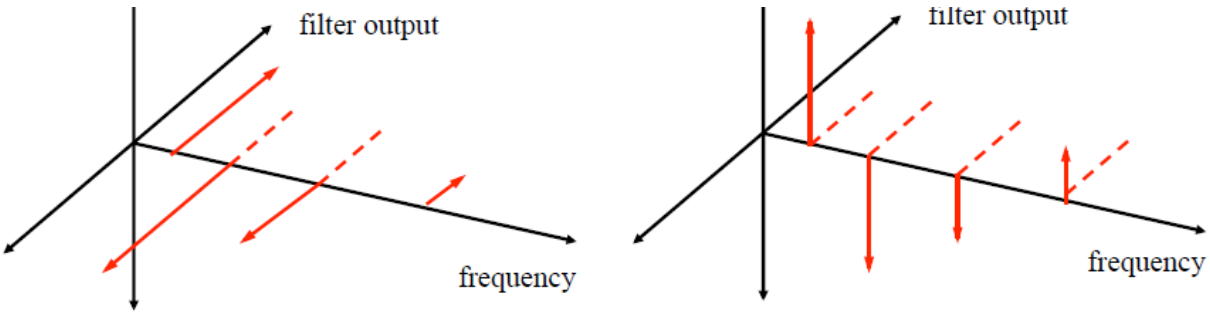

In practice, the shape of the signal output defines symmetry and asymmetry (Figure 3-12) for a given signal. When the signal is first convolved with the even filter it removes the DC component from the image signal. Band-passed filters scale the image signal, with respect to the frequency scale of the filter, which produces the even component of the image signal. The odd filter is then convolved with that output, producing the Hilbert transform of the signal at the frequency scale of the filter or, the odd component of the signal.

Given that local energy is the modulus of a signal and its Hilbert transform, the modulus of the even and odd components of a signal provides the local energy for some scale of frequency. The local energy at a particular scale approximates the Fourier component of that scale. That is:

- Where $e_n(x)$ and $o_n(x)$ are the even and odd filter convolutions with the signal respectively. The even and odd components define a complex energy vector at a given scale that is defined as the local energy for a given signal. The total local energy is the modulus of the sum of all of these vectors over all scales.

- In 2D, the transfer function of the even symmetric filter is defined by two log-Gaussian bells placed symmetrically about the origin in the real frequency domain. The placement of the bells in the frequency domain is dependent on frequency scale and orientation. However, in practice, the log-Gabor filter is formed by first defining a band-passed filter (a well formed by rotating a 1D log-Gabor filter about its axis), which determines frequency scale and a spread filter determines the orientation (Kovesi 2007). The convolution of the two filters forms a 2D log-Gabor filter for a given frequency scale and orientation. In this thesis, the band-passed filter is referred to as the log-Gabor filter and treated separately from spread filters. An example of a 2D log-Gabor Filter is shown in Figure 3-13.

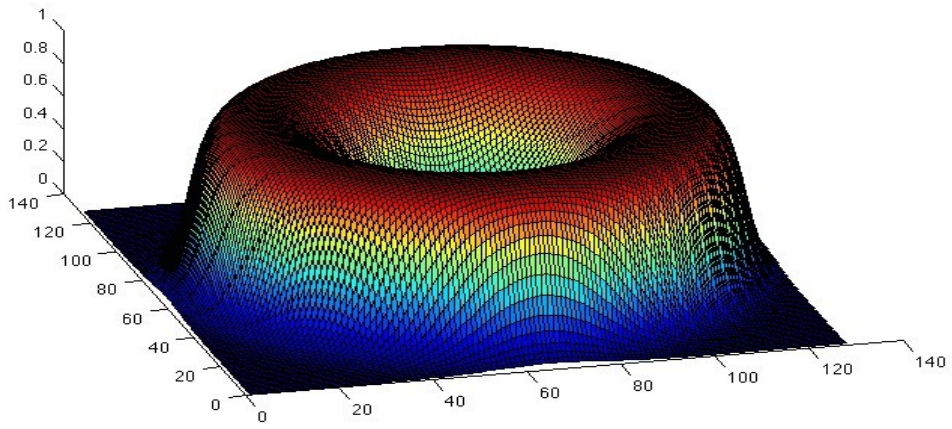

Figure 3-13: A two-dimensional log-Gabor filter.

The centre of the well in the filter response (Figure 3-13) represents the origin. The radial distance of the well from the origin, as well as the breadth of the curve, is dependent upon the frequency scale of that filter. Note, the horizontal axis represents frequency, not log-frequency, so the filter curve will not appear to be Gaussian.

To cover the entire frequency spectrum, a set of log-Gabor filters with different frequency scales are spaced so that the overlap between adjacent filters provides a uniform response. While the number of frequency scales used depends upon the application, the spread and spacing of filters mostly remains unchanged.

The Gaussian functions used to design log-Gabor filters are defined in log-frequency. In fact, this property is the fundamental reason for using log-Gabor filters. Image features occur at extremely localised points in the spatial domain, and are characterised by a wide range of frequencies in the frequency domain (for example, the step edge of a square wave). Therefore, filters that provide broad spectral coverage and maximal spatial localisation will respond better to image features (Field 1987) and (Kovesi 1997). Using log-Gaussian functions, log-Gabor filters have almost no limits on their spectral spread and therefore have very localised spatial characteristics. In addition, log-Gabor filters have no static offset known as a DC component (the log of frequency at zero is a singularity) and have also been shown to accurately model the amplitude spectra of natural images (Field 1987).

Kovesi designs require each filter to cover the same log-frequency spread (usually between one to two octaves); hence, the lowest frequency scale covers the smallest frequency spread and has the broadest spatial characteristics. The highest frequency scale covers the largest frequency spread, but has the most localised spatial characteristics. This means that approximate Fourier terms (the local energy for each scale) are built up from increasingly localised terms. Further, since the highest frequency scale has the largest spectral coverage, which mostly consists of noise, that scale's response can be used to estimate the level of noise within the image (Kovesi, 2007).

3.2.6 Spread Filters and Orientation

The function of spread filters is to evenly subdivide the frequency domain over orientation into independent and localised regions. The choice of balance between independence and localisation is dependent on the particular feature profiles within an image (Field 1987 & Kovesi 1996). Since the frequency domain is axially symmetric, spread filters are constructed by defining orientation vectors that are evenly spaced in the 180° half-space. The cosine of the angular distance away from a particular orientation vector forms a cosine distribution (an approximation of a Gaussian distribution).

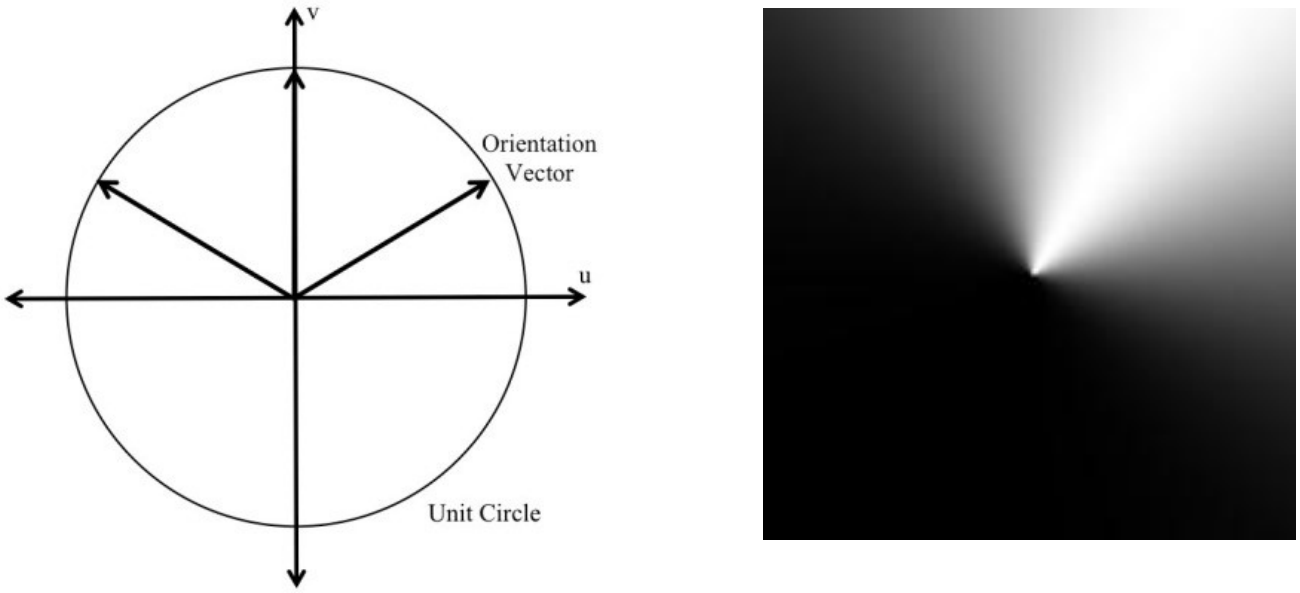

Figure 3-14: Three orientation vectors subdividing the half-plane and the 2D spread filter for a particular orientation

The direction of the spread filter is the orientation of the signal in the 2D plane between the real axis and the imaginary axis of the 2D Fourier transform. This orientation defines the localisation of the energy vector as bound by the wavelet transformation. Aligned vectors have maximum energy. This process searches the spread filter orientation to find where the local energy is maximal. For every point, the energy is calculated at each orientation, but only the maximal energy and orientation are noted. All other energy vectors are discarded. Phase symmetry and phase congruency rely upon the orientation vectors being equal for feature detection.

The spread filter for this distribution is mapped to the angle between adjacent vectors. Spread filters are designed so that they evenly divide the frequency domain. They need to be symmetric so that no particular orientation is favoured over any other orientation. Phase congruency is calculated and normalised with respect to each orientation. Hence, the sum of phase congruency for all orientations is the total phase congruency response of an image. That can be expressed as:

$$PC(x) = \sum_{o} \frac{\sum_n A_{n,o} \cos\left(\varphi_{n,o}\,(x) - \overline{\varphi_o}\,(x)\right)}{\sum_n A_{n,o}} \qquad (3\text{-}13)$$

Spread filters effectively localise phase congruency normalisation, so that features are scaled according to the distribution of other features within its locality. The spread filter depends upon the frequency of the image and, the orientation represents the angle between the real and imaginary parts of the 2D Fourier transform. Both frequency and orientation give rise to the local energy content of the resultant vector.

The shape of the first three spread filters is shown in Figure 3-15. For even coverage, the sum of each spread filter should be 1. This defines the orientation of the filter for a particular scale, as the orientation that produces the maximum value of the entire spread filter set. Non-maximal orientations are discarded. The scale and orientation identify any features detected.

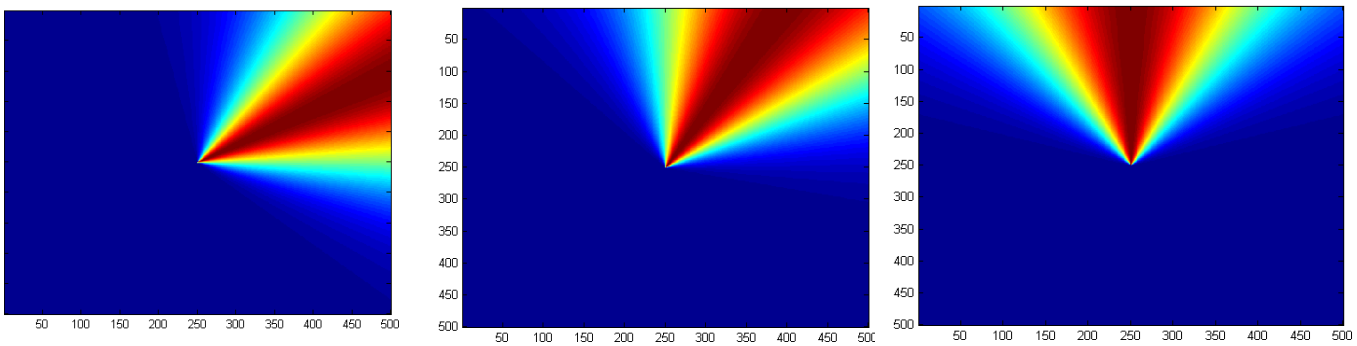

Figure 3-15: First three spread filter orientations from a six-orientation calculation.

3.3 2D Monogenic Signal Filtering

A monogenic filter offers a computationally efficient manner of calculating Fourier components within the image. They are less computationally intensive than spread filters and are less complex to set up than directions along which the filters operate. Monogenic filters were tested for functionality and ease of implementation.

The main limitation of monogenic filters is the lack of localisation in frequency data with respect to orientation. The weighting function calculates the spread of frequencies with respect to scale. Consequently, any dominant features that exist across all scales of frequency are the prominent features in the final phase congruency response. The benefit of using orientation to further localise energy for a specific frequency is that the features for a given orientation will only be considered against other features in that orientation. Since all features would then be weighted with respect to their direct locality, finer features would have a greater likelihood of being included in the final response. In addition, the accuracy of monogenic filters is further hampered by the approximation used to calculate phase congruency rather than starting with a rigorous 2D FT. The use of monogenic filters is a compromise between computational expense and accuracy. In the calculation of phase symmetry, where the imaginary part of the signal is small compared to the real part of the signal, monogenic filters are well suited to phase symmetry calculations.

A monogenic signal is the Riesz transformation of a multidimensional signal (Felsberg M and Sommer G 2001) . The analytic signal is the multidimensional generalisation of the monogenic signal and the Riesz transform is similarly the multidimensional generalisation of the Hilbert transform. Of particular importance is when the monogenic signal splits the identity property. Wherein, the modulus of this complex signal represents local amplitude or energy and its argument is representative of local phase (Felsberg M and Sommer G 2001). These two quantities are fundamental for the calculation of phase congruency. To aid developing an understanding of monogenic signals and their application, monogenic signals will first be discussed in two dimensions and then extended to three dimensions.

In one dimension, the Hilbert transform is characterised by the following transfer function in the frequency domain:

$$H(u) = isign(u) \ = i \ \frac{u}{|u|} \tag{3-14}$$

Similarly, in two dimensions, the Riesz transform is the Hilbert transform but with u as a vector quantity, namely $\boldsymbol{u} = [u_1, u_2]^{\mathrm{T}}$, and can be represented as follows,

$$H(u) = i \ \frac{u}{|u|} \tag{3-15}$$

$$H_1(u_1, u_2) = i \ \frac{u_1}{\sqrt{{u_1}^2 + {u_2}^2}} \tag{3-16}$$

$$H_2(u_1, u_2) = i \ \frac{u_2}{\sqrt{{u_1}^2 + {u_2}^2}} \tag{3-17}$$

Here, u_1 and u_2 are the orthogonal axes in the frequency domain. Feldsberg notes that this Riesz transform vector has unit length for all orientations. Since u_1 and u_2 are also odd symmetric, the Riesz transform exhibits the same properties as the 1D Hilbert transform (Felsberg M and Sommer G 2001). The components of this vector, H_1 and H_2, are referred to as monogenic filters. In practice, each of the monogenic filters is multiplied by the Fourier transform of the signal, which is representative of the following convolution in the spatial domain:

$$f_M = \begin{pmatrix} h_1 * f \\ h_2 * f \\ f \end{pmatrix} \tag{3-18}$$

Where f_M is the monogenic signal, f is the original signal, and, h_1 and h_2 are the spatial domain equivalents of H_1 and H_2 respectively. Hence, the monogenic signal of a 2D signal exists in 3D space with orthogonal axes $h_1 * f$, $h_2 * f$ and f. It is a multidimensional complex number whose modulus is representative of local amplitude and two angular arguments are representative of local phase and orientation (Felsberg M and Sommer G 2004). Since monogenic filters lack frequency selectivity, log-Gabor filters are used to divide the frequency domain into bands or scales of frequency. Monogenic filters are convolved with each scale to find their respective monogenic signals

For a particular scale of frequency, the modulus of its monogenic signal gives the local energy or amplitude for that scale.

$$A_n = \sqrt{(h_1 * f_n)^2 + (h_2 * f_n)^2 + f_n^2} \tag{3-19}$$

Where A_n is the local amplitude at some scale n, and f_n is the signal convolved with a log-Gabor filter of scale n (that is, f_n is the signal composed solely of frequencies within the n_{th} scale). This situation can be represented geometrically by a vector defined in a spherical coordinate system:

$$\begin{matrix} & f_n & A_n \cos(\varphi) \\ h_1 * & f_n = & A_n \sin(\varphi)\cos(\theta) \\ h_2 * & f_n & A_n \sin(\varphi)\cos(\theta) \end{matrix} \tag{3-20}$$

Note that $h_1 * f_n$, $h_2 * f_n$ and f_n represent the orthogonal axes of the monogenic signal. Here, the angular quantities (φ and θ) represent the local phase and local orientation of the monogenic signal respectively. This provides the following representation of the monogenic signal (Figure 6-1):

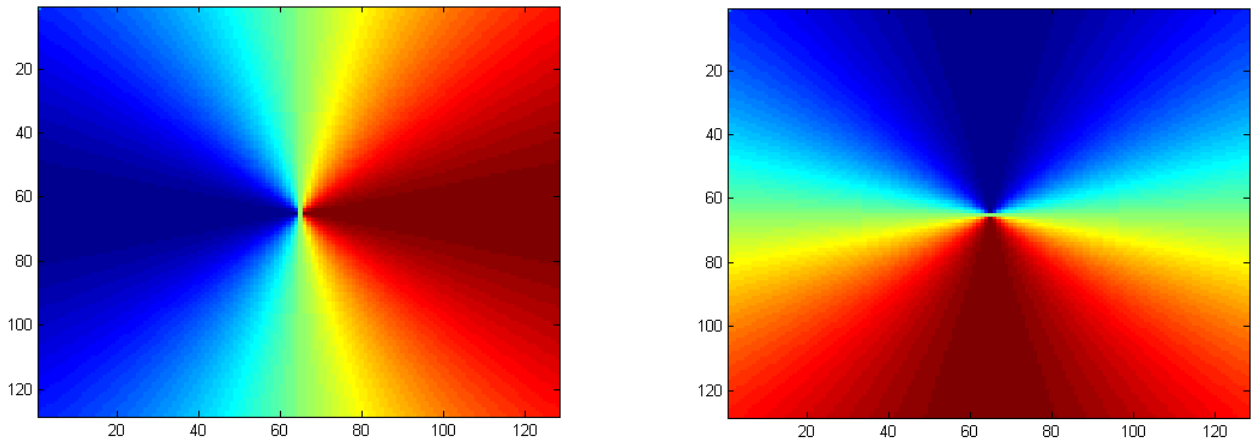

Figure 3-16: Frequency domain view of H1 monogenic filter (left) and Frequency domain view of H2 (right)

3.3.1 Noise Compensation

The noise threshold also eliminates small responses. The noise circle indicates that if the result is negative (noise threshold is greater than local energy) the local energy is set to zero. This ensures that the phase symmetry measure remains bounded between 0 and 1. The constant threshold takes the form of a noise circle. If the vector sum of the frequency component lies within the noise circle, then the response component is zero. The threshold is subtracted from the measure when the sum lies outside the circle, resulting in a lower measure of phase symmetry, as shown in Figure 3-18.

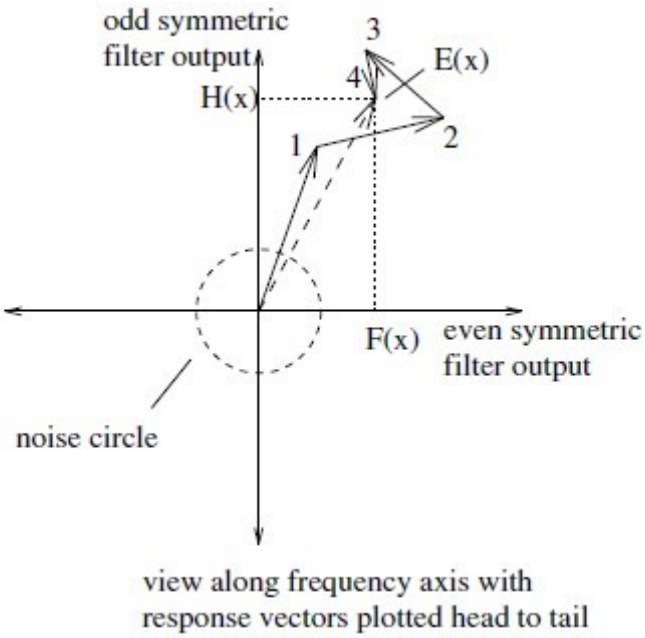

Figure 3-17: 1D geometric illustration of noise threshold

As it stands, e as shown by the noise circle in Figure 3-18. A form of noise compensation is required. In his method, Kovesi estimates the level of noise using the Rayleigh distribution (Figure 3-20). The sample mean and deviation are used to set a threshold on the local energy for any given orientation is shown in Figure 3-20

Whilst the threshold may be set manually, it is desirable to have a threshold that is invariant to the image parameters, such as brightness. This is consistent with the criteria for a good line detection algorithm as set out in section 3. The

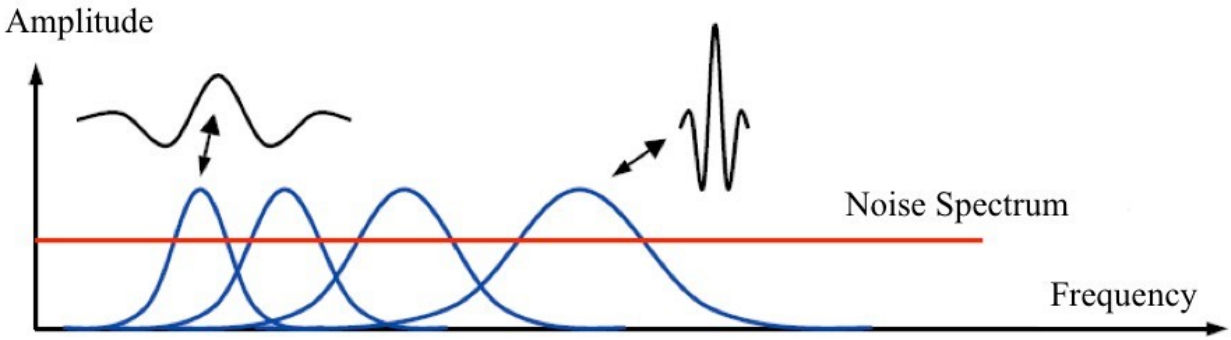

Figure 3-18: The distribution of frequency scales over the frequency domain

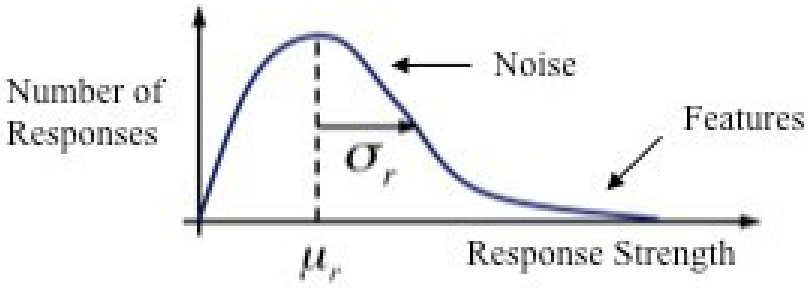

Figure 3-19: The Rayleigh distribution characterised by its mean, μ_r and variance, σ

amount of noise present within the image is estimated to accomplish good line detection. Consider the smallest scale filter, which also has the largest frequency bandwidth. As the noise spectrum is mostly flat, then the smallest scale filter will subsequently respond the mostly to noise. The smallest scale filter also has the smallest spatial extent and is therefore, most of the time only responding to noise outlined in Figure 3-20 above.

Since the highest frequency scale covers the largest bandwidth and the noise spectrum is relatively uniform, the highest frequency also responds the most to noise (see Figure 3-19). The highest frequency scale has the largest spectral coverage and therefore responds the most to noise.

A robust estimate for noise present in the image can be based on the smallest scale filter response. This was achieved by constructing a histogram of the smallest scale filter responses for all points in the signal. The resultant histogram was best characterised by the Rayleigh distribution (shown above). Note that, as the highest frequency scale also has the smallest spatial scale, most of the time it will only respond to noise (Kovesi 1999). Therefore, the highest frequency scale can be used to provide an accurate model of the level of noise within the image. It is the magnitude of the local energy vector responses to a particular scale that produces the Rayleigh distribution.

A Gaussian distribution was initially used to model noise; however, a Raleigh distribution was found to give better results in this case.

The distribution located around the mean is the result of noise in the image, while the 'tail' is the result of the stronger responses formed by features contained within the image. Features correspond to the much larger responses and are located further from the mean. The mean μ_r and variance σ_r of the distribution are characterised by one parameter obtained from the median of the distribution. This approach minimises the influence of features in the result. The noise threshold, T, may then be expressed as Equation 3.14 below.

$$T = \mu_r + k\,\sigma_r \qquad \text{(3-14}$$

The threshold and variance are used to modify the expressions for both phase symmetry and phase congruency. Where k is the distance away from the mean (μ_r) and is expressed in terms of the number standard deviations (σ_r). One or two standard deviations are usually sufficient to approximate the level of noise. However, particularly noisy images may require much larger values than two standard deviations. In the calculation of phase congruency and phase symmetry, this threshold is calculated separately for each orientation and applied directly to the total local energy. This compensation modifies the expressions for both phase symmetry and phase congruency, which are derived in chapter 4.

The parameter k controls the noise threshold and specifies the noise in terms of standard deviations away from the mean; *k* is then an image invariant parameter for specifying noise compensation. Table 3-1 gives the confidence levels for varying values of *k*. The confidence level represents the probability that the feature observed is in fact there, and is not noise.

Table 3-1: Confidence level as a function of standard deviation

Standard Deviations	Confidence Level (%)
1	68.2
2	95.4
3	99.6

Chapter 4 Two-Dimensional Phase Symmetry and Phase Congruency

This chapter introduces the concepts of phase symmetry and phase congruency and reviews the Kovesi method for their calculation. The chapter also deals with the development of the Kovesi method from one dimension to two dimensions.

4.1 Phase Symmetry and Phase Congruency

The concepts of phase congruency ("PC") and phase symmetry ("PS") were first presented in the local energy model of feature detection, developed by Murrone et al. (1987). The local energy model postulates that image features such as lines, edges and corners correspond to points where the local frequency components are in phase. Furthermore, lines and dots correspond to points of phase symmetry. At these features, the Fourier components are at maxima or minima of their cycles, and are symmetric about that point.

The concepts of phase congruency and phase symmetry are illustrated geometrically in Figure 4-1. At the step edge of the square waveform, the Fourier components are in phase. This corresponds to a point of phase congruency, as the Fourier components are not symmetric about the step edge. At the circled red areas of the square and triangular waveforms, the Fourier components are maximally or minimally in phase. These points correspond to locations of phase symmetry as the Fourier components are symmetric about these points. The red-circled areas correspond to points of phase symmetry, whilst the blue-circled area corresponds to a point of Phase Congruency

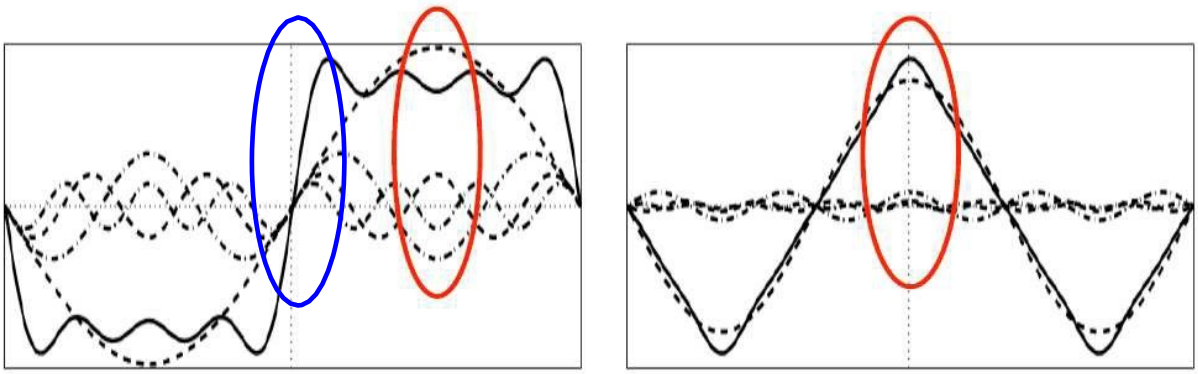

Figure 4-1: Square and triangular waveform decompositions.

The calculation of phase symmetry and/or phase congruency accurately requires the computation of all Fourier terms at all frequencies. This is extremely expensive in computational terms. The use of these features needs to be computationally efficient for the method to be feasible. Dr Kovesi has simplified the computational rigors to provide a good estimate of the Fourier decomposition over a limited scale at reasonable computational effort. These short cut estimates coincide with the peaks in the FT components and implement the FT as wavelets of limited extent. Whilst the resultant sum is not rigorous, it is predictive of the fully implemented FT retaining the same direction and magnitude properties of the full Fourier implementation, at a fraction of its computational cost.

4.2 Calculating Phase Symmetry and Phase Congruency

Phase congruency and phase symmetry are difficult quantities to calculate, so early methods (such as that presented by Venkatesh et al. 1989; Robbins 1996; Robins 1999) looked for the peaks in the local energy function, which are proportional to phase congruency and phase symmetry. Kovesi (1999) developed a method to calculate phase congruency and phase symmetry, without the need to calculate all components of the Fourier Transform. From this short cut method of evaluation, the 2D phase symmetry and phase congruency methods formed the basis for the 3D algorithm developed below. There are few differences between the phase congruency and phase symmetry methods, as both phase symmetry and phase congruency, rely only upon the phase of the frequency components at a particular point.

Consider first the 1D case of the Fourier transform. In Figure 4-2, four discrete Fourier components form a waveform, such as a square wave, are plotted head to tail on the complex plane.

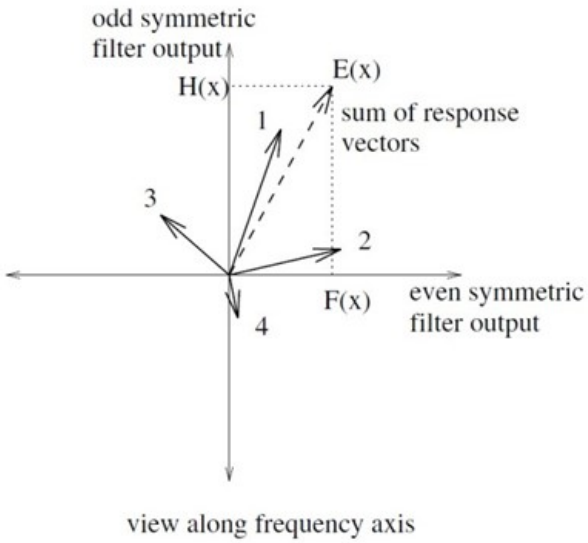

Figure 4-2: Geometric representation of four complex valued phase symmetry vectors along the one dimensional frequency axis

Phase symmetry uses this vector relationship between A_n and E(x) as:

$$PS(x) = \frac{E(x)}{\sum_n A_n} \tag{4-1}$$

$$0 < PS < 1 \tag{4-2}$$

Phase congruency also uses the vector relationships as:

$$\mathrm{PC(x)} = \sum_n \frac{w_o(x)E(x)}{\sum_n A_n} \tag{4-3}$$

The derivation of these relationships will be developed more rigorously later in this chapter.

4.3 Band Pass Filters

The local energy is the total real component formed by all the individual Fourier components in Figure 4-2 and considered as the 'vector' energy. For phase congruency, the local energy is the total vector sum of the Fourier components. The total path length gives the 'absolute' energy of the vector. The definition of phase symmetry is the ratio of the extent of the signal (vector sum of the component) divided by the sum of its individual component parts; the bounds of the phase symmetry values are given in Equation 4-1.

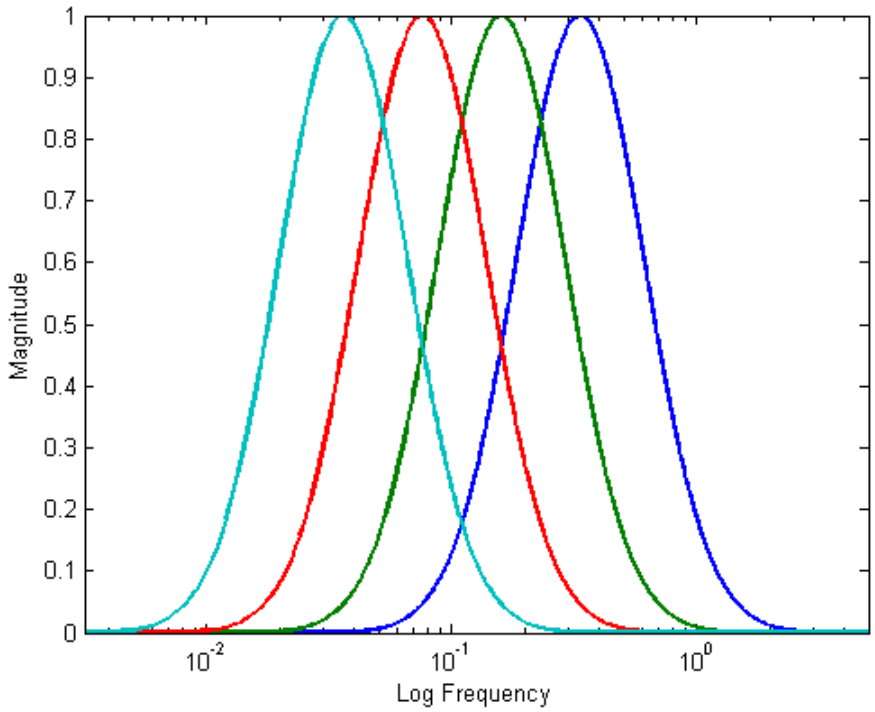

Figure 4-3: Set of four band pass filters

At a point of phase symmetry, the Fourier components (as displayed in Figure 4.2) will line up with the real axis. The local energy will then be equal to the total path length, giving a phase symmetry measure of 1. The Fourier components of the points of low phase symmetry have a random alignment. The resulting local energy vector will be small relative to the total path length and a low measure of phase symmetry will result.

The wavelet transform is used to obtain local frequency information at each point in the signal to calculate the local energy and sum of the Fourier components. In practice, the wavelet transform is approximated by a set of band pass filters which provide more than enough accuracy for the purposes of image feature detection. Kovesi builds on the approach of Morlet et al. (1982) and Field (1987), by using log-Gabor filters in quadrature to form the band pass filter set.

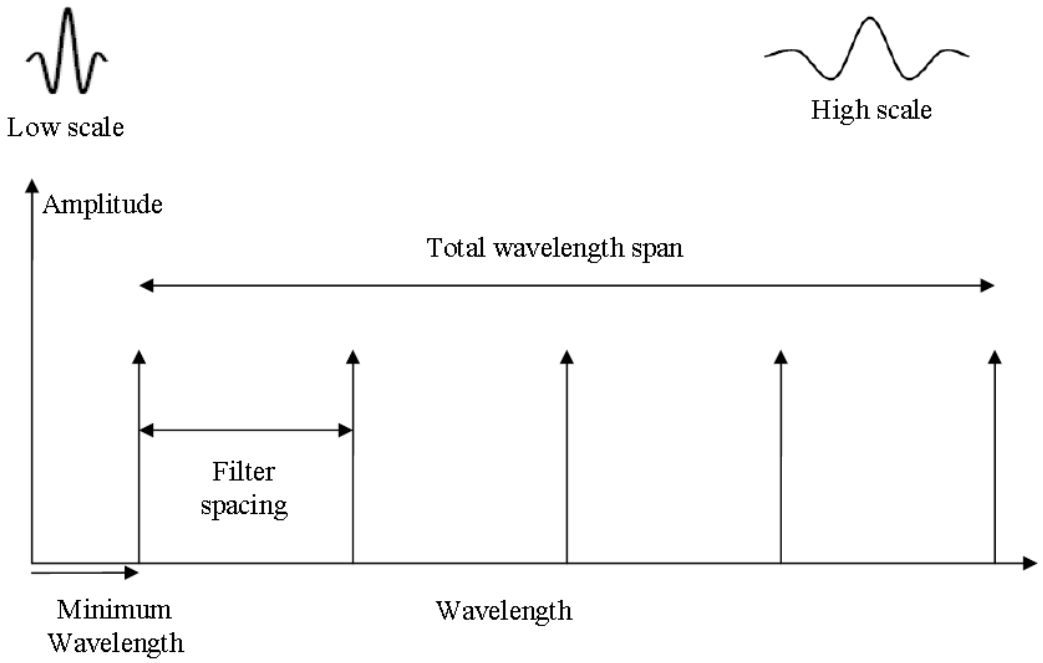

Figure 4-4: Construction of a five-band passed filter along the frequency domain.

The mathematical definition of the band pass filters satisfies Equations 4-4 and 4-5 below, as well as the set of four band pass filters as shown in Figure 4-3. During setup, the spread or coverage of the filter bank is computed to provide an even frequency coverage.

$$G(w) = e^{\frac{-\left(\log\left(\frac{w}{w_0}\right)\right)^2}{2\left(\log\left(\frac{k}{w_0}\right)\right)^2}} \tag{4-4}$$

$$w_0 = \lambda_{min} * mult^{(S-1)}$$

where $\kappa = Bandwidth\ of\ filter$

$\lambda_{min} = Minimum\ band\ pass\ fiter\ wavelength$

$mult = band\ pass\ filter\ separation$

$S = Band\ pass\ filter\ S\ scale$

The local frequency information is obtained by convolving the even and odd band pass filters with the image signal (with the DC component removed) forms the band pass filter response vector for each scale given by Equation 4-5.

$$[\ e_n(x),\ \ o_n(x)] = [\ I(x) * M_n^e\ ,\ \ I(x) * M_n^o\ ] \qquad (4\text{-}4)$$

$$I(x) = Signal\ with\ DC\ component\ removed$$

$$M_n^e = Even\ band\ pass\ filter\ for\ scale\ n$$

$$M_n^o = Odd\ band\ pass\ filter\ for\ scale\ n$$

The band pass filter response vector represents the frequency component of the signal in the locality of the point for a particular scale. The response vectors are shown in Figures 4-4 and 4-5.

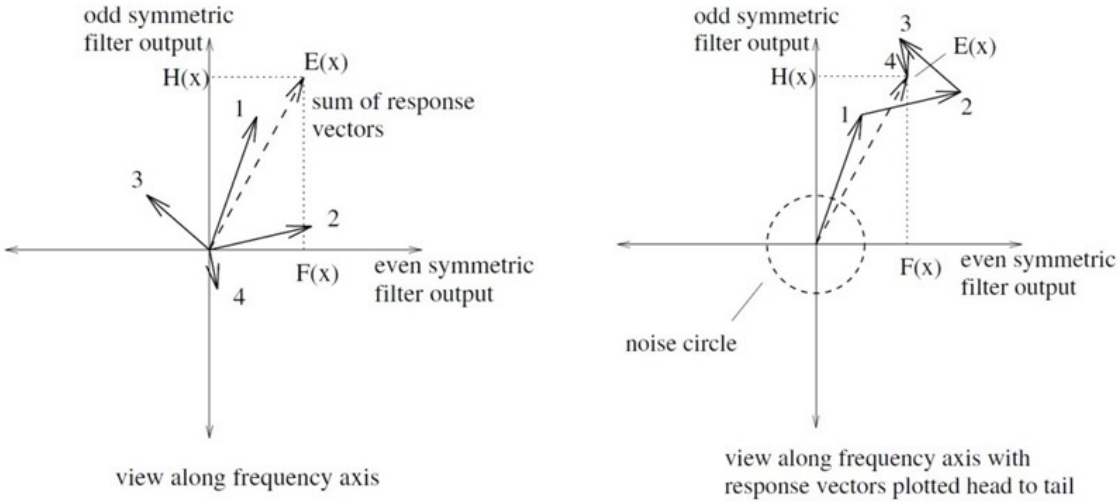

Figure 4-5: Geometric view of Local Energy response E(x)

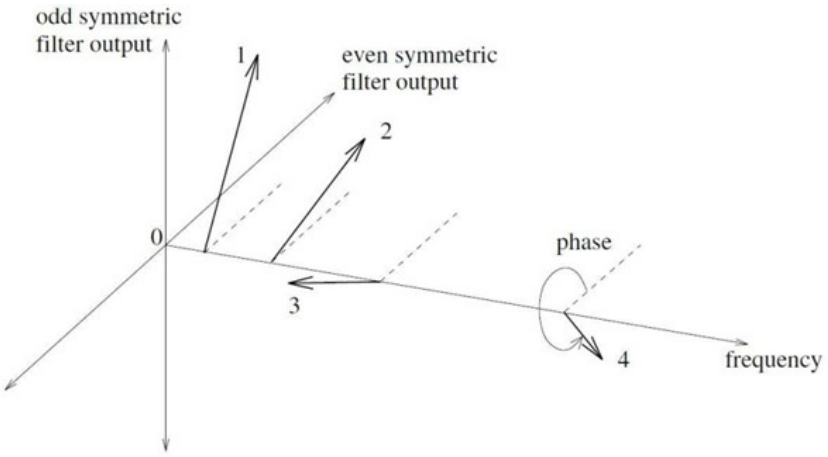

Figure 4-6: Band passed filter responses.

Note the similarities between phase symmetry and phase congruency. The local energy for phase congruency corresponds to the total vector sum of the Fourier components and the sum of the real components for phase symmetry (taken from Kovesi, 1999).

From Figure 4-6 the magnitude of a Fourier component at a particular scale *n* is equal to the magnitude of the band pass filter response vector at that scale. The path length of the Fourier components can therefore be approximated by the sum of the magnitudes of the responses over several different scales; Equation 4-6 gives the resultant expression for path length.

$$\sum_n A_n(x) \;\cong\; \sum_n \sqrt{e_n(x)^2 + o_n(x)^2} \qquad (4\text{-}5)$$

It can also be seen from Figure 4-4 that local energy for phase congruency may be obtained from the sum over all scales of the filter outputs, given mathematically in Equations 4-8, 4-9 and 4-10. The local energy for phase symmetry is obtained from the sum of the real responses, given by *F(x)* in Equation 4-8

$$\mathrm{F}(x) \;\cong\; \sum_n e_n\,(x) \qquad (4\text{-}6)$$

$$H(x) \cong \sum_n o_n(x) \tag{4-7}$$

$$E(x) = \sqrt{F(x)^2 + H(x)^2} \cong \sqrt{\sum_n e_n(x)^2 + \sum_n o_n(x)^2} \tag{4-8}$$

It is important to space the band pass filter elements such that the spread is uniform and that the area under each filter is constant. When the overlapping response is added, the result should be approximately the same. That is, the sum of the two components should match the maximum peak height. Using bandpass filters, good estimates of the Fourier components at a particular frequency can be achieved. The bandpass filter can be used to select components of particular frequency (or fixed pixel width) and effect segmentation of objects within the image.

4.4 Refinements to Kovesi's Calculation Method

This subsection describes additions made to the Kovesi method for 3D biological images.

The initial measure of phase symmetry had several issues including the following:

- Performs badly when the frequency components are small;
- Performs badly when one or nearly one frequency component is present;
- Offers poor feature localisation; and
- Responds badly to noise.

Small responses arise from the current measure phase symmetry which is a normalised quantity. Whilst having the advantage of being invariant to image brightness and contrast, the current measure does not account for the size of the response. Therefore, small responses are weighted the same as large responses, and upset the calculation. Adding a small constant to the denominator of the phase symmetry expression to prevent division by zero solves this problem. Phase congruency was modified to incorporate this correction.

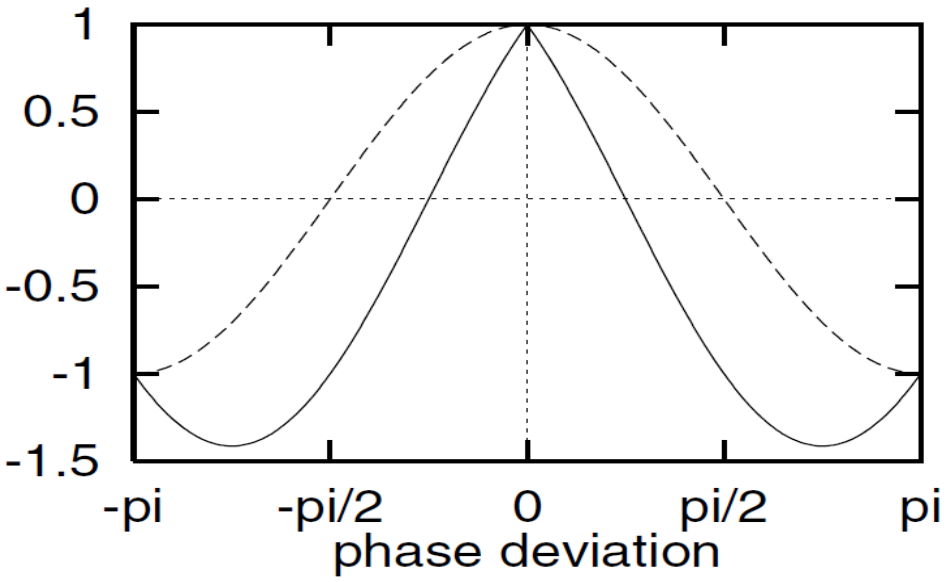

Figure 4-7: Two different measures of phase deviation

The dotted line is the cosine of phase deviation, while the solid line is the difference between the cosine and the absolute sine of phase deviation. The solid line provides a much more localised measure

The issue of poor localisation arises because the expression for local energy varies with the cosine of the phase angles. The cosine function has minimum gradient around the origin, resulting in a nearly constant local energy. Modifying the expression for local energy, the localisation of the phase symmetry method is improved by the inclusion of the odd symmetric filter response in the calculation, as shown by Equation 4-11. This new measure for local energy offers much better localisation as the sine function has a maximum gradient at the origin. Inverse trigonometric functions improve the localisation of the local energy; however, this adds significantly to the computation time. This is equivalent to looking for the minimum odd band-passed filter response and to the maximum even band-passed filter response illustrated in Figure 4-5. The increase in localisation is displayed in Figure 4-6. The cosine function varies very little about the origin whereas the new measure for local energy drops away sharply, as the distance from the origin increases.

4.5 Calculating Phase Symmetry

The local energy model asserts that features exist at points where the Fourier series components of a signal are maximally in phase (Morrone M and Owens R 1987). The Fourier series of a square wave, for example, has maximal phase congruency at the rise and fall of each step (Figure 4-7). At other points within the signal, the individual Fourier components move out of phase and consequently, phase congruency is low. It should be noted that here, phase refers to local phase, which is the phase of a signal at some position *x*.

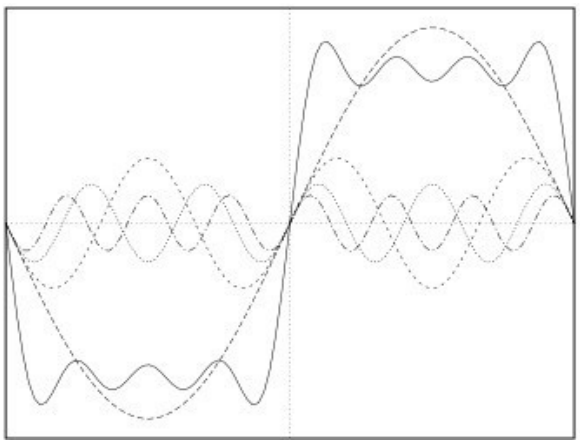

Figure 4-8 : Fourier series construction of a square wave

Dotted lines represent Fourier components and the solid line represents the sum of these components. Note that at the step edge all of the Fourier components are in phase. Phase congruency is then a measure invariably linked to the local phase of the Fourier components of a signal. The Fourier expansion of a signal, I, at a position x, is defined as

$$\mathrm{I}(\mathrm{x}) = \sum_{\mathrm{n}} \mathrm{A_n} \cos(2\pi \mathrm{n x} + \varphi_{\mathrm{no}}) = \sum_{\mathrm{n}} \mathrm{A_n} \cos(\varphi_{\mathrm{n}}(\mathrm{x})) \qquad (4\text{-}9)$$

Here, A_n represents the amplitude of the n^{th} Fourier component, φ_{no} the phase offset, and $\varphi_n(x)$, the local phase of that component at a position x. Lending from phasor notation, each Fourier component can be represented as a complex vector of magnitude, A_n and phase angle, $\varphi_n(x)$. The local energy of a given signal is defined as the magnitude of the vector sum of local Fourier components or, more formally, as the modulus of a signal and its Hilbert transform.

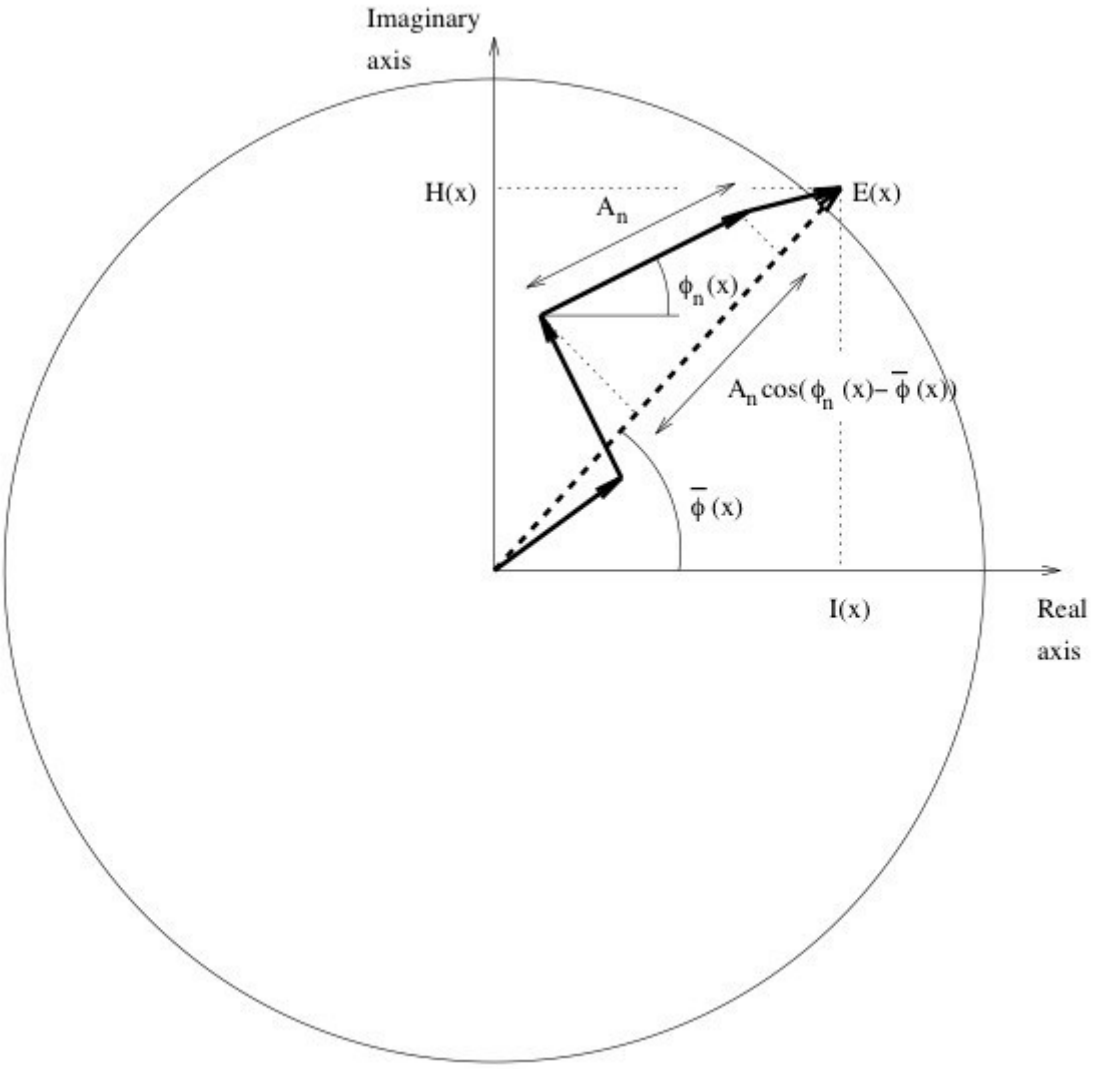

Figure 4-9: The vector summation of individual Fourier components, head to tail

Note that when the phases for all components are equal, local energy is at a maximum and is equal to the sum of the amplitudes of the Fourier components. Hence, local energy is directly proportional to phase congruency. It was on this basis that Morrone and Owens developed the local energy model (Morrone & Owen 1987).

The vector summation of all individual Fourier components 'head-to-tail' produces the resultant local energy vector. Local energy is a maximum when the phases for all components are equal.

Note that here:

- $\varphi(x)$ refers to the amplitude weighted mean local phase of all the Fourier components;

- I(x) represents the signal; and

- H(x) is its Hilbert transform.

However, local energy is not dimensionless but dependent on the amplitude of the signal, and in relation to an image, is susceptible to contrast (Kovesi 1999).

Each component vector contributes $A_n \cos(\varphi_n(x) - \varphi(x))$ to local energy, where $\varphi_n(x) - \varphi(x)$ is the deviation in phase away from the amplitude weighted mean. Therefore, local energy is defined as a maximum when nearly all energy is a maximum when there is no deviation in phase, and a minimum when the phase deviation is ±90°. That is when all Fourier terms are orthogonal to the local energy vector. It is the cosine of this phase deviation that provides the direct relationship to phase congruency. Local energy is phase congruency scaled by the sum of Fourier amplitudes – a relationship formally proven by Venkatesh and Owens (1987).

Geometrically, this is the same as defining phase congruency as the ratio between local energy and the total path length of the Fourier components. This is on this basis that the notion of phase congruency is extended to 2D signals.

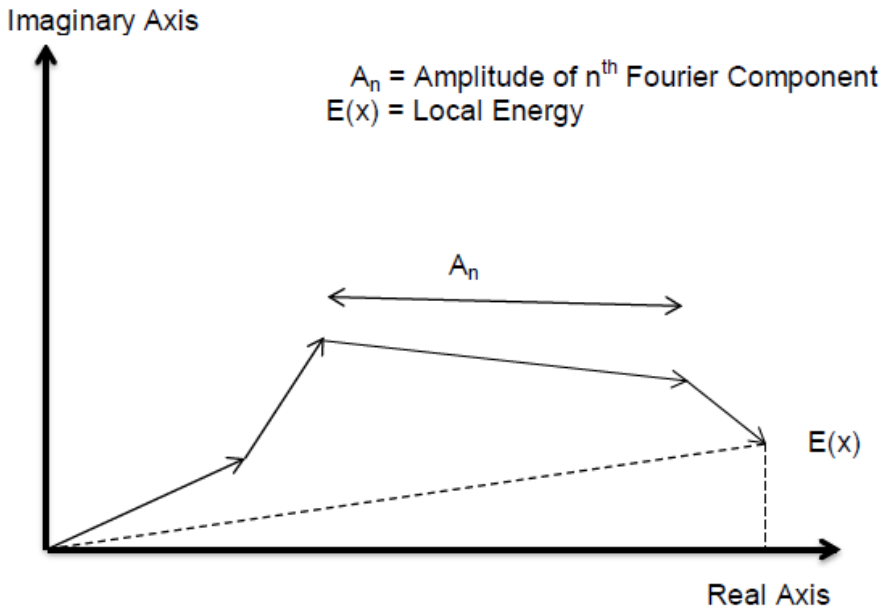

Figure 4-10: Geometric representation Fourier components: A_n and total energy E(x).

In practice, bands, or scales of frequency in the FT of an image are used to approximate the signal's frequency Fourier components. For each scale of frequency, the local energy vector for that scale provides the complex vector representation of the corresponding Fourier component. In practice, the complex vector representation of the n^{th} Fourier component is defined by the image at the n^{th} scale (the real part) and its Hilbert transform (the imaginary part).

This chapter follows on from the methodology developed (Kovesi, 1999), wherein, quadrature pairs of log-Gabor filters are used to simultaneously scale the frequency domain and produce the local energy vector at each scale (instead of using the Hilbert transform, where a pair of filters with a 90-degree phase shift provides a measure of local energy). This methodology was used to develop the 2D phase congruency algorithm and establishment of the filters required to estimate phase congruency.

Further, spread filters are used to localise analysis to set orientations in the frequency domain. For each orientation, phase congruency is calculated and weighted by the spread of frequencies across all scales on that orientation. The final phase congruency response of an image is the sum of phase congruency over all orientations. This chapter details the method developed for the calculation of 2D phase congruency, which is analogous to the phase symmetry described in the previous chapter.

The local energy is the total real component formed by all the individual Fourier components in Figure 4-2 and considered as the 'vector' energy. For phase congruency, the local energy is the total vector sum of the Fourier components. The total path length gives the 'absolute' energy of the vector. The definition of phase symmetry is the ratio given in Equation 4-1 and the bounds of the phase symmetry measure are given in Equation 4-2.

$$PS(x) = \frac{E_n}{\sum_n A_n} \tag{4-10}$$

$$0 < PS(x) < 1 \tag{4-11}$$

At a point of phase symmetry, the Fourier components (as displayed in Figure 4-2) will line up with the real axis. The local energy will then be equal to the total path length, giving a phase symmetry measure of 1. The Fourier components of points of low phase symmetry have a random alignment. The resulting local energy vector will be small relative to the total path length, and a low measure of phase symmetry will result.

From Figure 4-4 the magnitude of a Fourier component at a particular scale *n* is equal to the magnitude of the band pass filter response vector at that scale. The path length of the Fourier components can therefore be approximated by summing the magnitudes of the responses over several different scales. Equation 4-18 gives the resultant

$$\sum_n A_n(x) = \sum_n \sqrt{e_n(x)^2 + o_n(x)^2} \tag{4-12}$$

$$F(x) \cong \sum_n e_n(x) \tag{4-13}$$

$$H(x) \cong \sum_n o_n(x) \tag{4-14}$$

$$E(x) = \sqrt{F(x)^2 + H(x)^2} \cong \sqrt{\left(\sum_n e_n(x)\right)^2 + \left(\sum_n o_n(x)\right)^2} \tag{4-15}$$

$$PS(x) = \frac{E(x)}{\sum_n A_n + \varepsilon} \tag{4-16}$$

With the introduction of noise reduction (chapter 3.2.7) the expression for phase symmetry is modified by the threshold, T, and epsilon, ϵ to avoid zero division:

$$PS(x) = \frac{|E(x) - T|}{\sum_n A_n + \varepsilon} \tag{4-17}$$

The band-passed filter response vector represents the frequency component of the signal in the locality of the point for a particular scale. In Figure 4-11 in section 4-6, the response vectors are plotted.

$$E(x) = \sum_n A_n \left(|\cos(\emptyset_n(x))| - |\sin(\emptyset_n(x))| \right) \tag{4-18}$$

$$PS(x) = \frac{|\sum_n A_n \left(|\cos(\emptyset_n(x))| - |\sin(\emptyset_n(x))| \right) - T|}{\sum_n A_n + \varepsilon} \tag{4-20}$$

4.6 Calculating Phase Congruency

In practice, for each spread filter orientation, a local energy vector is found for each scale. Phase congruency for an orientation is the ratio between the modulus of the sum of each scale local energy vector (the total local energy) and the total path length taken by those vectors. Since features should be characterised by a wide spread of frequencies, a weighting function, $w(x)$, is used to scale phase congruency in accordance with the relative spread of frequencies over a given orientation. Finally, the total phase congruency is the sum of phase congruency over all orientations.

$$\mathrm{PC(x)} = \sum_{n} \frac{w_o(x)E(x)}{\sum_n A_n} \tag{4-21}$$

$$PC(x) = \sum_{0} \frac{w_o(x)\sum_n \left(A_{n,o}\cos\left(\emptyset_{n,o}\ (x)\ -\ \overline{\emptyset_n}\,(x)\ \right)\right)}{\sum_n A_n} \tag{4-22}$$

Where w_o (x) is the weighting function for a particular orientation and is determined by the total path length of local energy vectors (sum of local amplitudes) divided by the magnitude of the largest vector over the number of scales used.

As the weighting function, will always be used, it has consequently been dropped from notation. Note that phase congruency is a function of the cosine of phase deviation. Therefore, phase congruency has a near zero slope at points of maximum phase congruency and provides a poorly localised response to features (shown as the dotted line in Figure 4-7) (Kovesi 2007). This is identical to the argument used for phase symmetry.

A much more efficient approach is to use the difference between the cosine and absolute sine of phase deviation (shown as the solid line in Figure 4-7). This measure provides an almost linear relationship with phase deviation, and therefore provides a much more localised and accurate measure of phase congruency (Kovesi 1999). This relationship is also used in the calculation of phase symmetry. Phase congruency becomes:

$$\mathrm{PC(x)} = \sum_n \frac{w_o(x)E(x)}{\sum_n A_n} \tag{4-23}$$

$$\mathrm{PC(x)} = \sum_0 \frac{w_o(x)\sum_n\left(A_{n,o}\cos\left(\emptyset_{n,o}(x) - \overline{\emptyset_n}(x)\right) - \left|\sin\left(\emptyset_{n,o}(x) - \overline{\emptyset_n}(x)\right)\right|\right)}{\sum_n A_n} \tag{4-24}$$

$$\mathrm{PC(x)} = \sum_n \frac{w_o(x)\sum_n A_{n,o}\ \Delta\emptyset_{n,o}}{\sum_n A_n} \tag{4-25}$$

The cosine and sine of phase deviation are calculated by the dot and cross products between total local energy vector and a scale's local energy vector respectively. In practice, this measure distinctly defines features, whereas before, features would appear blurred.

Referencing back to the section on noise compensation in section 3.2.7, the phase congruency expression was modified by calculating the threshold separately for each orientation and applied to the total local energy. The expression for phase congruency becomes:

$$PC(x) = \sum_n \frac{|E(x) - T|}{\sum_n A_n + \epsilon} \tag{4-26}$$

$$PC(x) = \sum_n \frac{\left|\sum_n \left(A_{n,o}\cos\left(\varphi_{n,o}(x) - \varphi_n(x)\right)\right) - T_o\right|}{\sum_n A_n \sum_n A_n + \epsilon} \tag{4-19}$$

Chapter 5 Two-Dimensional Software Performance

This chapter deals with the two-dimensional performance of the software developed in this study in relation to image segmentation and noise rejection.

The phase symmetry and phase congruency methods produced the best results for the identification and segmentation of features. Traditional gradient based methods such as the Canny and Sobel edge detectors failed to provide good results in a noisy 3D environment. The Canny and Sobel edge detectors are derived from image brightness and contrast, parameters which vary widely between images. The Kovesi phase symmetry and phase congruency methods are limited in that only 2D images are processed. Fully developed 3D programs would provide better results from the image stack by dealing with:

- Resolution of fibres not aligned with the 2D plane; and
- Noise rejection by including data from adjacent planes.

The 2D software was developed from Kovesi's work to provide alternative filter configurations and faster performance. This software performance is illustrated in this chapter against test images collected for software evaluation.

5.1 Sample Images

The following images are of twelve-month-old sheep femoral condyle cartilages. Samples were harvested from a load bearing region of the femoral condyle and washed in 0.9% Phosphate Buffered Saline ("PBS"). The samples were then stained with 0.05% FITC for five minutes and washed with PBS until the wash liquid was clear. The samples were then placed in a thin bottom petri dish and imaged using an inversed Leica LSCM. The data was collected at 1.4 micron intervals on the z axis and 0.635 microns in the x and y directions giving images of 1024 x 1024 voxels. Two specimens (sheep id 080 and sheep id 150) were imaged using an x63 oil immersion Plan APOCHROMAT objective lens. This sample was the second confocal image that I collected. This image has been used extensively to show the improvement that signal processing gives to both image quality and feature detection. The image was also the first image that showed collagen fibres.

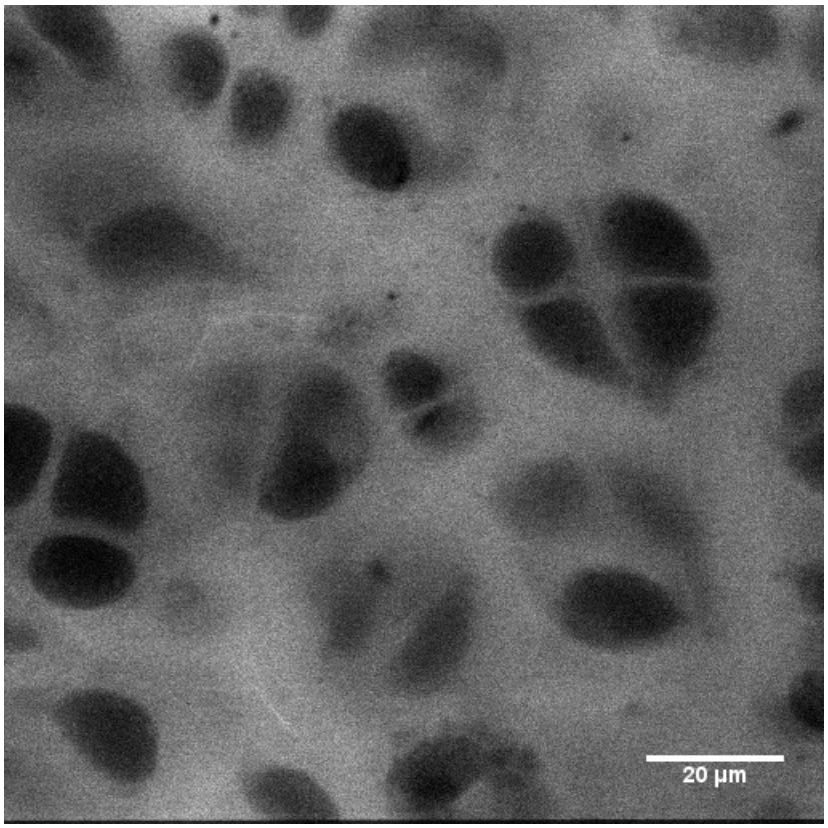

Image 5-1: Raw image

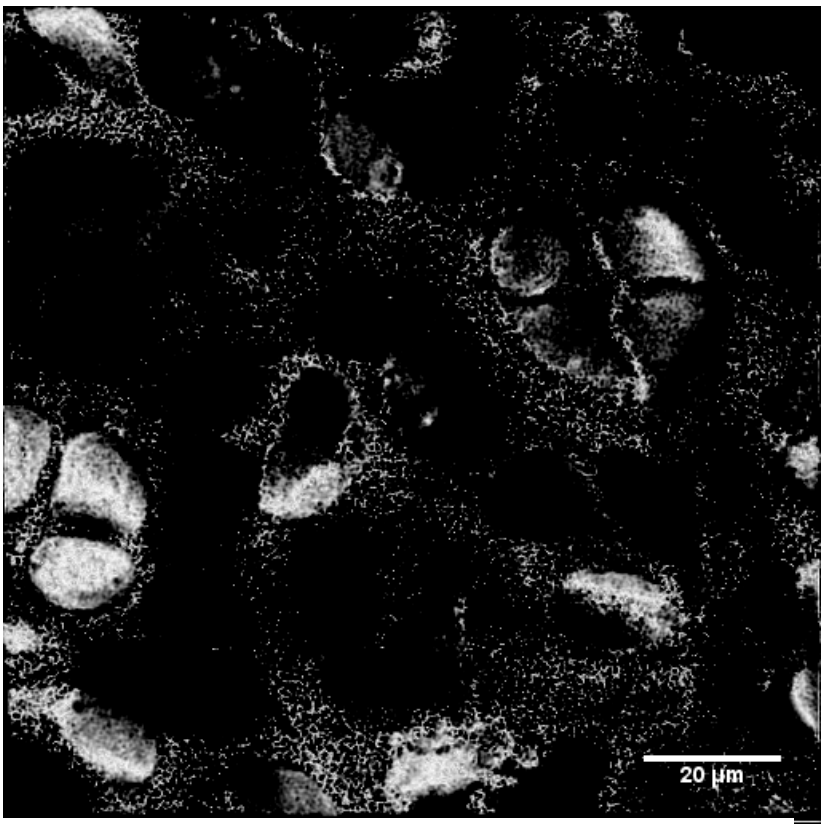

Image 5-2: Wavelength range too wide producing poorly defined chondrocytes

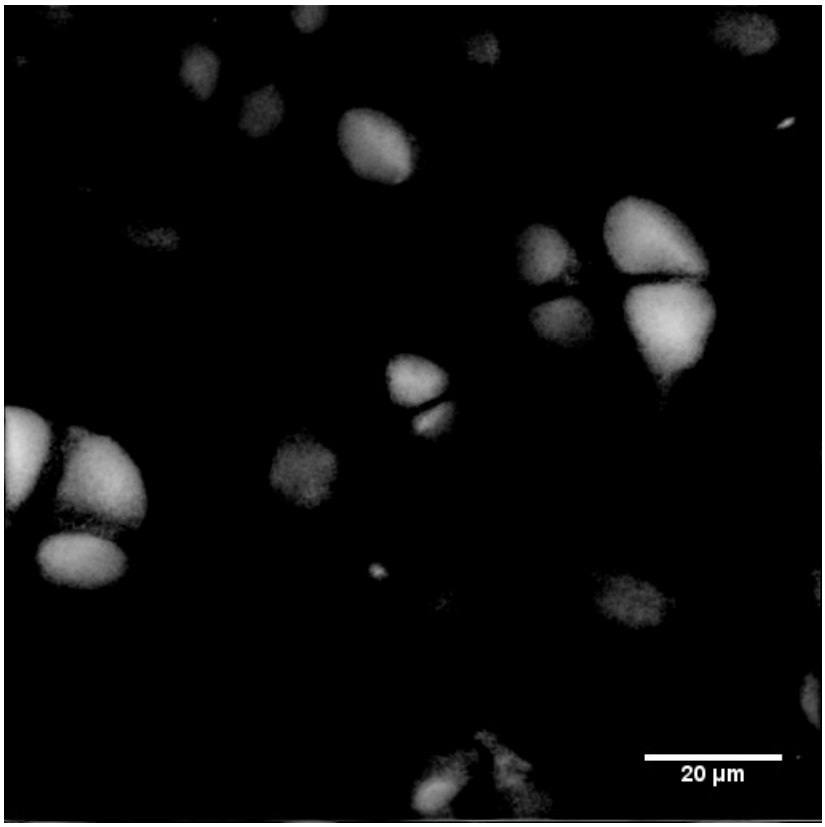

Image 5-3: Wavelength range too short producing poor detection performance

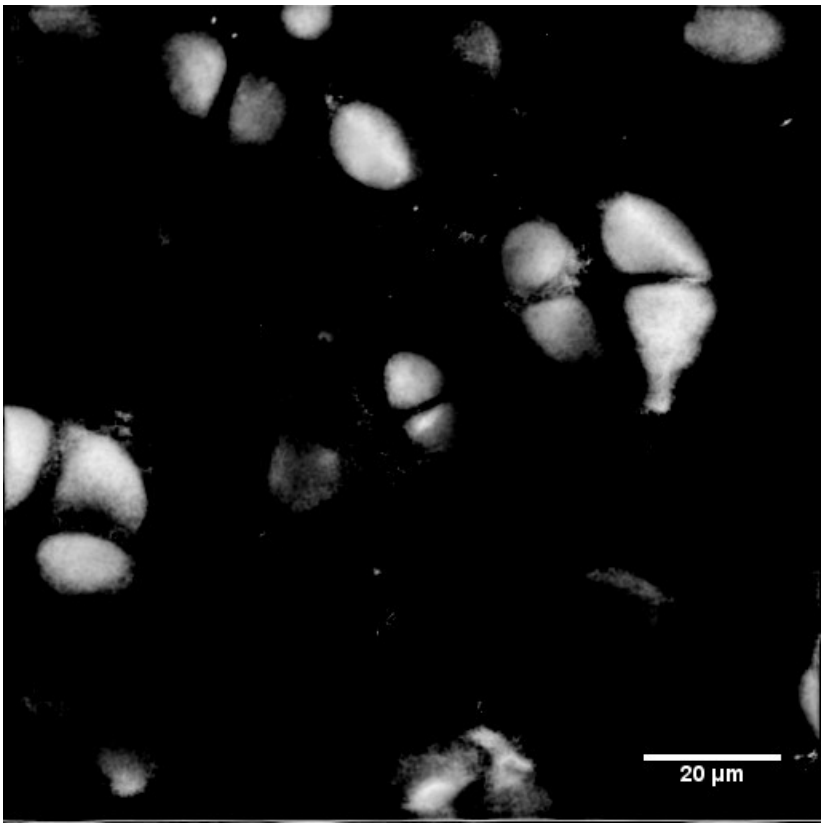

Image 5-4: Near optimal wavelength range

Images 5-1 through 5-4 show the effect of band-passed filters as a mechanism for noise reduction and chondrocyte separation.

Image 5-1 shows a raw frame from a stack of images of young sheep cartilage. The image shows viable chondrocytes as seen by the dark circular objects within the image. Collagen II fibres can be seen in the background as a light fuzzy cotton wool like substance. Individual collagen bundles are also visible between the chondrocytes. This image was passed through several band-passed filters of varying wavelength in an attempt to segregate the image into its component parts.

Image 5-2 shows the output of the band-passed filter with a wavelength range that is too wide. The resulting image is poorly defined with the chondrocytes missing edges and smaller in diameter than the original images. Note that the resultant image has been synthesised from the 2D bit mask defining the component objects; convolved with the original image and finally inverted. The image looks photorealistic as the original brightness is preserved by the mask and the intensity map of the raw image. Note that the smaller fibres have been eliminated from the sample.

Image 5-3 shows the effect of too narrow wavelength filter. The detection of the chondrocytes is poor with many missing. The separation of the chondrocytes from the background is in complete. Again, the image is inverted. This is the same image processing as performed in Image 5-2 but the wavelength is too short resulting in poor separation of features.

Image 5-4 shows a better selection of wavelength. Most of the small features have been eliminated whist preserving the larger chondrocytes. The bit mask has been preserved the shape of the cellular groups, however, some of the fainter cells have been removed.

5.2 2-D Phase Symmetry Performance

This subsection describes the automated segmentation possible with the developed image processing.

5.2.1 Band Passed Filter Results

After reading the image and constructing the filters bands, the image is segmented into several different frequency components using the constructed band-passed filter bank. The setup of the band pass filter bank was found to influence the phase symmetry segmentation output and allowed for a wide range of different features to be segmented.

Images 5-6 through 5-9 display the decomposition of an ovine articular image into four separate band-passed components, when looking for collagen fibres. It was found that for collagen fibres, band passed images with wavelengths smaller than 2 pixels responded almost entirely to noise, producing poor, noisy phase symmetry results. This is consistent with the Nyquist theorem, which states that it is not possible to sample frequencies higher than half the sample rate. In the case of images, this corresponds to a minimum wavelength of 2 pixels.

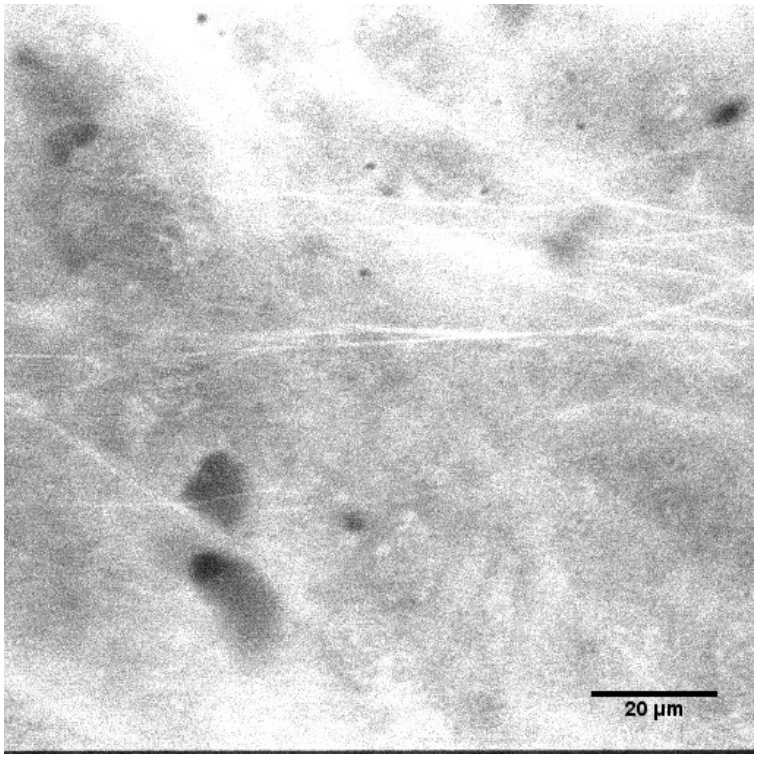

Image 5-5: Original image of ovine articular cartilage from sheep 150.

The output images are shown inverted with respect to the original Image 5-5.

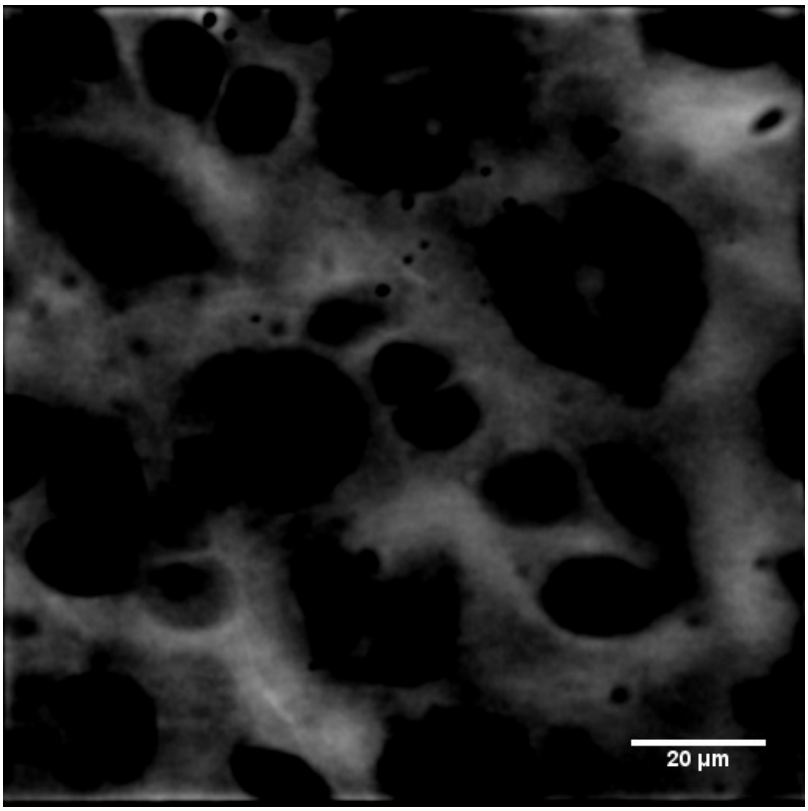

Image 5-6: Band passed image with minimum wavelength of 5 pixels

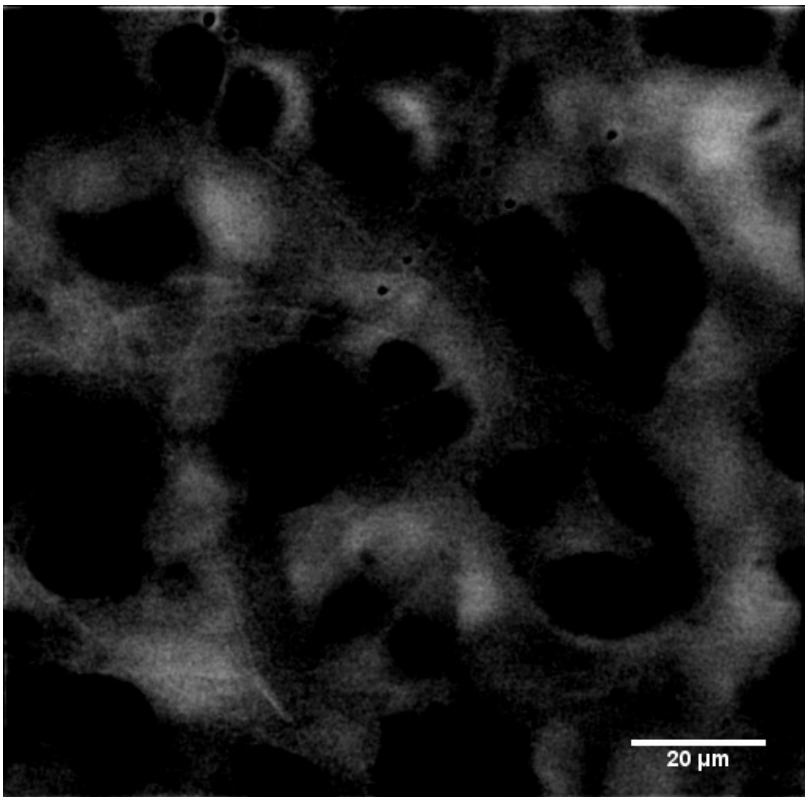

Image 5-7: Band passed image with minimum wavelength of 12 pixels

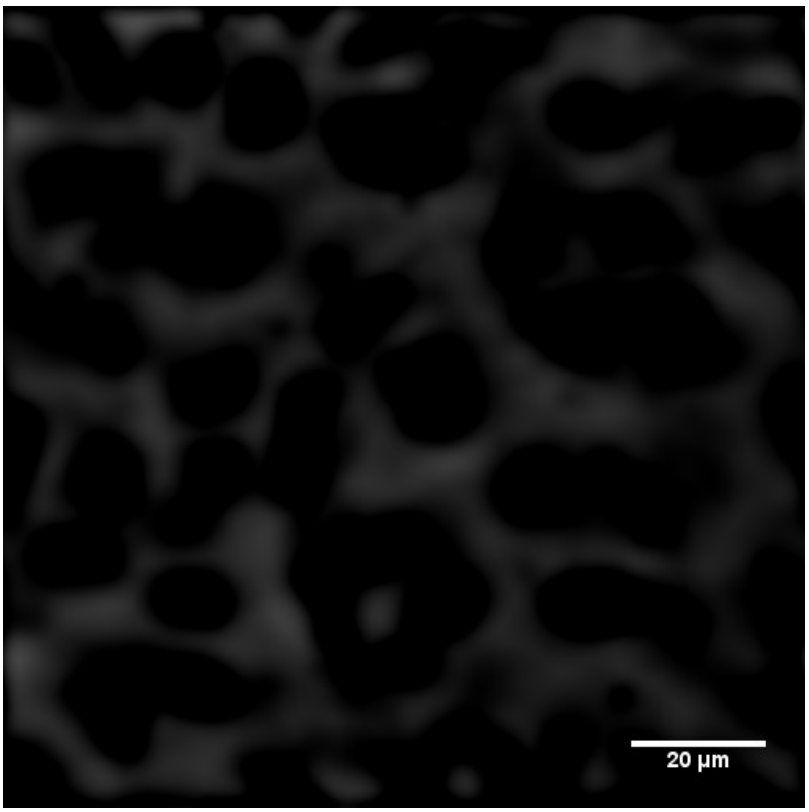

Image 5-8: Band passed image with minimum wavelength of 29 pixels

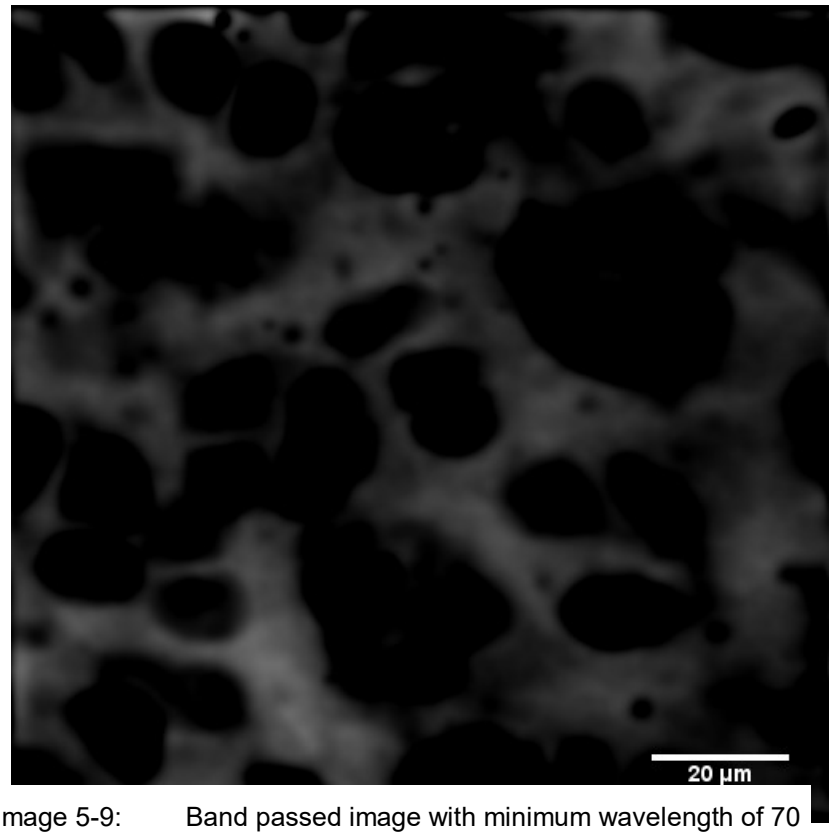

Image 5-9: Band passed image with minimum wavelength of 70 pixels

Setting the minimum wavelength at least 3 pixels, a larger amount of the noise present in the image was rejected. Adjusting the range covered by the band pass filters, it is possible to bias the phase symmetry output to look for different features based upon their frequency (wavelength) response. Smaller features are favoured by short wavelength filters, but excluded by long wavelengths.

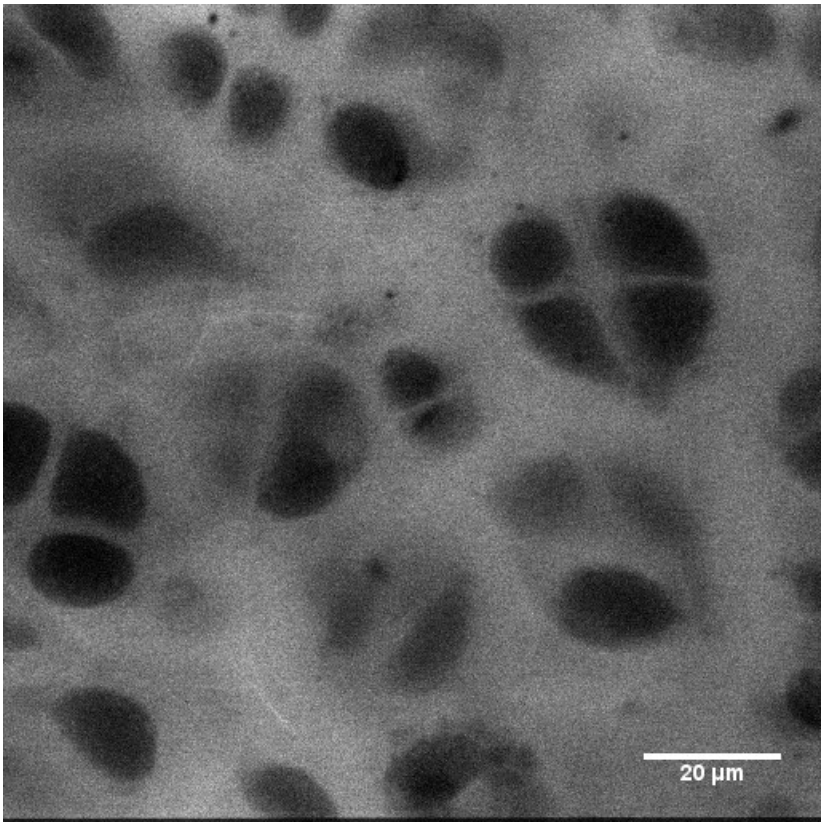

Image 5-10: Original image. Processed images are shown with dark symmetry [i.e. inverted with respect to this image]

Selecting appropriate minimum wavelength and number of scales provides a mechanism to segregate the features according to size. If depiction of only the collagen I fibres were desired, it was found that the band pass filters should be set up to cover wavelengths shorter than 8 pixels. If the collagen II fibres were desired, the band pass filters should be set up over much larger wavelengths, up to 25 pixels. By varying the band pass filter coverage of these regions, both types of collagen can be depicted.

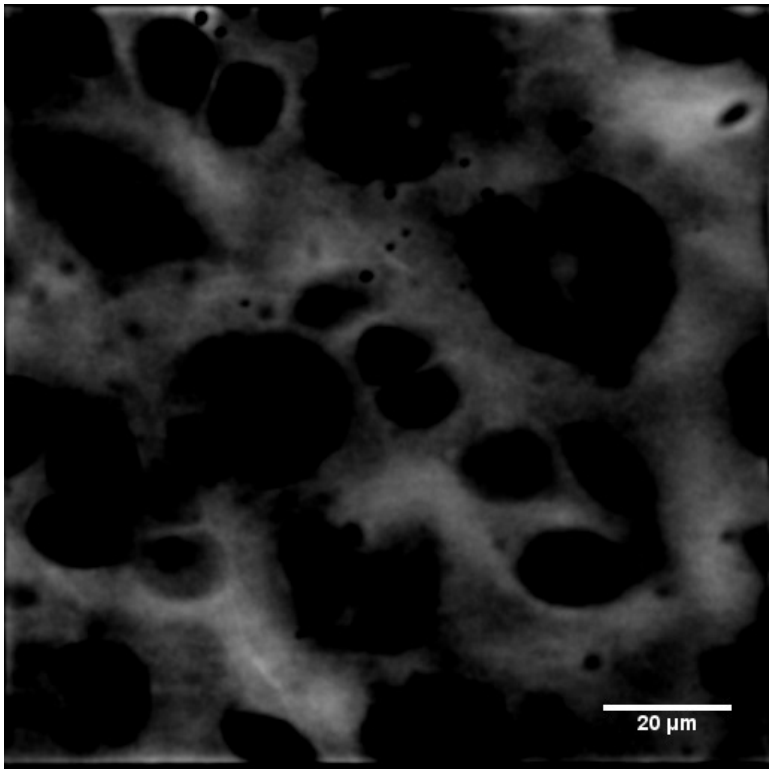

Image 5-11: Collagen phase symmetry bandwidth coverage with variable filter bank wavelength coverage of 5 pixels

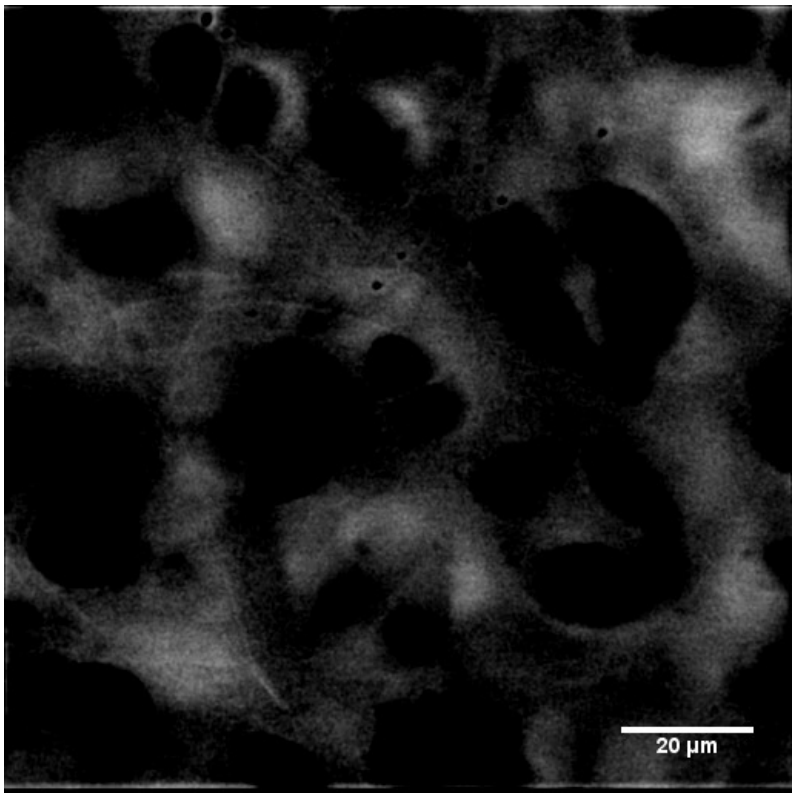

Image 5-12: Collagen phase symmetry bandwidth coverage with variable filter bank wavelength coverage of 12 pixels

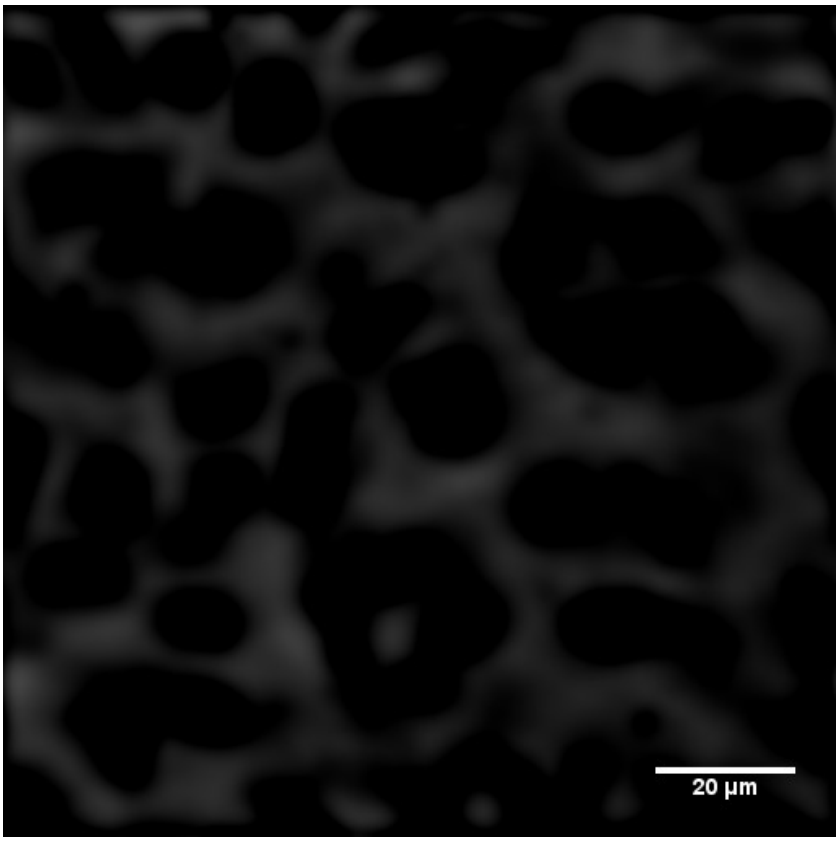

Image 5-14: Collagen phase symmetry bandwidth coverage with variable filter bank wavelength coverage of 29 pixels

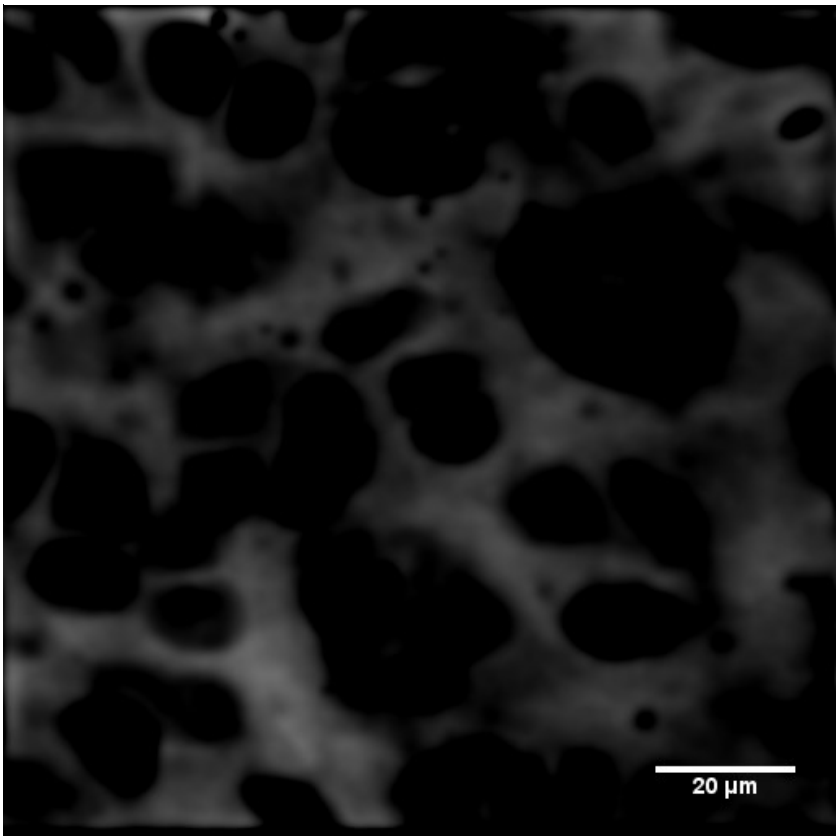

Image 5-13: Collagen phase symmetry bandwidth coverage with variable filter bank wavelength coverage of 70 pixels

Images 5-12 to 5-14 display a set of four band-passed images when looking for chondrocytes in the original Image 5-11. In this case the phase symmetry algorithm would look for dark areas on a white background. The dark chondrocytes were picked up well by all band pass filters. Due to the larger size of the chondrocytes compared to the collagen fibres, larger wavelengths are typically used in their detection. Band passed images with extremely large wavelengths, such as Image 5-15, with minimum wavelength of 70 pixels, do not exhibit sharp well defined edges, leading to blurred phase symmetry results.

5.2.2 Collagen Fibre Segmentation

Images 5-15 to 5-18 display the results of varying the filter bank bandwidth, whilst keeping the minimum wavelength constant when looking for collagen fibres for the raw Image 5-15. The effect on the phase symmetry output of too large a filter bank bandwidth can be seen in Image 5-16. The bulk of the fibres are not easily visualised, however, good noise rejection was achieved, evident from the dark background reducing the phase symmetry method's invariance, to image brightness and contrast.

Image 5-17 displays the phase symmetry result for too small a filter bank bandwidth. There is a large amount of speckled noise present throughout, arising primarily from the larger influence of the shorter wavelength filter. The smaller bandwidth also reduces the effectiveness of the phase symmetry algorithm, thus delivering poor performance over small frequency ranges.

Image 5-18 displays the phase symmetry result for what was the optimal trade-off between the too short a minimum wavelength and too long a filter bandwidth. In a research setting, the user would set up the filter bank according to their own requirements for separation and noise rejection.

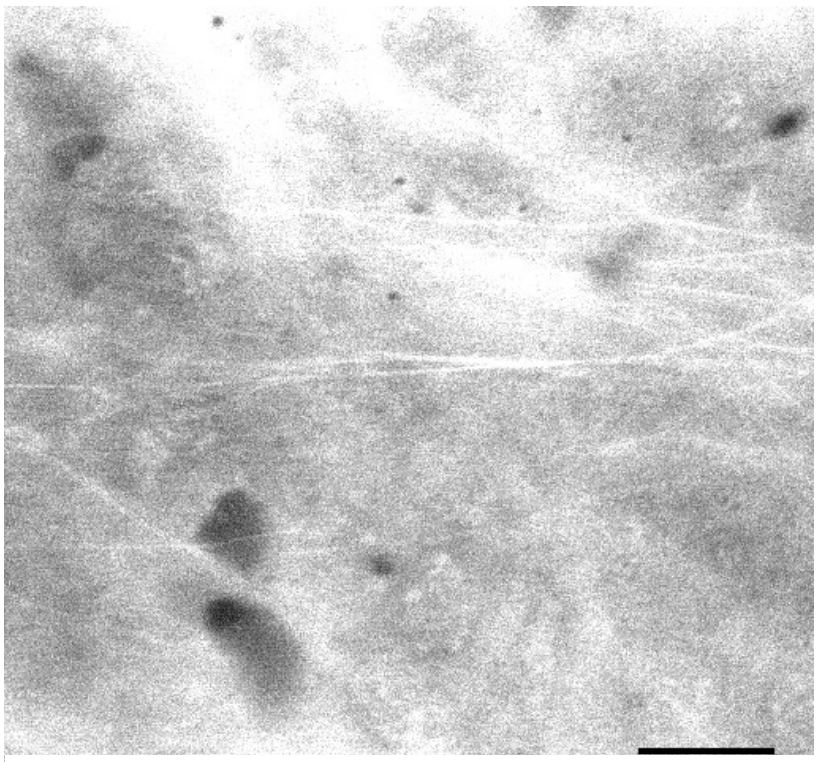

Image 5-15: Bright field image one year old ovine cartilage.

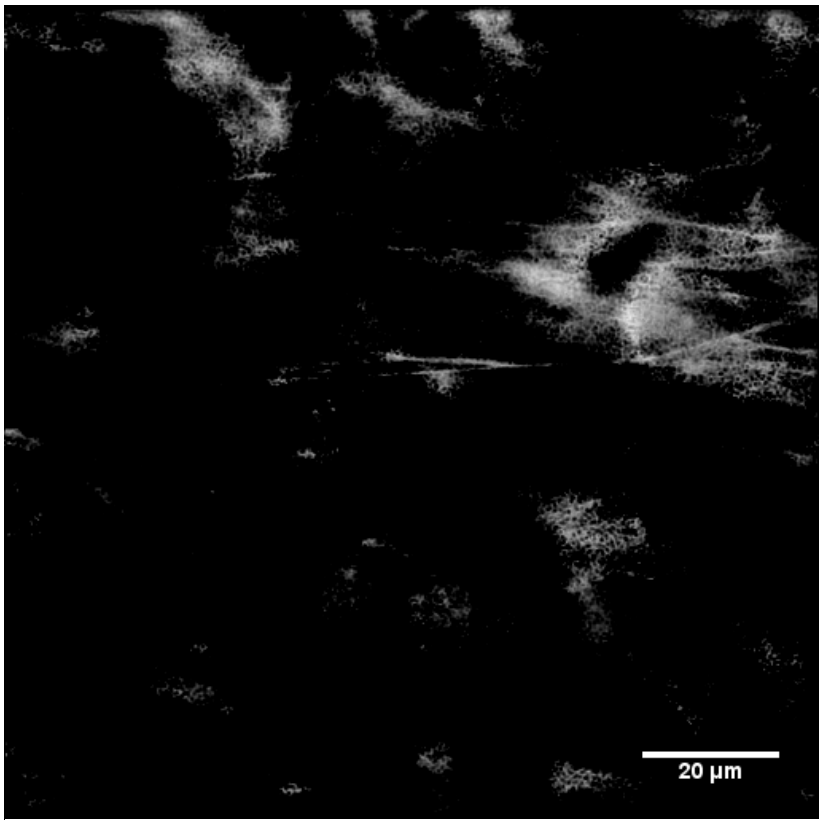

Image 5-16: inverted image showing bright patchy spots and artefacts resulting from too long a wavelength

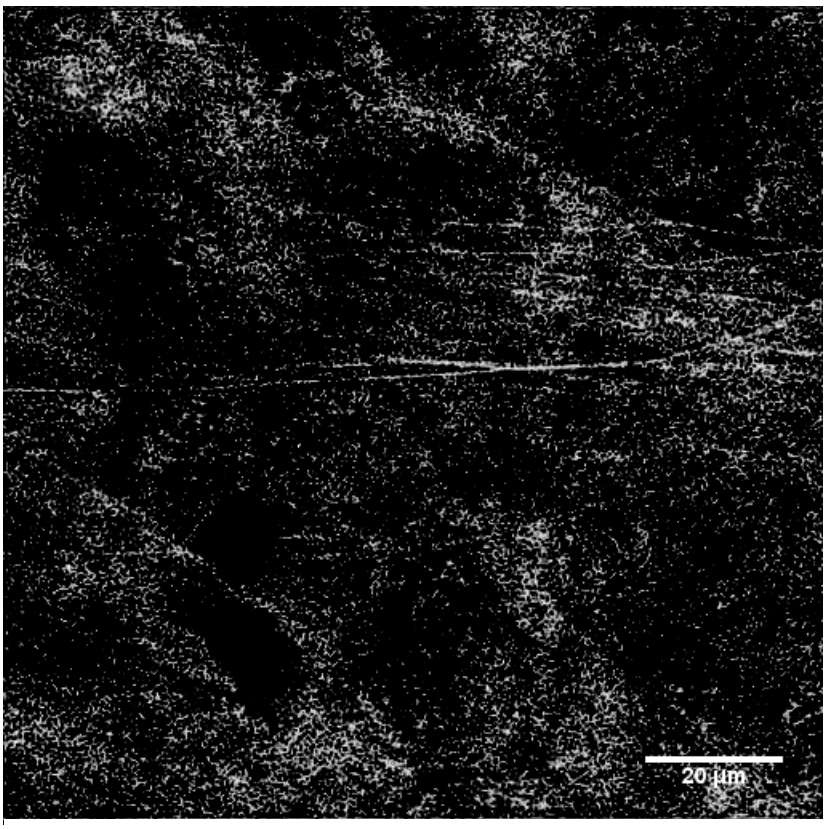

Image 5-17: Inverted image showing speckled noise resulting from too short a wavelength

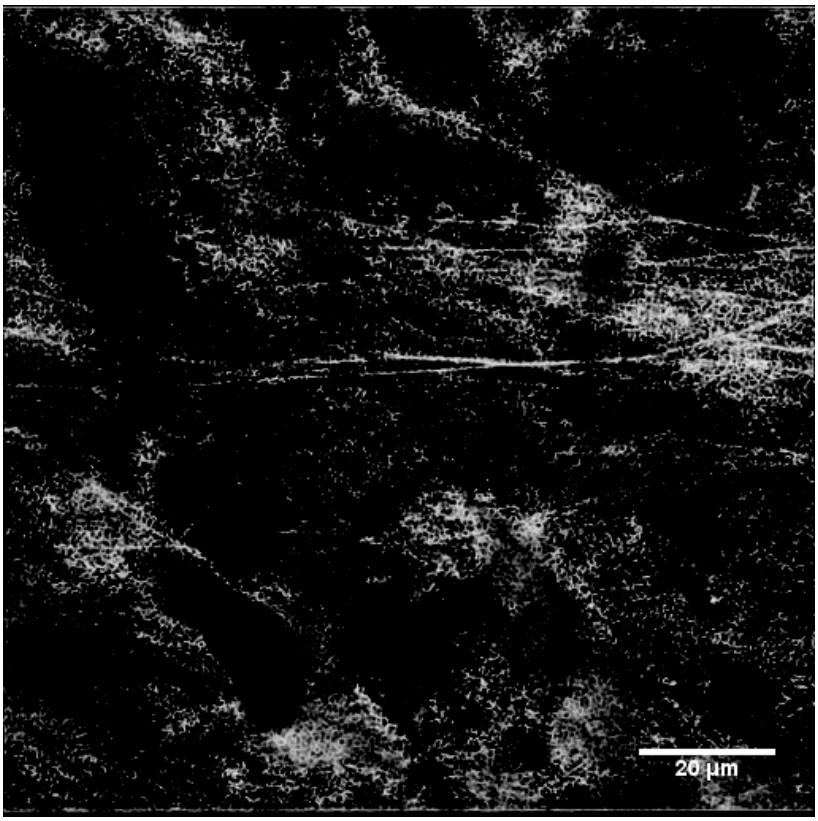

Image 5-18: Inverted image showing near optimal feature separation

5.3 Chondrocyte Segmentation

Images 5-19 to 5-22 display the chondrocyte phase symmetry results for a variety of filter bank bandwidths, with the minimum filter wavelength kept constant.

The phase symmetry result of having too small a filter bank bandwidth is displayed in Image 5-20 where cell responses are eroded as the filter wavelengths are much smaller than those used to segregate the chondrocytes. The chondrocytes in the phase symmetry result also have features on them, another sign that the filter bank wavelengths are too small, as the features being picked up by the phase symmetry algorithm are much smaller than the chondrocytes.

Image 5-21 displays the phase symmetry result for too large a filter bank bandwidth. Whilst delivering excellent noise rejection, when compared with the original image, the cell edges are not clearly defined. This is due to the increased contribution from the large-scale filters that offer poor localisation.

Image 5-22 displays the optimal result. As the size of chondrocytes varies very little, it is unlikely that these parameters will need to be adjusted at all in the future. The table below summarises the optimal filter bank parameters for both collagen fibres and chondrocytes.

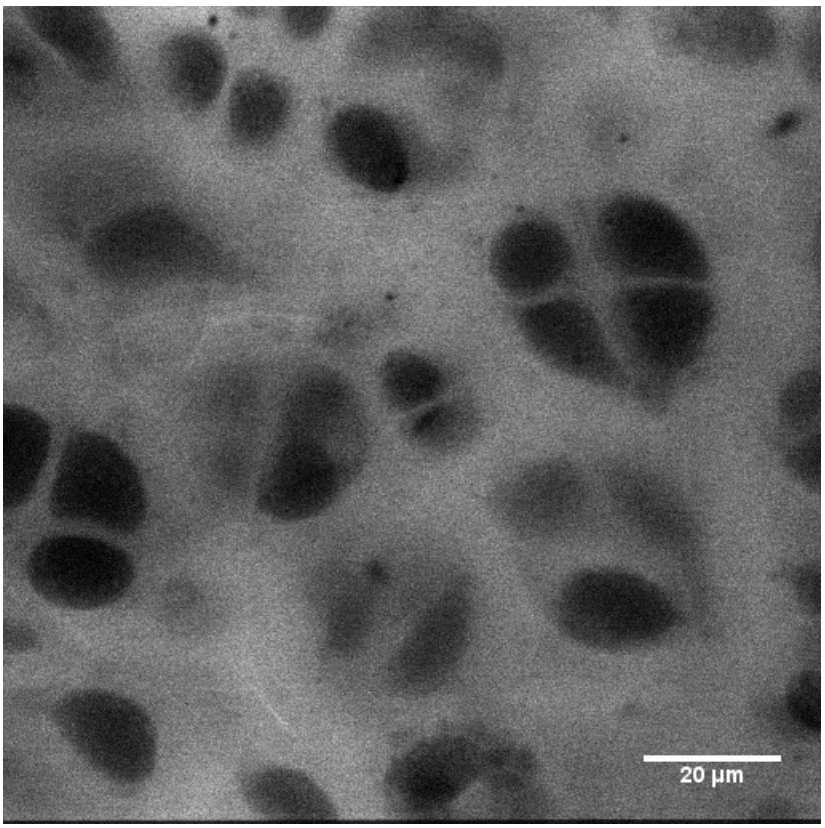

Image 5-19: Chondrocytes from a 129 day gestation sheep

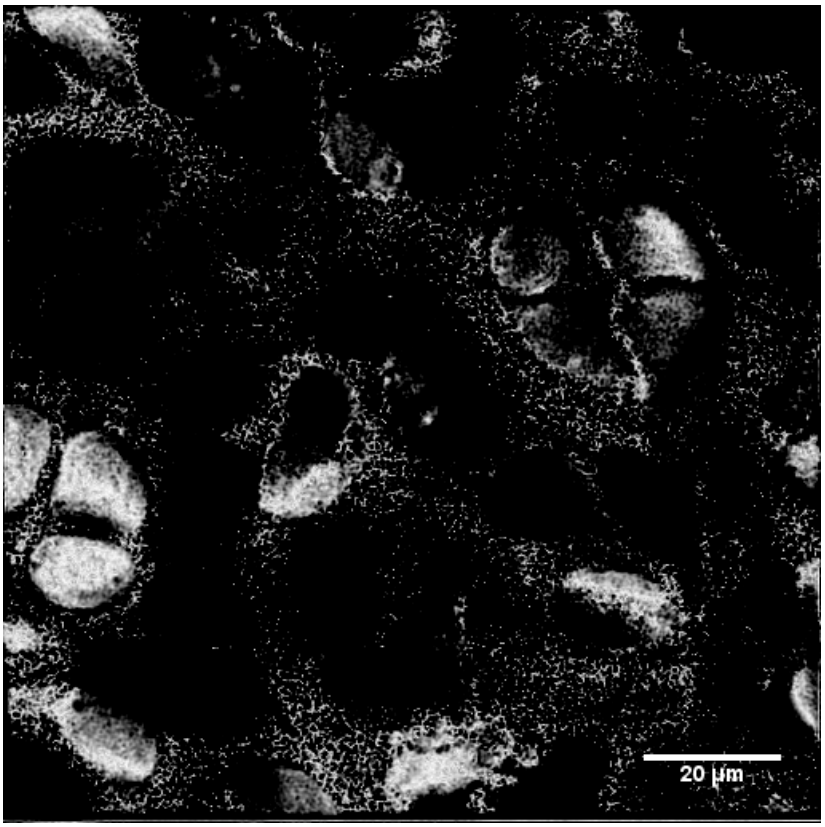

Image 5-20: Inverted image showing the effect of too short a wavelength range

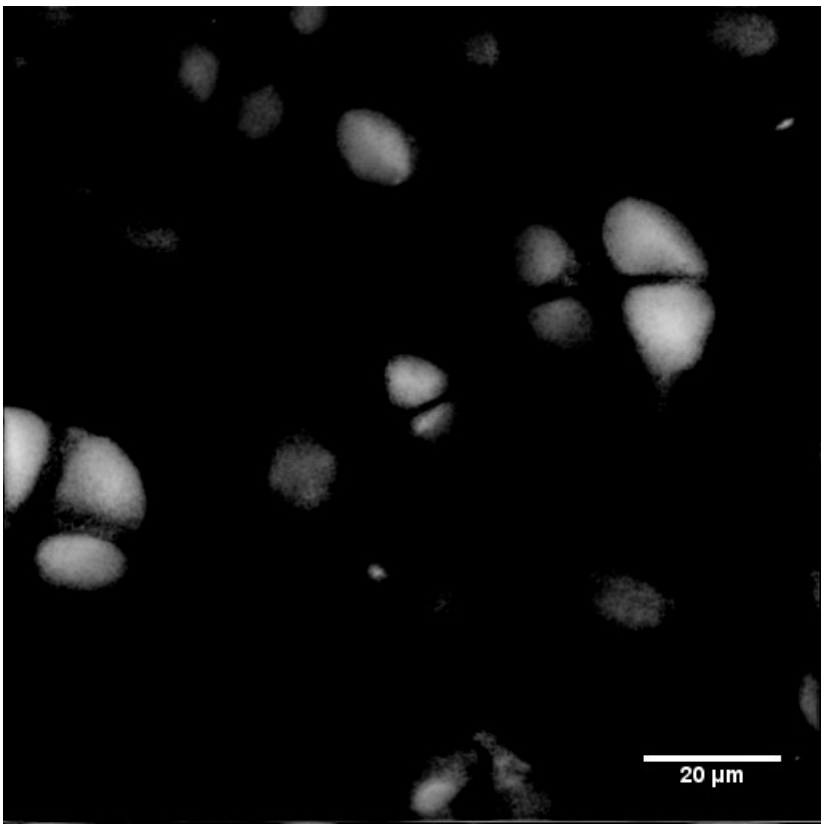

Image 5-21: Inverted image showing the effects of too long a wavelength range

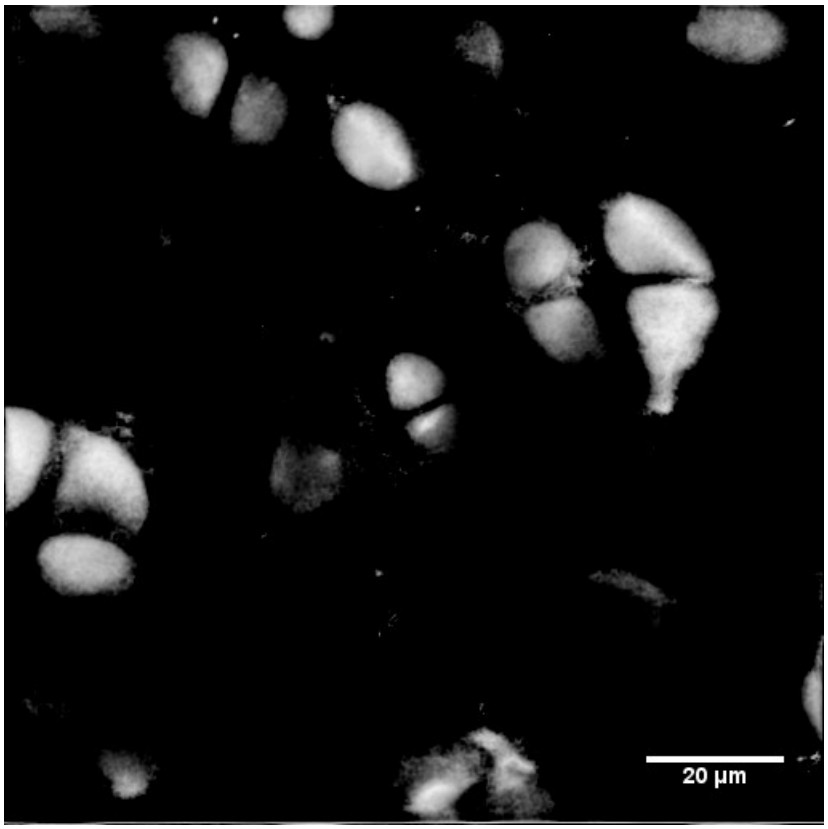

Image 5-22: Near optimal wavelength range settings

Table 5-1: Parameter settings for object segmentation (cartilage)

Parameter	Collagen Detection	Chondrocyte Detection
Polarity	1 (white background)	-1 (dark background)
No of band pass filters	6	6
Minimum wavelength	3	5
Filter spacing	1.2	1.4
Filter bandwidth	0.55 (1 octave)	0.55 (1 octave)

5.4 Noise Compensation Results

Image 5-25 below displays the results of the noise compensation algorithm. It can be seen from image 5-23, that the noise compensation method overcompensates, resulting in a dark image with most of the features removed. It can be seen from image 5-24 that the improvements in performance made by the 3D algorithm, by including data from adjacent planes dramatically increased the noise rejection, to a level where noise compensation might not be required at all. The collagen II fibres have also all been removed in image 5-25. This indicates that the noise compensation algorithm is not able to discern between noise in the Image and the collagen II fibre regions.

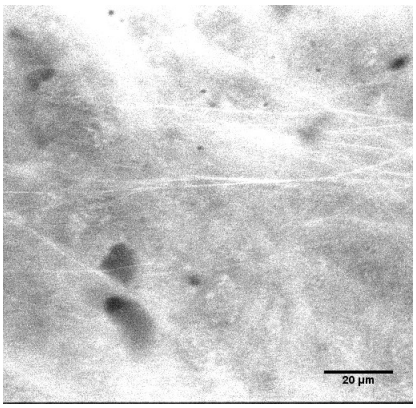

Image 5-23: Original image 1024 x 1024

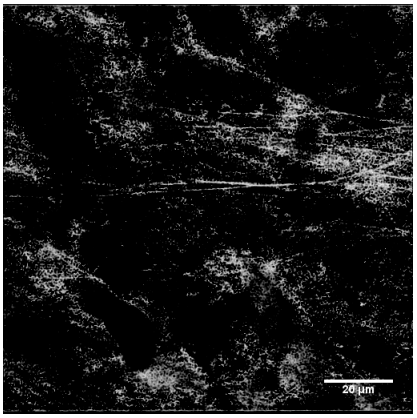

Image 5-24: Uncompensated image

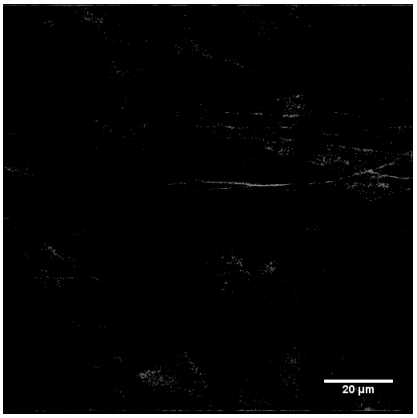

Image 5-25: Noise compensated

The poor performance of the noise compensation algorithm is because the bulk of the response in the phase symmetry output arises from the collagen II fibres. This patchy response is much weaker than what would normally be expected from identifiable features and therefore occupies the region surrounding the mean, along with the image noise.

The noise compensation algorithm removes both the noise and the collagen II fibres. This is not necessarily a bad result, as the noise compensation algorithm can be used as another method of image segmentation to enhance the collagen I fibres, with respect to collagen II fibres. Subtracting the noise compensated result from the uncompensated image would remove all the strong features (collagen I fibres) and leave the collagen II fibres.

The 2D image processing worked well when confined to a single image slice. However, the integration of the processed 2D slices into 3D objects showed deficiencies at the slice boundaries and was unable to perform 3D feature extraction to the same accuracy and ease as the 2D software. This showed up as discontinuities the extraction and detection of edges turning in the xz and yz planes. Therefore, the 2D software was extended to work in a true 3D environment.

Chapter 6 Extension of Phase Symmetry and Phase Congruency from 2D to 3D

This section covers the development of the software from 2D phase symmetry and 2D phase congruency to their respective 3D algorithms. It also develops the idea of signal 3D filtering as a means of noise reduction and display.

As stated in chapters 4 and 5, 2D approaches work well on individual slices within a 3D image; however, the integration of 2D slices into a coherent 3D structure has severe limitations with respect to curvature of objects in the z axis. These limitations provided to reason to extend the 2D image processing into 3D. Limitations in visualization of the rectangular prisms into an easily manipulated 3D structure dictated that it was better to reshape the voxels into cubic elements, which then allowed filtering of the image prior to 3D segmentation.

The extension of processing from 2D phase symmetry and local energy methods to 3D had been sought since 1990 and was moderately unsuccessful due to the large computational resources required and the difficulties with constructing the directional 3D filter. Recent advances in computing power have made a 3D algorithm for phase congruency feasible for use on a desktop computer. The project undertaken here was to develop a 3D based feature identification algorithm based on the 2D phase symmetry and 2D phase congruency using short cut calculation methods devised by Kovesi. The purpose of the work was to enhance confocal microscope images of articular cartilage.

In doing so the question became one of filter design that is, which filter gave the best compromise between accuracy and computational speed. The use of spread filters to calculate phase congruency provides a substantial increase in the level of detail extracted from the original image. Spread filters along standard orientation direction also gave good results for phase congruency. Monogenic filters offered some improvement in computational efficiency and computer program coding. These experiments are discussed below.

6.1 3D Monogenic Filters

The difficulties in implementing efficient 3D spread functions led to an alternative approach using monogenic filters. Monogenic filters provide the directional components of a composite spread filter (Felsberg M and Sommer G 2000). Monogenic filters represent a search for an odd filter with an isotropic energy distribution. Monogenic 2D filters were introduced in section 3.3.2. These are now extended to 3D filters with the orientation and phase angle are shown in Figure 6-1.

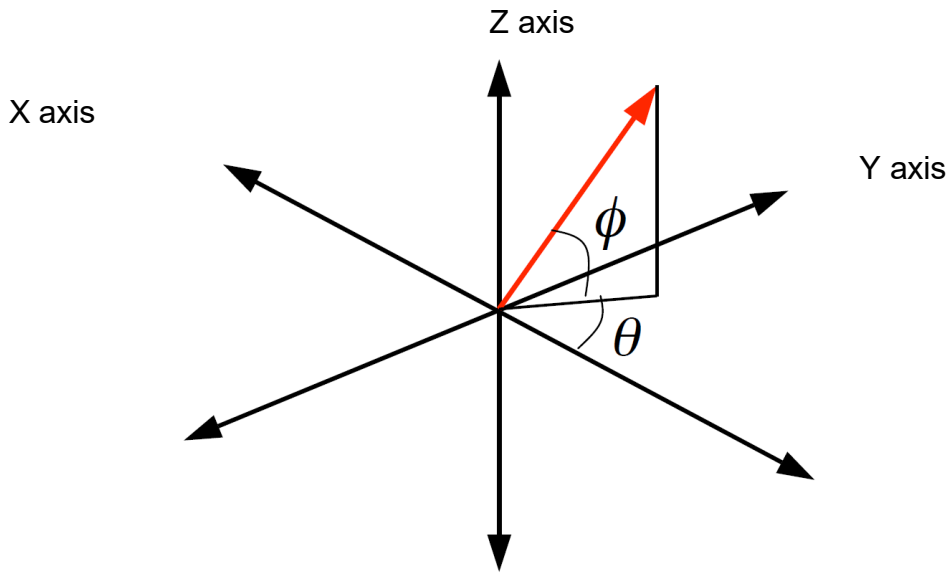

Figure 6-1: 3D representation of orientation (θ) and phase angle (φ)

The monogenic filter corresponding to the axial direction can be added to the 2D monogenic filter to produce a 3D filter. The 3D filter equations are given by the definitions of the monogenic filters (H_1 , H_2 and H_3) and converted to the component monogenic filter in real space for h_1 , $h_2$and h_3 as shown below.

$$H_1(u_1, u_2, u_3) = i\frac{u_1}{\sqrt{{u_1}^2 + {u_2}^2 + {u_3}^2}} \tag{6-1}$$

$$H_2(u_1, u_2, u_3) = i\frac{u_2}{\sqrt{{u_1}^2 + {u_2}^2 + {u_3}^2}} \quad (6\text{-}2)$$

$$H_3(u_1, u_2, u_3) = i\frac{u_3}{\sqrt{{u_1}^2 + {u_2}^2 + {u_3}^2}} \quad (6\text{-}3)$$

This extends the Equations for the local energy:

$$E_n(x) = |f_n| - \sqrt{(h_1 * f_n)^2 + (h_2 * f_n)^2 + (h_3 * f_n)^2} \quad (6\text{-}1)$$

Fourier component path length:

$$A_n = \sqrt{f_n^2 + (h_1 * f_n)^2 + (h_2 * f_n)^2 + (h_3 * f_n)^2} \quad (6\text{-}5)$$

And phase symmetry:

$$PS = \sum_n \frac{|f_n| - \sqrt{(h_1 * f_n)^2 + (h_2 * f_n)^2 + (h_3 * f_n)^2}}{\sqrt{f_n^2 + (h_1 * f_n)^2 + (h_2 * f_n)^2 + (h_3 * f_n)^2}} \quad (6\text{-}6)$$

Where * is the convolution operator.

The 2D version omits the h_3 terms and the φ angle. The direction of phase symmetry is defined as the maximum phase symmetry in:

$$\theta = a\,tan^{-1}\left(\frac{\sum_n h_2 * f_n}{\sum_n h_1 * f_n}\right) \quad (6\text{-}2)$$

$$\Phi = a\,tan^{-1}\left(\frac{\sum_n h_3 * f_n}{\sum_n h_1 * f_n}\right) \quad (6\text{-}8)$$

The main advantage of using monogenic filters instead of spread functions is the reduction in computational time, as the convolution is only performed once. This eliminates the need to quantise data over a set number of directions and so reduce any artefacts due to quantisation over multiple directions.

6.1.1 Scaling Monogenic Filters

The monogenic filter approach can be modified to account for compression in each of the primary directions. For confocal images, the x and y directions are the same scale but the z direction represents a larger scale. The general approach is to scale the voxel sizes to be the same. The equations for phase symmetry are thus unaltered as the scaling compensation is dependent upon the scaling of the monogenic filter.

The general scale Equation assumes that:

$$\boldsymbol{a\,dx = b\,dy = c\,dz} \tag{6-9}$$

$$h_1(u_1, u_2, u_3) = i\frac{au_1}{\sqrt{a^2\,{u_1}^2 + b^2\,{u_2}^2 + c^2\,{u_3}^2}} \tag{6-10}$$

$$h_2(u_1, u_2, u_3) = i\frac{bu_2}{\sqrt{a^2\,{u_1}^2 + b^2\,{u_2}^2 + c^2\,{u_3}^2}} \tag{6-11}$$

$$h_3(u_1, u_2, u_3) = i\frac{cu_3}{\sqrt{a^2\,{u_1}^2 + b^2\,{u_2}^2 + c^2\,{u_3}^2}} \tag{6-12}$$

For confocal microscopy, the coefficients (a and b) are usually 1 and thus $dx = dy$ giving:

$$h_1(u_1, u_2, u_3) = i\frac{u_1}{\sqrt{{u_1}^2 + {u_2}^2 + c^2\,{u_3}^2}} \tag{6-13}$$

$$h_2(u_1, u_2, u_3) = i\frac{u_2}{\sqrt{{u_1}^2 + {u_2}^2 + c^2\,{u_3}^2}} \tag{6-14}$$

$$h_3(u_1, u_2, u_3) = i\frac{cu_3}{\sqrt{{u_1}^2 + {u_2}^2 + c^2\,{u_3}^2}} \tag{6-15}$$

Whilst it is practical to scale the monogenic filters to account for the uneven voxel size (i.e. $a \neq b \neq c \neq 1$), it was found to be useful to scale the images to ensure that all sides of the voxel were equal. This assisted in the subsequent display of 3D volumes of the image stacks. This reduced Equations (6-14) to Equations (6-1, 6-2 and 6-3). In practice, the removal of scaling by image expansion reduced the number of artefacts introduced when the z axis was compressed (i.e. low values with respect to x and y values). These disappeared when a = b = c in the three directions of the image. This also overcomes additional complexity in evaluating gradients with z axis components.

As identified in section 4.1, the normalised nature of the Kovesi phase symmetry measure made it particularly susceptible to noise. The effect of noise was reduced by adding a noise threshold, T, resulting in a new phase symmetry measure, given in Equation 6-16 below.

$$PS(x) = \frac{|E(x) - T|}{\sum_n A_n + \varepsilon} \qquad (6\text{-}16)$$

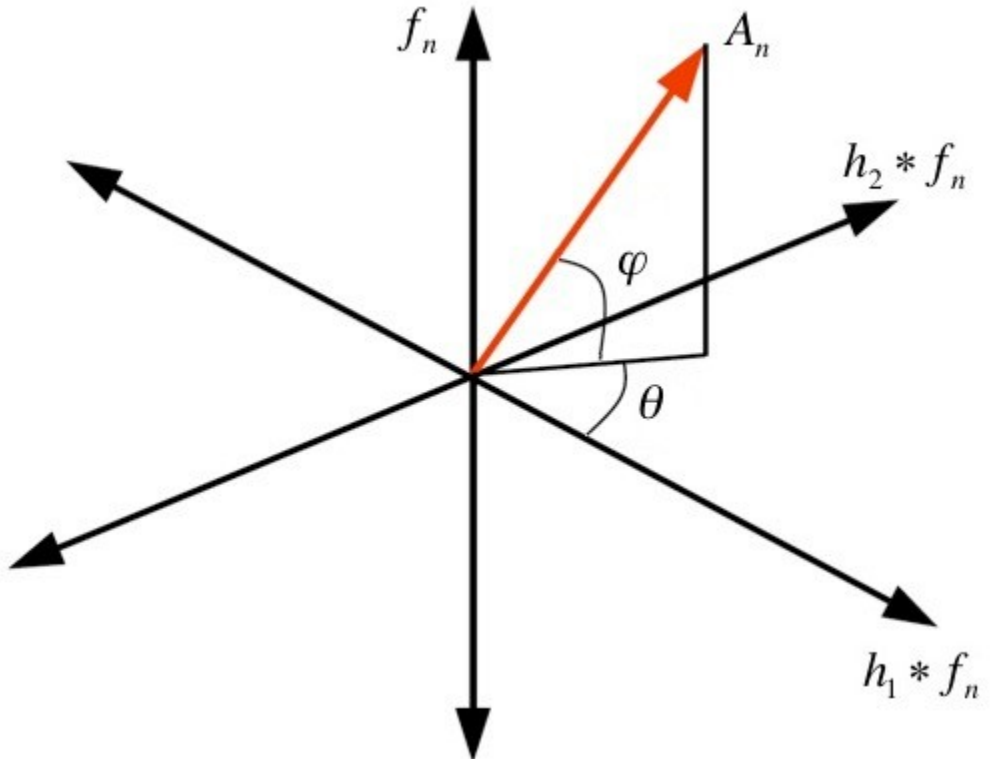

Figure 6-2: Geometric representation of the monogenic signal.

In the above Figure, the vector represents the local amplitude or energy of a signal at some scale n. Like the methodology used to calculate 2D phase congruency using spread filters, the monogenic signals for each scale are summed together to form a resultant monogenic signal vector. In addition, the local amplitudes for individual scales are also summed together to provide the total path length of the individual monogenic signals. It is the ratio of the modulus of the resultant monogenic signal (the total local energy) to the total monogenic signal path length that defines phase congruency.

That is:

$$PC = \frac{\sqrt{\sum_n (h_1 * f_n)^2 + \sum_n (h_2 * f_n)^2 + \sum_n (f_n)^2}}{\sum_n A_n} = \frac{E(x)}{\sum_n A_n} \qquad (6\text{-}17)$$

where $E(x)$ is the total local energy for the signal. Phase congruency is a maximum when the magnitude of the resultant vector is equal to the total path length of individual scale signals. This occurs when there is no deviation in phase between scales.

$$PC = \sum_n (\cos(\Delta\varphi_n) \; - \; |\sin(\Delta\varphi_n) \; |) \tag{6-3}$$

$$PC = 1 - \; \sum_n \Delta\varphi_{n_n} \tag{6-19}$$

$$PC \; \approx 1 \; - \frac{E(x)}{\sum_n A_n} \tag{6-20}$$

Here, $\Delta\varphi_n$, represents the weighted phase deviation away from the resultant vector. The procedure shown in Equation 6-19 follows the approach adapted by Kovesi from (Felsberg M and Sommer G 2001).

Compared to the above derivation for 2D phase congruency, the extension to 3D is relatively simple. The monogenic filters are defined in equation 6-10, 6-11 and 6-12.

Resulting in the following monogenic signal for some scale n:

$$f_M = \begin{pmatrix} h_1 * f_n \\ h_2 * f_n \\ h_3 * f_n \\ f_n \end{pmatrix} \tag{6-21}$$

This analysis for scaled monogenic filters follows that for phase symmetry but in practice gives much poorer results than uniform monogenic filters. The analysis of the monogenic filter with the calculation of phase congruency stopped at this stage and directional filters were used to calculate phase congruency.

While the geometrical interpretation of the signal becomes obscure due to the complexity in visualising coordinate systems of order 4D or more (i.e. three complex planes arranged in a 3D pattern), the vector principles from before remain much the same. Hence, the local amplitude for some scale n is defined as:

$$A_n = \sqrt{(h_1 * f_n)^2 + (h_2 * f_n)^2 + (h_3 * f_n)^2 + (f_n)^2} \quad \text{(6-22)}$$

From Equation 6-23, the corresponding calculation for phase congruency

$$PC = \frac{\sqrt{(\sum_n h_1 * f_n)^2 + (\sum_n h_2 * f_n)^2 + \sum_n (h_3 * f_n)^2 + (\sum_n f_n)^2}}{\sum_n A_n} \quad \text{(6-23)}$$

Note the difference in the calculation of phase symmetry compared to phase congruency is in the calculation of local energy. For phase symmetry, the total local energy is defined as the sum of the difference between the magnitude of the band-passed signal f_n, and the modulus of the monogenic filter responses to that signal, $h_1 * f_n$, $h_2 * f_n$ and $h_3 * f_n$, over all scales. That is:

$$PC = \frac{\sum_n |f_n| - \sqrt{(\sum_n h_1 * f_n)^2 + (\sum_n h_2 * f_n)^2 + \sum_n (h_3 * f_n)^2}}{\sum_n A_n} \quad \text{(6-24)}$$

This definition of local energy changes with respect to the magnitude of the band-passed signal f_n, depending on the polarity of phase congruency being calculated.

Parameter selectivity for 3D phase congruency with monogenic filters remained much the same as the selectivity in 2D phase congruency. However, the use of monogenic filters reduced the number of subjective parameters used to determine phase congruency. Monogenic filters are predefined in their orientation (they act along the orthogonal axes of the frequency domain). Therefore, the number of orientations over which the frequency domain is analysed is no longer a parameter of choice. The monogenic filters do not operate along the same direction as the general spread filters and thus the convolution used to estimate phase congruency is further compromised.

This parameter segregation provides two main benefits:

- Monogenic filters operate over fewer orientations than spread filters, and therefore concede a considerable reduction in computational expense and the ability to process much larger images; and
- The removal of some objectivity created a more generalised phase congruency response that is not biased by interpretation.

It should be noted that monogenic filters process all orientations for a given scale of frequency at once. Hence, there was no localisation of frequency data with respect to orientation. Additionally, the monogenic filters benefit from a uniform scale in each direction. As monogenic filters have difficulty resolving finer features within a given image (the weighting function is more dependent on dominant features than finer features, as finer features are scaled out of the response).

Monogenic filters were tested on 3D phase symmetry and 3D phase congruency computations. The phase symmetry uses filters that are aligned mostly along the frequency axis in the complex response and were efficient and accurate in operation. However, in the case of phase congruency, the scale variations removed too much high frequency information from the signal resulting in too much loss of detail at short wavelengths. For this reason, direction filters were considered for phase congruency calculations.

6.2 3D Spread Filters

A platonic solid is one where each face of the solid is the same shape, each edge has the same length, and each vertex is met by the same number of faces. Most importantly, this means that adjacent vertices are separated by a constant angular distance, as are any two faces that share a common edge. Therefore, spread filters orientated along the surface normal of individual faces result in a reasonably even coverage of the frequency space. The remainder of this chapter will describe the design and operation of monogenic and spread filters. It will also test the response of these filters to a simple test image, as well as recognise any of their potential limitations. The first five platonic Figures are shown below:

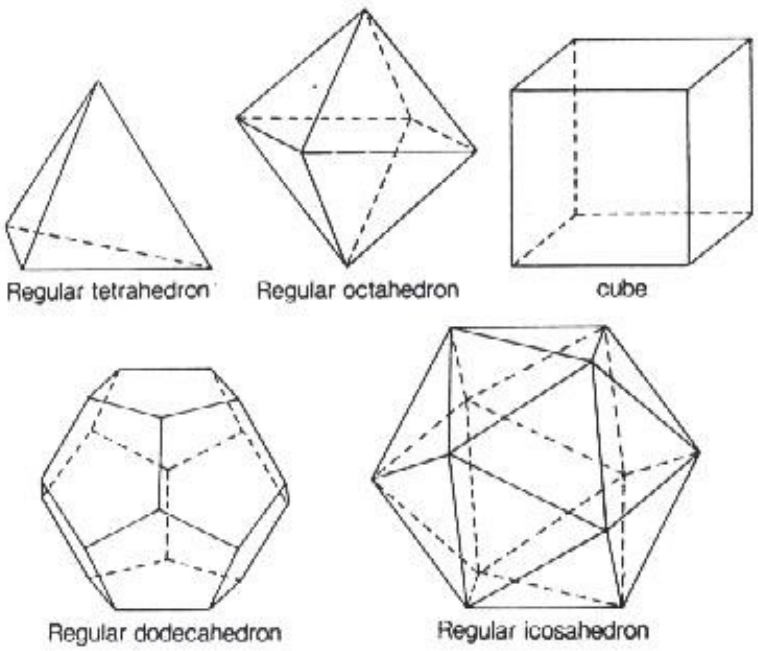

Figure 6-3: Regular platonic 3D figures. These can be used to define signal orientation for direction filters

Of the five available platonic solids, the icosahedron is used to approximate the even distribution of orientation vectors in the 3D frequency space. It has a total of 20 identical equilateral triangular faces that are connected by 12 vertices and 30 common edges, where each vertex connects five faces (Figure 6-4 and 6-4). Out of all the platonic solids, the icosahedron has the largest number of faces, and therefore the use of the surface normal vector to define orientation vectors provides the best coverage of the frequency space. An even coverage refers to the summation of all spread filters and is termed the spread cloud. It can cover half the frequency space with a mean value close to unity.

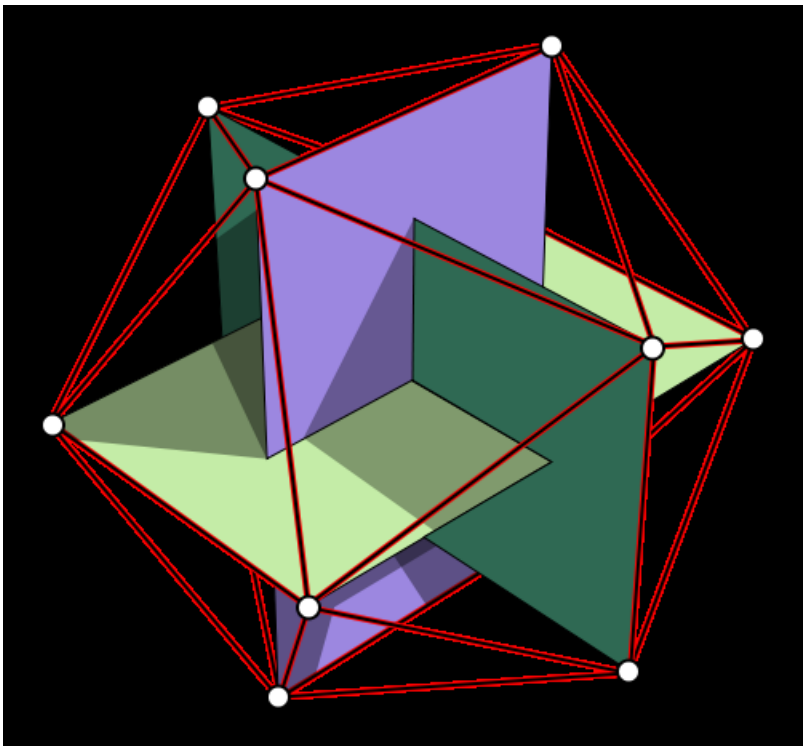

Figure 6-4: Structural layout of an icosahedron (Mathematic visualisation)

Regarding the icosahedron, it is the set of direction vectors pointing out from the origin to the centre of each face that forms the set of surface normal for all the faces, and it is these vectors that define the direction orientation vectors. Since the frequency domain is axially symmetric, only those vectors within the positive half of the frequency space need to be considered, leaving a total of 10 orientation vectors.

For a particular orientation vector, the radially symmetric cosine distribution is formed by the cosine of the angular distance away from that vector. This distribution is then scaled to the angular distance between directly adjacent faces (faces that share a common edge) to form the 3D spread filter for that orientation. In practice, the dot product between the orientation vector and each of three 3D matrices representing the x, y and z coordinate space (the three matrices together form a 3D matrix of vectors) and the orientation vector are used to find angular distance. This distance is then mapped by the angular distance between two directly adjacent faces, which is used as the argument for the cosine distribution. The resulting distribution is the 3D spread filter for that particular orientation vector.

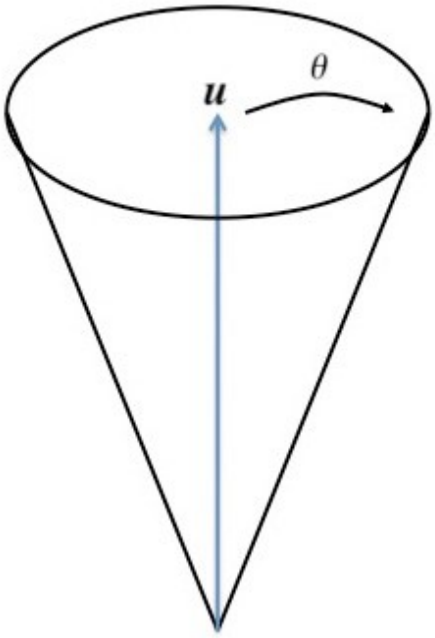

Figure 6-5: Construction of cosine distribution: u represents the orientation vector and θ represents the angular distance away from u.

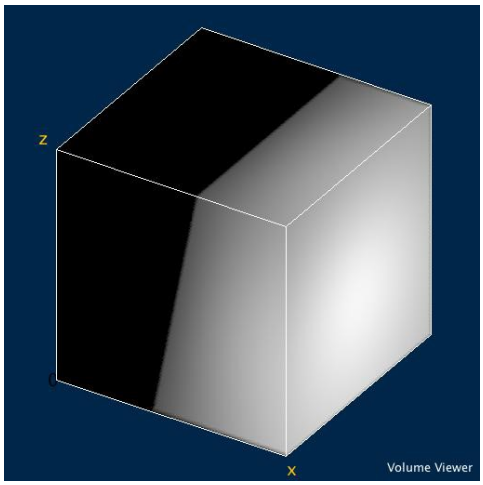

Figure 6-6: Cosine distribution as a function of the angular distance away from the orientation vector. (ImageJ visualisation)

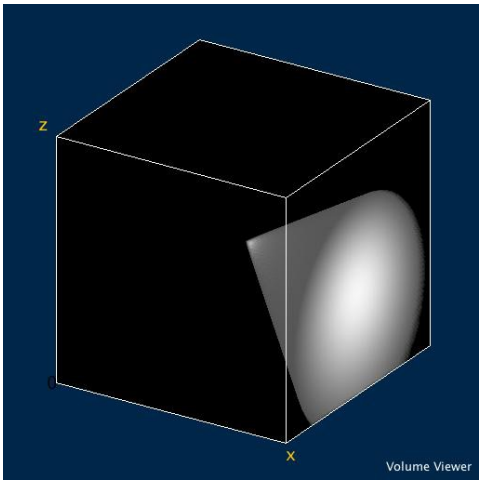

Figure 6-7: Resulting 3D spread filter. (ImageJ visualisation)

For an icosahedron, the angular distance between directly adjacent faces is constant throughout the solid. Each spread filter is mapped by the same quantity and identical shape and only varies in terms of orientation.

The sum over all spread filters should result in the spread cloud with a mean value close to unity, i.e. a uniform coverage of the frequency domain. However, while each face has three directly adjacent faces, they also connect to another eight faces, all of which are separated by a greater angular distance than the directly adjacent faces. Therefore, the spread is formed not just from the overlap of directly adjacent spread filters, but the overlap of all neighbouring filters as well. Figures 6-7and 6-8 shows the different coverage in the spread cloud when the mean varies from 80% to 98%.

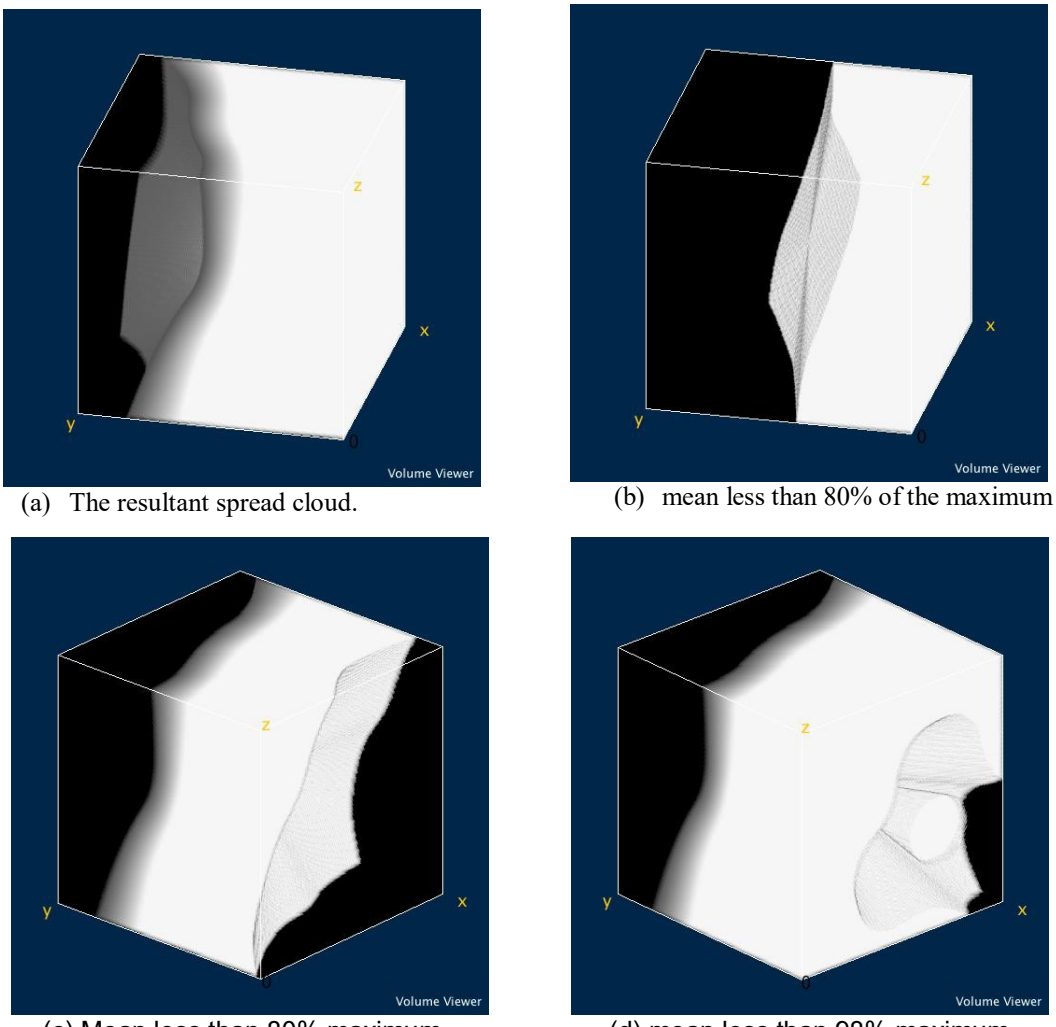

(a) The resultant spread cloud. (b) mean less than 80% of the maximum

(c) Mean less than 80% maximum (d) mean less than 98% maximum

Figure 6-8: Effect the mean on spread filters. Note that the resulting spread cloud encompasses more than a half space. At the same time the values greater than the mean almost perfectly cover a half space. (ImageJ visualisation).

In general, the half plane consists of values greater than the mean and the distribution of values, while consisting of peaks and dips, uniformly increases in magnitude towards the centre. The mean of values greater than the total mean is 2.44. Hence, this subset of the spread cloud is more heavily weighted towards the maximum, and has a 20 to 30% variation in magnitude. As an approximation to even coverage, this spread cloud is roughly uniform albeit with a sum much greater than unity magnitude. A mean value greater than unity acts to magnify the response of the filter, thereby, increasing its responsiveness to finer details.

6.3 3D Phase Symmetry Feature Detection

Articular cartilage images consist of chondrocytes, collagen fibres and loose collagen fibrils. A principal aim of this study was the automated segregation of LSCM images into component objects i.e. fibres, chondrocytes, and other features. Phase symmetry can be tuned to give broad feature detection and segregation. When these images are processed through dilation and filling, the outline of features can then be convolved with the original image to produce separate features that could be added together to give a cleaned composite image.

6.3.1 Chondrocytes

Phase congruency is essentially an edge detector and should merely respond to the edges of features and not their volumes. It seems odd then, that phase congruency through spread filters was not only able to detect detail on the edges of chondrocytes but also much of their volumes. Laser scanning confocal microscope images are characterised by poor axial resolution that causes chondrocytes to appear disproportionate in width to depth dimensions. This means that a 2D lateral plane within the image will show much larger dimensions for a chondrocyte than an axial plane.

Chondrocytes in the superficial layer appear as distorted 2D discs rather than spheres. This is due to the entrapment within the lacunae, also the z direction foreshortening makes the appearance worse than it is. Chondrocytes in the superficial layer are characterised as being relatively planar and parallel to the cartilage surface. Therefore, a chondrocyte in the axial direction appears as an edge, with its largest diameter towards its centre, and it is this response that is magnified by the spread filters. Hence, phase congruency through spread filters can resolve the internal of volume of a chondrocyte, while monogenic filter response is not amplified.

In comparison, phase symmetry provides a completely different measure of image feature as it measures points of local symmetry. Since the interior of a chondrocyte cell is encased by a roughly symmetrical cellular membrane, it consists of points of local symmetry or high phase symmetry. The interior of collagen fibres has high symmetry although due to their smaller dimensions only the larger fibres are resolved. In practice, any volumetric structure has some level of symmetry.

External regions are largely unsymmetrical due to noise and the distribution of other features. It is only the internal volume of cellular or fibrous bodies that are detected. All external details such as chondrocyte edges are ignored. Phase symmetry results seem to only contain a subset of information available in the space when compared with phase congruency through spread filters response. A particularly useful benefit for this is that it allows for the reasonably accurate segmentation of chondrocyte cells and collagen fibres and, the results are not interspaced with noise responses and unnecessary detail.

6.3.2 Collagen Fibres

In the results for the first test image, phase congruency through spread filters provides much more detail than any of the other measures used. The response was significantly more dominant and allowed for the clear visualisation of image features. This measure appears to show the internal fibril structure of collagen fibres; however, this level of detail was not replicated in any of the other measures.

The phase symmetry responses were also able to resolve collagen fibres, but not to same extent and amplification as phase congruency through spread filters.

6.4 3D Phase Congruency Feature Detection

This section analyses the phase congruency with spread filter response and the ability to resolve features from the original LSCM images. An attempt will also be made to qualitatively measure the amount of confidence that can be put in the phase congruency response.

During the development of 3D spread filters, some of the issues concerning the distribution of the spread cloud and frequency localisation were raised and considered.

One of the fundamental assumptions made in calculating phase congruency is that the division of the frequency domain into scales provides an accurate approximation to the Fourier components of the signal. While the issue of scale impacts all feature detection methods discussed before, it should be emphasised that the issue of scale is an approximation, and necessarily ignores the frequency distributions of some features at particular orientations.

The use of a platonic solid to model the distribution of spread filters failed to evenly cover the frequency half space. The sum of the components covering the space have a mean value greater than unity. Therefore, the phase congruency response is amplified, causing warping and blurring (or loss of localisation) in image features due to certain orientations being amplified or attenuated.

The extension of spread filters to 3D implies that frequency data is analysed in localised volumes rather than areas. This means that any feature within the image is considered with respect to its local volume. Hence, a feature that would appear dominant in a particular plane (for example, in 2D phase congruency) could be scaled into insignificance in 3D because of the consideration of features in a now wider locality. The 3D spread filters do not localise features to the same extent as 2D spread filters.

This study extended log-Gabor filters to 3D, due to their dependence on the dimensionality of radius. In order to calculate the local energy vector for a particular scale only a pair of quadrature filters were used, which gave local energy as a 2D complex vector. In comparison, the monogenic signal is four dimensional for a 3D image and consists of a 3D local energy component (one dimension is the original signal). This reduction in dimension was incorrectly assumed to be due to symmetry of log-Gabor filters, because in three dimensions there should be a triplet of filters in quadrature (a 90-degree phase shift along each orientation in the frequency domain).

In 2D phase congruency, the odd and even filters are combined into a singular filter, where the resulting real and imaginary parts of the output correspond to the odd and even components of the local energy vector (Kovesi, 2005). Since the same approach was employed in 3D phase congruency, the three quadrature filters were combined into singular filter, where the resulting odd component would be representative of the two odd filters.

The final issue in phase congruency through spread filters is one of computational expense. Spread filters result in more convolutions than monogenic filters, which puts demands on computer memory and increases processing time. It should be noted that computational expense has no impact on feature detection.

It should also be noted that the quality of the phase congruency response is a subjective assessment dependent upon the application, the desired features, and an understanding of what those features represent. However, this subjectivity relates to parameter choice and the interpretation of results. The phase congruency response can still be assessed in terms of how its limitations impact accuracy. The question of how well the response from 3D phase congruency through spread filters extracts features from LSCM images reverts to a discussion of the impact of blurring and warping, and their responses to noise. While the assumption made for log-Gabor filters may adversely impact the results, this impact cannot be measured at present, and is assumed to be minimal.

The most obvious solution for analysing 3D images is to simply analyse each 2D image in the stack individually. Indeed, this was the original method adopted. However, image features are not confined to 2D planes and image features are also aligned in a number of different orientations. The piecewise 2D analysis of a 3D image failed to accurately detect and localise those features that run axial to the 2D plane. A line running perfectly perpendicular to the plane appears as a dot or small blob within the 2D image; which would then likely be scaled out of analysis. To ensure the detection of all features, 3D images need to be processed as 3D images. Fortunately, the calculation and selection of orientation filters involved in determining phase congruency in 2D also extend to 3D.

The Fourier transform can be calculated in multiple dimensions, and considers an extra dimension resulting in a four-dimensional frequency domain. This domain is defined using a spherical coordinate system: the radius refers to frequency and the two angular quantities refer to orientation. Hence, the magnitude at a particular point in the frequency domain defines how much of a given frequency component exists along that orientation within the image.

As the dimensionality of log-Gabor filters depends entirely on its radius; the dimension of the radius determines the dimension of the filter. This property also implies the radial symmetry of the filters. Consequently, a 2D cross section of a 3D filter corresponds to the 2D representation of the same filter. In three dimensions, a log-Gabor filter is defined by a spherical band, where the magnitude of the band along the radius is defined by a log-Gaussian function. The radial distance of the band from the origin depends on the frequency scale for that filter.

It was not obvious that the 3D frequency space can be evenly and equally divided in terms of orientation. In fact, it was the complications involved in constructing and utilising 3D spread filters that led to the initial investigation of monogenic filters. Monogenic filters are complex valued filters that act along each orthogonal axis within the frequency domain. While these filters could detect features in 3D images at much greater speeds than spread filters, the resolution and clarity of resulting features was limited. With an emphasis on feature detail, it was the limitations of monogenic filters that motivated the development of 3D spread filters.

In 2D phase congruency, the frequency domain was expressed in terms of polar coordinates and, due to axial symmetry, only half of the 2D frequency plane needed be considered. Orientation vectors were then defined along angles that equally divided the 180° half space, with these used as a basis to construct spread filters from the cosine distribution of angles from that vector. Similarly, the 3D half space can be expressed in terms of spherical coordinates with orientation defined by two angular variables. For a unit sphere, the equal division of just one of these variables creates a wedge. This implies that further division by the second variable results in spread filters that are neither symmetric nor equal in volume or shape (such as seen by the divisions created by lines of latitude and longitude on a globe).

Such a design would result in an uneven measure of phase congruency over different orientations; a feature considered in a narrow locality of frequency would appear more prominent than the same feature considered in a wider locality. There would also be significant difficulty in constructing a spread filter using a cosine or similar distribution unless it was radially symmetric. A non-symmetric and non-separable filter will also negatively impact phase information (Kovesi 1996).

Spread filters need to be radially symmetric and to be composed of some form of distribution, so that the addition of adjacent filters produces an even spread in the frequency domain. A clear 3D parallel of 2D spread filters is a search light or cone defined by some orientation vector with a cosine distribution that runs radially from that vector. The problem then became one of finding the distribution of orientation vectors that enabled an even spread. An equivalent problem is finding an even distribution of circles over the surface of a unit sphere; a topic of considerable interest amongst mathematicians, engineers, and scientists. Many of the solutions developed, such as the use of repulsion models, are considerably complicated and fail to arrive at a perfect solution. To this end, this thesis used an approximate distribution through the surface normal of a platonic solid.

6.5 Three-Dimensional Software Results

This subsection demonstrates the effectiveness and results of 3D image processing.

One of the main goals of this thesis was to develop an imaging solution that would automatically quantify the parameters enabling the rapid and easily identify articular cartilage health in a clinical environment. Such a device provides an early detection system for osteoarthritis, to gauge the effectiveness of osteoarthritis treatment regimens and to identify areas of articular cartilage needing replacement. To accomplish these objectives, the important image features are segmented from the original image and de-noised using a line and dot detector. It is desirable to have a line and dot detection algorithm that is:

- Processing a typical image in less than a minute on a desktop computer;
- Invariant to image brightness and contrast;
- Invariant to the different techniques, microscopes and stains that are used;
- Able to cover all images with a single set of parameters;
- Expandable to cover other feature types;
- Able to detect both collagen fibres and chondrocytes; and

- An image independent method of specifying noise compensation.

The phase symmetry method developed by Kovesi offers promise and has identified as currently providing the best results. Traditional gradient based methods such as the canny edge detector fail to provide good results, as they are dependent on image brightness and contrast. These parameters vary widely between images. The Kovesi phase symmetry method is however limited as it only processes images in 2D. A true 3D program would provide better:

- Resolution of fibres not aligned with the 2D plane; and
- Noise rejection by including data from adjacent planes.

Extension of phase symmetry and local energy methods to 3D has been attempted since 1990. However, these attempts were unsuccessful due to the large computational resources required and difficulties constructing the directional 3D filter. However, recent advances in computing power have made a 3D algorithm feasible for use on a desktop computer. The project undertaken here was to develop a 3D based feature identification algorithm based on the 2D phase symmetry and 2D phase congruency methods developed by Kovesi, for enhancing confocal microscope images of AC

The 3D images created using confocal microscopy must be processed as a 2D image set, leading to poor results for features not aligned with the imaging plane and poor noise rejection. The primary objective of this project was to extend the phase symmetry algorithm to 3D.

Software was written to automate the processing of the confocal microscope images and to create composite false colour images from the original greyscale confocal microscope images. The important image features, namely collagen fibres and chondrocyte cells, once identified are artificially highlighted by artificial colouring. This has been used to display confocal images more clearly. Black and white images from early testing of my results are also extensively used in this work as well.

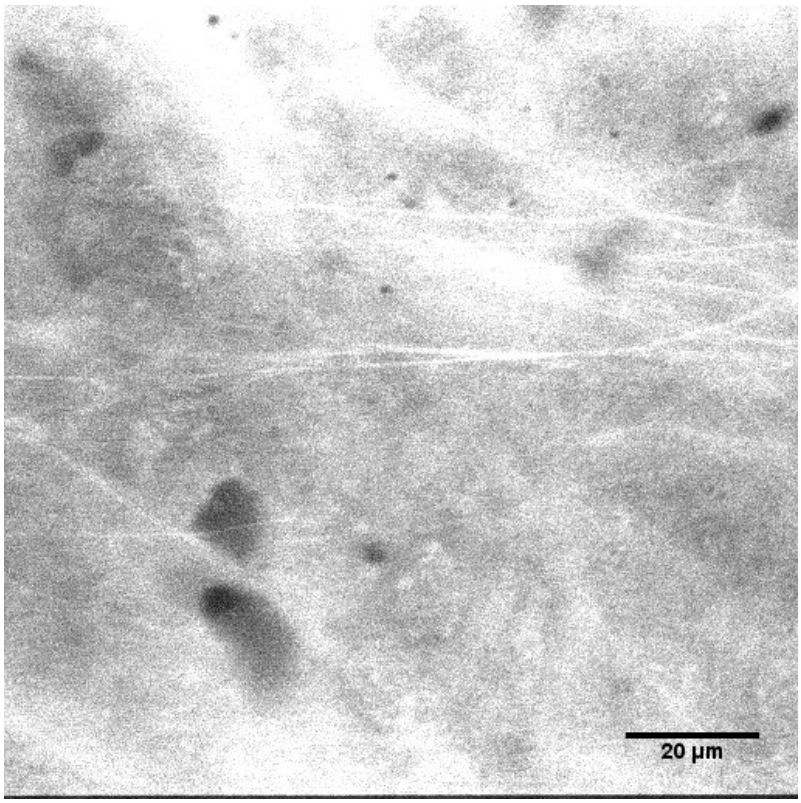

Image 6-1: Comparison between 2D and 3D phase symmetry – Raw image

A number of approaches were investigated for extending the phase symmetry algorithm approach to 3D. Monogenic filters were found to provide the best results and lowest computation time. It was found that image compression due to non-isotropic confocal microscope resolution could be well compensated for by scaling the distance vectors used to construct the filter set. Intensity based image normalisation prior to image processing was found to improve the performance of the phase symmetry algorithm.

The phase symmetry method was found to provide excellent results in the segmentation of chondrocyte cells and good collagen fibres. 3D volume views created using ImageJ show that the 3D algorithm provided useful data. The 3D algorithm was successfully able to segment collagen fibres surrounding the chondrocyte cells, which the 2D algorithm was unable to do. Images 6-1, 6-2 and 6-3 shows the differences between 2D and 3D processing.

The 3D result offers a substantial increase in performance. The regions of collagen II fibres are distinct and visible in the 3D output compared to the 2D output. The symmetry output containing more useful information

Image 6-3: Comparison between 2D and 3D phase symmetry – 2D Phase symmetry result

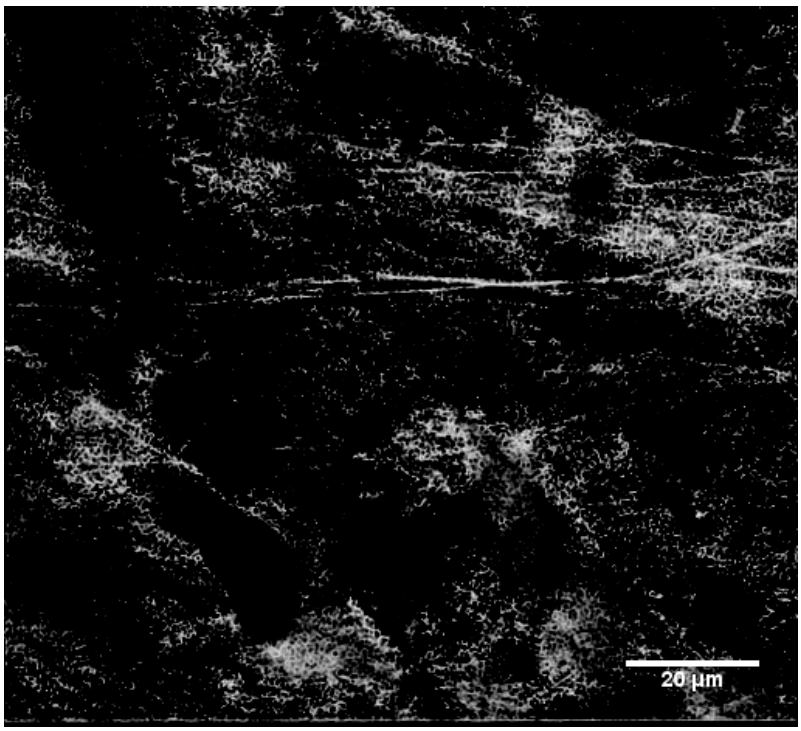

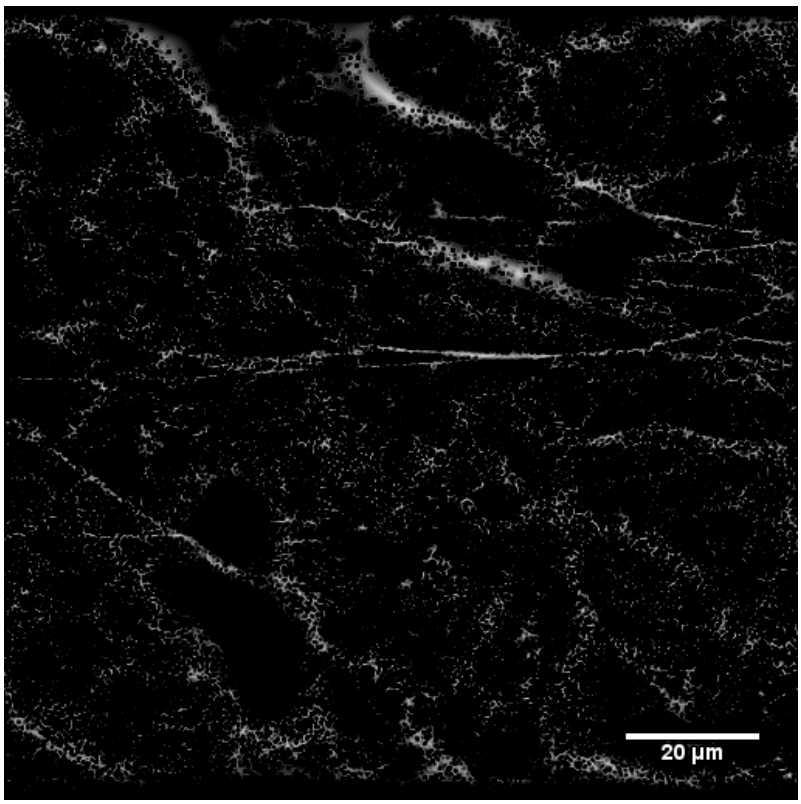

Image 6-2: Comparison between 2D and 3D phase symmetry – 2D Phase symmetry from 3D processing

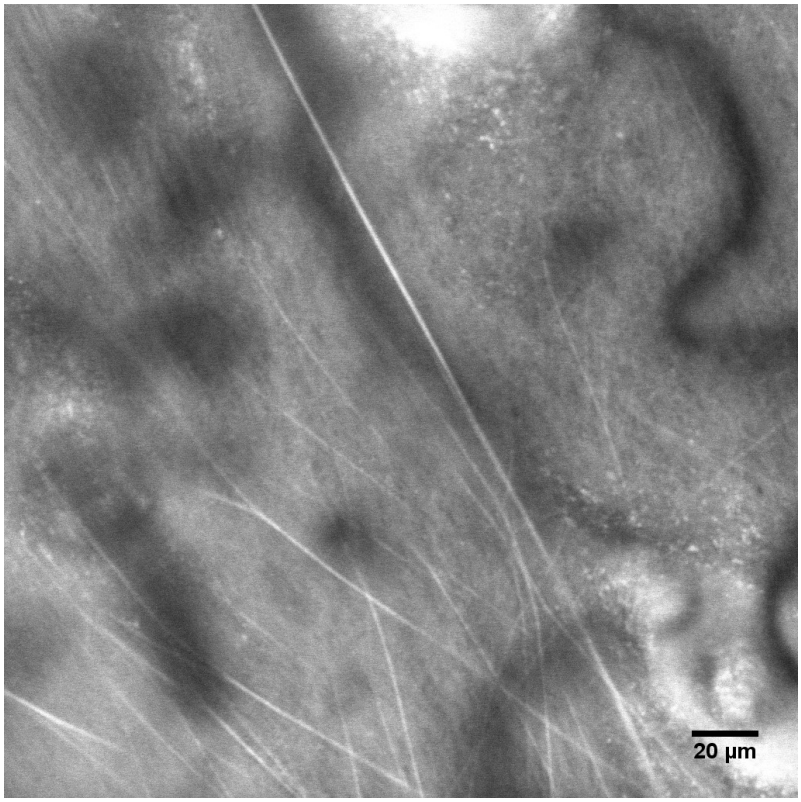

Image 6-4: Raw image

Image 6-5: Comparison of 2D and 3D phase symmetry results
–2D Phase symmetry result

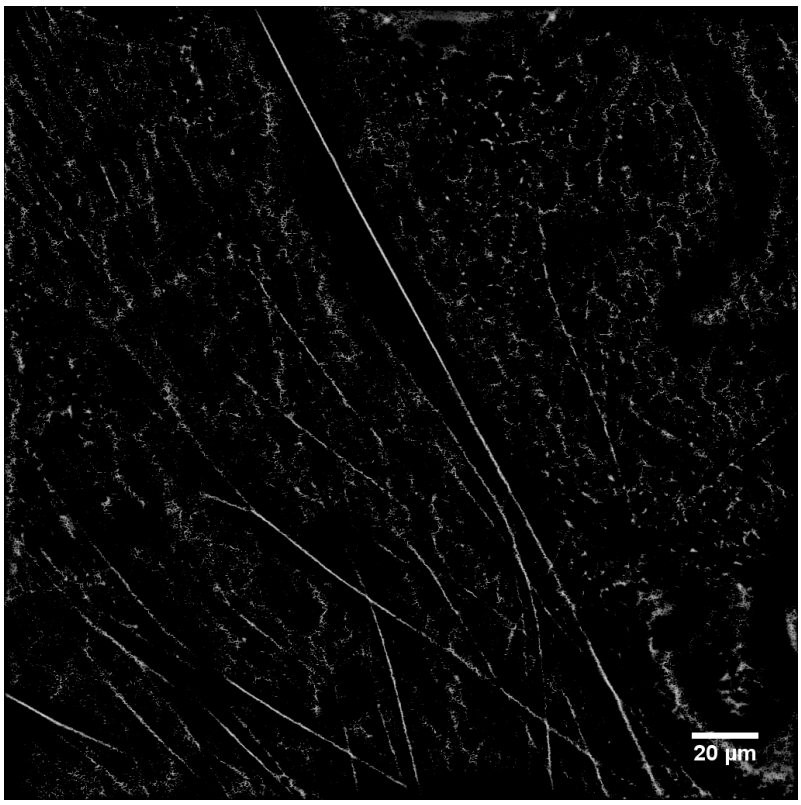

Image 6-6: Comparison of 2D and 3D phase symmetry results –2D Phase symmetry result

The 2D phase symmetry displays the collagen I fibres slightly better than the 2D version from 3D phase symmetry, this is believed to be due to the fact that some of the fibres lie mostly in adjacent planes

6.6 Phase Congruency Performance Results

All tests carried out in this section used Image 6-7 as the raw image prior to application of filtering.

Image 6-8: 2D slice from the 3D sample Image 6-7 using Matlab for image display

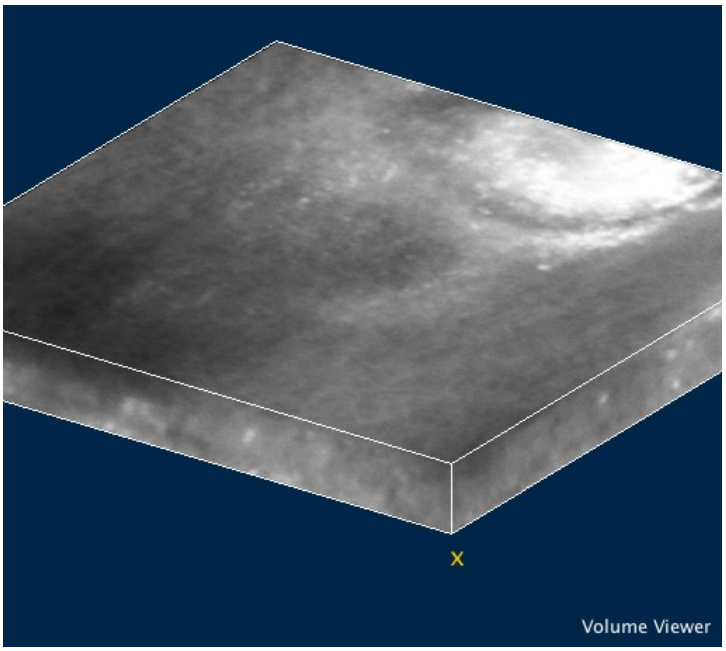

Image 6-7: Test Images used for evaluating phase congruency

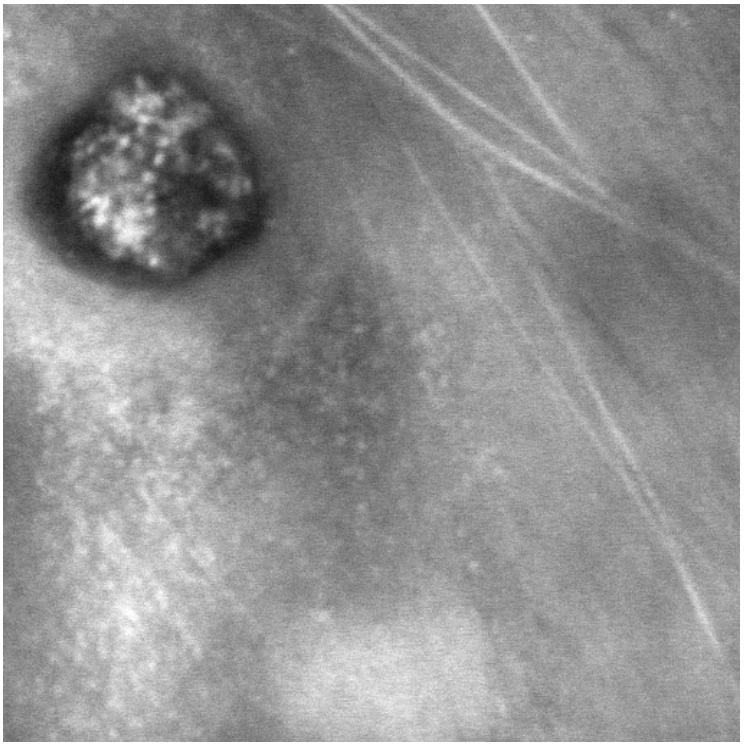

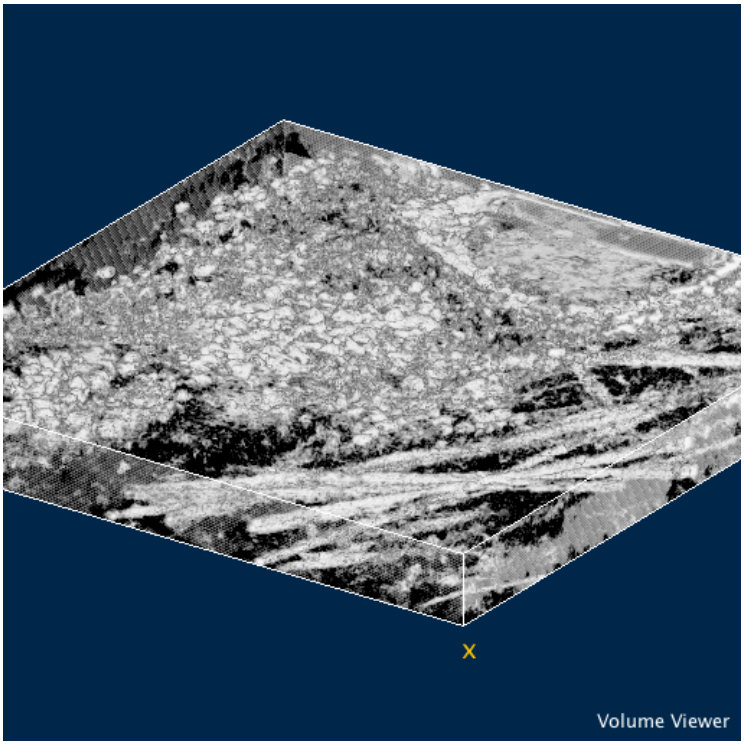

Image 6-9: Feature detection using phase congruency with spread filter

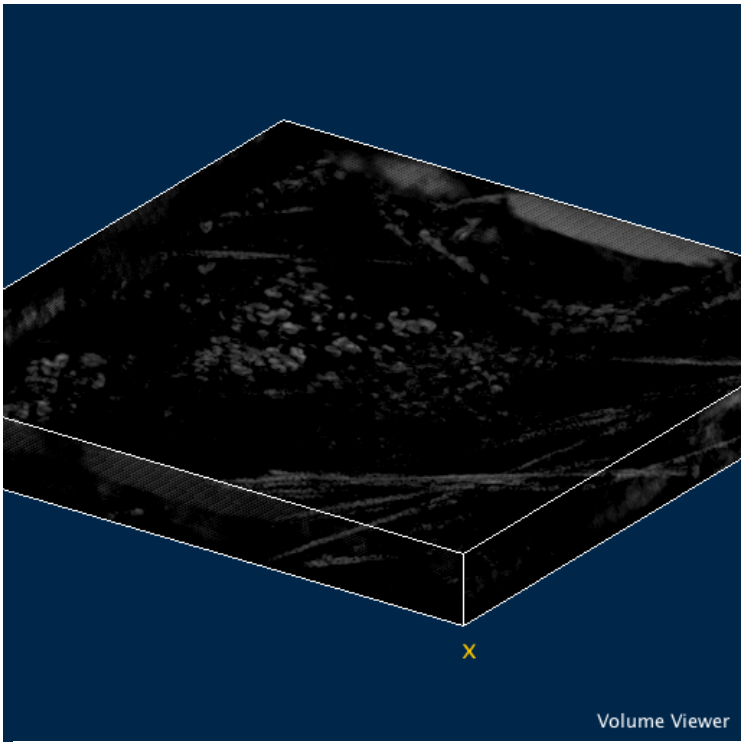

Image 6-10: Feature detection using phase congruency with monogenic filters

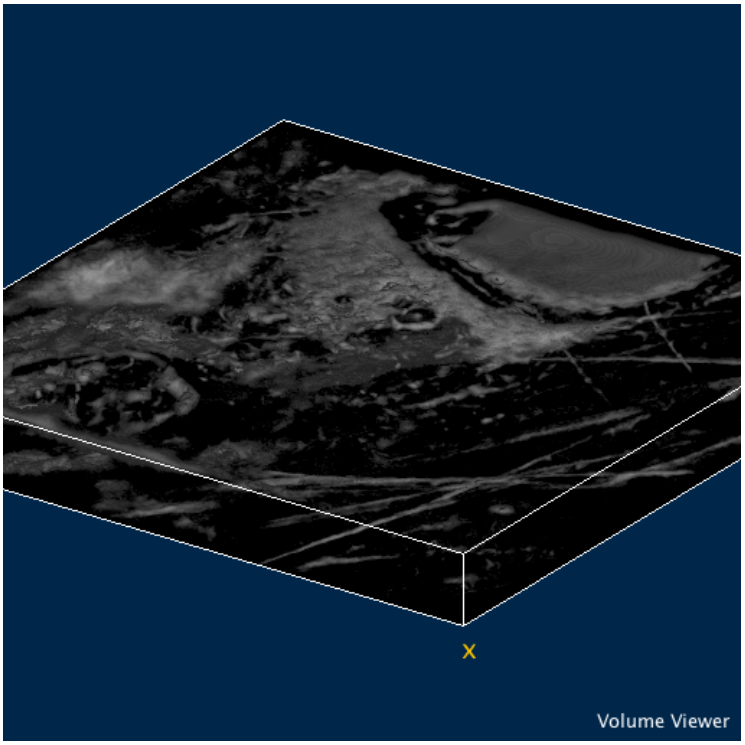

Image 6-11: Feature detection using phase symmetry and spread filters

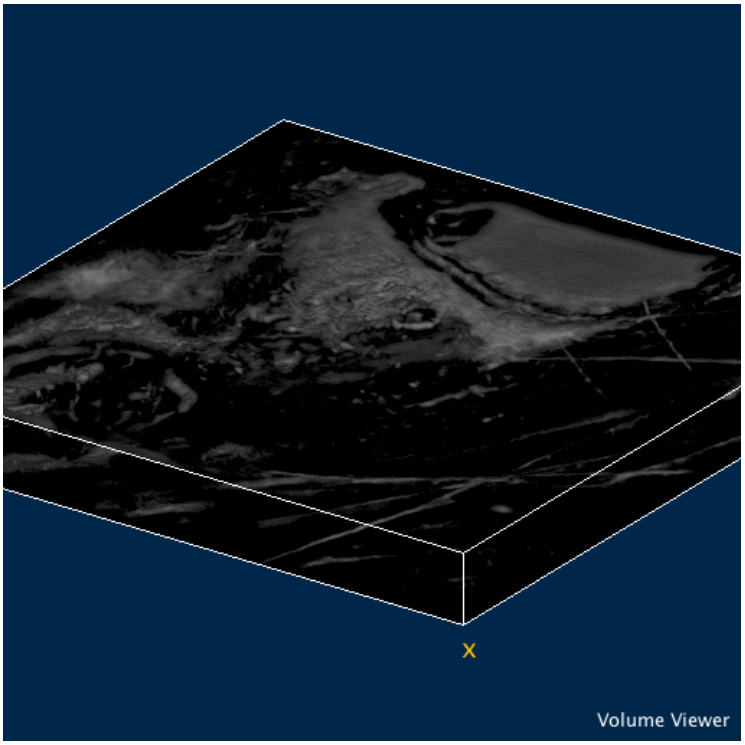

Image 6-12: Feature detection using phase symmetry and monogenic filers

Images 6-9 and 6-10 show the effect of spread filters and monogenic filters on phase congruency, while Images 6-11 and 6-12 show the effect of spread filters and monogenic filters on phase symmetry.

2D phase congruency has an even distribution of spread filters:

- Already been shown to accurately detect edges in the presence of noise; and
- Is not impacted by any other features other than those that exist within the 2D plane.

The 2D phase congruency processing has resolved individual fibrils from within the fibres and the result is not to noise. This implies that 3D phase congruency also resolves the internal structure.

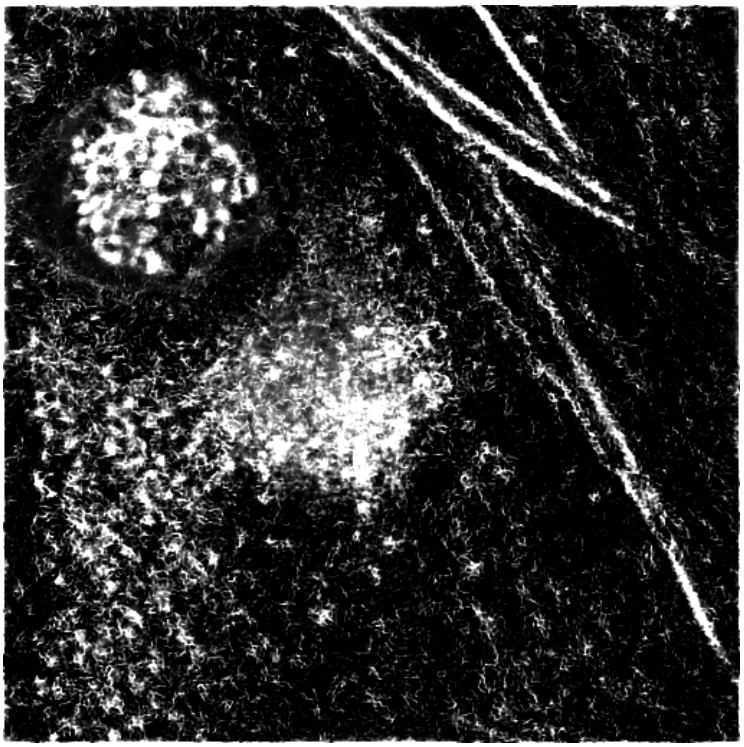

Image 6-14: 2D cross-section of Image 6_8 - 2D phase congruency with spread filter

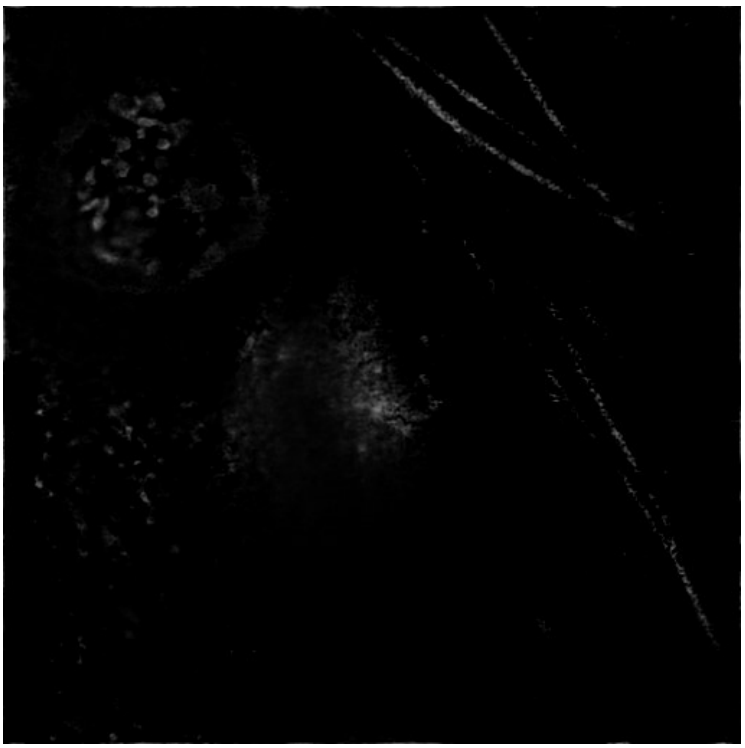

Image 6-13: 2D cross-section of Image 6_8 -2D phase congruency with monogenic filter

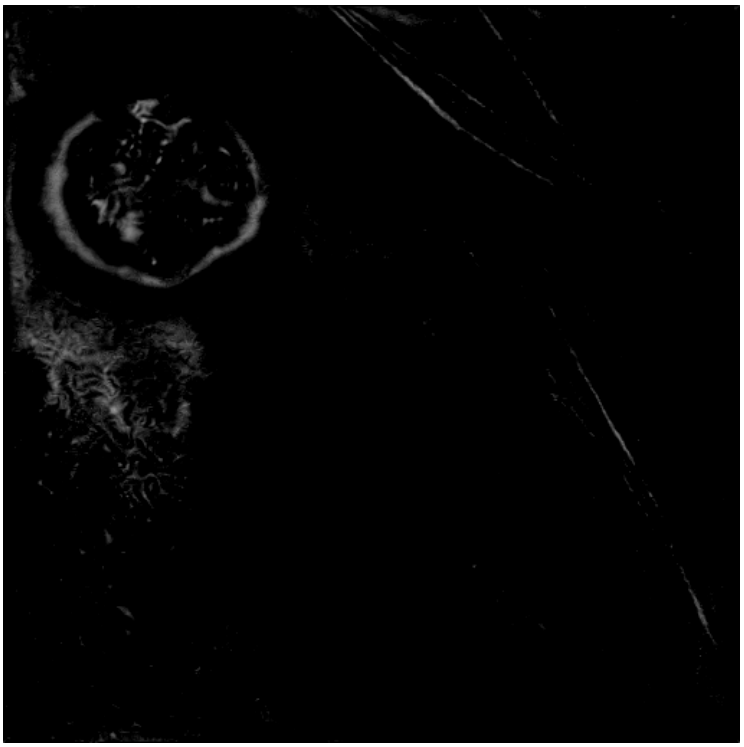

Image 6-16: 2D cross-section of Image 6_8 -2D phase symmetry with spread filter

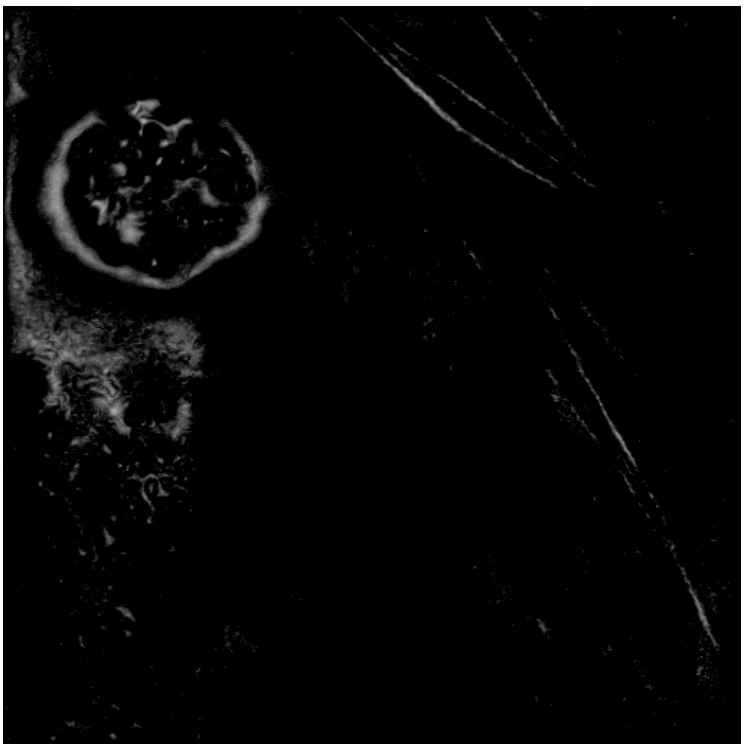

Image 6-15: 2D cross-section of Image 6_8 - 2D Phase symmetry with monogenic filter

Images 6-13 to 6-16 show 2D phase congruency result using spread filters identifying the internal composition of the large fibre bundles. 2D Monogenic filters with phase congruency fails to show fibres. 2D Phase symmetry is also poor here.

During the development of 3D spread filters, some of the issues concerning the distribution of the spread cloud and frequency localisation were raised and considered.

The following provides a summary of these and other issues, and how they impact on the detection of features:

- One of the fundamental assumptions made in calculating phase congruency is that the division of the frequency domain into scales provides an accurate approximation to the Fourier components of the signal. While the issue of scale impacts all feature detection methods discussed herein, it should be emphasised that this is an approximation and necessarily ignores the frequency distributions of some features.

- The use of a platonic solid to model the distribution of spread filters results in a spread cloud that fails to evenly cover the frequency half space and has a mean value greater than unity. Therefore, the phase congruency response is amplified, causing blurring (or loss of localisation) in image features, and warping, due to certain orientations being amplified or attenuated.

- The extension of spread filters to 3D implies that frequency data is analysed in localised volumes rather than areas. This means that any feature within the image is considered with respect to its local volume. Hence, a feature that would appear dominant in a particular plane (for example, in 2D phase congruency) could be scaled into insignificance in 3D because of the consideration of features in a now wider locality. Therefore, 3D spread filters cannot localise features to the same extent as 2D spread filters.

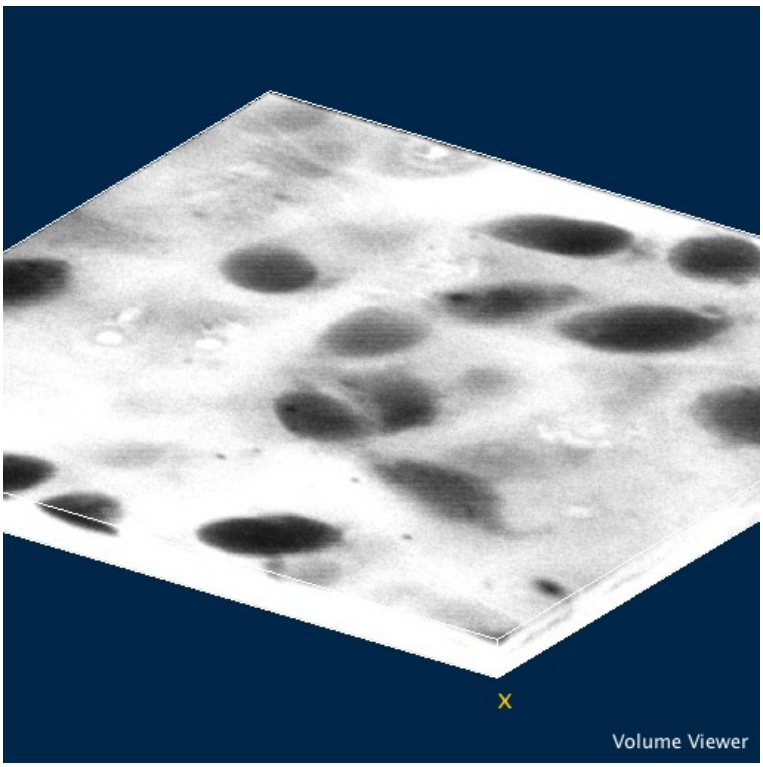

Image 6-18: Test nonspecific segregation – raw image

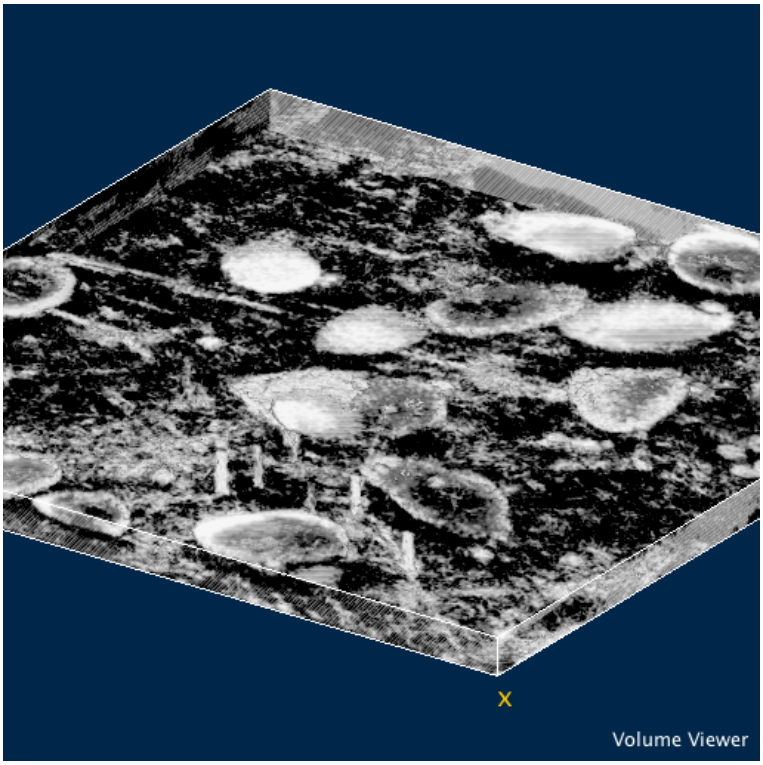

Image 6-17: Test nonspecific segregation – Phase congruency with spread filters

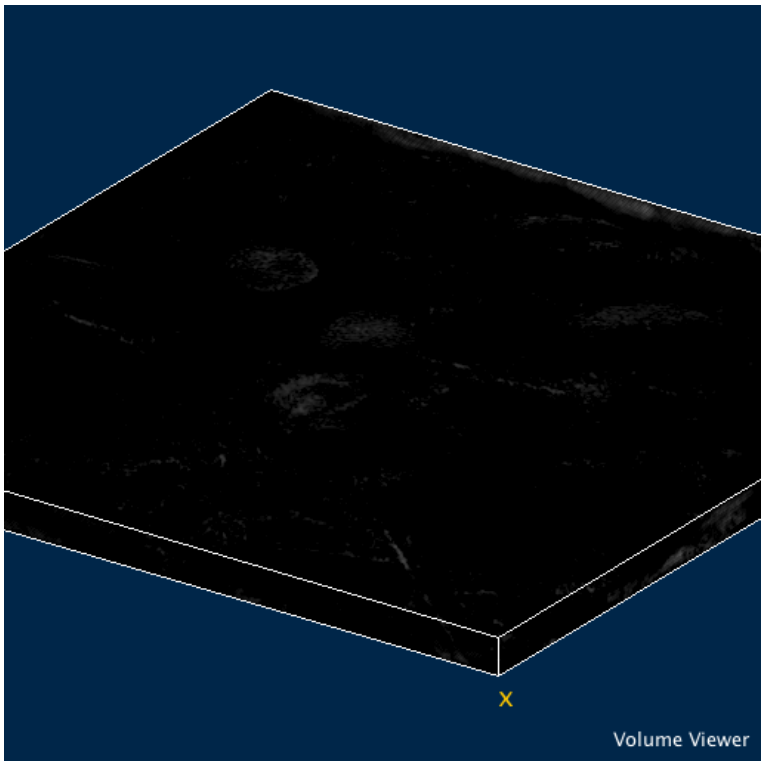

Image 6-19: Test nonspecific segregation – Phase congruency with monogenic filters has provided almost no response at all

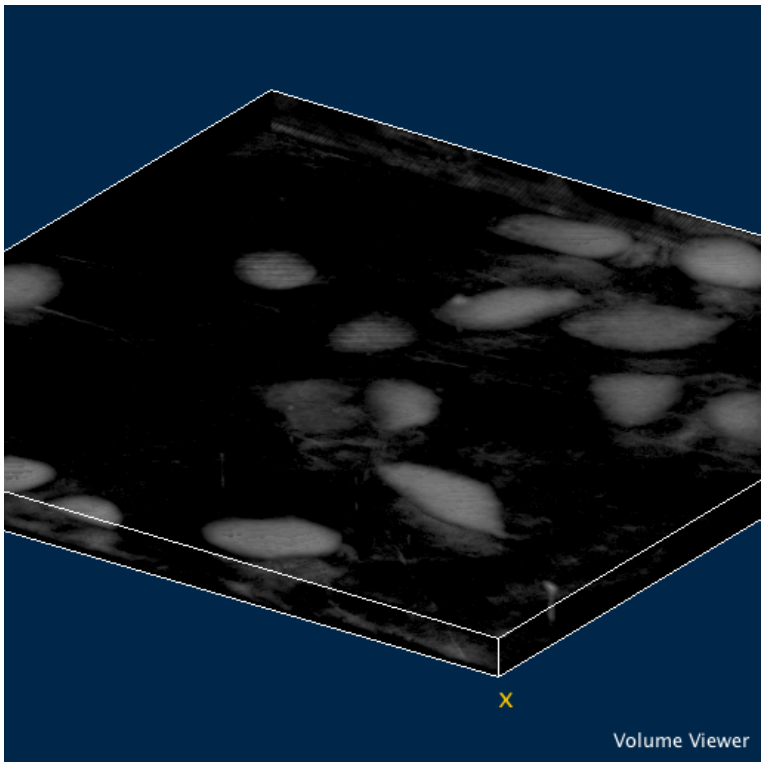

Image 6-20: Test nonspecific segregation – Phase symmetry with spread filters

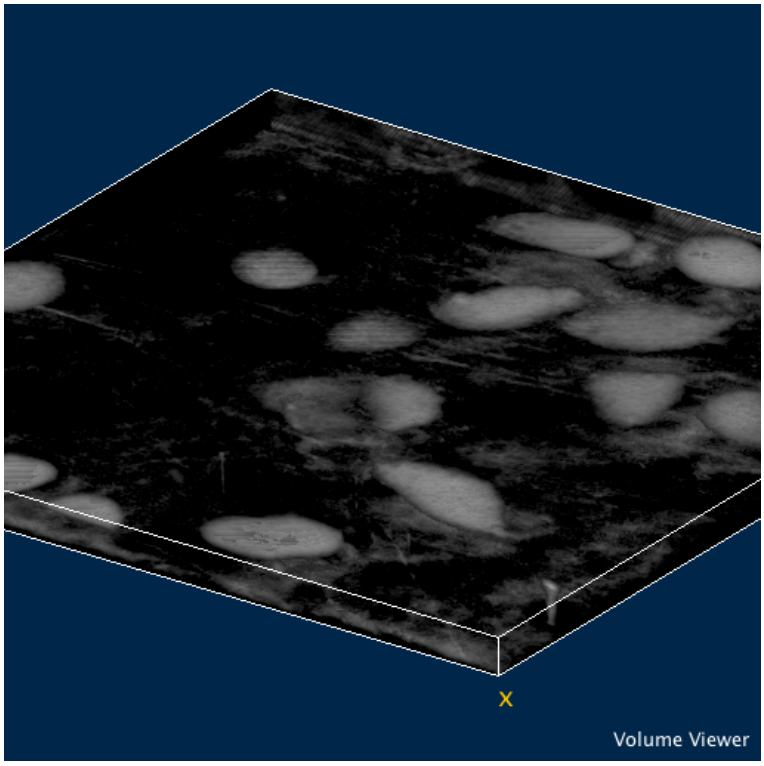

Image 6-21: Test nonspecific segregation – Phase symmetry with spread filters

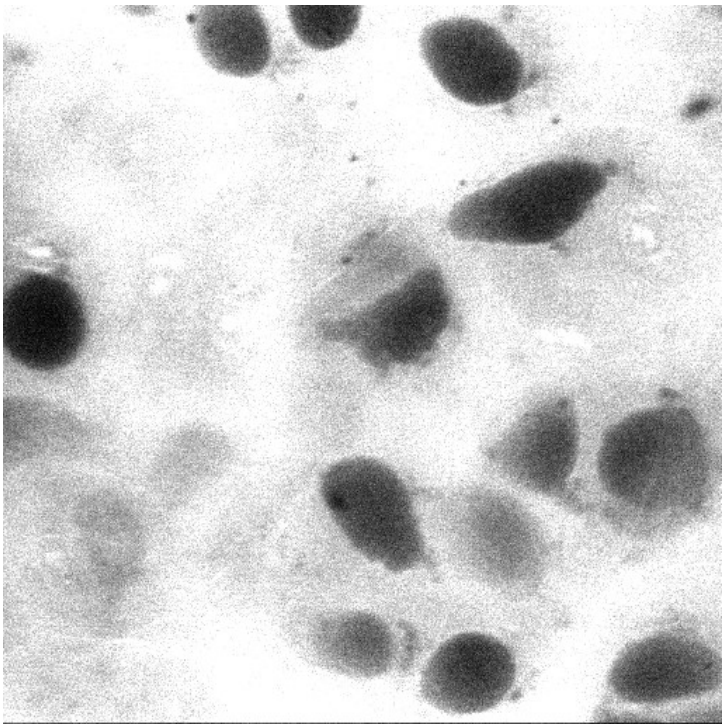

Image 6-22: 2D Filter comparison – raw image

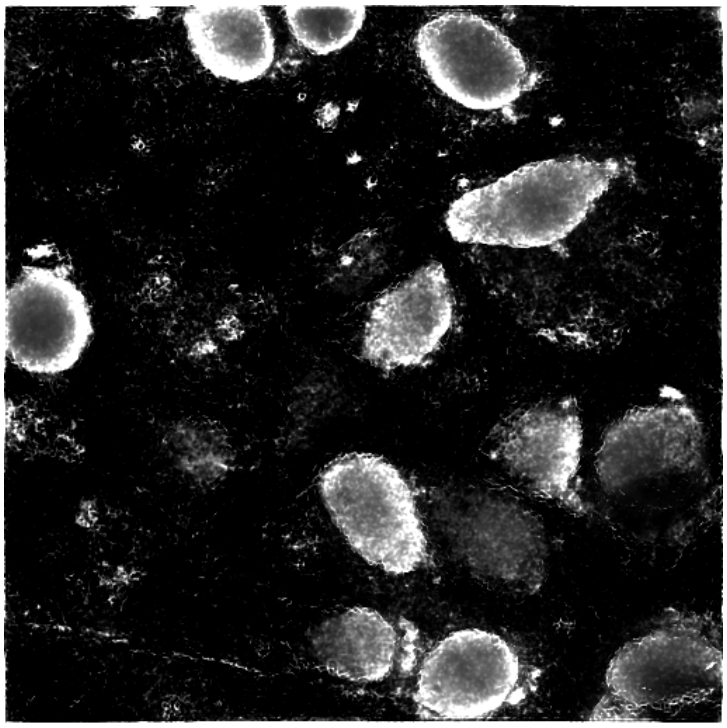

Image 6-23: 2D Filter comparison – phase symmetry with spread filters

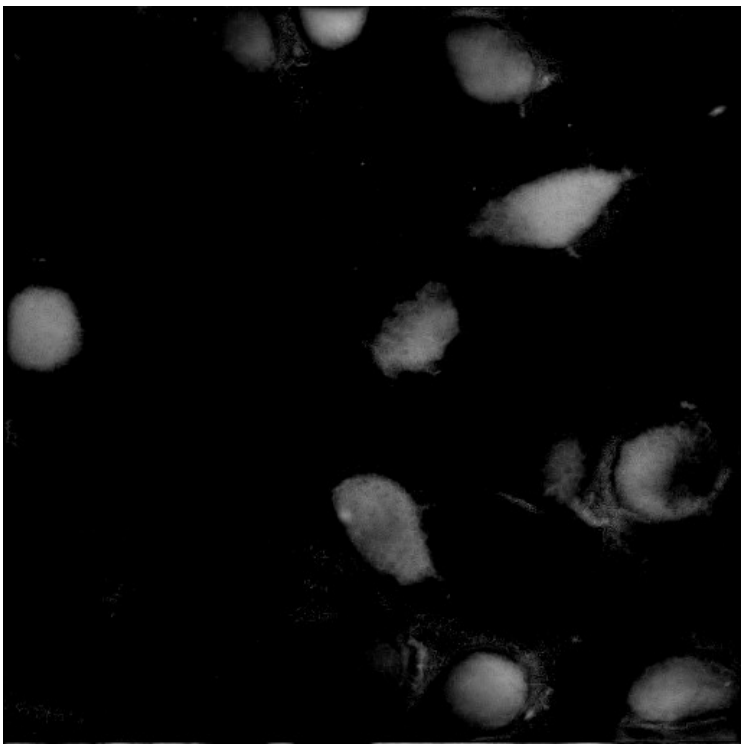

Image 6-24 2D Filter comparison – phase congruency with monogenic filters

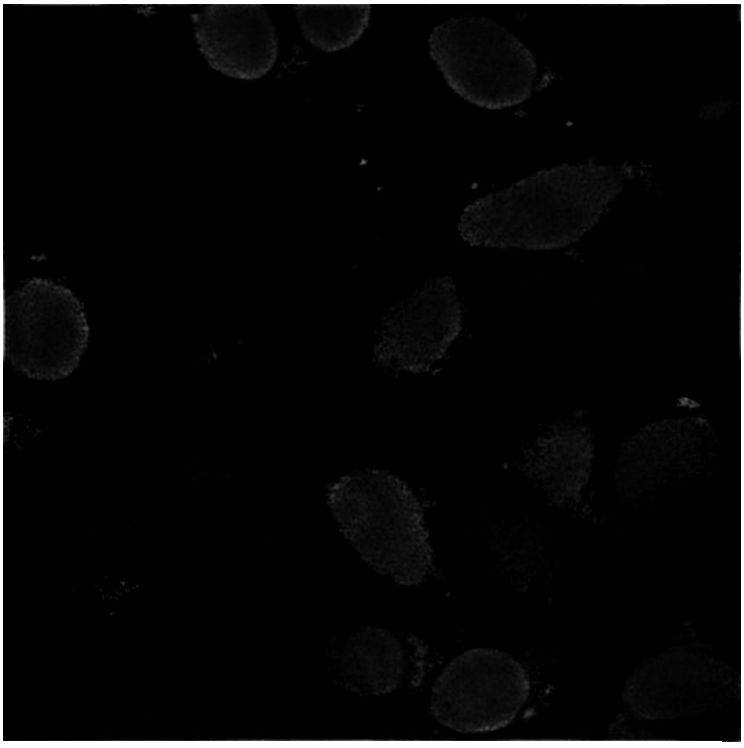

Image 6-25: 2D Filter comparison – phase congruency with monogenic filters

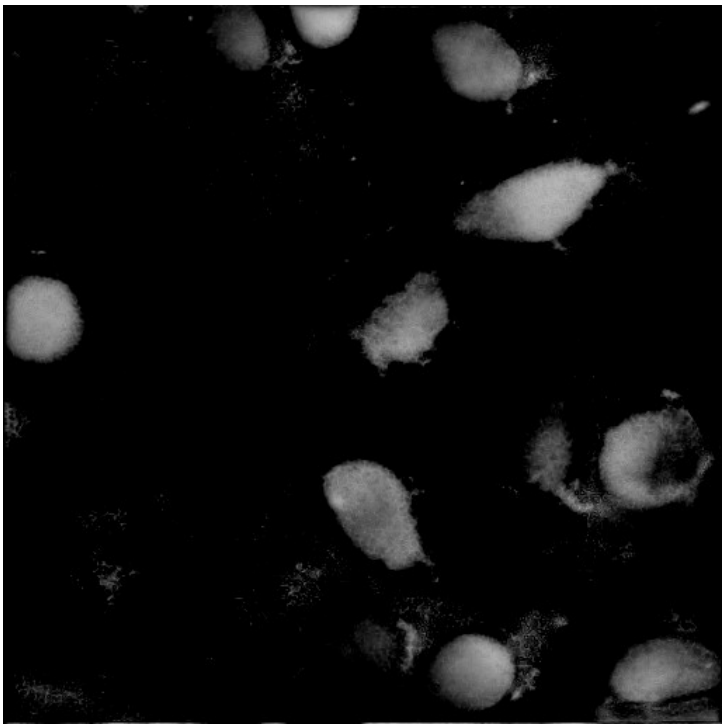

Image 6-26: 2D Filter comparison – phase congruency with spread filters

The 3D visualisation, phase congruency through monogenic filters has provided a faint response, and shows the outline of chondrocyte cell. Additionally, phase congruency through spread filters resolves more chondrocyte cells and in more detail than through phase symmetry. Images 6-23 through 6-26 demonstrate the performance differences between 3D phase congruency and phase symmetry in feature segregation. This study extended log-Gabor filters to 3D due to their dependence on the dimensionality of radius. For the calculation of the local energy vector at a particular scale, only a pair of quadrature filters are used which gave local energy as a 2D complex vector. In comparison, the monogenic signal is four dimensional for a 3D image, and consists of a 3D local energy component plus the original signal. This reduction in dimension was incorrectly assumed to be due to symmetry of log-Gabor filters, as in three dimensions there should be a triplet of filters in quadrature (a 90-degree phase shift along each orientation in the frequency domain). In 2D phase congruency, the odd and even filters are combined into a single filter where the resulting real and imaginary parts of the output correspond to the odd and even components of the local energy vector. Since the same approach was employed in 3D phase congruency, the three quadrature filters were combined into single filter where the resulting odd component would be representative of the two odd filters

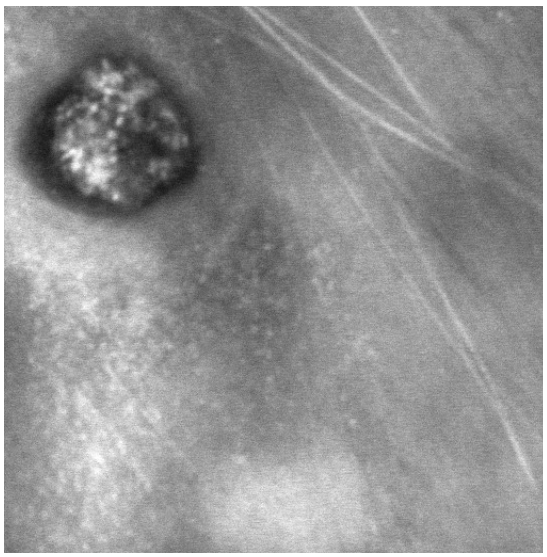

Original Image

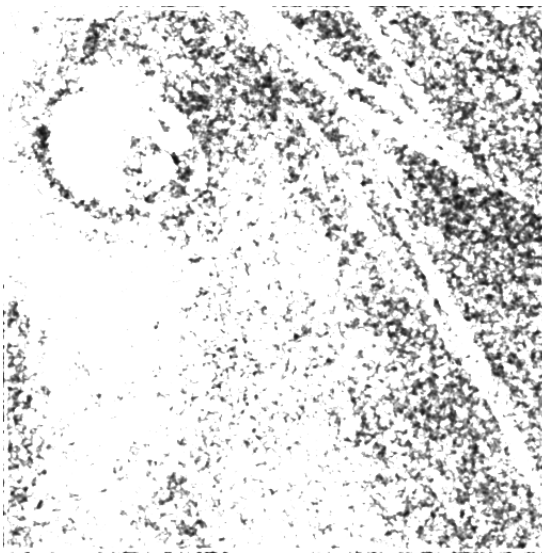

Harris corner detector

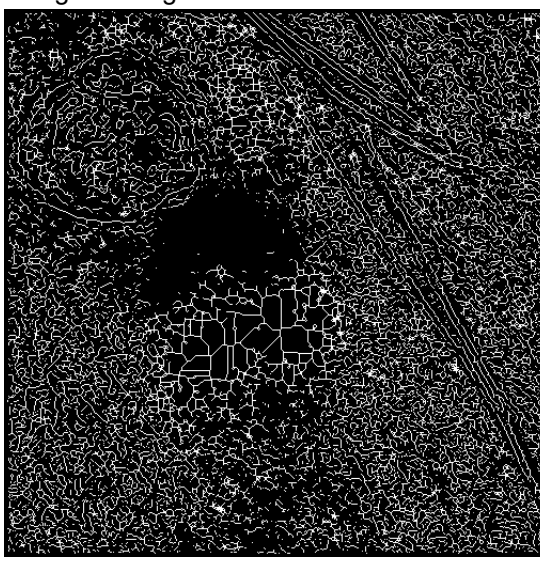

Canny edge detector

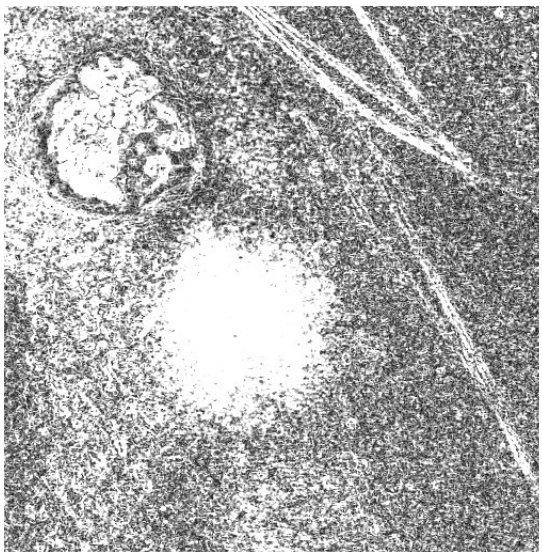

Sobel filter

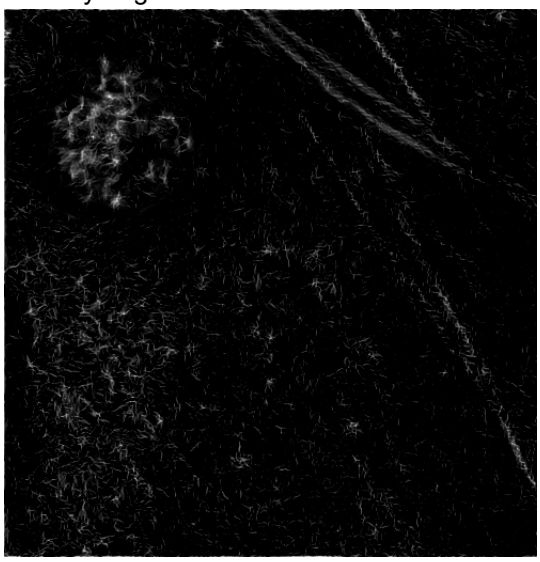

2D phase congruency image

3D phase congruency image

Image 6-27 Fibre Detection – Notice that whist Canny and Harris detectors provide almost no collagen detail, the Sobel filter provides some fibre structure, however, not all fibres were detected. The phase congruency test images provided most fibre detail.

In the Image 6-27, the Sobel filter response indicates a fibril structure along the edges of collagen fibres and hence, supports the existence of these features in the original image. The gap present along the centre of fibres is due to the gradient being zero at those points. It should also be noted that the response is blurred in a similar manner to 3D phase congruency and could be the result of axial features. In comparison, the Harris corner detector shows that there is a considerable amount of corner features along fibres, while the Canny edge detector merely shows the edges for the collagen fibres. Interestingly, the Canny edge detector is used in image processing, but given the results, phase congruency provides far more useful information. However, neither the Canny edge or Harris corner detectors provide any information on the internal structure of collagen fibres.

From the 2D phase congruency and Sobel filter responses, (Image 6-27) it is reasonable to conclude that 3D phase congruency through spread filters is responding to the internal fibrillar structure of collagen fibres. The resultant 3D image has more segregated objects and less noise present.

Chapter 7 Developed Software - Conclusions

This section outlines the output from the developed 3D software. It demonstrates the use in the segmentation of 3D objects found within 3D images. A comparison with 2D techniques is included.

Two methods for identification and segmentation of objects within an image were successfully implemented using phase symmetry and phase congruency filters.

The algorithm developed represents the first successful extension of the phase symmetry method from 2D to 3D. Additionally, the 3D version was fitted with monogenic filtering which is computationally feasible on a desktop computer. The modified programs have been incorporated into Kovesi's distribution suite for phase symmetry and phase congruency. Kovesi deemed that this algorithm was working successfully.

7.1 Phase Symmetry Conclusions

It was found that the 3D phase symmetry algorithm displayed much potential in the study of confocal microscope images of AC and could satisfy all the functionality of image segregation and performance on a desktop computer. The 3D algorithm was found to provide a distinct increase in performance over the 2D algorithm, especially for resolving thin features such as collagen II fibres. This can be attributed to the inclusion of data from adjacent planes into the calculations. The ability to resolve collagen fibres not aligned with the image sections was also improved. The 3D algorithm was also able to successfully segment the collagen fibre network surrounding the chondrocytes, while the 2D algorithm was less successful.

The 2D analysis was not able to resolve 3D objects satisfactorily as the changes in gradient along the radial direction (z axis) were not calculated from one slice to the next accurately. The 3D routines were found to be more efficient and effective when the change in scale was the same in each direction. This is especially true as the z axis angle is either very low or very high.

The 2D reconstruction also suffers from the fact that changes between slices show the 3D sections as a series of concentric 2D sections rather than as a single surface encompassing the volume under consideration. Whilst the 2D slice is accurate, within the slice, the image does not take into account the slices immediately adjacent and thus does not select objects that continue in direction normal to the slice. 3D segmentation overcomes these restrictions giving true 3D surface volumes upon which to base the image segmentation. 2D segmentation introduces artefacts due to the partial surface recognition of the volumes of interest.

The 3D algorithm was found to be sensitive to brightness variations between image slices. These variations in image brightness were successfully compensated for by normalising each image in the image stack with an intensity based algorithm. The intensity approach delivered better results than the peak based approach due to the wide variation in image brightness and contrast in each image section.

Spatial image compression in the axial direction arising from variable image slide spacing and poorer axial resolution was successfully accounted for by scaling the axial distance vector used to construct the monogenic filters and the band pass filter. However, separate removal of axial compression by image expansion improved the displayed image using ImageJ. The removal of axial compression also improved Gaussian noise removal by making all gradient estimates of equal strength.

The setup of the band pass filter bank was found to influence the phase symmetry routine output. By varying the wavelength span of the filter bank, different scale features could be segmented from the image. It is possible to tune the filter to recursively extract information from a very small scale to a very large scale, and then to reconstruct the object by adding the scale based sub-images together to form a true representation of the object over multiple scales.

A control program was written to automate the image analysis process and create a 3D composite colour image based on the phase symmetry or phase congruency results. Composite colour images created by the control program displayed promising results. The chondrocytes could be identified out and possessed sharply defined edges. The collagen fibre network could be seen to surround the chondrocyte cells and large individual collagen I fibres could also be seen in the 3D image. This is discussed in section 7.4

7.2 Phase Congruency Conclusions

This study extended 2D phase congruency to 3D using both monogenic and spread filters for feature extraction from laser scanning confocal microscopy (LSCM) images of articular cartilage. Spread filters were used to localise frequency with respect to orientation and were designed using 3D cones with a cosine distribution running radially from their centres. The surface normal of an icosahedron were used to approximate the even distribution of spread filters over the frequency space. This approximation was found to result in uneven frequency spread causing amplification, blurring, and warping of the phase congruency response. This approximation also resulted in the amplification of finer details and the resolution of axial features. Analysis of the impact of blurring and warping, and their responses to noise, found that spread filters enhanced the detection of collagen fibres within the image to such an extent that individual fibrils along the fibres were visible. Spread filters were also shown to provide significantly more detail than phase congruency through monogenic filters or any phase symmetry measure.

This study provides a new perspective on the capabilities LSCM and provides a new image processing technique for the analysis of 3D images. This comes at the cost of evaluation of the spread filter directions in forming the new images. Testing indicated that the more directions used, the finer the resolution could be estimated, within the bounds of noise generation. At very small direction dihedral angles, the computation became excessive and it was found that neighbouring direction cones needed to be averaged to reduce noise and correctly segment individual objects from each other.

It is important to understand that a single object within the image will have similar phase orientation and phase offset in the two-dimensional imaginary plane generated by the signal analysis. The size of the object segment is dependent upon the scale of the image viewed. It is important, therefore, to tune the filters to select the segments isolated.

The use of noise compensation has a dramatic impact on the quality of response. Noise compensation adequately estimates the level of noise within the image and in doing so, provides a far more localised response than the results for the original test image.

However, with noise compensation, the phase congruency response still concedes a considerable amount of erosion which is due to the amplification of noise within the image. In comparison, without noise compensation phase congruency is still able to detect features within the original image, but is unable to discern between real features and noise. While this may seem reasonable, as noise profiles within an image are features, monogenic filters could provide an accurate response without noise compensation. Spread filters worked more accurately with noise compensation, providing reliable feature detection. One reason for this is that the uneven spread cloud amplification could change the distribution of local energy over scale and in effect, change the form of the weighting function. Hence, noise features could appear just as dominant as image features.

Alternatively, it may be that monogenic filters provide a more accurate measure of local energy. With log-Gabor filters, local energy is 2D for any multidimensional signal (i.e. 2n dimensional for an n dimensional signal). With monogenic filters, local energy is n+1 dimensional for an n dimensional signal).

Three-dimensional phase congruency has better noise reduction when used with log-Gabor directional filters based upon direction vectors derived from the plutonic solid known as the icosahedron. This can be fed back to the 2D slices that constitute the raw image giving improved performance in both noise rejection and feature detection. The software is written so that additional processing using phase symmetry can additionally give clearer image results.

As with phase symmetry the removal of spatial image compression in the axial direction improves the basic geometry for the filters to operate. Certainly, 3D phase congruency gives better performance in fibre movement between 2D image slices.

7.3 Image Preparation and Intensity Equalisation

The noise compensation algorithm was found to provide an uneven de-noising performance, as the bulk of the image features are collagen II fibres which gave weak phase symmetry and phase congruency responses. However, medial filtering to remove spikey noise in the localised image improved the software de-noising performance and aided the algorithm for feature segmentation

The main feature of image preparation is the need for intensity equalisation over the entire stack space. The signal decreases with depth and this required compensation to ensure that features traversing between stacks had similar brightness. Also, the mean brightness of each stack was equalised to ensure a clear transition from one image frame to the next.

The display of each image was controlled by the ImageJ visualisation processes. These worked more efficiently when the voxel displayed was a cube rather than a rectangular prism. Image equalisation to resize the stack frame to ensure that each direction had the same scale was unnecessary for the operation of the 3D software. However, axial compensation was required to get a clear and understandable image produced. This also required the relative voxel lengths to be input to the imaging software. Using sub-voxel interpolation of the axial dimension gave uniform cubic voxels, which in turn allowed for reprocessing of images and the storage of images in a format that other ImageJ filters could be directly applied.

ImageJ has a set of smoothing filters that are commonly used to clean raw data files. A decision was made to use these filters rather than the set developed using Matlab at the commencement of this thesis. Equalisation allows the geometry to be interpreted in terms of regular spherical co-ordinates i.e. distance expressed as a radius, and two angles to give direction (Figure 6-2). Operations that use 3D smoothing or averaging algorithms are easier to implement as a series of concentric spheres and directly using existing ImageJ functions. This prompted the decision to rewrite all developed software as ImageJ filters and to release these filters to the ImageJ user community.

7.4 Composite Colour Image Results

The following images display a 3D composite colour volume view of a confocal microscope image of AC. The visualisation was created using ImageJ, an open source image processing software package. The volume viewer plug-in (included in the package) was used to create the volume views. Better 3D visualisation tools do exist, however ImageJ was chosen as it is widely used and accepted in the microscopy community.

A routine was developed to segregate the cartilage components into chondrocytes and collagen fibres into separate images that can be used as is or can be artificially coloured and used to form composite colour images. These segmented images were transformed into monochromatic colour versions of the grey scale input image with red being assigned to the fibre component and green to the cellular component. These components were subtracted from the original image and the background was coloured blue. The resultant processed image was saved as a 24-bit true Red, Blue Green coloured image ("RGB"), which was printed to assist with visualisation.

The chondrocytes appear prominently in the colour image and are sharply defined. Large regions of dense collagen II fibres can be seen encasing the chondrocytes. The collagen fibres are also layered over the chondrocytes, encasing the chondrocytes in a 3D web of collagen fibres. This represents a significant improvement over the 2D phase symmetry method, which was unable to properly resolve the collagen fibres surrounding the chondrocytes. Individual strands of collagen I fibres can also be made out near the AC surface.

The algorithm developed here represents the first successful extension of the phase symmetry method to 3D that is computationally feasible on a desktop computer. Dr Kovesi has examined these results and concluded that the algorithm was working successfully. This algorithm has been included into Kovesi's distribution.

It was found that the 3D phase symmetry algorithm displayed much potential in the study of confocal microscope images of AC. The 3D algorithm was found to provide a distinct increase in performance over the 2D algorithm, especially for resolving collagen II fibres. This can be attributed to the inclusion of data from adjacent planes into the calculation. The ability to resolve collagen fibres not only aligned with the image sections was also improved. This 3D algorithm was also able to segment the collagen fibre network surrounding the chondrocytes, which the 2D algorithm had been unable to do.

The following images display the use of the segregation and artificial colouring of individual objects based upon their size in terms of voxel length. The images are separated by a series of band-passed filters into separate files. These are in turn used to identify specific objects using non-maximal suppression for each orientation. Each object type is saved individually and is used to select photo realistic objects from the raw images. These are then combined to give composite 3D images as desired.

The 3D algorithm was found to be sensitive to brightness variations between image slices. These variations in image brightness were successfully compensated for by normalising each image in the image stack with an intensity based algorithm. The intensity approach delivered better results than the peak signal based approach due to the wide variation in image brightness and contrast in each image section. Expanding the stack set using sub-voxel estimation provided faster processing and near optimal results at the expense of increasing the number of voxel slices to be processed.

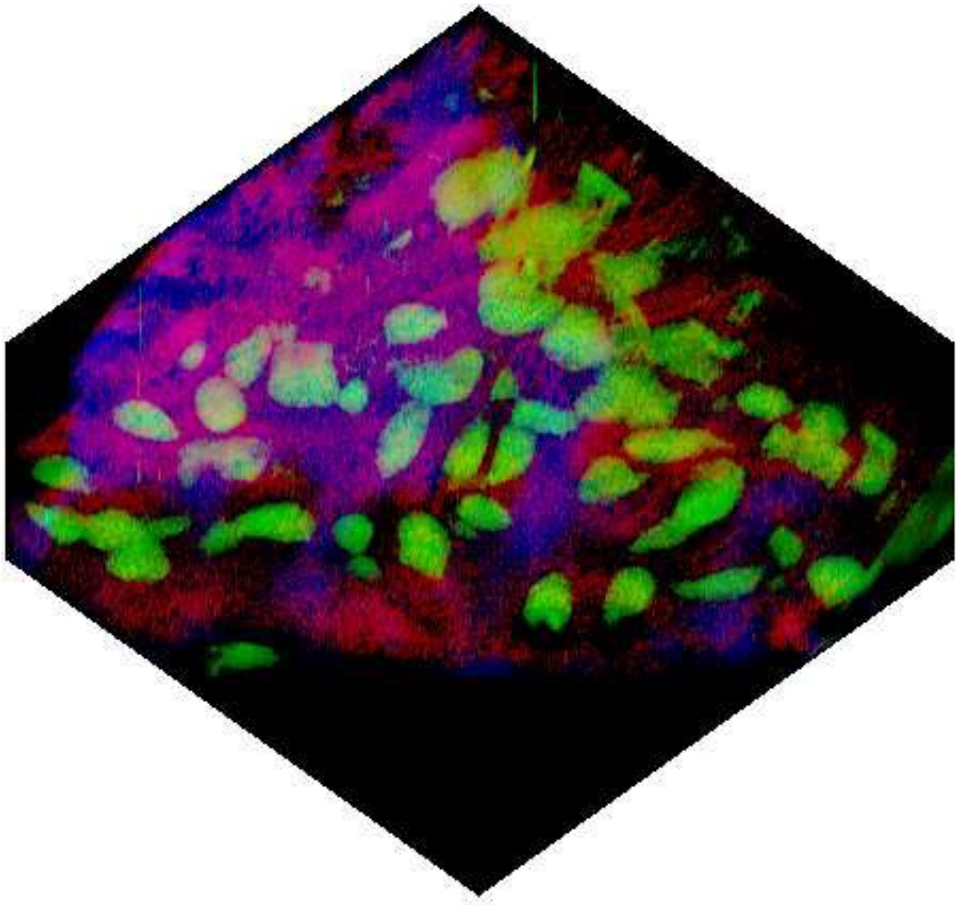

Figure 7-1: 3D composite view created using ImageJ. (1) Chondrocyte cells feature prominently and have well defined edges [in green]. (2) Collagen I fibres close to the AC surface [in red]. (3) Dense regions of collagen II fibres surrounding the chondrocyte cells [in blue].

The setup of the band-passed filter bank was found to greatly influence the phase symmetry routine output. By varying the wavelength span of the filter bank, different features could be segmented from the image. The noise compensation algorithm was found to provide poor de-noising performance as the bulk of the image features are collagen II fibres, which give weak phase symmetry responses. The chondrocytes could be distinguished and possessed sharply defined edges. The collagen fibre network could be seen to surround the chondrocyte cells and large individual collagen I fibres could also be seen in the 3D image.

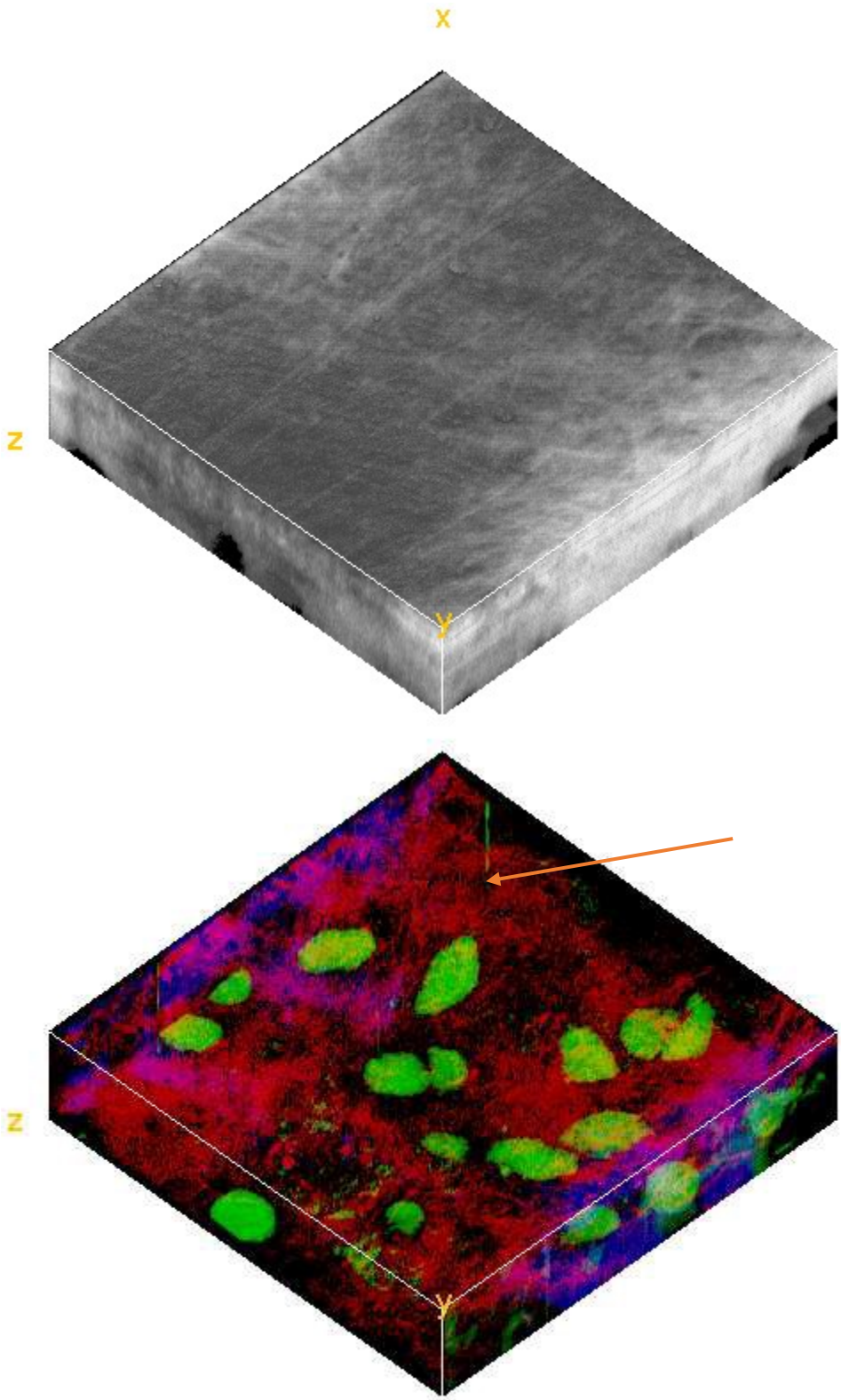

Figure 7-2: Image size sheep 83 - 1024 x 1024 x 73 both original and coloured volume views.

The chondrocytes surrounded by fields of collagen fibres feature prominently. The arrow points to a piece of debris on the lens resolved into an axial feature. This exhibits the performance of the 3D algorithm for detecting features, not aligned with the image plane.

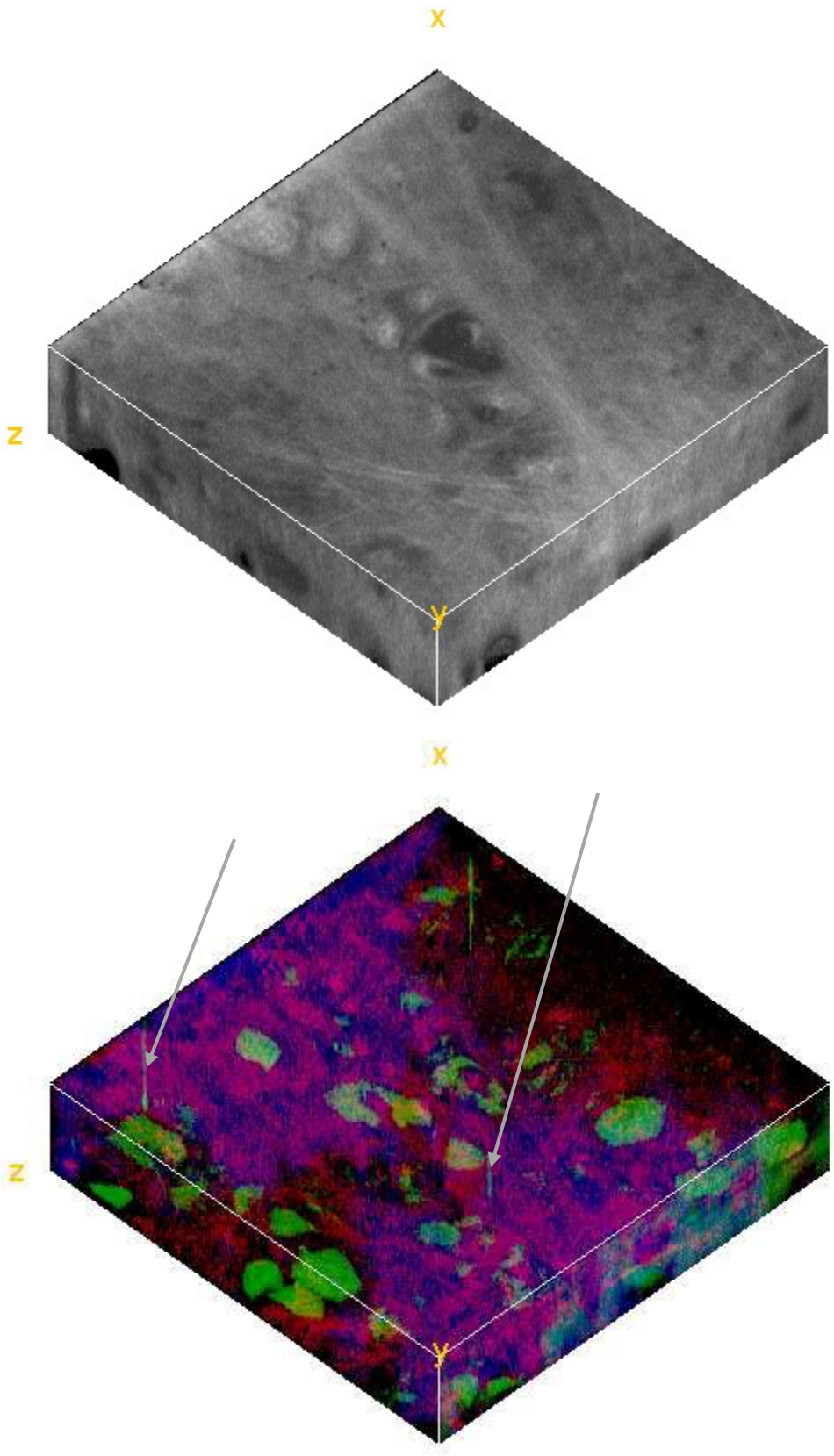

Figure 7-3: 3D Image sheep 87, size 1024 x 1024 x 76 both original and volume views.

The arrows point to pieces of debris on the lens that were resolved into axial features. This exhibits the performance of the 3D algorithm for detecting features not aligned with the image plane.

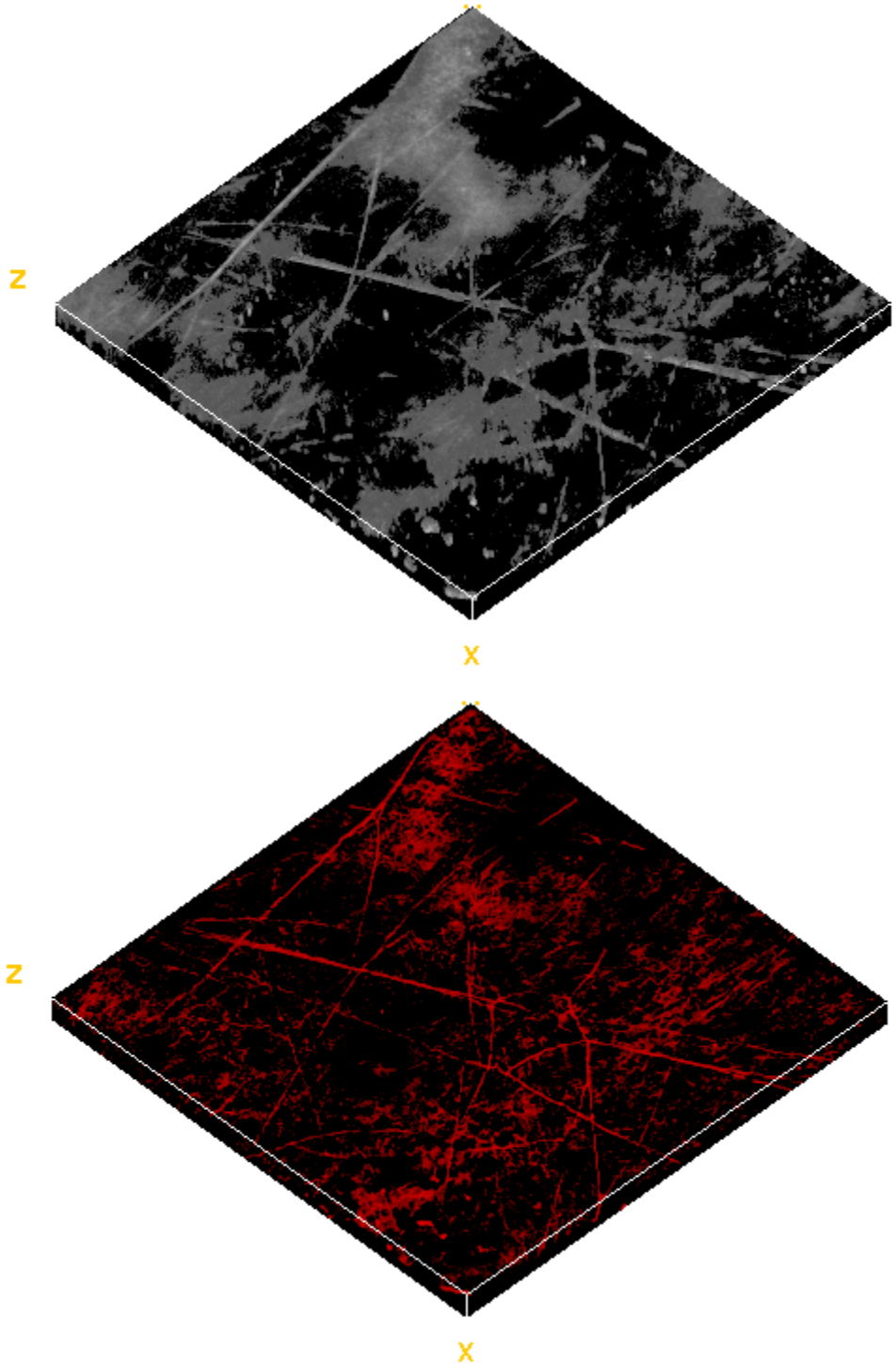

Figure 7-4: 3D image of sheep 137 size 102 4x 1024 x 15 both original and coloured volume views.

There were no chondrocytes identified in the image and the collagen only view is presented. The collagen view provides a distinct increase in image clarity. The original image used thresholding to attempt to remove some of the noise present.

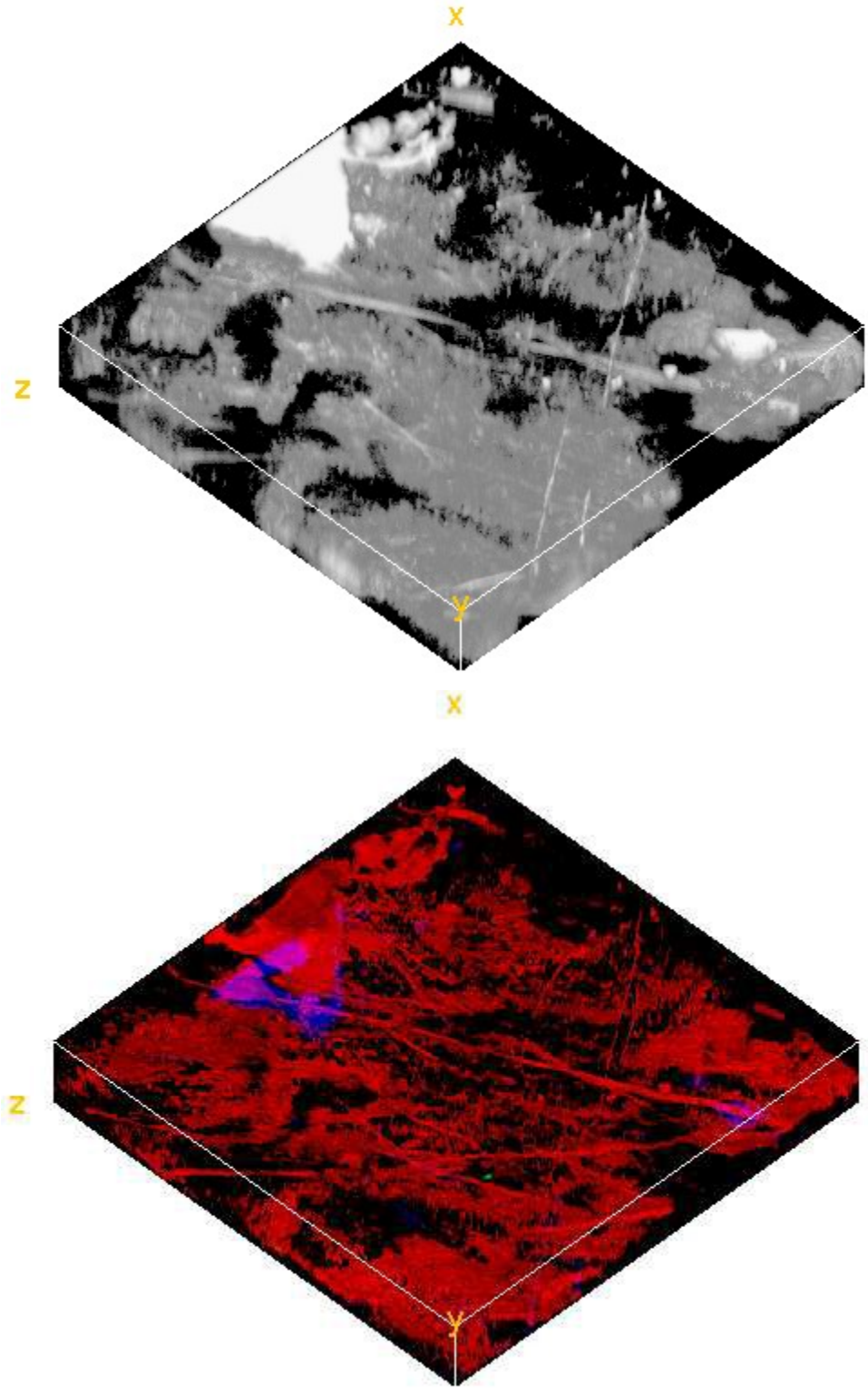

Figure 7-5: 3D image of sheep 165 size 1024 x1024 x 40. Both original and volume views

There were no chondrocytes present in the image, only the collagen is present. The collagen only view provides a distinct increase in image clarity. The original image used thresholding to attempt to remove some of the noise present. The large white patch present in the original image was also successfully removed.

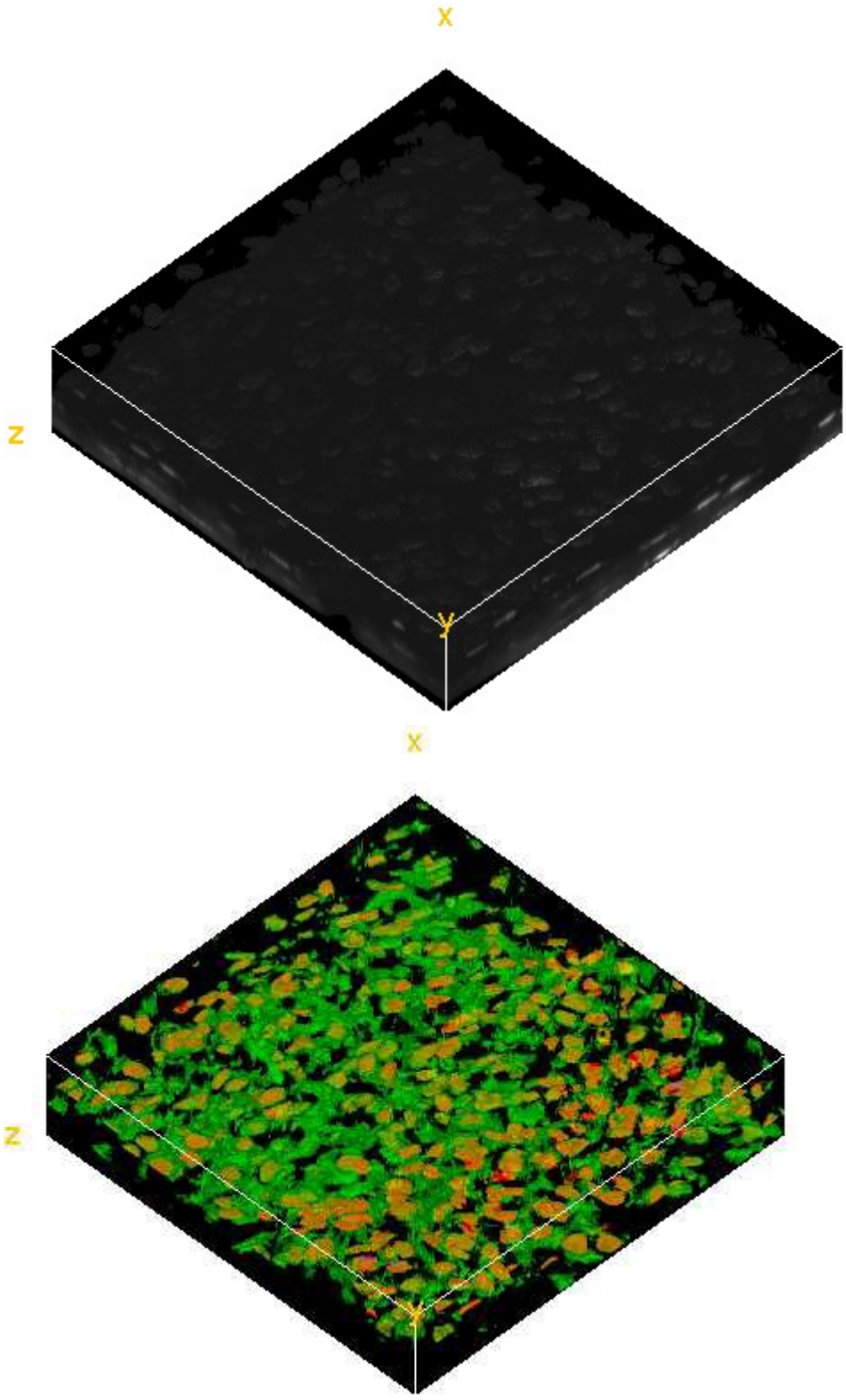

Figure 7-6: Sheep 127 size 1024 x 1024 x 55 Original and coloured chondrocyte selections

The polarity of the collagen phase symmetry algorithm was inverted enabling the search for chondrocytes. In this way, the chondrocytes could be coloured differently corresponding with response strength.

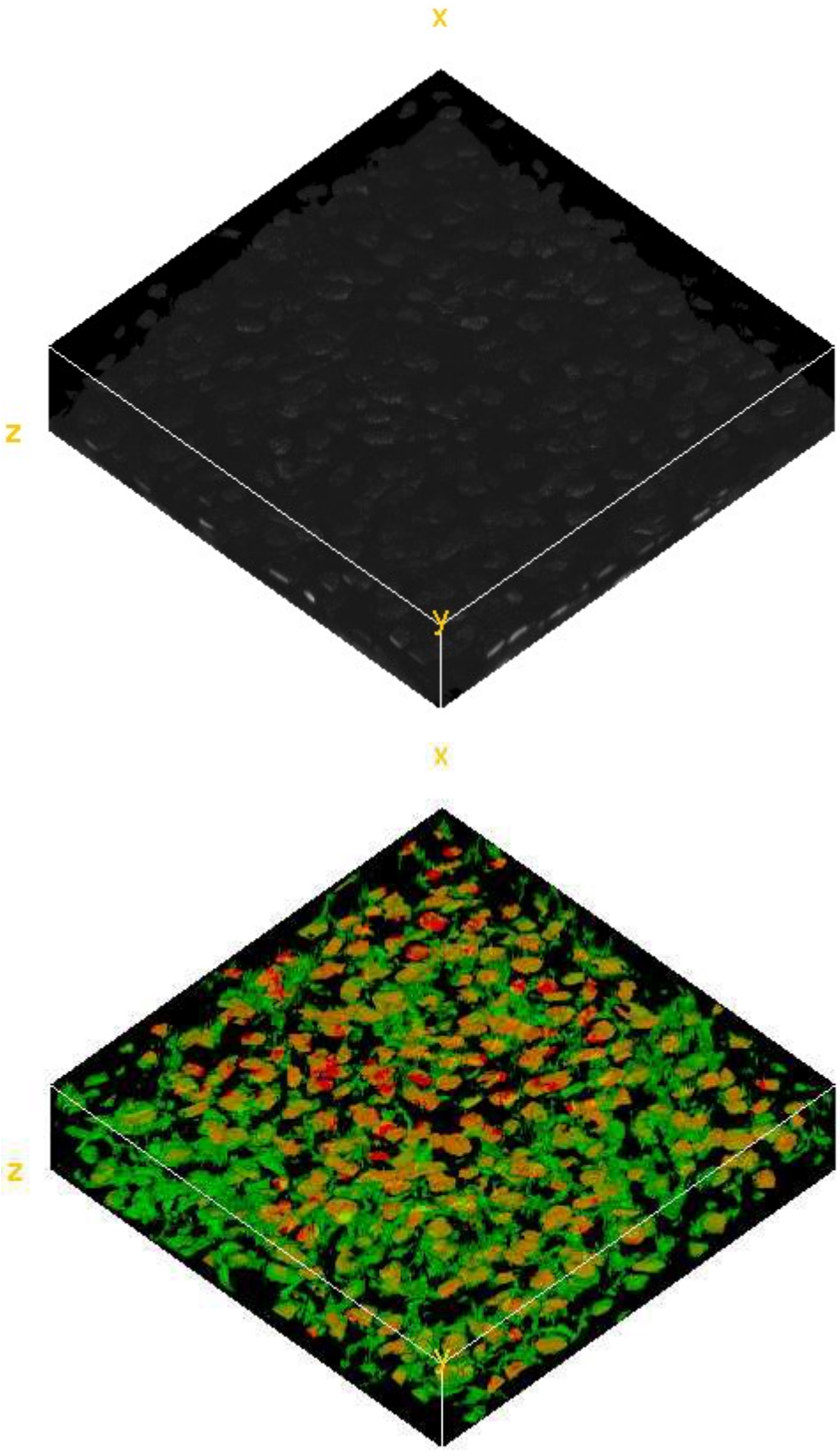

Figure 7-7: Sheep 127 image size 1024 x 1024 x 55 - same image as previous page

Shows chondrocyte enhancement where colour variation is based upon object strength. Yellow/red cells are deformed and trapped within lacunae. The green cells are viable chondrocytes.

Chapter 8 Test Procedures and Mechanical Test Rig

This section sets out the standard test procedures adopted for animal studies.

It represents the end of the development of image processing routines and describes the field work that gave rise to the need to improve the available image processing. These tests were conducted prior to software development phase of the project.

This is the second part of the thesis: the first part has described the software development to enhance 3D visualization; this part provides a summary of the laboratory work conducted to examine the mechanical properties of hyaline cartilage. These tests used animals of different age groups to get some insight into the development of cartilage with growth in the specimen studies.

The studies were conducted over a protracted period as a series of short pilot exercises to explore the different factors that affect cartilage growth. As such the results are statistically significant, but due to the lack repetition, the errors associated with some of the mechanical readings would be smaller if more samples were available at the time the study was completed. All studies were assisted by undergraduate students to complete the processing of the samples available. The test procedures were the same for each study and are described herein.

In these studies, articular cartilage samples were taken from 93 individual sheep ranging in age from 90-days gestation to five years old and 30 individual pig samples taken from three to six months of age. The bulk of the ovine (sheep) were taken from 123-days gestation to seven weeks postnatal and one to three years old. Some mature, five years old ewes were sampled to compare prenatal cartilage with that of mature adult sheep.

The femoral condyle was chosen as the sample origin, due to the possibility of taking more than one sample per tissue at particular places on the condyle. For the smaller sheep, this was limited, due to the smaller size of the tissue sample. The entire synovial joint was harvested including the femoral condyle, the patella, menisci, and tibial plateau, to avoid damaging the articular cartilage. The knee was subsequently disassembled to reveal the femoral condyles and was processed immediately, except in the case of 90-day and 100-day old samples, which were frozen for a period of six weeks before processing. The maximum number of samples taken from the 90-day and 100-day old femoral head was two, due to the limited size of the condyle.

At processing, the image quality of the frozen samples was poor due to dehydration of bound water surrounding the collagen fibres and hence the 90-day and 100-day samples were excluded from the study.

It was possible to harvest and clean the femoral condyles, without disturbing the articular cartilage, with relative ease. The sheep were made available through the Large Animal Facility at UWA and the harvesting was carried out at the Shenton Park Research Station. All the sheep sample joints used were excess (waste) material taken from sheep used in the study of foetal lung development by Rd. Graham Polglase and his research group with UWA ethic approval number 07/100/565.

Figure 8-1 is a diagram of a human knee joint and describes the medical terminology used to define various parts of the knee joint anatomy. Animal knee joint anatomy is very similar in the way it is described however, its overall appearance differs due to the lack of an upright posture.

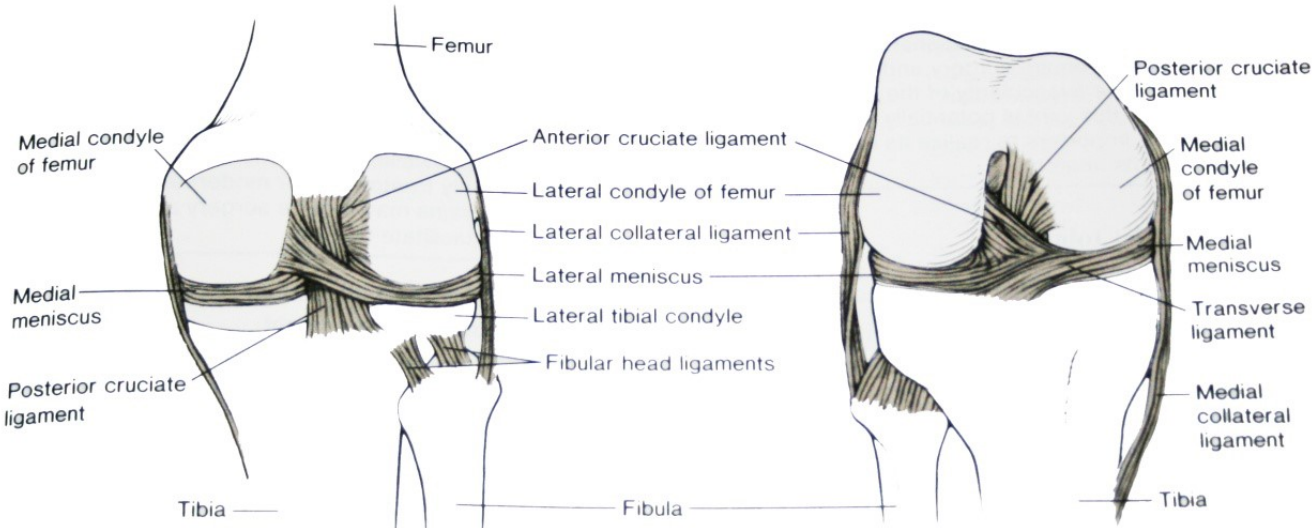

Figure 8-1: Anatomy of human (left leg) knee joint (Van De Graff and Fox, 1986)

8.1 Sample Selection

The sample selection was determined by the availability of sheep used in the prenatal study. The femoral condyles were used and the position was labelled according to the design in Table 8-1. This gave three different load bearing sites across the femur: non-load bearing; semi-load bearing; and load bearing.

Fresh samples were preferred as the imaging of these fibres was easier and gave more definite results. The 90 day and 100 day samples were fixed with para-formaldehyde and frozen for six weeks prior to imaging. As a result, these images were not clear. These two sample dates where the samples were frozen and stored have been excluded from the study.

The ages of samples used in these studies were:

- 123-day gestation;
- 129 / 130-day gestation;
- 140-day gestation (full term);
- seven weeks postnatal;
- Adult sheep (one to two years old); and
- Mature sheep (three to five years old).

8.2 Sample Preparation, Imaging, and Staining

A 3mm diameter biopsy punch was used to isolate a cylindrical section of cartilage at a particular site (shown in Table 8-1). A scalpel marked the orientation of the sample with respect to the normal vertical stance of the joint. A 1-2mm slice was then taken from the superficial end of the cylindrical sample. All samples were aligned according to the marking, to preserve the same orientation from the femoral head.

These samples were then placed in a 0.9% phosphate buffered saline solution (PBS) prior to use. The samples were stained with 0 5 grams/L FITC (fluorescein) in 0.9% PBS for 3.5 minutes and then rinsed in 0.9% PBS until the rinse was clear.

These samples were patted dry with paper towel and then mounted on a glass slide under a 0.17mm thick cover slide. An upright Optiscan F900e confocal microscope fitted with an oil immersion X63 objective lens with a numerical aperture of 1.4 was used to view the top 50, microns in 1.4 micron thick steps. A 300 micron by 300-micron square region of the sample was recorded with an output format of 512 x 512 pixels.

The main measurements taken relate to the thickness of the superficial layer and the observation of the fibre types and orientation within the superficial layer.

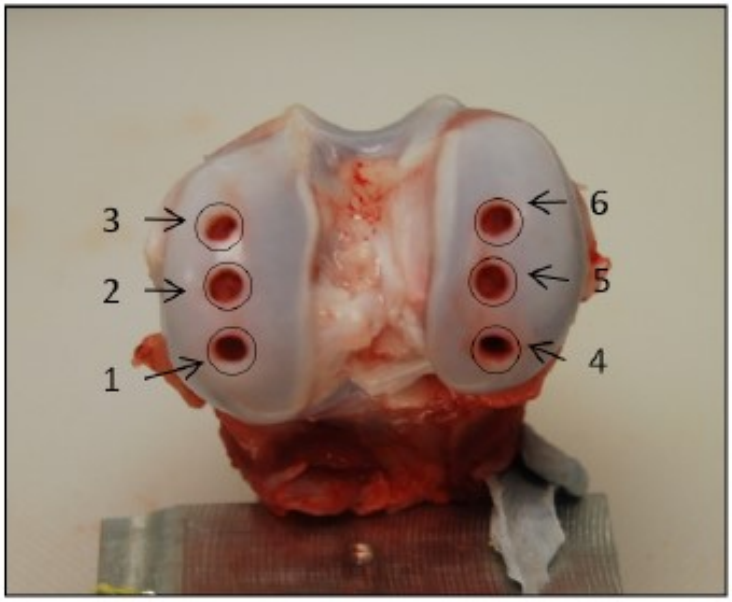

Figure 8-2: A dissected ovine knee joint showing sample locations. Sites 1-3 denote the lateral condyle, posterior (1), central (2) and anterior (3). Sites 4-6 denote the medial condyle.

8.3 Sample Sites on Femoral Condyle

Six different anatomically loaded sites from the femoral condyle were identified in these observations whenever the trochlea was not sampled. These same six locations were always used unless otherwise stated.

Two additional locations were used when the trochlea was sampled.

Figure 8-3: Sample sites showing the trochlea (sites 7 and 8) were sampled.

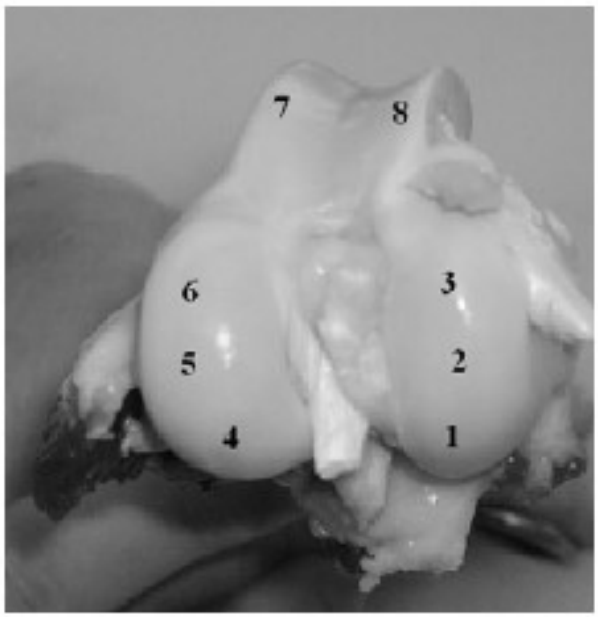

The trochlea is the indented grove shown at the top of Figure 7-3. Samples were taken from the medial and lateral sides of the trochlea, which is a non-weight bearing part of the joint, being used to guide the patella during sliding motion. The load bearing properties of each site are described in the following table.

Table 8-1: Sampling regions for ovine femoral condyle

Site	***Location / Loaded Region / Description***	
1	*location*	**Posterior region of the lateral condyle**
	anatomical load	Loaded.
PLC	The most loaded point on the lateral condyle due to the high level of knee flexion present in standing sheep.	
2	*location*	**Central region of lateral condyle**
	anatomical load	Semi loaded region.
CLC	This position is loaded in compression, when the sheep's leg is highly extended and exhibits shear due to the nearby attachment of the lateral collateral ligament.	
3	*location*	**Anterior region of lateral condyle**.
	anatomical load	Semi loaded region.
ALC	This position is loaded in compression, when the sheep's leg is highly extended and exhibits shear due to the nearby attachment of the lateral collateral ligament.	
4	*location*	**Posterior region of the medial condyle**.
	anatomical load	Loaded.
PMC	Post birth this is the most highly loaded region of the medial condyle due to the high level of passive flexion within the ovine knee	
5	*location*	**Central region of the medial condyle**.
	anatomical load	Semi loaded region.
CMC	This position is loaded in compression during high extension. There is no nearby ligament attachment to provide large shear loads	
6	*location*	**Anterior region of the medial condyle**.
	anatomical load	Semi loaded region.
AMC	This position is loaded in compression during high extension. There is no nearby ligament attachment to provide large shear loads	

7 **MT**	*location*	**Medial side of the trochlea**.
	anatomical load	Non-weight bearing.
	The trochlea provides the cartilage coated articular surface for the relative movement between the patella and femur but carries no significant load at any stage of the animal's life	
8 **LT**	*location*	**Lateral side of the trochlea**.
	anatomical load	Non-weight bearing.
	The trochlea provides the cartilage coated articular surface for the relative movement between the patella and femur but carries no significant load at any stage of the animal's life	

8.4 Image Analysis

All images were processed and measurements of features were computed using the z axis at 1.4 microns. Subsequently the images have been de-noised using a Gaussian filter and median filter. This study was completed prior to the introduction of image normalisation; however, the results are clear and good descriptions were obtained. Image normalisation is routinely used as it permits clearer fibre detection and the measurement of individual fibres. This gives uniform gradients so that a direct comparison of the partial gradients $\partial \mathrm{F}/\partial \mathrm{x}$, $\partial \mathrm{F}/\partial \mathrm{y}$ and $\partial \mathrm{F}/\partial \mathrm{z}$ are possible. This process proved to be sufficient, together with phase symmetry, to separate the fibres from the cells.

The depth of fibre growth and cell growth was recorded for each sample to determine the thickness of the lamina splendens and the orientation of fibre matrix. Two sets of samples were processed: one set of six from the left knee and a further set from the right knee. The general appearance of the sample sets was similar but differed in detail due to the small window size imaged.

Fibre Recognition is displayed in Images 8-1, 8-2, and 8-3.

Collagen fibres are stained by FITC and appear as thin bright lines on the Image 8-1 (A). Contrastingly, chondrocytes can be observed as both dark and light spots. The dark chondrocytes represent viable cells, Image 8-2 (B). These cells are believed to maintain the integrity of their membranes and hence do not absorb any FITC. Conversely, the light spots represent chondrocyte cells that are non-viable in Image 8-2 (C). Their membranes are believed to be damaged and hence allow FITC to penetrate and stain the internal structure of the cell.

Research has indicated that the superficial zone of AC primarily contains collagen fibres of types I and III (Teshima et al., 2004). Type I is classified as forming tightly packed fibre bundles (1-5μm in diameter) while Type III has been shown to form a loose network of thin fibres (0.5-1.5μm in diameter). It is therefore reasonable to infer that the two different forms of collagen fibres discovered in this study would most likely be types I and III. Based on their documented sizes and typical structure, the bundled fibres would represent type III collagen and the individual fibres would represent type I collagen.

Significant background staining was observed in nearly all of the images produced. This indicates that a particular type of collagen was present in the tissue but that its individual fibres could not be resolved. The cause of this background staining is the presence of type II collagen fibres. Type II collagen accounts for approximately 90% of the collagen fibres contained within AC (Eyre, 2001). Therefore, it would be reasonable to assume that it would be present in most of the samples

Type II collagen has been classified as forming a network of extremely thin fibre bundles 0.02-0.03μm in diameter (Montes and Junquiera, 1988). The lateral resolution of the microscope used for this study was 0.23μm. Hence, any individual type II collagen fibre bundles would not be resolved in images taken in this study.

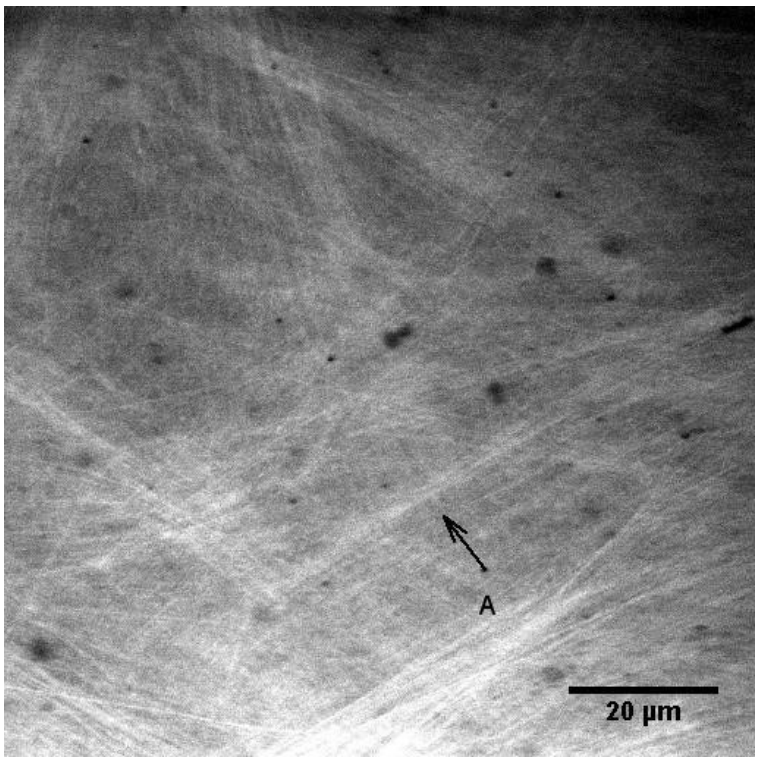

Image 8-1: Collagen fires (type I and type III) shown singly and as bundles [A]

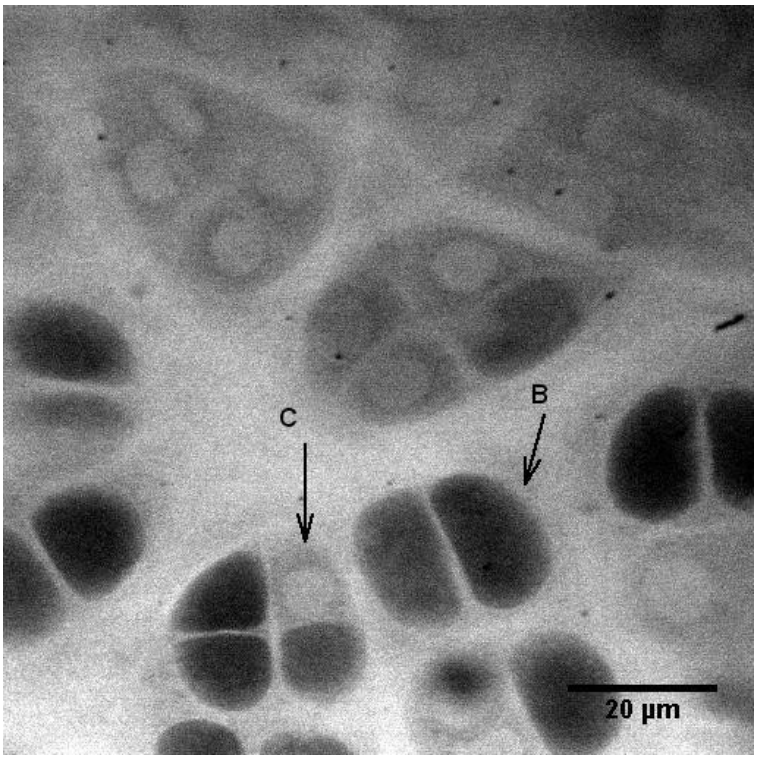

Image 8-2: Collagen type I and type III fibres [A] are shown singly and as interwoven bundles.

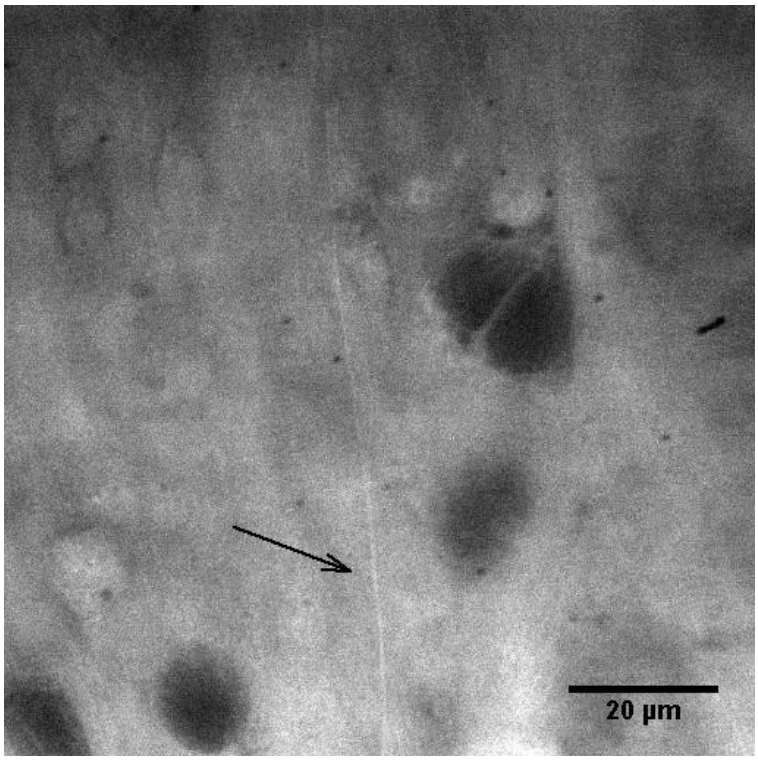

Image 8-3: Single thin bundle of collagen fibre (type I or type III)

8.5 Compression Testing Rig

Studies were conducted using both sheep (ovine) and pig (porcine) models over a period of four years. The actual model used depended upon the availability of test samples, and the detailed procedures changed with particular samples and with each study.

Unconfined and confined compression of AC was performed using a custom-built device (Figure 8-4). The cartilage stage (or cartilage recess) rests upon an Entran® ELFM-B1-50N load cell rated to 50 Newtons force, which in turn rests upon a linear translation stage (Thorlabs, Inc product code MT1-Z6). Translation of the stage compresses the cartilage sample against the stationary indentometer or the cylinder, depending on the compression regime.

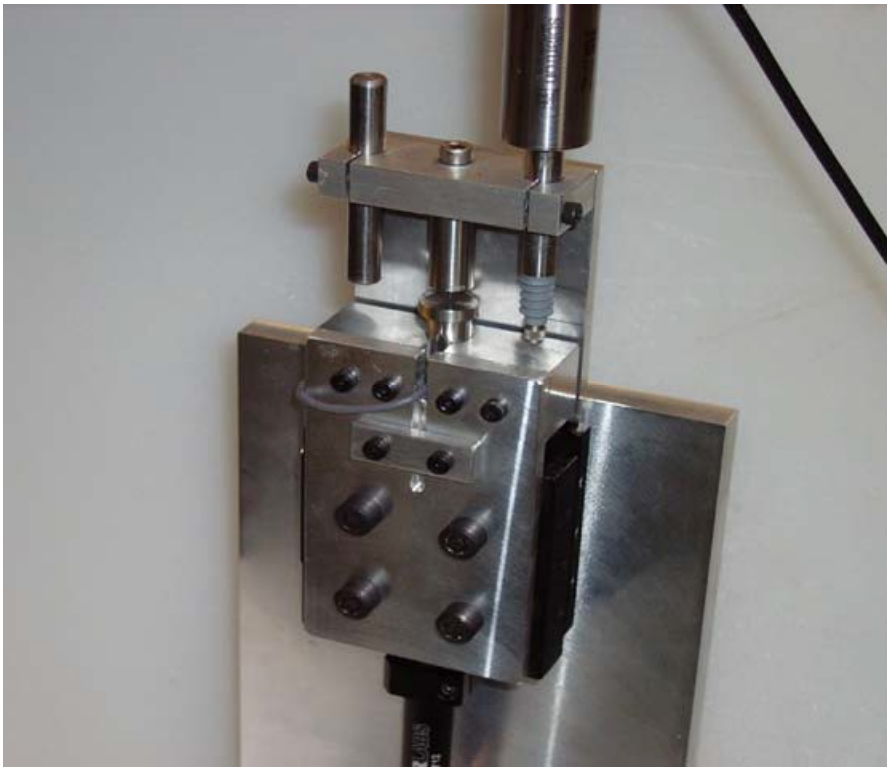

Figure 8-4: Compression testing rig loaded with an unconfined compression head.

Actuation of the stage was realised by a servo-motorised micrometre (Thorlabs, Inc model Z612B), equipped with a rotary optical encoder providing translational measurements. A linear voltage distance transducer ("LVDT" Solatron® DG 2.5) provides a secondary channel through which the translation of the stage is measured. Calibration of the LVDT indicated a useful working range of approximately 800μm. Additionally, the LVDT was used to ensure a repeatable starting point for repeat compressions of individual AC samples. Motion control and data acquisition for both the load cell and the LVDT were performed by a National Instruments PCI-7344 motion control card at 5Hz frequency.

The raw signals were input through a National Instruments MC-4SA servo amplifier system. All motion was controlled using a custom designed graphical user interface.

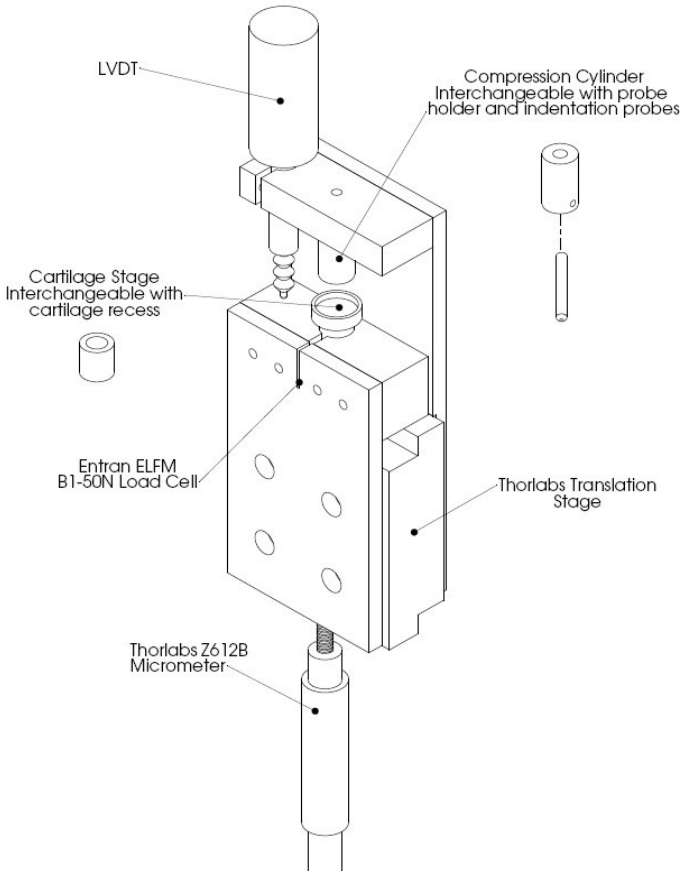

Figure 8-5: Drawing of compression testing rig

The test rig monitors the force applied to the sample, the distance of the platen above the sample and the platen drive position. The data readings are stored internally and can be down-loaded following the completion of the test. Controls allow for rapid movement of the platen, single-step of platen movement, platen velocity rate and end movement position. Several different mechanical tests can also be selected (ramp compression, stress-relaxation compression, thickness determination and creep testing).

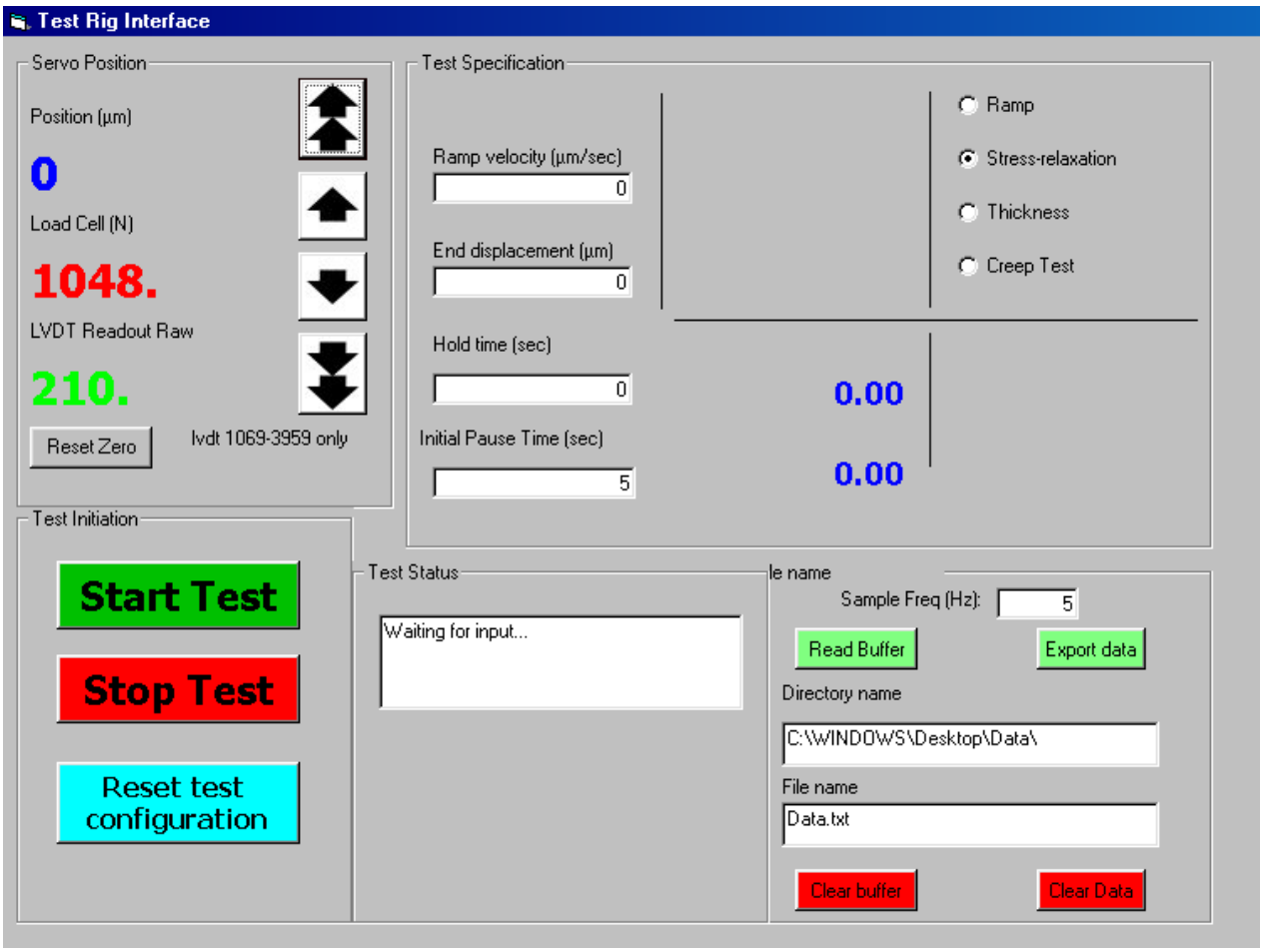

Figure 8-6: Compression rig control interface

Figure 8-6 shows the screen-shot of the custom graphical user interface (“GUI”) used for compression testing. The GUI allows the user control over compression parameters including compression velocity, compression length and holding times for stress relaxation protocols

Numerical data was produced for both LSCM and unconfined compression results. To test the statistical relevance of any differences observed in the results, hypothesis testing was undertaken. The statistical test for the hypothesis used in this study was an independent two sample t-tests (also known as Welch's t-test). Depending on the result being compared:

- A sample size, mean and standard deviation were calculated for each sample position.
- Two different sample positions were tested at a time using the following equations:

$$Welch_{\,t} = \frac{Sample\ Mean_1 - Sample\ Mean_2}{\sqrt{\frac{Variance_1}{Sample\ Size_1} + \frac{Variance_1}{Sample\ Size_1}}} \quad (8\text{-}1)$$

$$Welch_{\,df} = \frac{\left[\frac{Variance_1}{Sample\ Size_1} + \frac{Variance_2}{Sample\ Size_2}\right]^2}{\frac{\left[\frac{Variance_1}{Sample\ Size_1}\right]^2}{Sample\ Size_1 - 1} + \frac{\left[\frac{Variance_1}{Sample\ Size_1}\right]^2}{Sample\ Size_2 - 1}} \quad (8\text{-}2)$$

These equations provided a *t* statistic (Equation 8-1) and degree of freedom (Equation 8-2) that could be used on a student's *t*-distribution to determine a level of confidence that the two samples were statistically different. This procedure was repeated for a comparison of all sampling positions during the study series described below.

Chapter 9 Study 1: Mechanical Testing of Ovine Femoral Cartilage

Over the period of this work, several small-scale studies were conducted upon waste animal samples, as they became available. *This study examined the topological difference in mechanical properties in three-year-old sheep.*

9.1 Study Objectives

This was a topological study to measure any discernible differences in mechanical properties of three-year-old sheep cartilage. The study also observed the effects of specimen fixation upon the quality of images.

A total of four sheep were available for the study, giving twelve sample joints. Each joint was sampled with 3mm biopsy specimens taken at the eight sample positions shown in chapter 8.

This mechanical testing, based upon topological studies was assisted by Michael Smith.

9.2 Effect of Paraformaldehyde Fixation on Imaging

Fixing samples in a paraformaldehyde solution is a common technique used to preserve their original structure. Images of fresh samples are contrasted in Figures 9-1, 9-4 and 9-7 with those that have been fixed in paraformaldehyde for periods of two weeks and three months. Three images are presented from each case to highlight the differences in appearance of both collagen fibres and chondrocyte cells. The first set of images was taken from near the surface of the samples where individual fibres were expected (Figures 9-2 and 9-3). The next set came from slightly deeper into the tissue, in the region where bundled fibres were commonly observed in fresh samples (Figures 9-5 and 9-6). The final set shows chondrocyte cells from deep within the specimens (Figures 9-8 and 9-9).

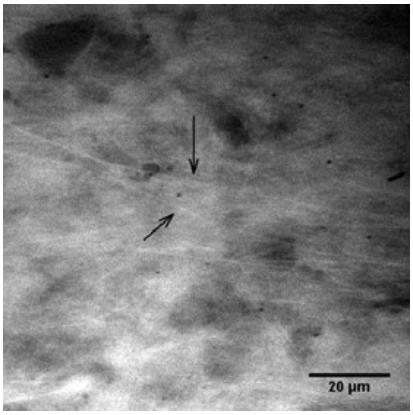

Image 9-1: Fresh individual fibres

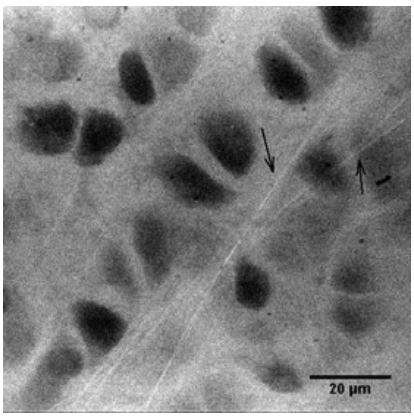

Image 9-2: Two week fixed individual fibres

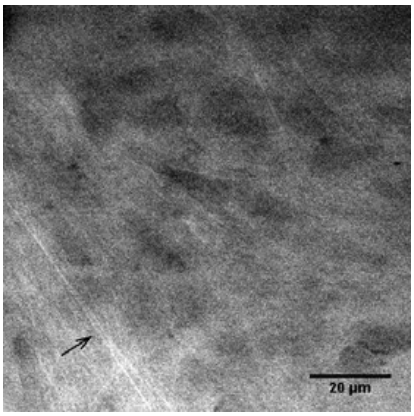

Image 9-3: Three month fixed individual fibres

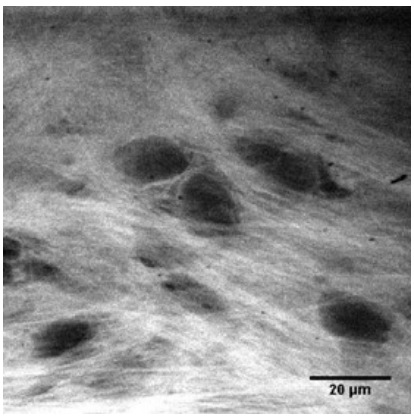

Image 9-4: Fresh bundled fibres

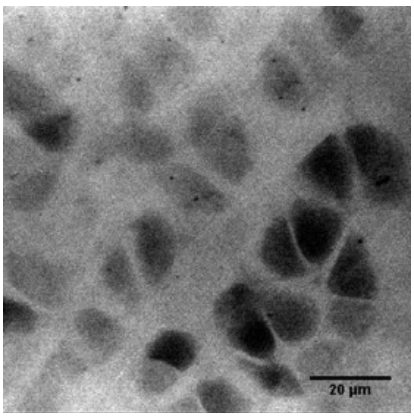

Image 9-5: Two week fixed bundled fibres

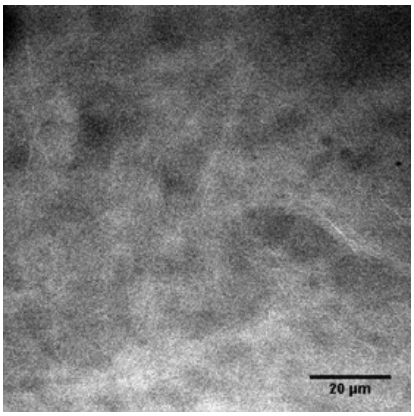

Image 9-6: Three month fixed bundled fibres

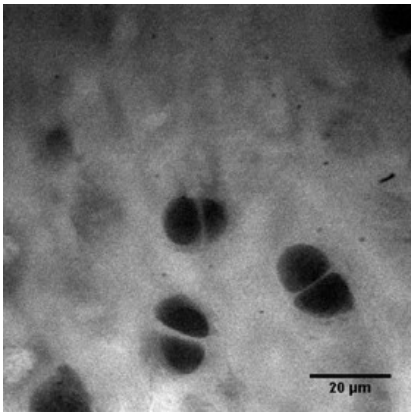

Image 9-7: Fresh chondrocytes

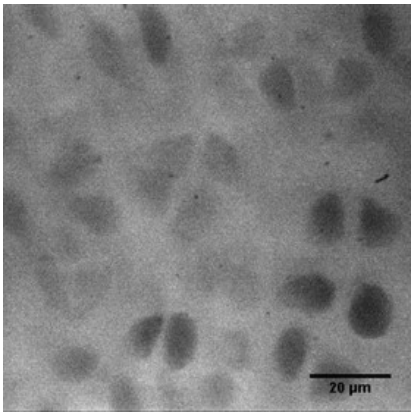

Image 9-8: Two week fixed chondrocytes

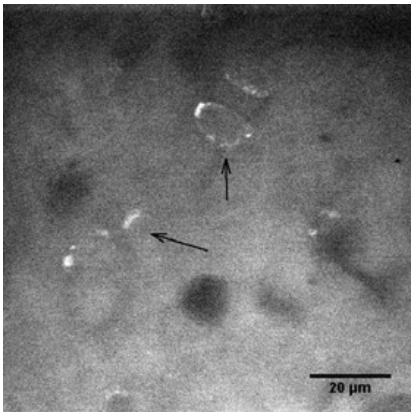

Image 9-9: Three month fixed chondrocytes

The differences between the images were quite noticeable, with respect to both clarity and structure of the cartilage. The three month fixed samples were not very clear and it was hard to identify information regarding their structure. Some individual fibres could be distinguished but no bundled fibres could be observed in regions where they were expected. Chondrocyte cells were still easily identified after three months in paraformaldehyde and there appeared to be an increase in the amount of non-viable cells in comparison to fresh tissue.

Samples fixed for two weeks allowed for quite clear observation of individual fibres. Bundled fibres however, were unable to be seen in most cases. Chondrocytes were easily identified. In comparison to fresh samples, there appeared to be no significant difference in the amounts of non-viable cells.

When evaluating the differences in the images obtained it became quite clear that imaging samples as soon as possible after they have been collected is the preferred option. Images from fresh samples are much clearer and are hence easier to gather information from. If a study required detailed information about collagen fibres to be gathered, then the samples fixed for three months would be useless. Only a few individual fibres could be seen with no bundled fibres observed. The specimens fixed for two weeks gave more information, with images displaying many individual fibres, but only some bundled fibres.

The two-week fixed samples could still be used as a tool for analysing collagen fibres, but the preferred option was to use fresh specimens that display clear collagen structure.

Analysis of chondrocytes is an important area of study due to their ability to synthesise and repair the other components of AC. Specimens having been fixed for three months still displayed a considerable amount of information with respect to the size, density, and viability of chondrocytes. These samples were useful for the purposes of this investigation.

The same behaviour was observed for the specimens fixed for two weeks in paraformaldehyde. The only obvious difference observed was an increase in the amount of non-viable cells with extended fixing time. Therefore, it can be concluded that the samples fixed in paraformaldehyde for a period extending to three months still provide useful information regarding chondrocytes, with the understanding that only the viability of the cells should be affected.

9.3 Ovine Cartilage – Three-Year-Old Sheep

9.3.1 Stiffness Testing in Three-Year-Old Sheep Femoral Head Cartilage

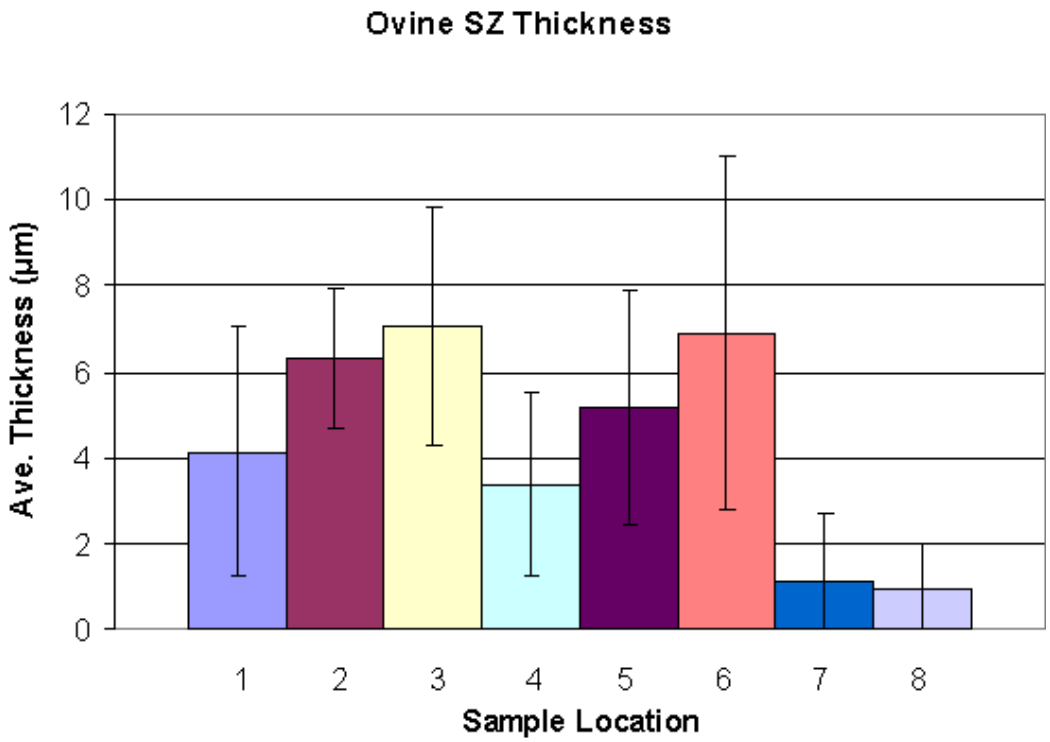

Figure 9-1: Superficial cartilage thickness in three-year-old sheep showing standard deviation

The ovine results (Figure 9-1) displayed similar trends to the porcine specimens found in study 4 with regards to trochlea thickness. The superficial zones of the trochlea samples appeared to be thinner than any of the samples removed from the condyles. This was confirmed on a confidence level of 95%, which for natural tissue that has high variability, demonstrated the strong possibility of this trend was significant. As with pig samples, the trochlea in sheep is predominantly unweighted. Hence, it is plausible that this region did not require as much fibrous layer protection as the condyle regions.

A secondary trend observed from the ovine results was that the thinnest superficial zones on the condyles were observed at the main weight bearing regions. The large standard deviations in the results meant that this observation was only supported at a confidence level of 80%. Although this trend appeared possible, it was not supported strongly by statistical analysis. Relative small sample size, difficulty in obtaining exact sample positions and the highly variable nature of biological tissue could have caused statistical errors to occur.

Study 5 found similar trends in prenatal and postnatal sheep; therefore, simply inferring that these traits are due to wear in mature animals cannot be made. It is much more likely to be due to a combination of genetic factors as well as degradation of the tissue. Further study involving specimens of various ages is required to establish a better understanding of this issue.

A relationship between superficial zone depth and comparative weight bearing was investigated for ovine specimens. Similarly, to pig samples, the sheep samples displayed counterintuitive trends with regards to this relationship. The trochlea had the thinnest superficial zones but on the condyles the predominant weight bearing regions appeared to have thinner surface layers than those found on less weight bearing areas. Therefore, a conclusive relationship could not be formed, indicating that more study is required to understand the complex nature of AC and its uppermost layer.

9.3.2 Comparison of Ovine and Porcine LSCM Results

The results obtained from LSCM for ovine and porcine specimens contained interesting information. The trends viewed for superficial zone depth were quite similar across both species with the thinnest surface layers being found on the trochlea. With respect to the medial and lateral condyles, the two species also appeared to show thinner superficial zones on the predominant weight bearing regions. The major differences surrounded the clarity and type of collagen observed and the relative size difference of the superficial zones. Porcine specimens in study 2 showed clear collagen fibres in most images obtained from their condyles. In comparison, the ovine samples showed virtually no visible collagen fibres. Although the trends relating to superficial zone thickness were similar for both species, the comparative magnitude of these numbers indicated that the porcine specimens typically had thicker superficial zones for corresponding regions on their condyles.

The two sample groups come from different species and this would normally be the main variable identified with the differences seen in structure and depth of the fibrous layer. However, this is unlikely to be the only major factor in understanding the variations between the two specimen groups.

When comparing data from study 5 it was found that type I and III collagen fibres could be distinguished in early maturing sheep with the thickness of this collagen being larger than that seen in the mature ovine specimens in this study. Therefore, the difference in ages of the specimens could be an equally important reason for the observed variations between the ovine and porcine results.

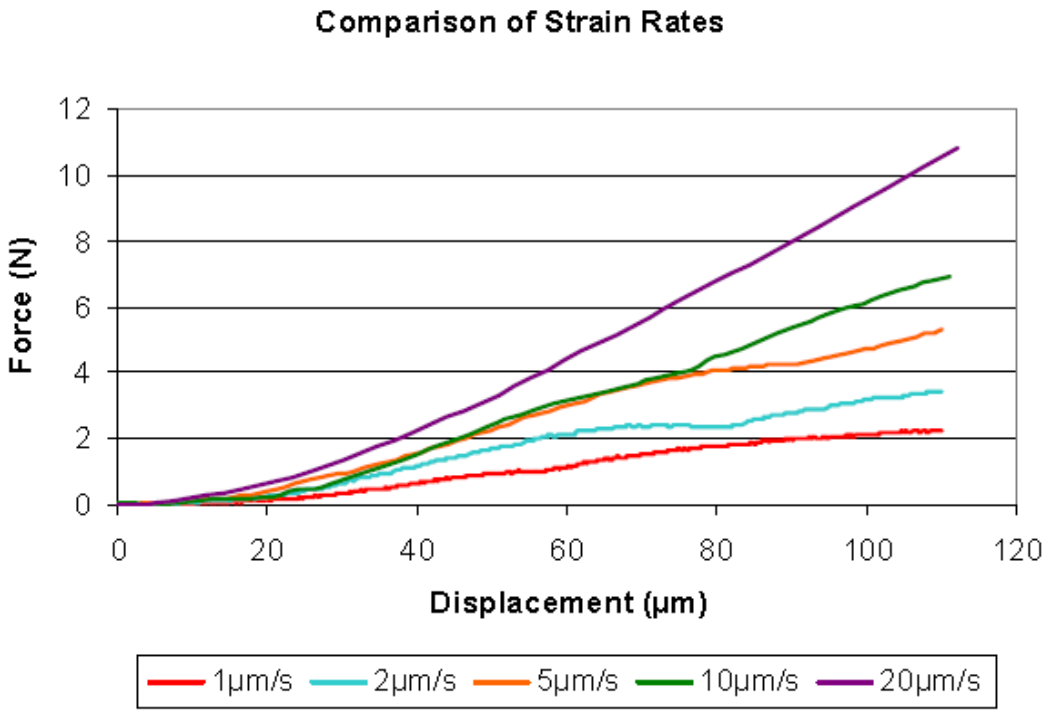

Figure 9-2: Force-displacement of porcine cartilage at various strain rates

The results seemed to confirm the depth dependent nature of the stiffness properties of AC. Early deformation of the tissue typically brought a quadratic style relationship with force before a more linear response was viewed as the compression neared 15%. Some curves did display regions that were unexpectedly flat or negative in gradient (particularly seen on the smaller strain rates). Varying the strain rate, at which the tissue was compressed, produced pronounced differences in stiffness response of the samples. Increasing the strain rate appeared to result in the tissue absorbing a greater force for the same displacement. This response seems to agree with the notion that AC is a material with viscoelastic properties.

The depth dependent response of the samples can be explained by the way the AC initially compresses primarily in the upper layers of the tissue, resulting in a non-uniform strain field (Guilak et al., 1995). The tissue closer to the surface absorbs initial, smaller forces before the deeper layers of AC compress with larger loads.

The unexpected flat regions of the curves could be due to relaxation in the tissue. Another possibility is that repeated compressions permanently damaged the samples.

Proteoglycans combine with collagen fibres to provide the resistance to compression within AC (Mow et al., 2005). Therefore, the nature of proteoglycan movement within AC provides an understanding as to why strain rate is an important factor for articular cartilage's mechanical properties. Proteoglycan flow through the network of collagen fibres, is not only restricted by the fibres themselves but also by the viscous drag created in the extra cellular matrix fluid (Mow et al., 2005). By performing compression in a decreased amount of time (i.e. greater strain rate), proteoglycans have less time to flow through the network of collagen fibres and equilibrate strain in the tissue.

9.3.3 Stiffness Variation

Calculating the gradient of the linear component from Figure 9-2 allows for a comparison of stiffness due to strain rate. Figure 9-3 shows that there was a relationship between stiffness and strain rate that appeared to be quite linear for the range of compression rates used in this study. The results highlight the viscoelastic nature of AC under these conditions, with a dependence on strain rates being observed. As the strain rate is lowered the proteoglycans have more time to flow and equilibrate the tissue. This should eventually reach a point where the response seen is purely from equilibrated samples, hence allowing an equilibrium stiffness to be equated.

Differences in stiffness were observed between all tested rates of compression. Therefore, to gain a greater insight into the mechanical properties of AC, samples should be tested over a wider range of strain rates (i.e. below 1μm/s and above 20μm/s) to observe when the tissue's stiffness becomes independent of rate of compression. This could not be achieved in this particular study due to restrictions based on current testing rig capability and sample availability.

Accurately identifying the response of AC to varying strain rates was an important way of detecting early signs of osteoarthritis. A comparison of arthritic tissue samples against healthy specimens may discover key differences in the way they respond to various rates of compression.

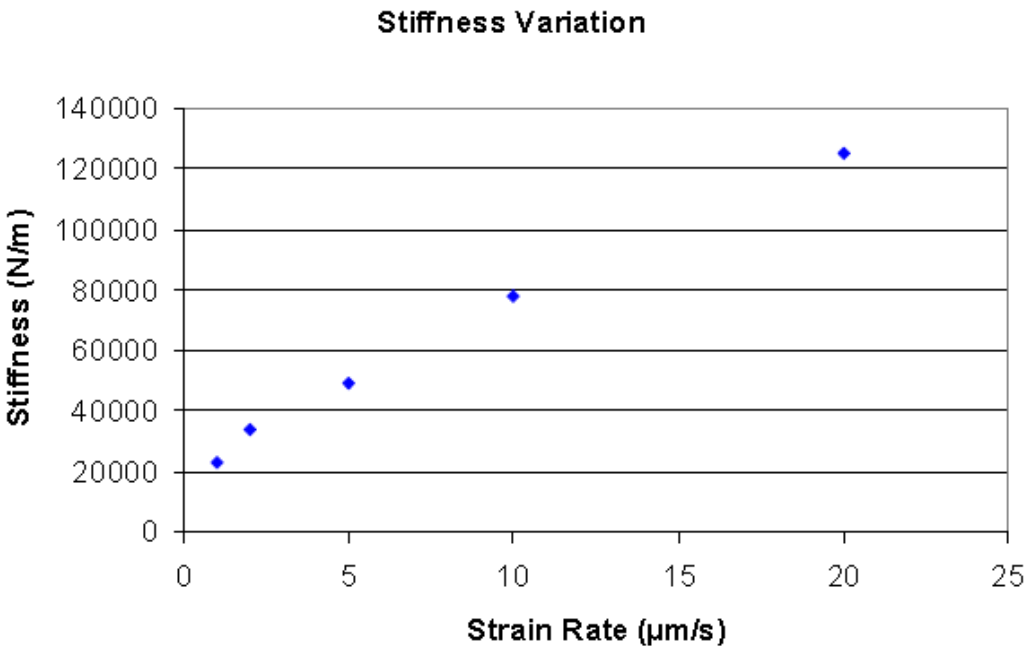

Figure 9-3: Calculated stiffness for porcine cartilage at various strain rates

9.3.4 Tangential Stiffness

The behaviour of AC under compression is dependent on strain rate. To comprehensively compare the stiffness of various AC samples this variable must be considered and analysed. However, with the limited number of samples and time available in this study, not all specimens could be tested at different strain rates. It was therefore chosen to test all porcine and ovine samples at one single strain rate (10µm/s) and compare the tangential stiffness calculated in the linear zone of each stress-strain curve. This calculated value is by no means a comprehensive indicator of the stiffness properties of the tissue however it is a good measure for a simplified topographical comparison (Figure 9-4).

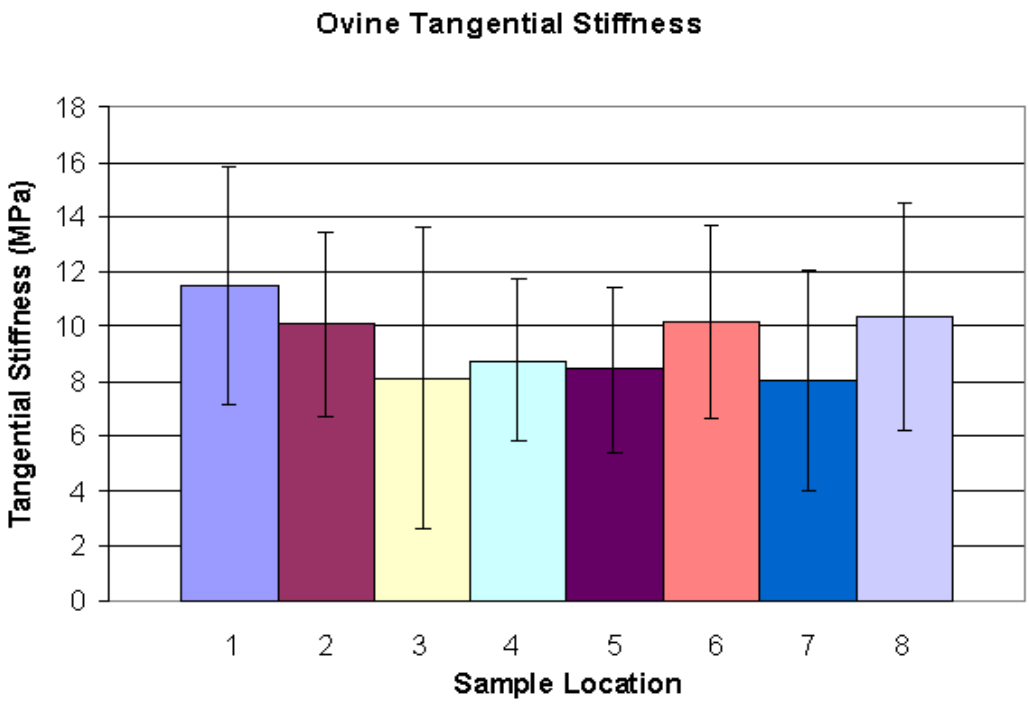

Figure 9-4: Topological variation showing standard deviation in calculated tangential stiffness for ovine cartilage.

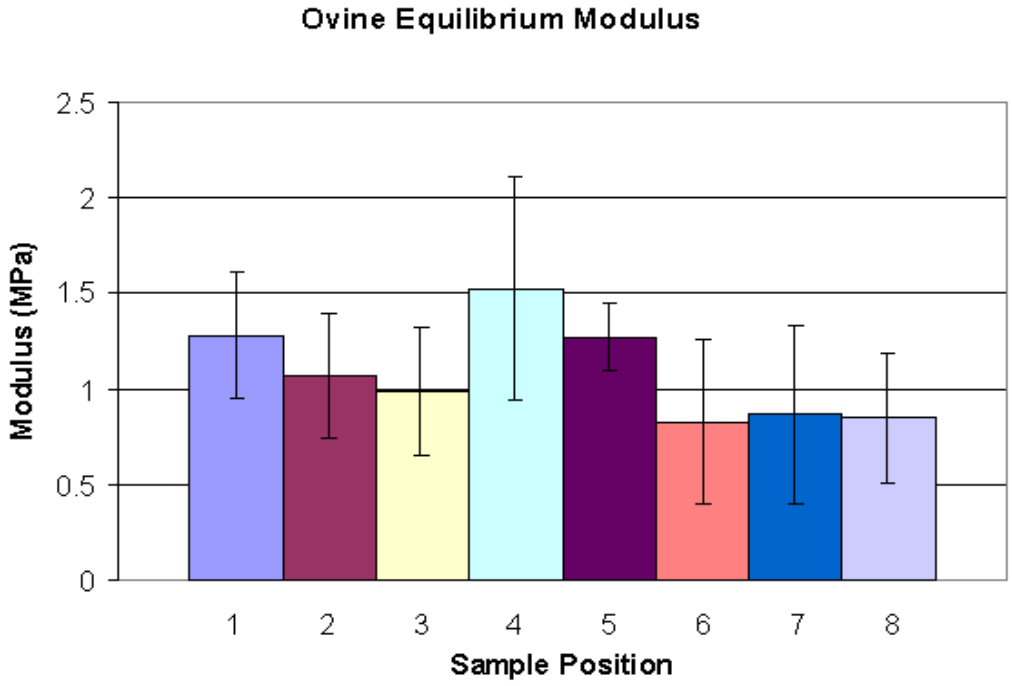

Figure 9-5: Calculated equilibrium modulus for ovine samples showing standard deviation in measurement

Unlike their results for tangential stiffness (Figure 9-4), there did appear to be a trend relating topographical location and equilibrium modulus for the ovine specimens (Figure 9-5). The three highest average recorded values occurred at weight-bearing zones while the less loaded regions of positions 6, 7 and 8 had the lowest equilibrium moduli. Comparing all sample positions, a relationship between relative weight bearing and equilibrium modulus was confirmed at a confidence level of 85%.

The expectation of greater equilibrium modulus per larger anatomical weight bearing was viewed as a trend in the results although the confidence level achieved indicates that this inferred relationship for mature sheep needs further testing. The reasons for a stronger relationship not being displayed could be due to the small sample size combined with errors in sample preparation.

Interestingly, there was no apparent relationship for ovine samples for their tangential stiffness but there was one indicated for their equilibrium moduli. Equilibrium relaxation modulus is only measured after an extended period whereas the tangential stiffness was tested in just a few seconds. The extended relaxation time allows the tissue to display its mechanical properties more adequately.

9.3.5 Comparison of Ovine and Porcine Results

Both species displayed similar topographical trends with regards to equilibrium modulus although the porcine specimens showed a statistically stronger relationship. With respect to the magnitude of the relaxation modulus, the two species consistently displayed similar values. As with the results from study 4, this observation would be accounted for by the difference in age and species of the samples.

9.4 Imaging of Young Sheep Femoral Condyle Cartilage

Table 9-1: LSCM findings for sheep over a range of sites and ages (see chapter 8)

Sample Site	123-124 Days Gestation	129-130 Days Gestation	140 Days Gestation	7 Weeks Postnatal
PLC	• Highly cellular • Type I collagen • Viable cells at depth	• Fine type I Collagen • Viable cells at depth	• Fine type I Collagen • Lamina splendens thickness decreased • Viable cells at depth	• Thin layer of type I collagen • Viable cells at depth
CLC	• Interwoven type I collagen • Dense type III collagen bands at depths	• Type I collagen • No type III Collagen • Viable cells at depth	• Thin layer of type I collagen	• Thin layer of type I collagen • Cells becoming nonviable at depth
ALC	• Some type I collagen visible • Thick mats of type III collagen throughout	• Type I collagen still visible • Dense bands of type III collagen • Viable cells at depth	• Fine type I collagen throughout • Bands of type III collagen visible • Viable cells at depth	• samples showed type III collagen bands of collagen • Viable cells at depth
PMC	• Nonviable cells at the surface • Few collagen fibres • Viable cells at depth	• Nonviable cells at surface • Few collagen fibres • Viable cells at depth	• Sparse nonviable cells at surface • Viable cells at depth	• Sparse nonviable cells at surface • Viable cells at depth

Sample Site	123-124 Days Gestation	129-130 Days Gestation	140 Days Gestation	7 Weeks Postnatal
CMC	• Nonviable cells at the surface • Type III collagen • Few fibres • Banded fibres	• Type I collagen • Type III collagen no longer visible • Viable cells at depth	• Relatively thick layer of type I collagen • No type III collagen • Viable cells at depth	• Nonviable cells at the surface • Very few fibres in the lamina Splendens • Resembles the PMC • Viable cells at depth
AMC	• Numerous type I collagen fibres throughout • Occasional type III collagen • Viable cells at depth	• Few type I and type III collagen fibres • Nonviable cells at surface • Viable cells at depth	• Few type I collagen fibres • Nonviable cells at surface • Viable cells at depth	• Thin layer of type I collagen fibres • Viable cells at depth

Chapter 10 Study 2: Topological Differences Transversely Over Porcine Condyles

Study of topological variation in pig cartilage.

10.1 Study Objectives

This was a topological study to measure any discernible differences in mechanical properties of young porcine cartilage. The study also observed that the effects of specimen fixation upon the quality of images. The measurements taken for this study was assisted by undergraduate student Tom Ferguson.

A study was conducted to assess the collagen structure as it related to the loaded and unloaded regions of femoral condyles of pigs. This study assessed cartilage samples from different regions of the condyle to see what effect loading had upon the fibre growth. Ink split line studies were conducted upon the condyles to look for fibre structure visible over the loaded regions. In general, the porcine samples were fresh and gave better LSCM images than frozen ovine samples. This study formed the protocols for both imaging and storage of cartilage samples.

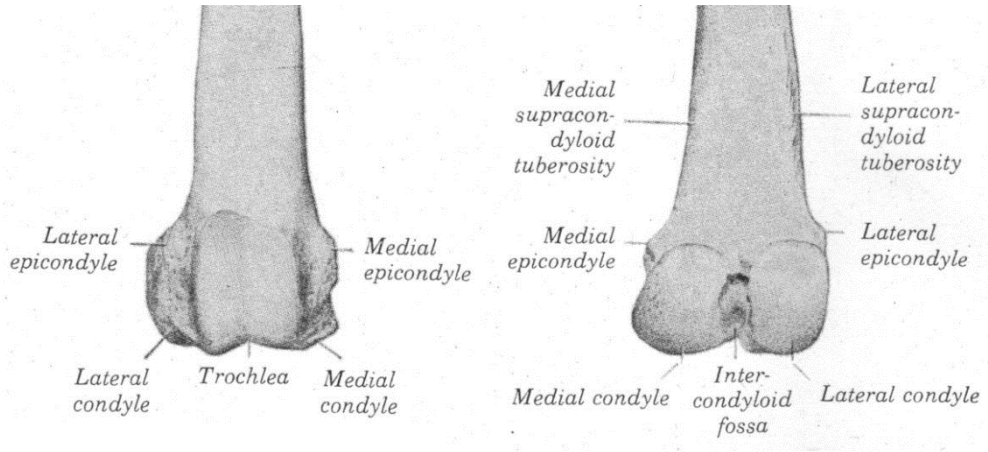

Figure 10-1: The distal extremity of the porcine (pig) femur (adapted from Sisson 1953)

The distal extremity of a porcine (pig) femur is shown below in Figure 10-1. The condyles sit on the tibial plateau and transmit the weight of the animal, while the trochlea forms a groove in which the patella, or kneecap, sides. Six porcine knee joints were sourced from the waste material from pigs slaughtered for unrelated experiments at the UWA Large Animal Facility. The pigs were between 8 and 12 weeks old and the knee joints were obtained an hour after slaughter.

10.2 Split Line Patterns and Sample Areas

After the distal extremity of the femur was removed from the knee joint, a split line pattern test was performed. A sewing needle of 1mm diameter was dipped in Indian ink. It was then inserted into the cartilage at an angle perpendicular to the articular surface to the depth of the subchondral bone. This was repeated in a regular array over the entire articular surface. When the array was complete, excess ink was removed from the cartilage surface by rinsing with distilled water.

The degree to which the collagen structure can be characterised over the articular surface is proportional to the number of samples taken across the surface. However, when removing a sample of cartilage from the joint, a significant amount of the surrounding area was also removed. It was also unavoidable that the surrounding area would be damaged.

Therefore, there was a physical limitation on the number of samples that could be obtained from each joint. Also, staining and imaging each sample was a time-consuming procedure. To satisfy these opposing constraints, the sampling system described below was decided upon as it allowed most, if not all, samples to be removed without damaging adjacent sample sites while still allowing the collagen structure to be characterised accurately.

Both the lateral and medial condyles were divided into nine sample areas, arranged in a three by three grid. The trochlea was divided into twelve areas, arranged in a three by four grid. Each sample site was given a unique numerical designation, as shown below in Figure 10-2, which will be used in the results section to describe which area that these results were obtained from. It is also useful, for further discussion, to define the front, back and centre line of the joint, as shown below. It should be noted that the same numerical designations were used for both left and right knee joints. Therefore, for a specific specimen, sample areas 1 to 9 could correspond to either a medial or lateral condyle, depending on whether the specimen was from a left or right knee joint.

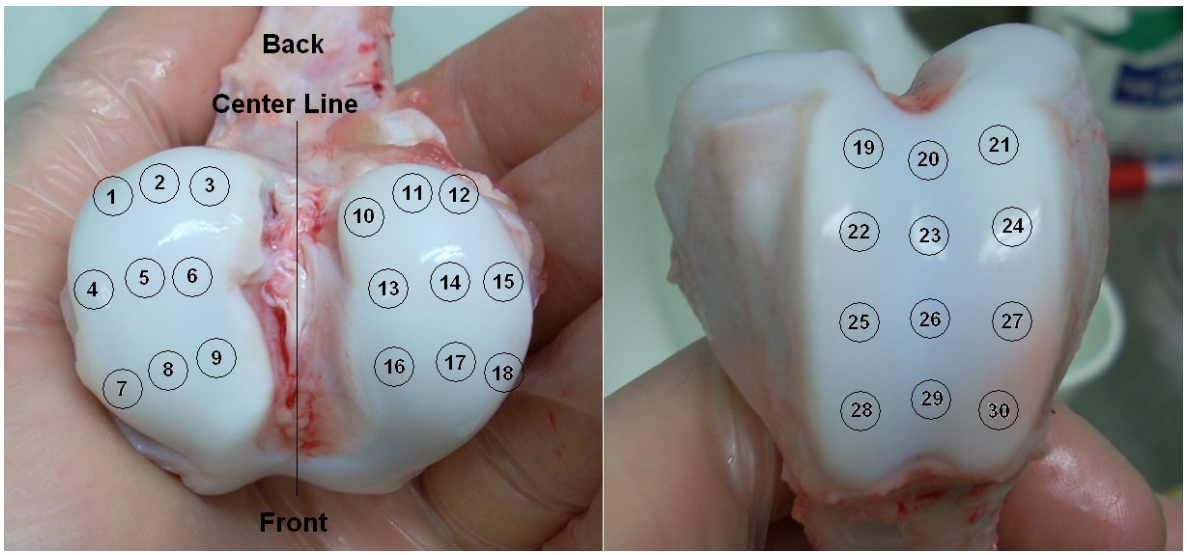

Figure 10-2: Sample areas and their numerical designations

Samples were taken from all the sites on the lateral and medial condyles (sample areas 1 to 18) in Figure 10-2. In comparison, only a representative selection of the sample areas on the trochlea was sought (sample areas 19 to 30) in Figure 10-2. The samples were stained by immersing them in a solution of 0.5g/L of FITC in distilled water for a period of three minutes before briefly being rinsed in saline solution.

10.3 Split Line Patterns

Split line patterns are a traditional technique used to visualise the predominant orientation of the collagen fibres in the superficial layer of articular cartilage. A summary of the results of these tests is shown in Figures 10-3 and 10-4.

Figure 10-3: The split line patterns created over four of the porcine femoral condyles

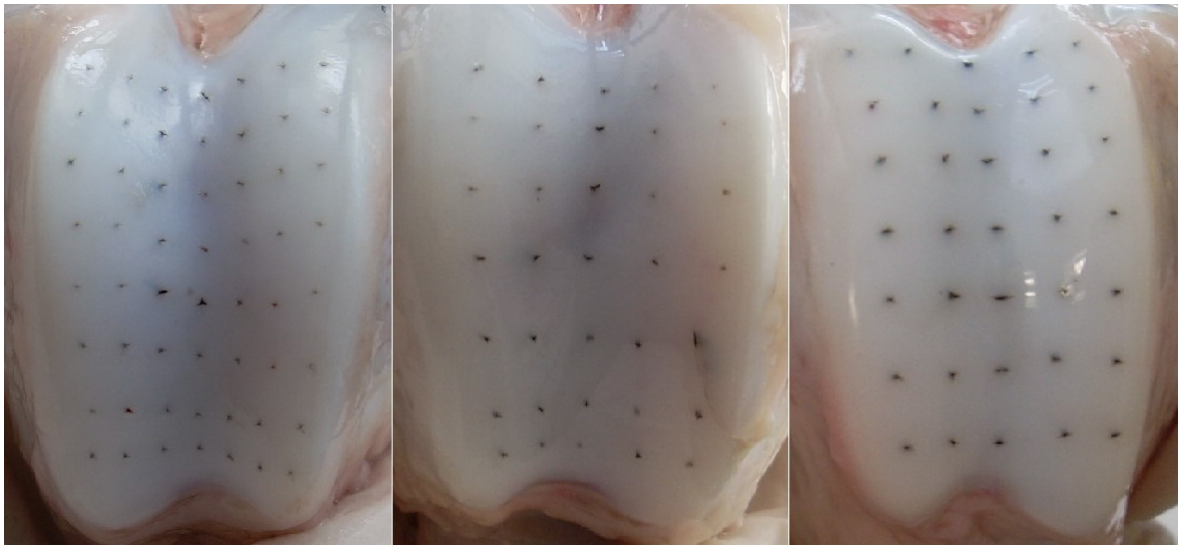

Figure 10-4: The split line pattern created over three of the porcine trochleae

In general, the porcine specimens did not produce strong split line patterns, with the cartilage usually showing little or no tendency to split in a particular direction. This ink split line behaviour showed that the collagen fibres were not strongly aligned in a particular direction.

Individual specimens did occasionally have regions that showed a strong tendency to split in a particular direction, such as the middle of the trochlea pictured on the right in Figure 10.4. However, the location of these regions, and the split line pattern in them, varied from specimen to specimen. Therefore, there was no observed systematic topographical relationship between specimens.

10.4 Topographical Differences in Collagen Structure

The fibrous collagen components of articular cartilage and the ground substance in which it is embedded in have similar refractive indexes and little pigmentation. Fluorescein Isothiocyanate was used as a stain to differentiate the collagen from the surrounding material. Re-usable putty was used between the cover slip and slide to hold the cover slip in place so that the oil immersion lens contacted the cover slip in an oil film to image the cartilage.

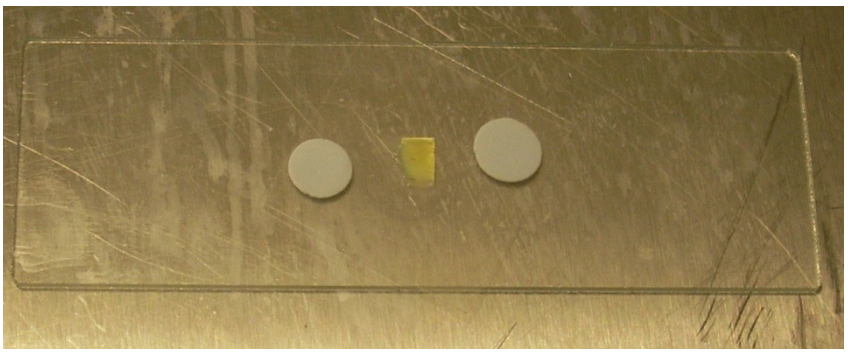

Figure 10-5: Method for mounting the cartilage for imaging

10.4.1 Femoral Condyle

Images 10-1 to 10-3 summarise the results obtained from the lateral condyle of a left knee joint from one of the porcine specimens. Therefore, the images down the right-hand side are from areas most distant from the centre line of the joint as well as most distant from the centre line of the animal. The images in Figure 10-5 correspond to sample sites towards the back of the condyle, and thus the images in Image 10-3 correspond to sample sites towards the front of the condyle. The images are representative of those collected. Raw images from all samples are available as stored data sets.

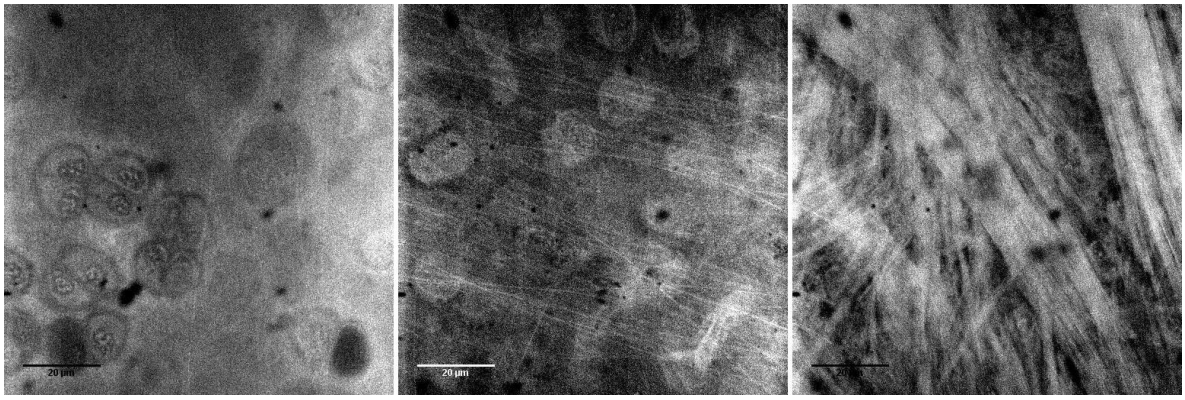

Image 10-1: Porcine specimen 1 collagen distribution (left image: sample area 10, centre image: sample area 11, right image: sample area 12)

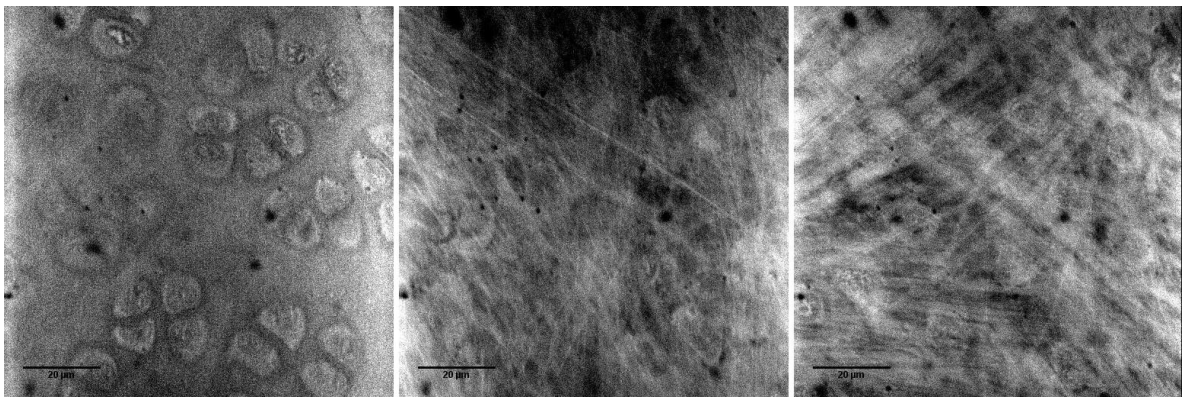

Image 10-2: Porcine specimen 1 collagen distribution (left image: sample area 13, centre image: sample area 14, right image: sample area 15)

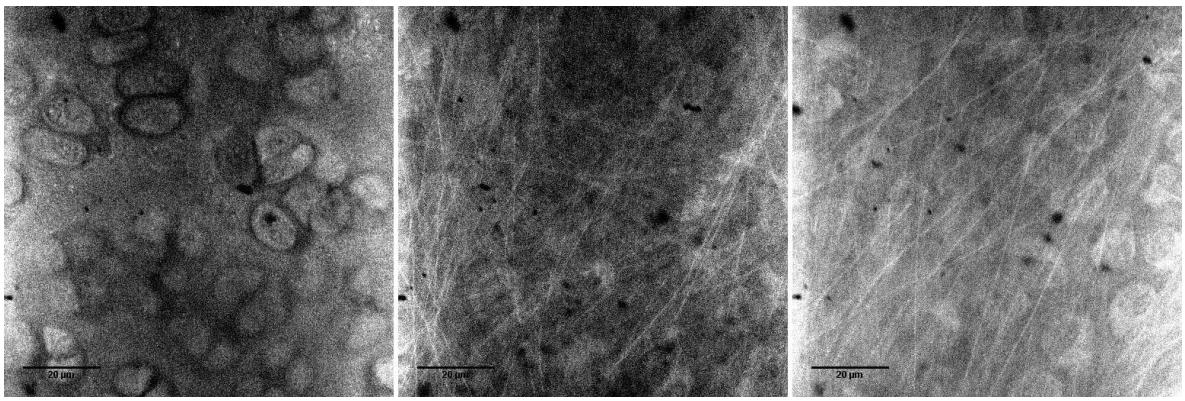

Image 10-3: Porcine specimen 1 collagen distribution (left image: sample area 16, centre image: sample area 17, right image: sample area 18)

Images 10-4 to 10-6 summarise the images obtained from the medial condyle of a right knee joint from another one of the porcine specimens. Therefore, the images down the right-hand side are again from areas most distant from the centre line of the joint. However, since they were taken from a medial condyle, they also correspond to the regions closest to the centre line of the animal. As before, the first row of images (Image 10-4) corresponds to sample sites at the back of the condyle, while the last row of images (Image 10-6) corresponds to sample sites at the font

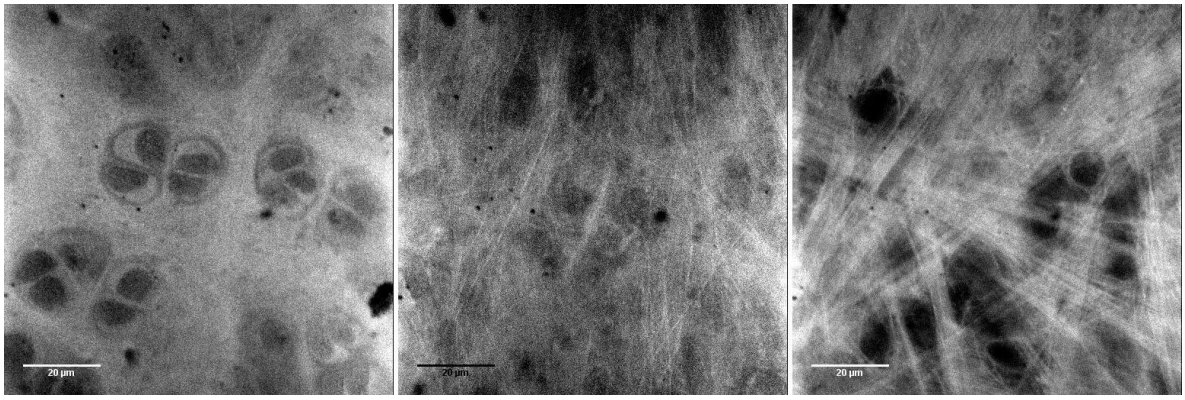

Image 10-4: Porcine specimen 2 collagen distribution (left image: sample area 10, centre image: sample area 11, right image: sample area 12)

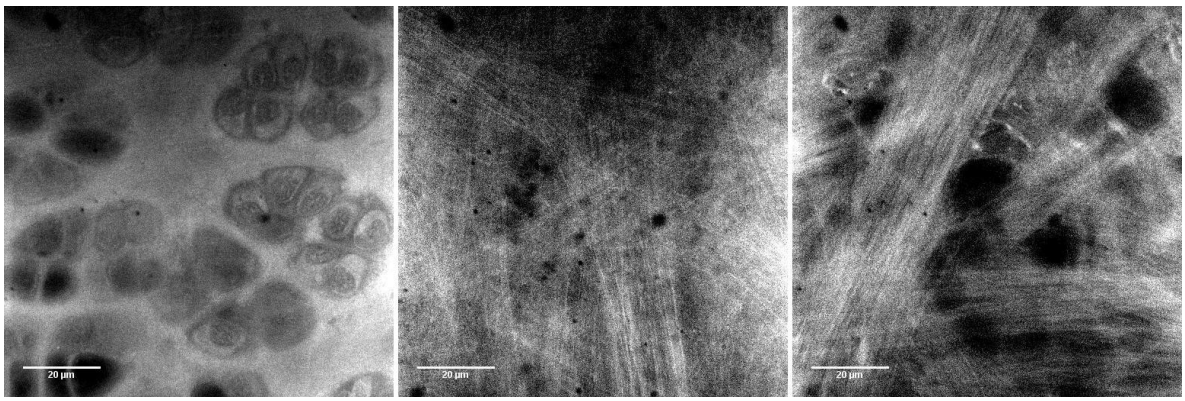

Image 10-5: Porcine specimen 2 collagen distribution (left image: sample area 13, centre image: sample area 14, right image: sample area 15)

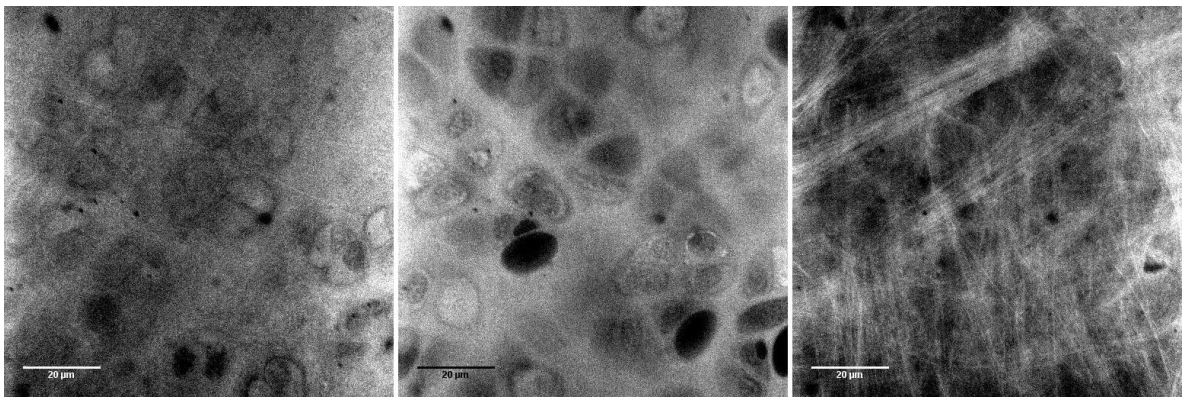

Image 10-6: Porcine specimen 2 collagen distribution (left image: sample area 16, centre image: sample area 17, right image: sample area 18)

From these images, there is a distinct difference in the collagen structure observed at different sample sites:

- Firstly, the collagen fibres tend to be larger, more numerous, and form larger bundles with increasing distance from the centre line of the joint. Typically, there were little or no fibres observed in the three regions adjacent to the centre line of the joint. In contrast, in the three sample areas furthest from the centre line of the joint, large fibres and bundles of fibres were observed. This was observed in all the porcine specimens.
- Secondly, the collagen fibres tend to be larger, more numerous, and form larger bundles with increasing distance from the front of the condyles. This was widely observed throughout the porcine specimens, although not as strongly as the trend described in the previous paragraph, with adjacent sample sites having less radically different structures.

Also, there were exceptions. For example, comparison of the centre images in Images 5.8 and 5.9 shows that the collagen fibres are slightly more numerous and form larger bundles at the centre of the condyle when compared with the back. Nevertheless, this trend was widely observed in the porcine specimens.

It can also be noted that there is no apparent difference in the observed collagen structure of the lateral condyle when compared to the medial condyle. In individual specimens, it was found that, on occasion, sample areas on one condyle appeared to have a different collagen structure than the counterpart on the opposite condyle. This was not systematic however, as it did not consistently correlate with any lateral and medial condyle configuration.

10.4.2 Trochlea

Images 10-7, 10-8, and 10-9 summarise the results obtained about the collagen structure of the trochlea of a specimen obtained from a left porcine knee.

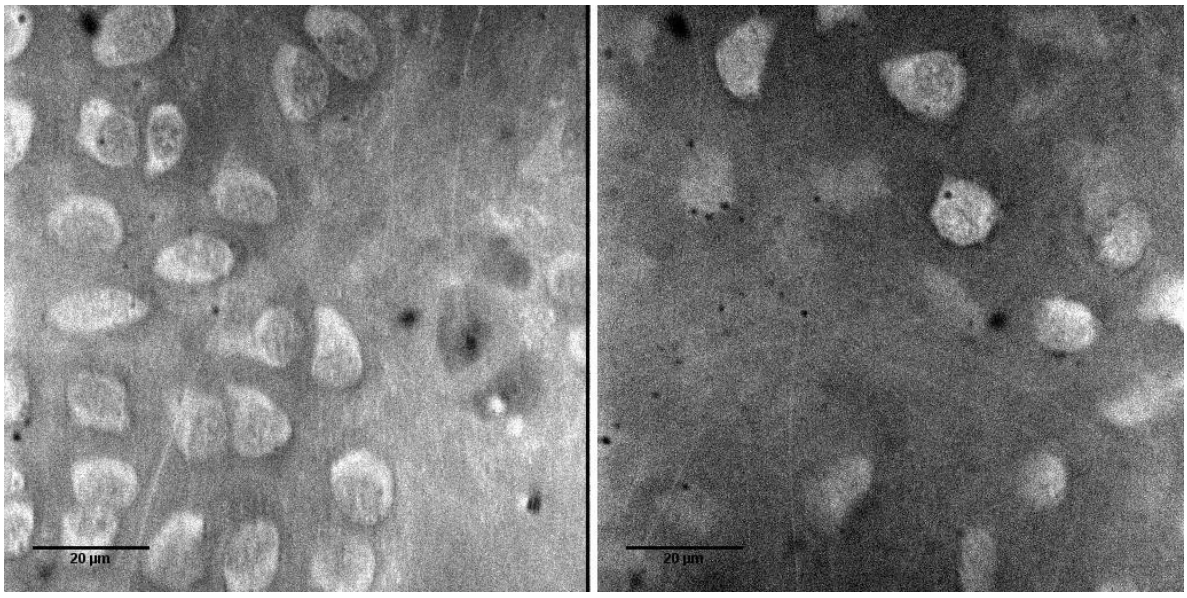

Image 10-7: Collagen structure of a lower sample site on the trochlea of porcine specimen 1 (left image: sample site 19) compared with a higher sample site (right image: sample site 25)

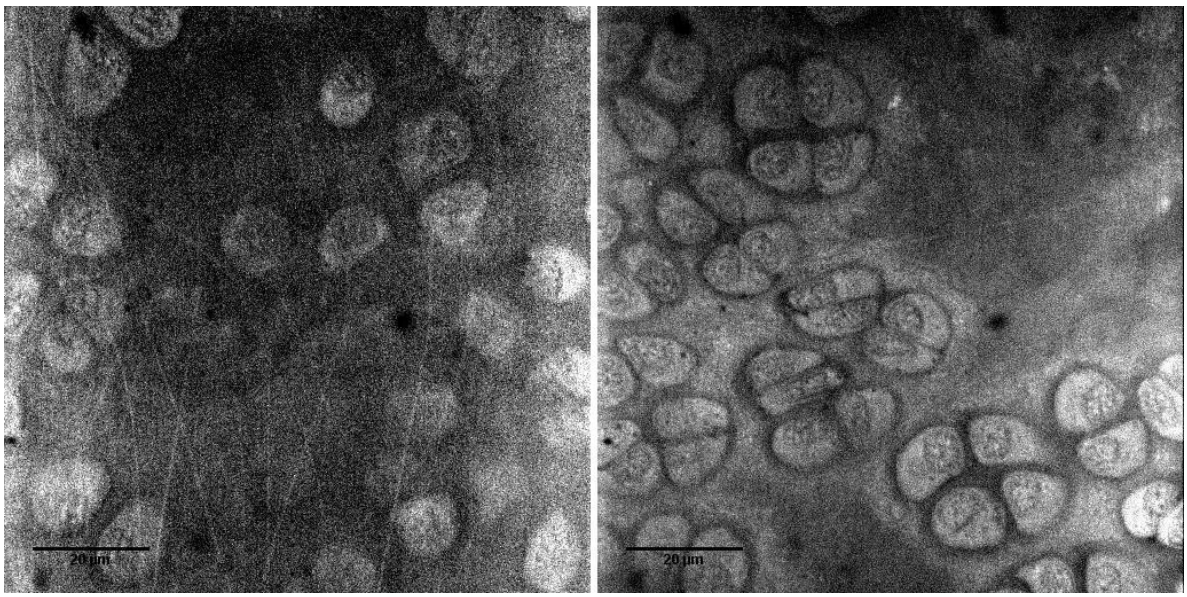

Image 10-8: Collagen structure of a central sample site on the trochlea of porcine specimen 1 (left image: sample site 23) compared with a peripheral sample site (right image: sample site 21)

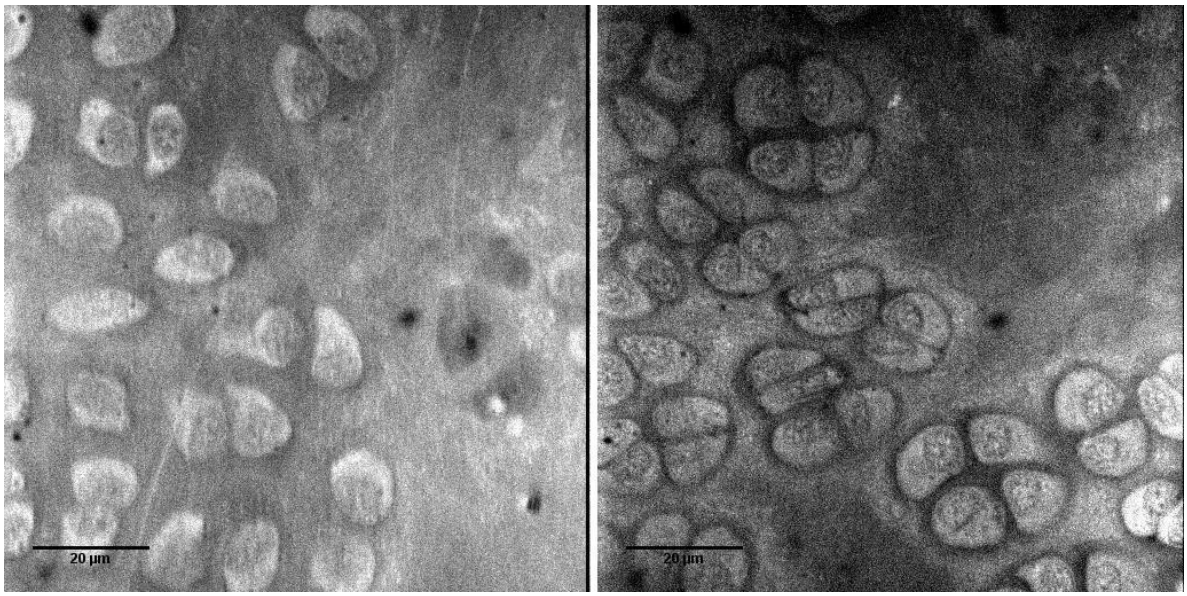

Image 10-9: Collagen structure of a sample site on the left of the trochlea of porcine specimen 1 (left image: sample site 19) compared with a sample site on the right (right image: sample site 21)

Images 10-10, 10-11, and 10-12 summarise the results obtained about the collagen structure of the trochlea of another porcine specimen, this time obtained from a right knee.

The porcine trochlea indicated that there was very little observable collagen structure throughout the whole trochlea. The collagen that was observable did not have a systematic distribution.

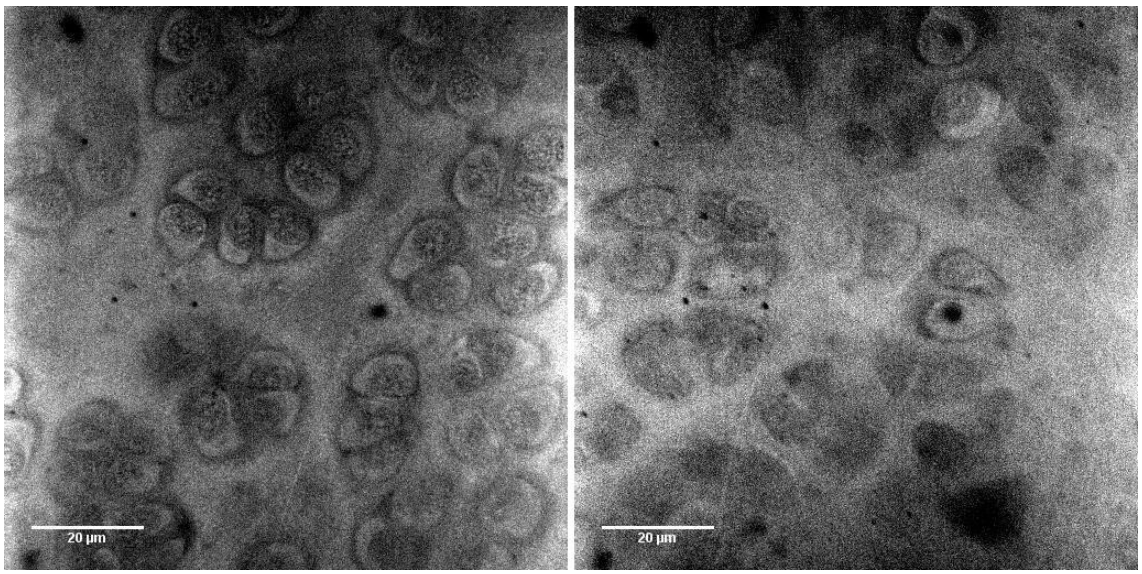

Image 10-10: Collagen structure of a lower sample site on the trochlea of porcine specimen 2 (left image: sample site 19) compared with a higher sample site (right image: sample site 28)

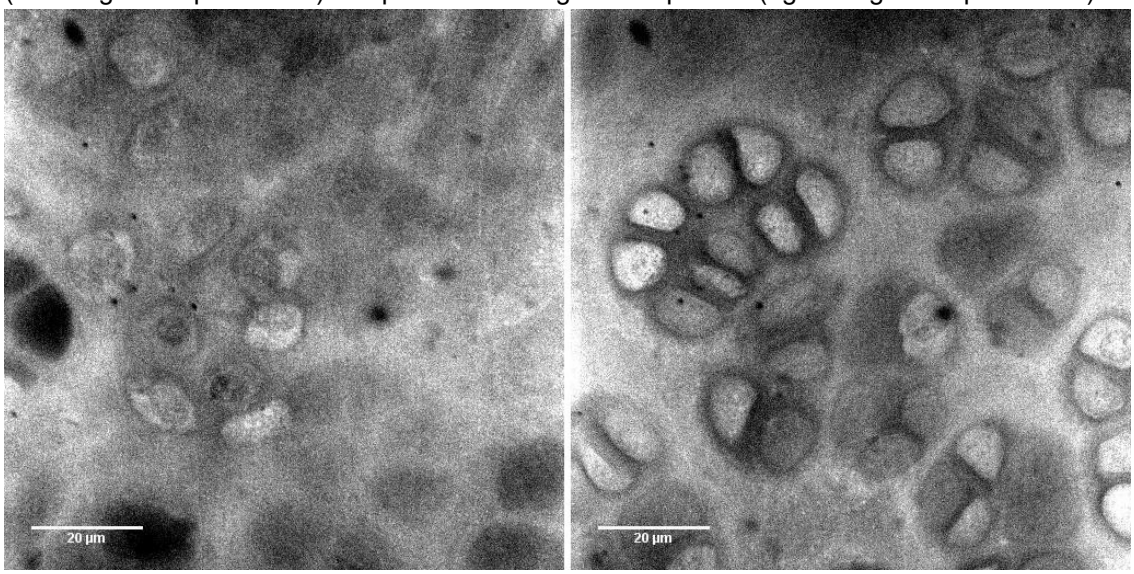

Image 10-11: Collagen structure of a central sample site on the trochlea of porcine specimen 2 (left image: sample site 23) compared with a peripheral sample site (right image: sample site 21)

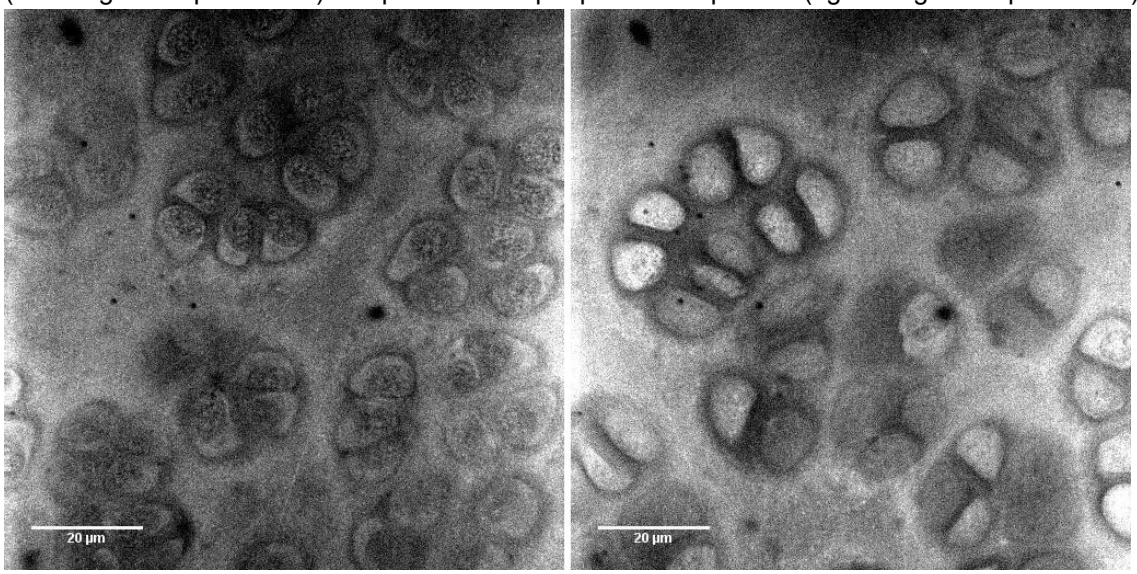

Image 10-12: Collagen structure of a sample site on the left of the trochlea of porcine specimen 2 (left image: sample site 19) compared with a sample site on the right (image: sample site 21)

10.5 Study 2 Findings

This study identified systematic differences in the observable collagen structure throughout the articular cartilage on the distal extremity of the porcine femur. The collagen fibres in the superficial zone of the femoral condyle tended to extend deeper and be more numerous, larger, and form larger bundles in regions towards the back of the femoral condyle and further away from the centre line of the joint. The trochlea was found to have little or no observable collagen fibres or systematic distribution.

The lack of systematic orientation of the collagen fibres in the superficial zone observable through visual inspection of the confocal images was confirmed with split line pattern tests. There were small regions of the split line pattern tests that indicated a predominant orientation, which was not observed in the corresponding confocal images. Likewise, some confocal images appeared to show a strong predominant orientation not detected in the corresponding split line patterns for those areas.

Chapter 11 Study 3: Topological Differences in Ovine Cartilage Samples

11.1 Study Objectives

This was a topological study to measure any discernible differences in mechanical properties of three-year old sheep cartilage. The study also observed the effects of specimen fixation upon the quality of images.

In this study 24 sheep joints were examined using the mechanical test rig to measure mechanical properties of the cartilage and under the LSCM to observe the fibre development from three sample groups: 124-day gestation, 128-day gestation and three-year old sheep. The measurements made in this study was assisted by an undergraduate student Alex Hayes. The sample sites locations are shown in Table 11-1. .

Table 11-1: Sample sites

Site Label	Anatomical Description
PMC	Posterior Medial Condyle
AMC	Anterior Medial Condyle
PLC	Posterior Lateral Condyle
ALC	Anterior Lateral Condyle
MT	Media Trochlea
LT	Lateral Trochlea

11.2 Superficial Zone Layer Thickness

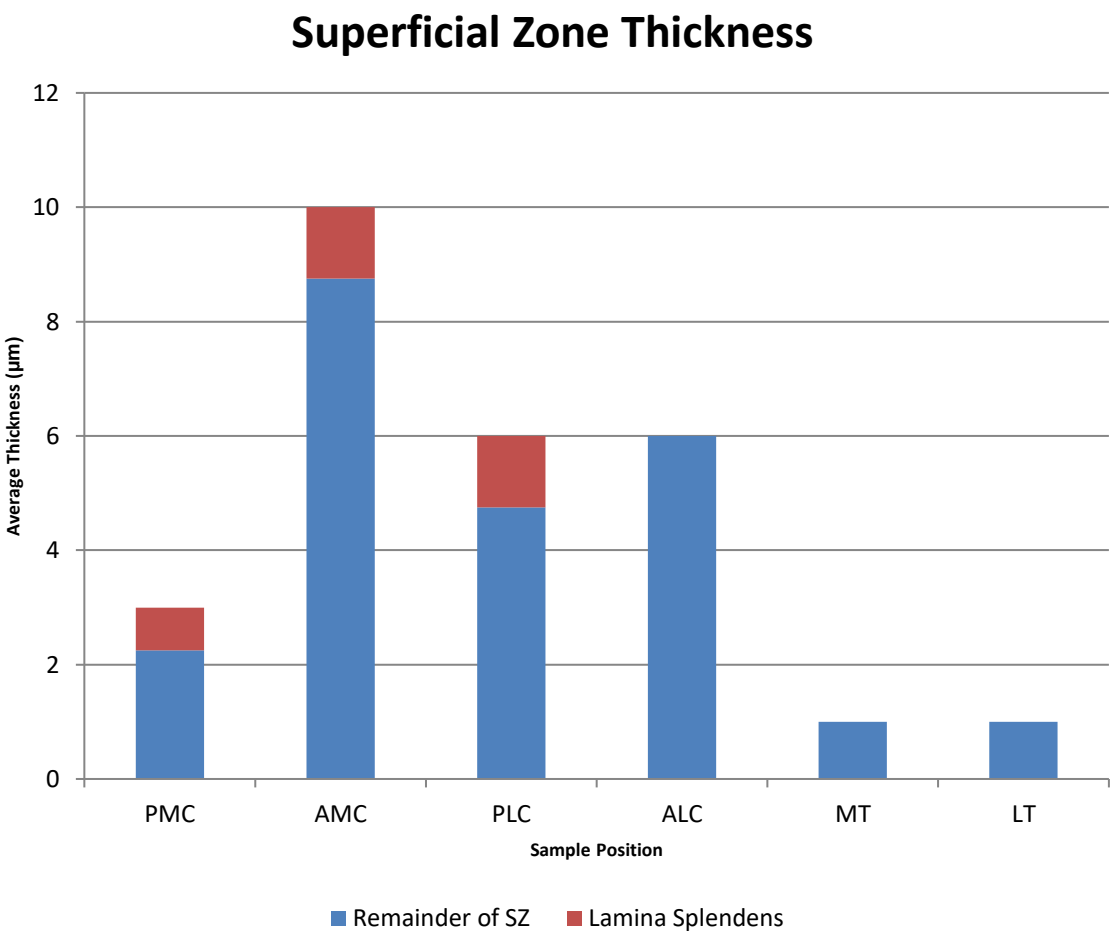

Figure 11-1: Thickness of Lamina Splendens and Superficial Zone in mature ovine samples

Based on the observations discussed above, the structural composition of the superficial zone was estimated in Figure 11-1. Each bar represents the average observable thickness of the superficial zone, with the top portion representing the thickness comprised by the lamina splendens.

It can be inferred that the thickness of the superficial zone appears to be influence by the physiological loading conditions encountered. Higher load bearing regions such as the PMC and PLC have a thinner superficial zone, while the low load bearing regions, such as the AMC and ALC, have a thicker superficial zone. In contrast, the non-load bearing regions had very thin superficial zones and little visible lamina splendens.

The PMC, AMC and PLC had very thin lamina splendens present on the surface. It was unclear whether they existed on the AMC. It has previously been reported that the lamina splendens in human cartilage is 4-8μm thick (Teshima *et al*., 1995).

11.3 Topographical Comparison of Samples

The confocal observations from the images have been summarised in Table 11-2. Images from this study have been archived as there were too many to present in printed form. However, the images are typical of those displayed in study 3.

Table 11-2: Observations of average ovine cartilage structure

	124 Days	128/129 Days	Mature
PMC	• Few type I • Rare type III • Chondrocyte density increasing with depth	• Few type I • Rare type III • Chondrocyte density lower	• No visible fibres • Lamina splendens present • Classical chondrocyte structure
AMC	• Type 1 fibres at surface • Some type III • Chondrocyte density increasing with depth	• Type 1 fibres at surface • Some type III • Chondrocyte density increasing with depth	• No visible fibres • Lamina splendens present • Classical chondrocyte structure
MT	• Few fibres present • Fibre type difficult to determine • Chondrocyte density constant	• Few fibres present • Fibre type difficult to determine • Chondrocyte density constant	• No visible fibres • Constant chondrocyte density

	124 Days	128/129 Days	Mature
PLC	• Anomalous layer at surface • Chondrocyte density increasing with depth	• Anomalous layer at surface • Chondrocyte density increasing with depth	• No visible fibres • Lamina splendens present • Classical chondrocyte structure • Collagen II fibres abundant
ALC	• Interwoven type I fibres • Some type III • Viable chondrocytes increasing with depth	• Interwoven type I fibres • Some type III • Viable chondrocytes increasing with depth	• No visible fibres • Viable chondrocytes at depth • Collagen II fibres abundant
LT	• Few fibres present • Fibre type difficult to determine • Chondrocyte density constant	• Few fibres present • Fibre type difficult to determine • Chondrocyte density constant	• No visible fibres • Constant chondrocyte density • Collagen II fibres abundant

11.4 Images

The following images represent the structure at the six sample positions at a depth of 0-5µm and 15-20µm for each age group post-analysis. Pre-processing images did not indicate the key observations using a grey scale as the diminished resolution caused the fine collagen fibres to become indistinguishable. A comparison is shown in the presence of the red collagen fibres in the lower right hand corner of the processed image that were previously indistinguishable in the unprocessed image. Arrows on the images identify fine fibres running diagonally through the region, indicating the presence of what can be assumed to be type I collagen. These are still difficult to see in the processed image; however, they are almost undetectable in the unprocessed image, showing the importance of processing to this study.

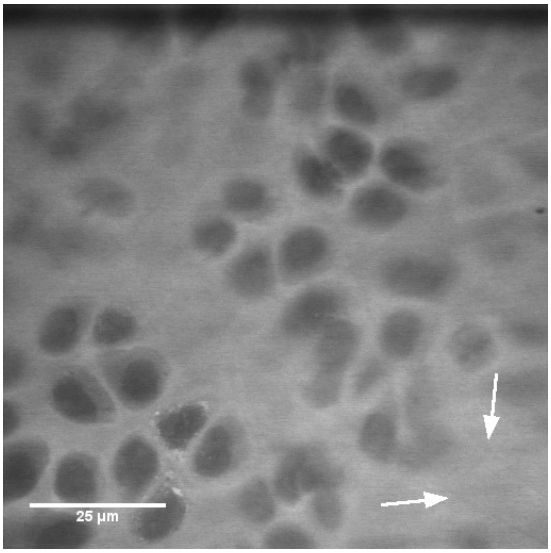

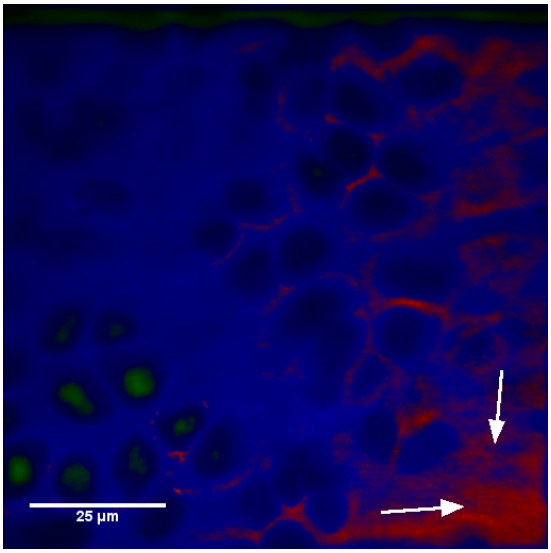

Image 11-1: Image before processing Image 11-2: Image after processing

11.4.1 Posterior Medial Condyle

The posterior medial condyle is one of the premier load bearing regions on the femoral head. This is due to the ovine knee being constantly flexed during passive activities. It is positioned towards the rear of the medial condyle on the inside of the knee. Images 11-3 to 11-8 illustrate the structure of the posterior medial condyle.

Due to the load bearing nature of the PMC, it was assumed that very few type I and type III collagen fibres would be found in the samples, as there is usually an increased density of type II collagen. This is true of mature sheep; however, it was not fully known whether this was the result of mechanical stimuli or biological development.

Collagen fibres were not commonly observed in this region at any age, with only a few type I collagen fibres being observed near the surface in some prenatal samples. Type III collagen was even more difficult to detect, occurring rarely, although this could be attributed to the extended exposure to paraformaldehyde as previously discussed. Similar results were found in studies 5 and 6. No visible fibres were found in the mature samples, which had been previously reported in studies 4 and 5. This can be attributed to the fact that as cartilage matures, the type I and type III fibres are replaced by type II (Yasui and Nimni, 1988). It can therefore be assumed that any collagen fibres present were of type II.

The density of chondrocytes near the surface of samples taken from the 124-day gestation sheep was low, increasing dramatically with depth until the density reached a plateau at 18μm into the sample. In comparison, the size of the cells decreased significantly with depth, starting at approximately 20-25μm in diameter near the surface compared to the 5-10μm encountered at the lower depths. The classical structure of horizontal, elongated sheets of chondrocytes near the surface and spherical, randomly arranged chondrocytes in the middle layer also appears to be developing in the younger sheep. Evidence of mitosis was visible in the chondrocytes seen during the developmental stage of the cartilage. Few non-viable cells were evident, most due also to the developmental stage of the cartilage.

Despite the small age difference between samples, the 128/129-day samples demonstrated a marked difference in chondrocyte structure. Cells near the surface were smaller at 10-15μm and decreasing with depth to 5-10μm. Cell density near the surface had significantly decreased, then increasing slowly until a density of the 124-day gestation sheep was reached at a depth of around 35μm. Chondrocytes in the middle region appeared to resemble those found in the younger sheep. The occurrence of mitosis was still regular and there were few non-viable cells.

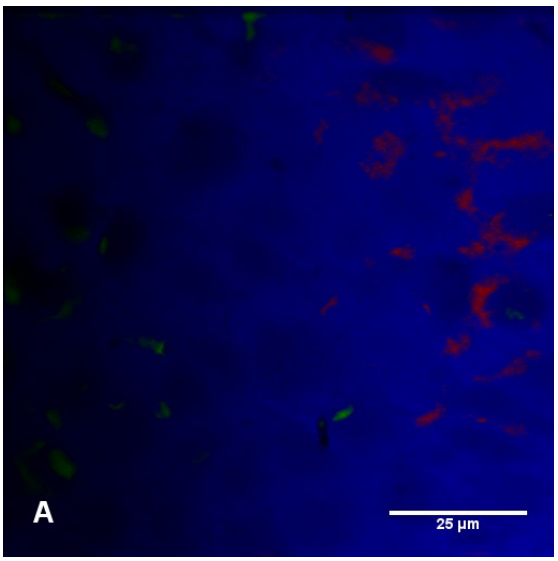

Image 11-3: 124-day gestation sheep – PMC @ 0.5µm below the surface

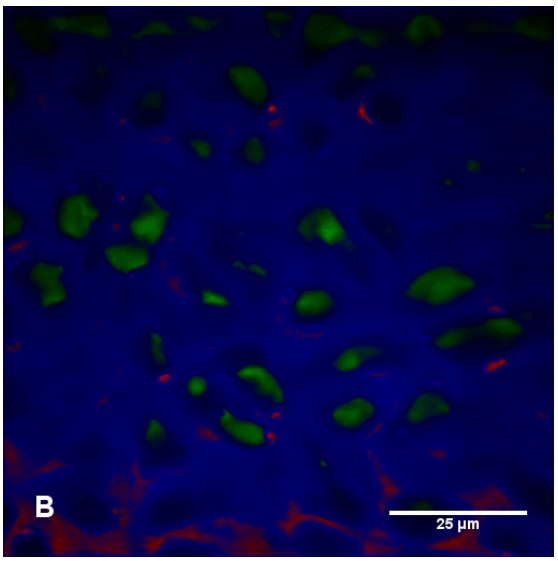

Image 11-4: 124-day gestation sheep – PMC @ 15µm below the surface

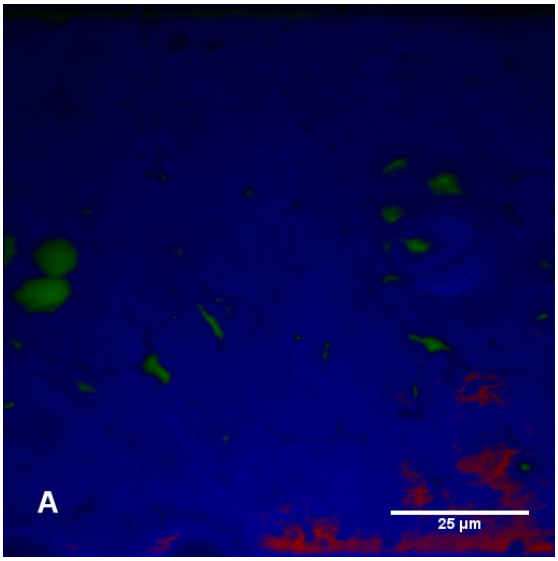

Image 11-5: 128-day gestation sheep – PMC @ 2.5µm below the surface

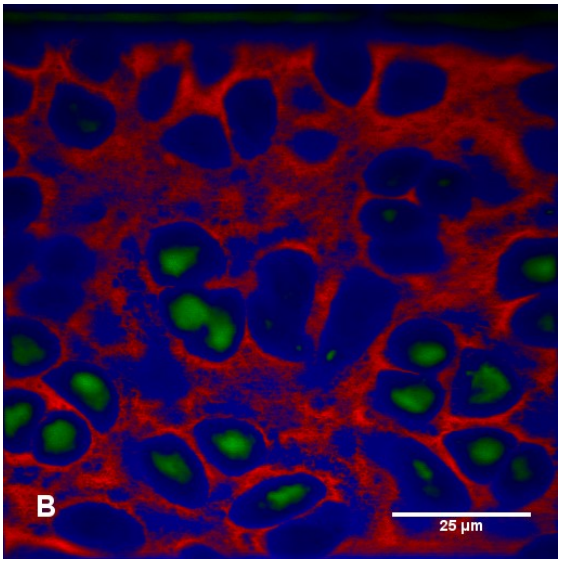

Image 11-6: 128-day gestation sheep – PMC @ 16.5µm below the surface

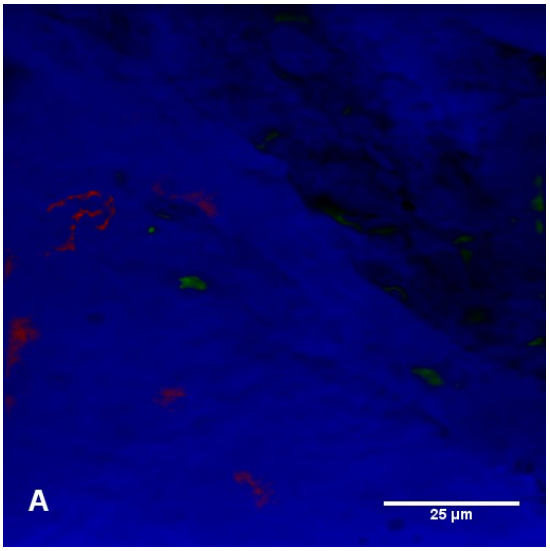

Image 11-7: Mature sheep – PMC @ 0.25µm below the surface

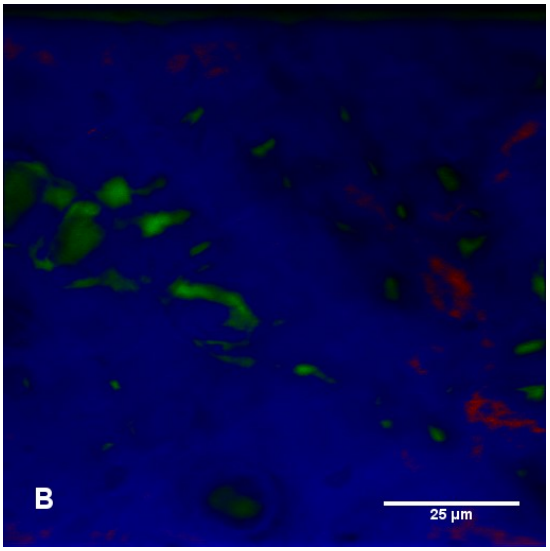

Image 11-8: Mature sheep – PMC @ 8µm below the surface

A small amount of damage was found on the surface of the mature samples, indicating the wear of the joint with age and loading. Samples also showed a thin layer of what appeared to be non-viable chondrocytes, although this was unconfirmed due to the low number of mature samples. A clear acellular region was present which was not present in the prenatal samples. This can be assumed to be the lamina splendens that had previously been reported to be acellular (Teshima *et al*., 1995). The lamina splendens were found to be 0.75-1µm thick in most samples. Directly beneath this surface layer, the chondrocytes were elongated and flattened into low density, horizontal sheets to a depth of 2.5-3µm. Cells in the middle region were more randomly arranged and were spherical in shape, confirming the classical structure of the chondrocytes. The density of cells was slightly lower than the prenatal sheep and there was no evidence of mitosis.

11.4.2 Anterior Medial Condyle

The anterior medial condyle ("AMC") is a low load bearing region on the ovine femoral head due to the region only being loaded during full extension of the knee. The AMC is positioned toward the front of the medial condyle on the inside of the knee. It was assumed that several type I and type III collagen fibres would be present due to the low load bearing nature of the region. Images 11-9 to 11-14 illustrate the structure at the anterior medial condyle.

There was evidence of type I collagen fibres being present in the upper layers of some of the prenatal sheep. Type III collagen was again difficult to detect although there appeared to be small amounts of it deeper in the tissue of the prenatal sheep. Again, the difficulty in this assessment could be attributed to the extended exposure to paraformaldehyde as previously discussed. Similar results were found in study 6 however, in study 5 found the cartilage in all age groups was found to be devoid of type III collagen. Once more, no visible fibres were found in the mature samples, also reported in studies 4 and 5.

Like the PMC, the density of chondrocytes near the surface of samples taken from the 124-day gestation sheep was low, increasing dramatically with depth until the density reached a plateau at 20μm into the sample. Density at this depth was lower than the PMC. The average size of the cells near the surface was also smaller and again decreased with depth. Sizes were 15-20μm in diameter near the surface compared to the 10μm visible at the lower depths. The classical structure of was not visible in this age group. Evidence of mitosis and limited non-viable cells were again seen throughout the cartilage.

In contrast to the PMC, there was little change in chondrocyte structure in the later stage of gestation (128/129 days). All cells were of similar size and density at all depths. Mitosis was still clear and again, there were very few non-viable cells.

Damage was again found on the surface of the mature samples. A clear acellular region was again present which was not seen in the prenatal samples, although no evidence of non-viable chondrocytes was seen unlike in the PMC region. The lamina splendens were found to be thicker at 1.25μm, which is most due to the region being low-load bearing. Directly beneath this surface layer, the chondrocytes were elongated and flattened into low density, horizontal sheets to a depth of 10μm. The larger depth of this region shows a thicker superficial zone, often associated with low load bearing regions. The classic structure was again seen, as the cells in the middle zone tended to be randomly arranged and spherical. The density of cells was significantly lower than the prenatal sheep and there was no evidence of mitosis.

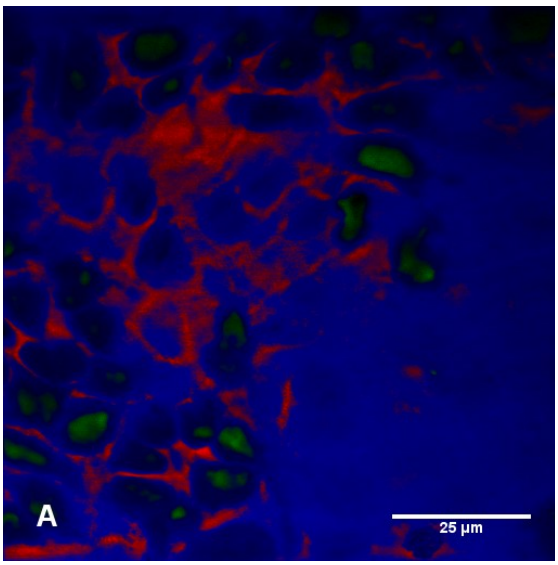

Image 11-9: 124-day gestation sheep – AMC @ (A) 3.5µm

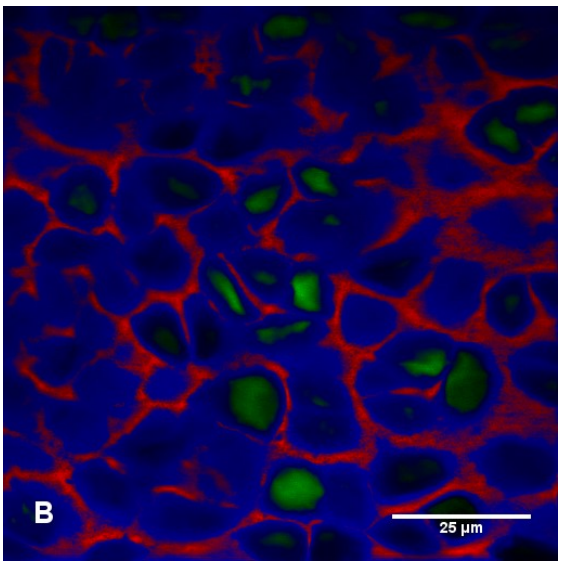

Image 11-10: 124-day gestation sheep – AMC @ (A) 11µm

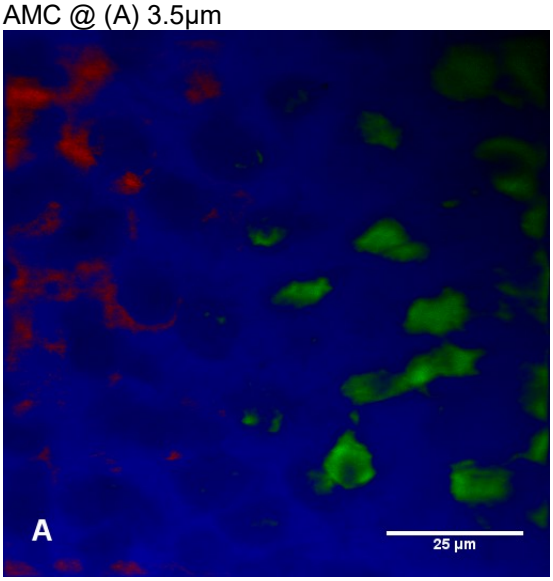

Image 11-11: 128-day gestation sheep – AMC @ (A) 5µm

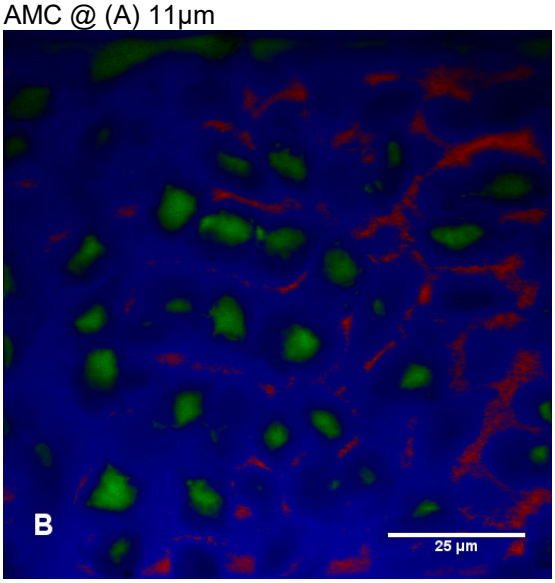

Image 11-12: 128-day gestation sheep – AMC @ (A) 19.5µm

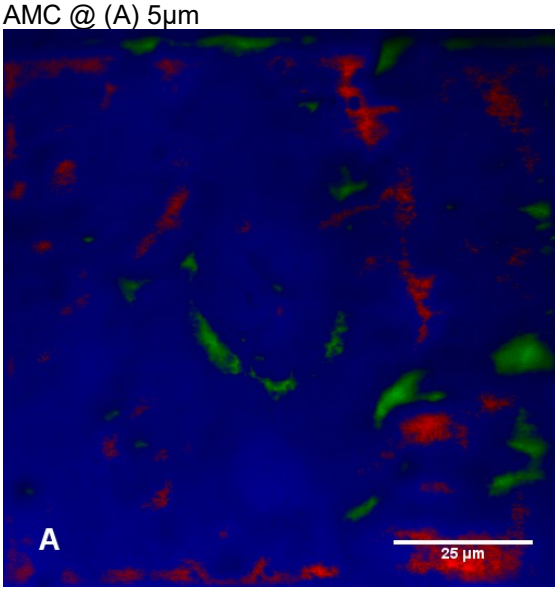

Image 11-13: Mature sheep – AMC @ (A) 4.25µm

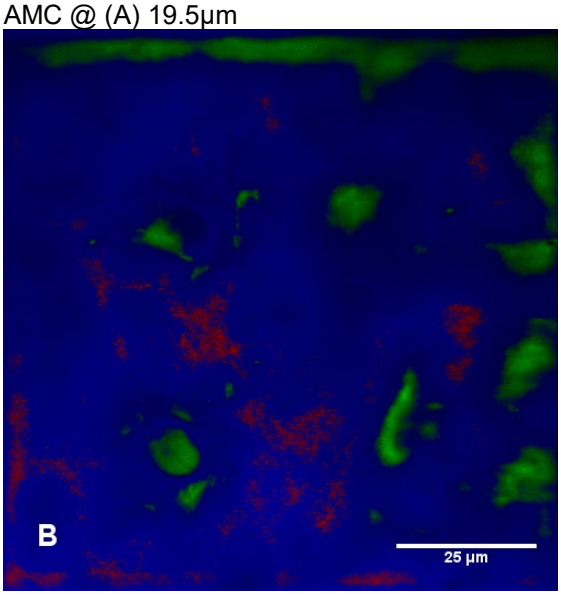

Image 11-14: Mature sheep – AMC @ (A) 17.5µm

11.4.3 Medial Trochlea

The medial trochlea region is a non-load bearing region on the ovine femoral head and offers a surface upon which the patella can slide. It is found on the front face of the head on the medial side. Results from this region did not match the expected structure based on previously imaged regions. The author attributes this to the trochlea being a non-load bearing region and, therefore, does not need a definitive structure to function correctly. Image 11-15 to 11-20 illustrate the structure at the medial trochlea.

Pre-natal sheep were found to have type I at varying depths within the tissue. Type III collagen was not detected, because of the fixation time. The findings agree with study 5 who found type I in some samples, but no type III collagen. Once more, no visible fibres were found in the mature samples, also reported in studies 4 and 5.

The density of chondrocytes was much more uniform than previously found in the 124-day gestation samples. Cells density did increase with depth although this was not a significant increase. Density was lower than earlier sites. The average size of the cells was like the AMC, being 15-20μm in diameter near the surface and 10μm at the lower depths. The classical structure of was not visible in this age group. Progression of mitosis was clear and few non-viable cells were found. There was little difference to this structure in the 128/129-day gestation sheep.

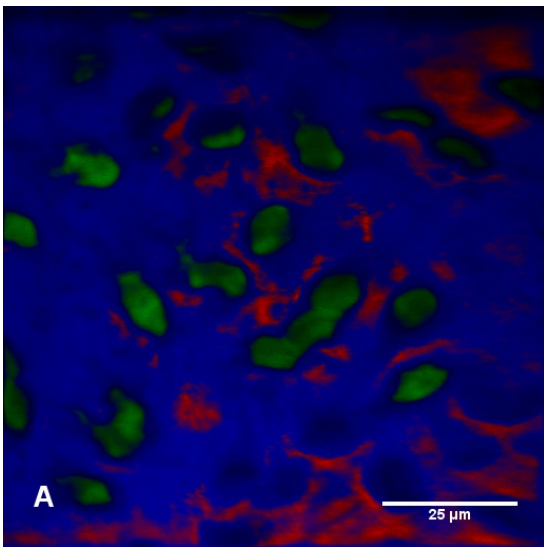

Image 11-15: 124-day gestation sheep – MT 4µm below the surface

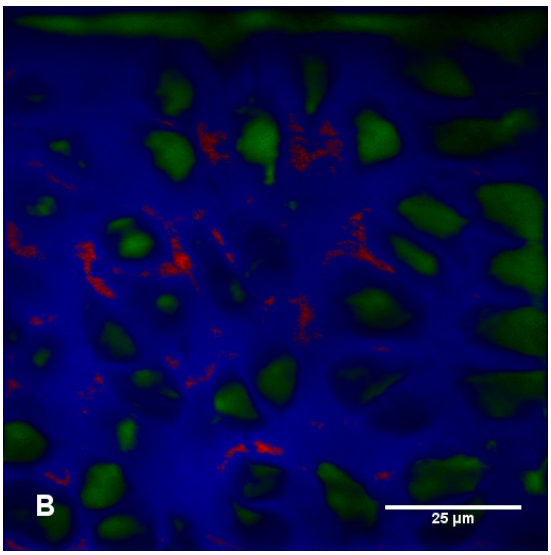

Image 11-16: 124-day gestation sheep – MT 18µm below the surface

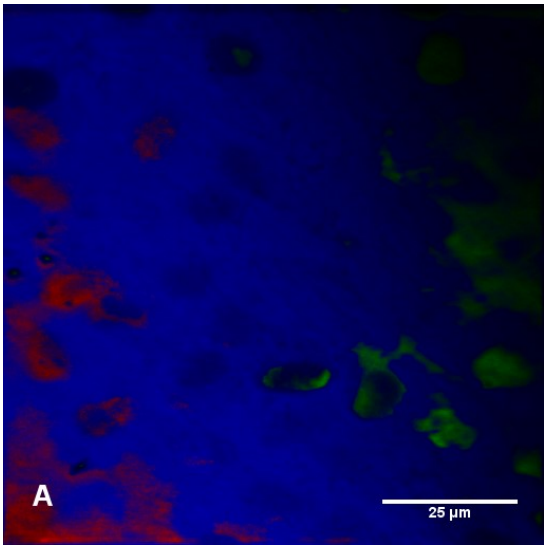

Image 11-17: 128-day gestation sheep – MT 0.5µm below the surface

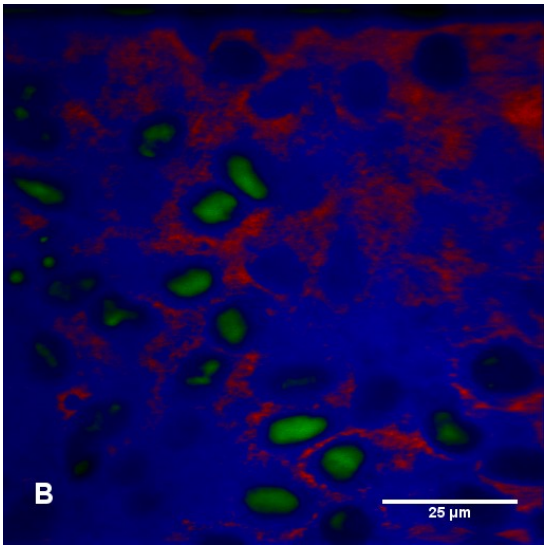

Image 11-18: 129-day gestation sheep – MT 10.5µm below the surface

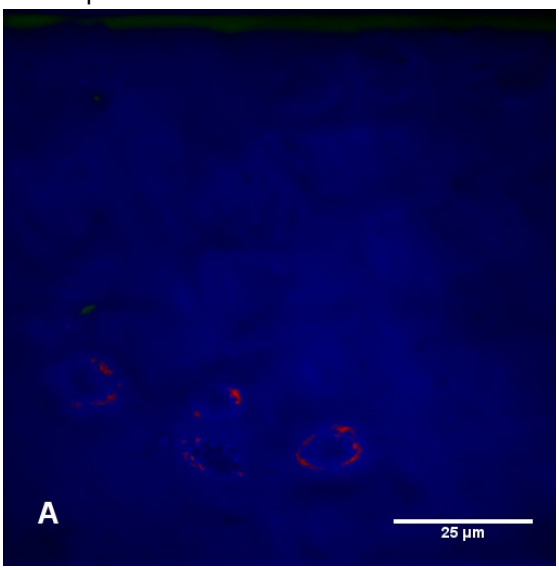

Image 11-19: Mature sheep – MT 8.75µm below the surface

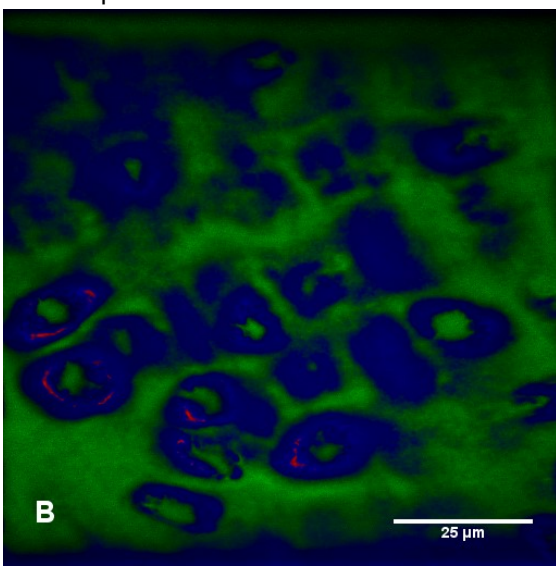

Image 11-20: Mature sheep – MT 20.5µm below the surface

11.4.4 Posterior Lateral Condyle

The posterior lateral condyle is another load bearing region on the ovine femoral head due to the region passive flexion of the knee. It is found toward at the rear of the lateral condyle on the outside of the knee. Images 11-21 to 11-26 illustrate the structure at the posterior lateral condyle.

Type I collagen fibres was present in the upper layers of the prenatal sheep. Type III collagen was found in some samples, but was again difficult to detect. Similar results were found in study 5. No visible fibres were found in the mature samples, also reported in study 4, although study 5 found type I collagen on the surface of some samples.

At the surface of some of the 124-day gestation sheep, a layer of randomly shaped dark patches was present, appearing to be mutated chondrocytes. The nature of these patches is unclear, however, the layer in which they were present did appear to be devoid of collagen I fibres. This contrasts with both authors who found that the surface layer was acellular but contained collagen I fibres. The remaining samples were vastly different to earlier sample sites. The average size of the cells near the surface was smaller and did not vary with depth. Sizes were 10μm in diameter and dense at all depths, again with little variation. The classical structure of was not visible in this age group. Mitosis appeared to be less frequent than previously found; however, there were still few non-viable cells. This contrasts with results in study 6 that found that non-viable chondrocytes were densely packed in the upper regions of the tissue. There was little change in structure in the 128/129-day age group, except for mitosis appearing more often in the deeper tissue.

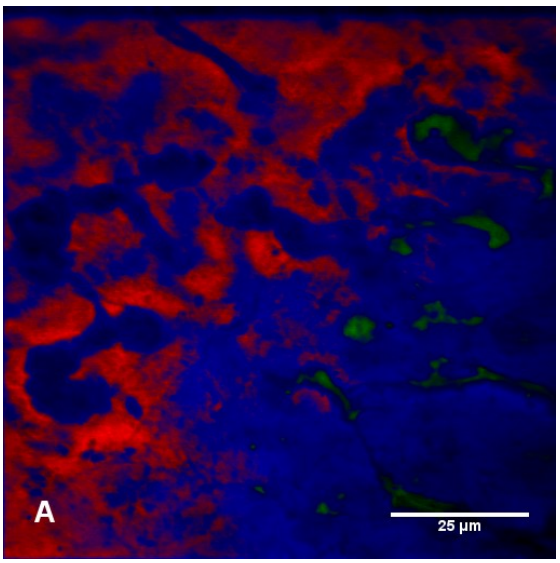

Image 11-21: 124-day gestation sheep PLC @ 3µm below the surface

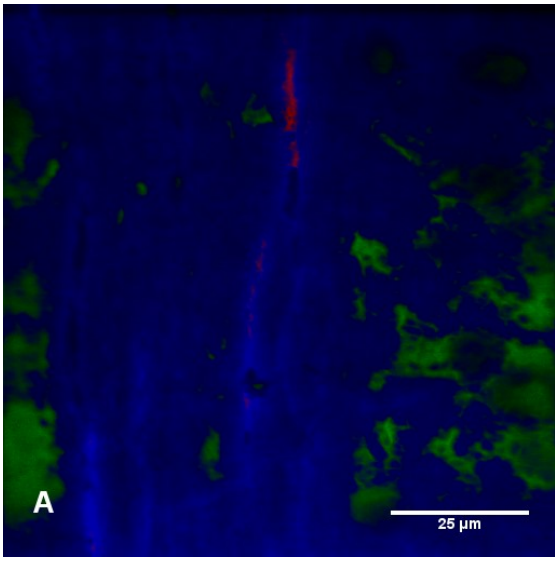

Image 11-22: 128-day gestation sheep PLC @ 6.5µm below the surface

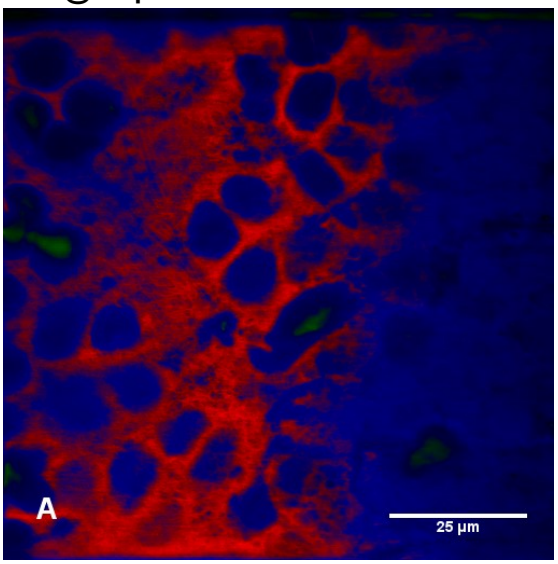

Image 11-23: Mature sheep PLC @ 1.25µm below the surface

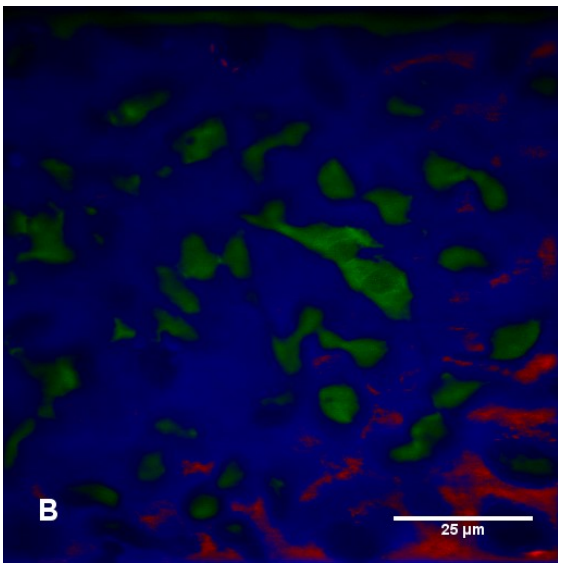

Image 11-24: 124-day gestation sheep PLC @ 16µm below the surface

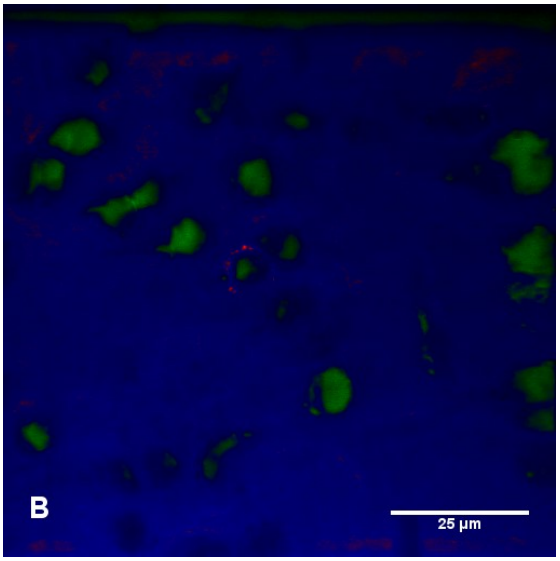

Image 11-25: 128-day gestation sheep PLC @ 21µm below the surface

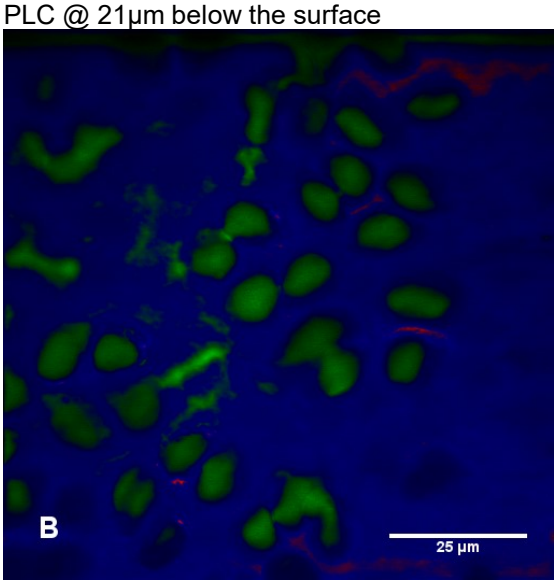

Image 11-26: Mature sheep PLC @ 17.25µm below the surface

The surface of the mature cartilage showed significant damage compared to the prenatal sheep. The acellular region was difficult to determine as the start of the horizontal clusters of chondrocytes could not be identified. An estimate of the thickness of the lamina splendens was 1.25μm based on observations of all samples. This would result in the depth of the superficial zone 6μm, falling between the PMC and AMC which is expected based on results found by study 4. The classic chondrocyte structure was present, as the cells in the middle zone tended to be randomly arranged and spherical. The density of cells was significantly lower than the prenatal sheep and there was no evidence of mitosis.

11.4.5 Anterior Lateral Condyle

The anterior lateral condyle is a low load bearing region on the ovine femoral head due to the region only being loaded during full extension of the knee. It is found toward the front of the lateral condyle on the outside of the knee. It was assumed that several type I and type III collagen fibres would be evident due to the low load bearing nature of the region. Images 11-27 to 11-32 illustrate the structure at the anterior lateral condyle.

As expected, the surface of the mature samples was again damaged. The superficial zone was found to be thick at 6μm, which is most due to the region being low-load bearing. Evidence of the typical elongated and flattened cells was not visible, and so the thickness of the lamina splendens was not able to be found.

The spherical morphology of cells in the middle zone was seen. The density of cells was significantly lower than the prenatal sheep and there was no evidence of mitosis.

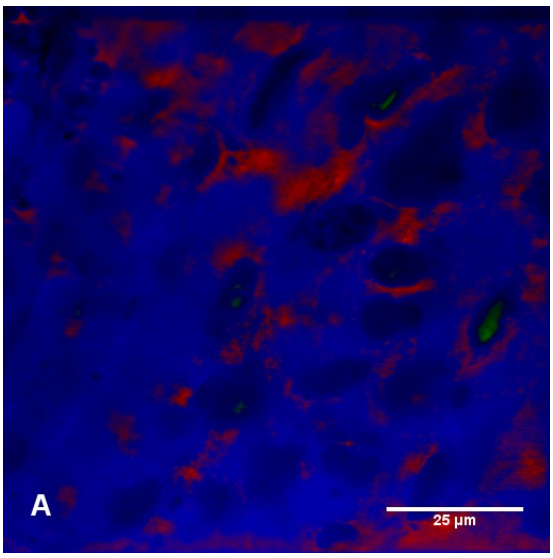

Image 11-27: 124-day gestation sheep ALC @ 4µm below the surface

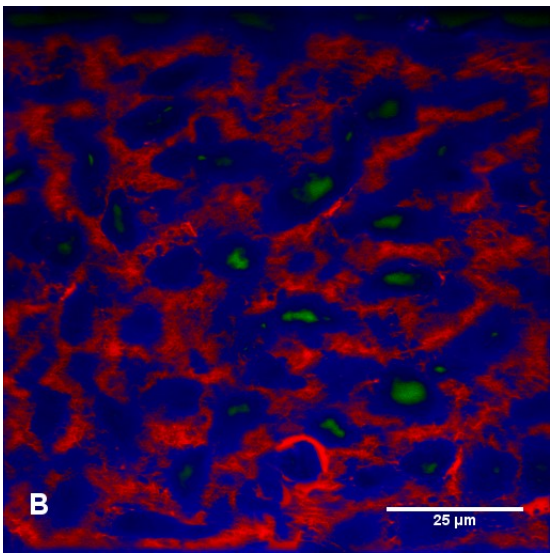

Image 11-28: 124-day gestation sheep ALC @ 15µm below the surface

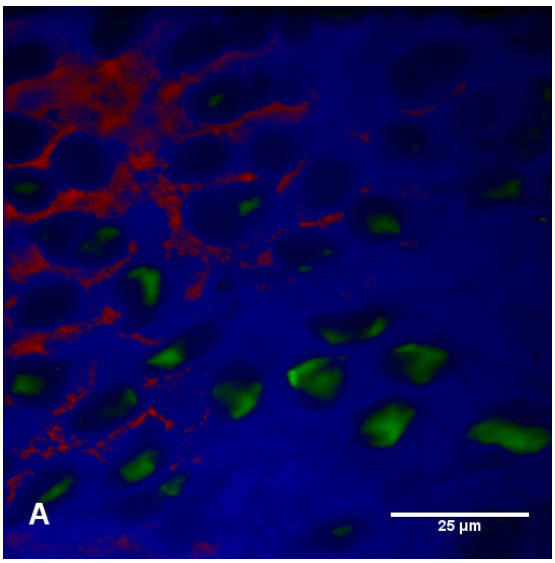

Image 11-29: 128-day gestation sheep ALC @ 2µm below the surface

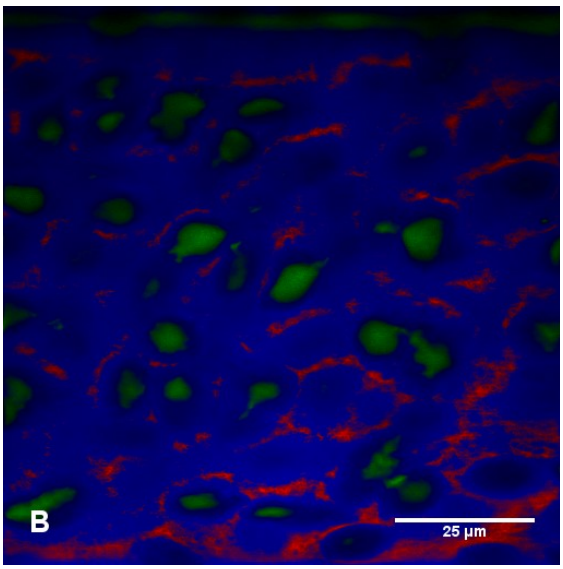

Image 11-30: 128-day gestation sheep ALC @ 19.5µm below the surface

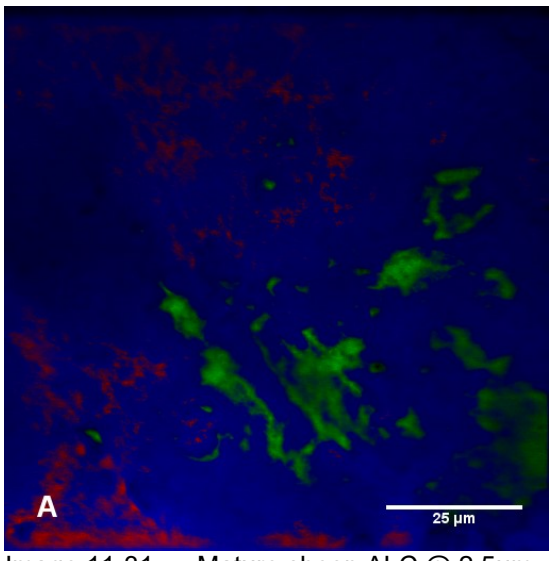

Image 11-31: Mature sheep ALC @ 2.5µm below the surface

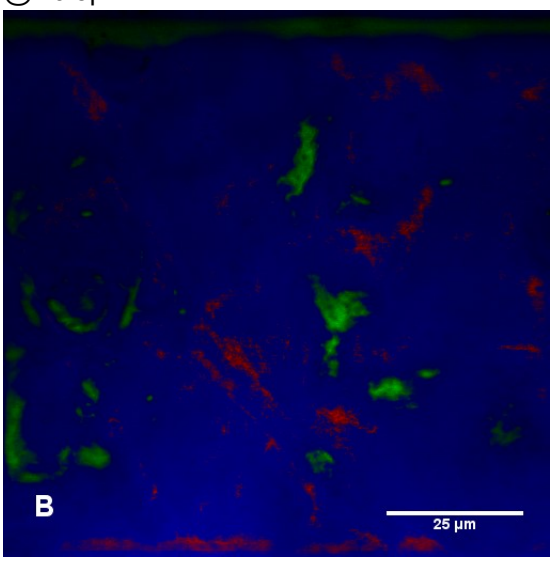

Image 11-32: Mature sheep ALC @ 11.5µm below the surface

11.4.6 Lateral Trochlea

The lateral trochlea region is found alongside the medial trochlea region, and as such is also a non-load bearing region. Images 11-33 to 11-38 illustrate the structure at the lateral trochlea. Results from the lateral trochlea were almost identical to the medial trochlea and as such will not be discussed again.

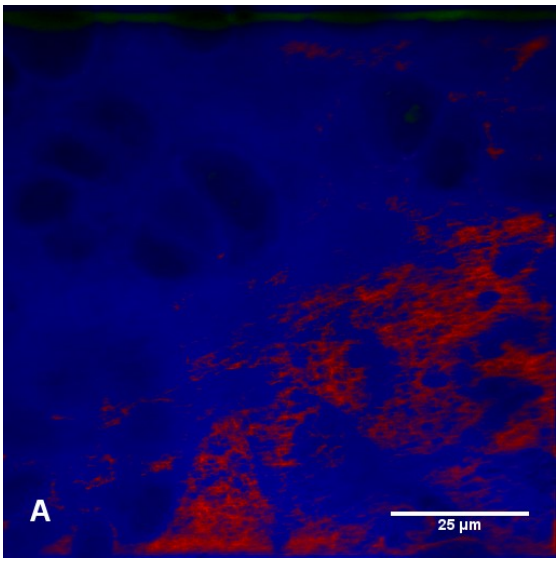

Image 11-33: 124-day gestation sheep – LT @ 9.0 µm below surface

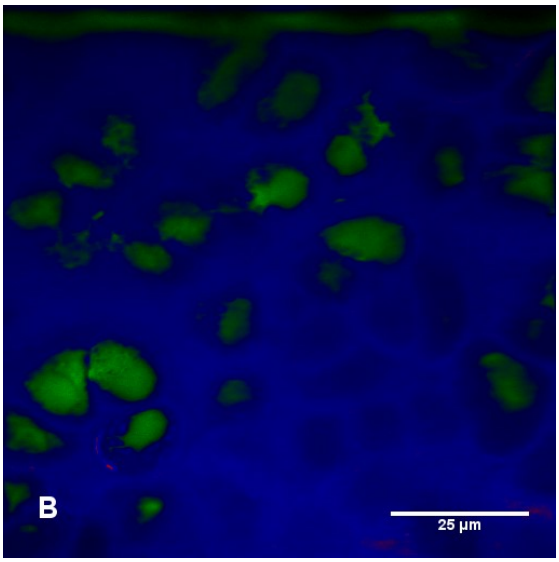

Image 11-34: 124-day gestation sheep – LT @ 18.5 µm below surface

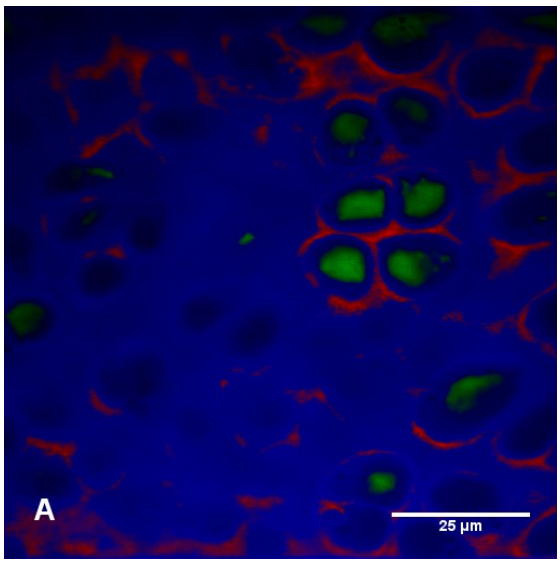

Image 11-35: 128-day gestation sheep – LT @ 8.5 µm below surface

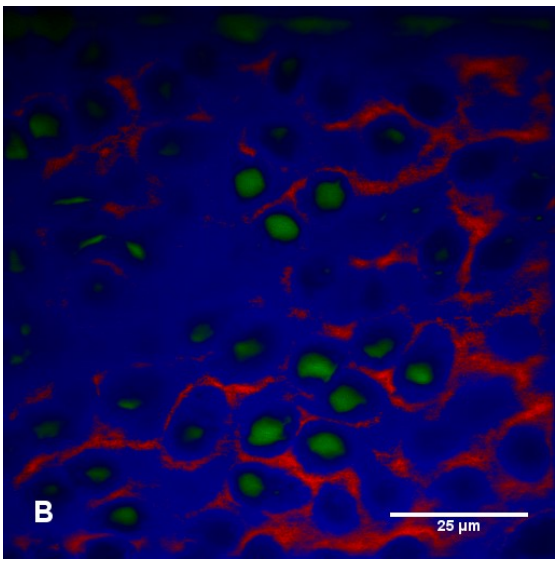

Image 11-36: 128-day gestation sheep – LT @ 21.0 µm below surface

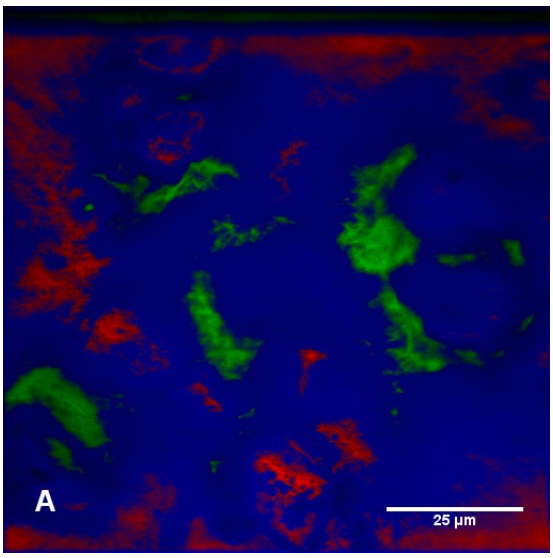

Image 11-37: Mature sheep – LT @ 4.24 µm below surface

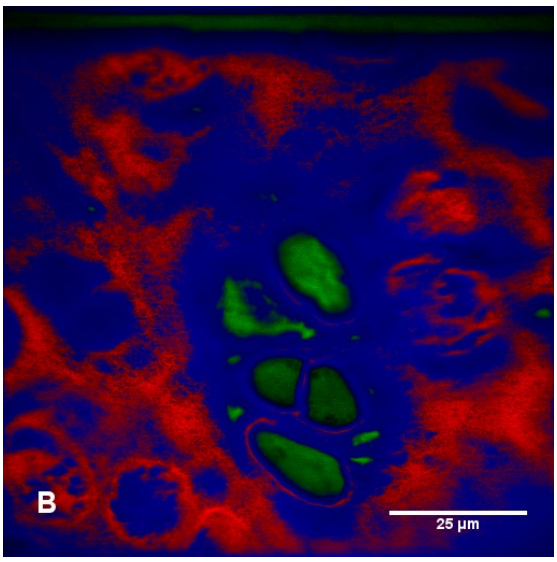

Image 11-38: Mature sheep – LT @ 21 µm below surface

There appears to be a distinct topographical variation in structure associated with the samples. Type I and type II collagen fibres were found to be present in the prenatal samples, in agreement with the findings made by Teshima *et al* (1995). Most of the load bearing regions were found to have fewer type I and III collagen fibres, in agreement with other studies conducted, while the ALC was found to resist shear loads associated with the ligament through an interwoven layer of type I fibres. The ALC was found to have moderate levels of both fibres although there was no distinct arrangement of these fibres. Due to the clarity of images, the depth of the layer of fibres and the quantity of fibres within this layer were determined. A review of the thickness of the fibrous layer or quantity of fibres varying with position and age has not previously been reported. It was clear that the developing cartilage contained higher levels type I fibres than the mature samples, which is attributed to the replacement of types I and III fibres with type II fibres during the development process (Yasui and Nimni, 1988).

Chondrocyte density was found to decrease slightly in the load bearing regions of the prenatal sheep; however, these was still a high density of cells at all depths undergoing varies stages of mitosis. This was expected due to the developmental age of the sheep. Chondrocyte density in the mature samples was found to decrease significantly, and represented the classical structure of chondrocytes, varying with depth.

An exception to these structural trends is the trochlea. It was found that despite being non-load bearing, there were minimal traces of type I and II collagen, although the density of cells was still larger than the load bearing regions. In the mature tissue, the classic chondrocyte arrangement was not seen, as spherical chondrocytes started immediately beneath the surface. This can be attributed to the different function of the cartilage in the trochlea (bearing surface for the patella) compared to the condyles (weight bearing).

Based on the above findings, it is possible that the classical structure of an acellular region, followed by horizontal sheets of flattened chondrocytes, and finally spherical chondrocytes, is a product of the deformation of the upper surfaces. The upper surface is designed to resist lateral expansion (Broom, 2009), and so it is possible that during the vertical deformation associated with this resistance, cells became deformed and were damaged. Deformation lower in the tissue is not as large, and so chondrocytes may be capable of deforming sufficiently with the cartilage to avoid damage. This would account for the acellular region at the surface, progressing to spherical chondrocytes deeper in the tissue of load bearing cartilage, and its absence from non-load bearing cartilage which does not undergo substantial deformation. Also, the surface cells are already deformed and entrapped in the lacunae. Compression testing may well have processed these cells to disintegration.

11.5 Viscoelastic Behaviour

Articular cartilage has previously been identified as a viscoelastic material (Mow *et al*., 2005); however, the exact behaviour under the full range of physiological loading conditions is unknown (Fulcher *et al*., 2009). To gain greater insight into the mechanical properties of articular cartilage, samples should be tested over a wide range of strain rates to figure out if the stiffness response of the tissue still is viscoelastic within the range of physiological conditions. Therefore, it is of interest in this study to decide this behaviour to fully appreciate the mechanical properties of articular cartilage.

Several samples were subject to stress-relaxation testing under a comprehensive range of strain rates, with a plot of load versus time constructed for each sample to display the relaxation response of the cartilage for each strain rate. The shape of plot was then compared to standard viscoelastic responses for polymers (Callister, 2007). Additionally, a plot of the stiffness of the sample at each strain rate was developed to identify the regions of viscous and elastic behaviours as a function of strain rate.

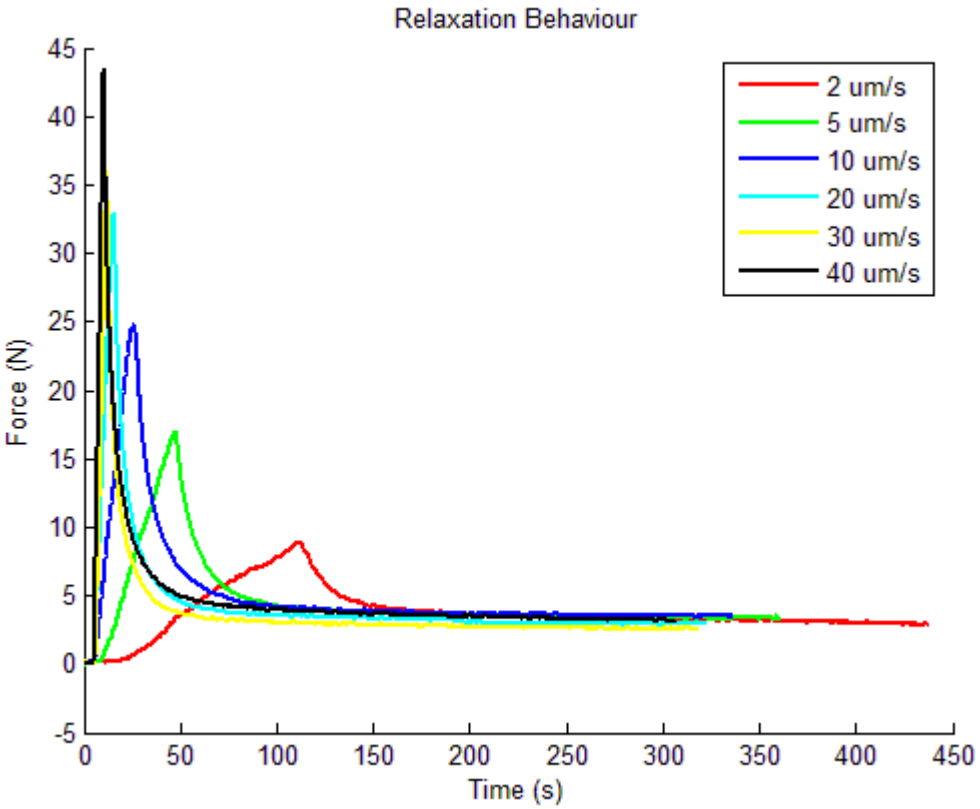

Figure 11-2: Example of viscoelastic relaxation behaviour

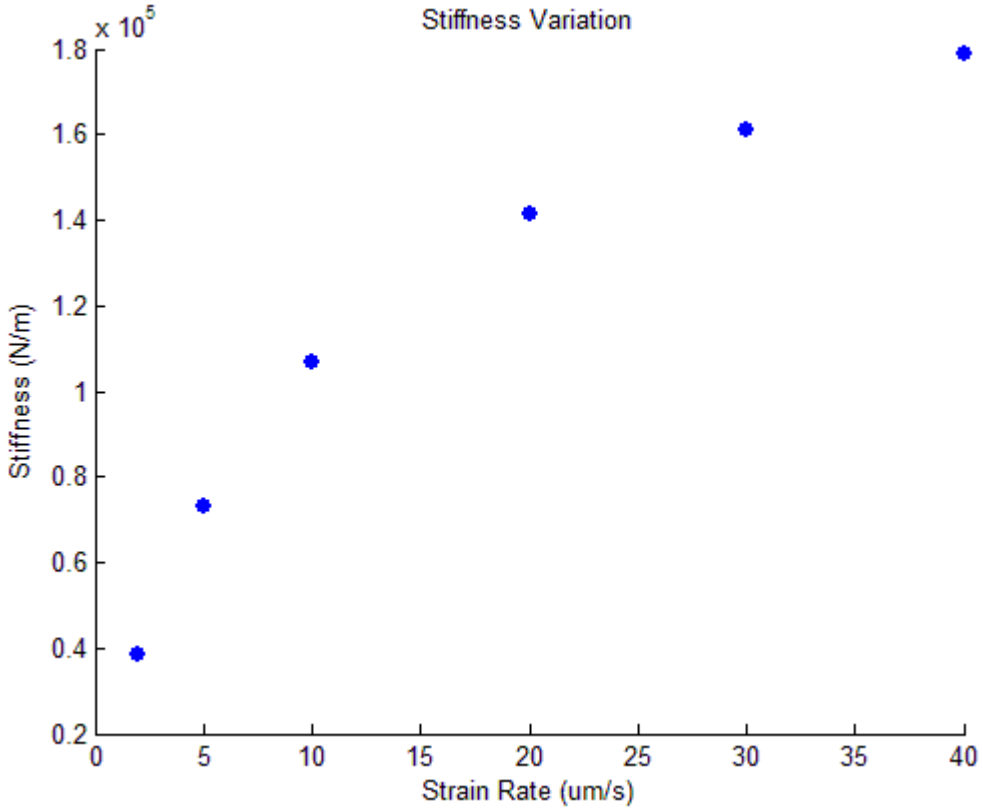

Figure 11-3: Example of viscoelastic stiffness behaviour

From a basic study of relaxation responses (Figure 11-2) and stiffness variation (Figure 11-3) it was concluded that cartilage exhibits viscoelastic behaviour across the entire range of strain rates tested; however, there is no evidence to suggest that this is dependent on the site-specific structure of the cartilage. It was found that there were two distinct regions of response as stiffness increased with strain rate (Figure 11-3), as the resistance of the cartilage changes from the proteoglycan controlled compressive stiffness to the collagen controlled tensile stiffness. It was observed that these two almost linear regions existed for the range of strain rates 2-10μm/s and 20-40μm/s, representing the viscous and elastic regions respectively. Strain rates below 2μm/s were not possible with the test rig available.

The depth dependent properties of articular cartilage can also be seen during compression in Figure 11-4. Initial deformation of the articular cartilage exhibits a quadratic response in relation to force, transitioning to a linear relationship as the strain increases. This depth dependent variation has been previously reported in this study.

The initial deformation of cartilage can be attributed to the upper surface of the cartilage conforming to the contact surface, thus increasing the load bearing area, and allowing for greater dissipation of the load and a reduction in peak load. Thus, the response of the cartilage to initial deformation may be the result of the presence of the most superficial layer.

The strain rate dependent behaviour of articular cartilage is also visible in Figure 11-4, as the gradient of the plots increases with strain rate. This indicates an increase in stiffness with increasing strain rate, allowing the cartilage to handle larger dynamic forces, such as those experienced during sport. This consistency with the viscoelastic modelling of articular cartilage across all the strain rates suggests that this behaviour exists for cartilage across the entire range of physiological loading conditions.

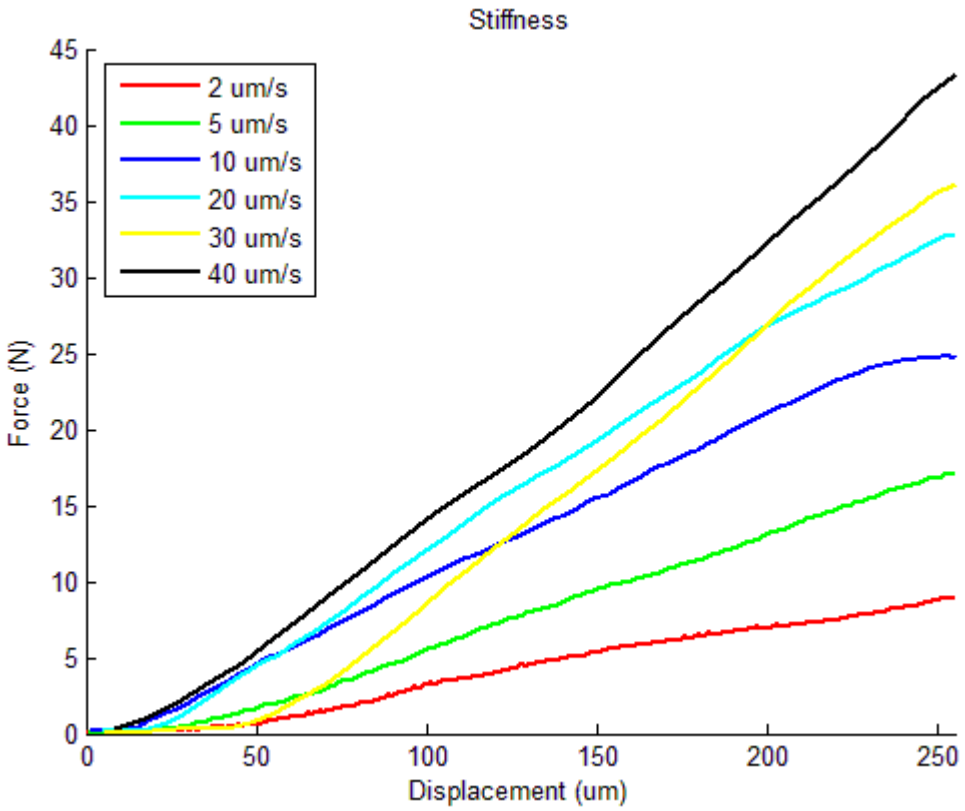

Figure 11-4: Example of a stiffness plot of articular cartilage

The lower stiffness of the cartilage during lower strain rates is the effect of relaxation occurring during compression. The slower application of load allows for some fluid flow prior to the final strain being reached, thus allowing the articular cartilage to distribute the load as it is gradually applied

The application of larger strain rates would limit the amount of fluid flow through the collagen network, leading to a greater force being experienced. The exact behaviour of the cartilage through the crossover region (10-20μm) was unclear, as it was unknown whether the effect of one resistance mechanism suddenly became dominant, or whether there was a point where neither was dominant and both resisted the compression equally.

Mature sample data in Figure11-5 showed no discernible relationship between sample position and stiffness. The difficulties in harvesting mature cartilage due to the thinner coating on the femoral head. The curvature of the condyle did not promote consistent sample thickness, leading to inconsistencies in mechanical properties across the sample. This could account for the highly variable nature of the data.

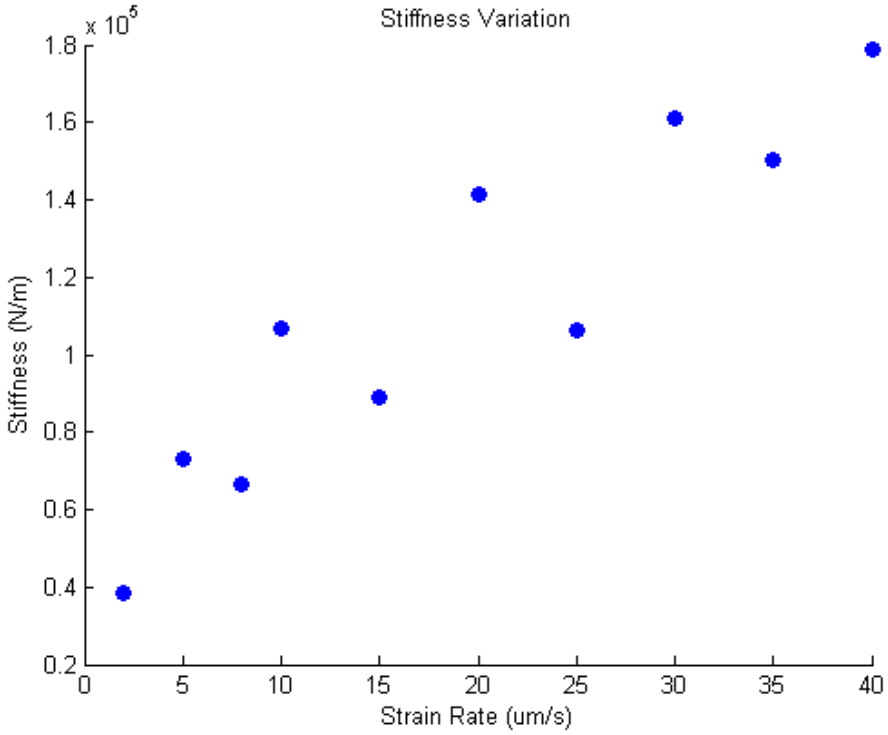

Figure 11-5: Viscoelastic stiffness behaviour across increased range of strain rates

The loss of proteoglycans is one of the first signs of osteoarthritis. Proteoglycans are also noted as being responsible for the compressive strength of cartilage. Finding the equilibrium stiffness of normal cartilage compared to that of osteoarthritic cartilage may help determine the early onset of osteoarthritis.

11.6 Tangential Stiffness

Determination of the tangential stiffness as a function of position allowed a study of the topographical variations in articular cartilage properties. The tangential stiffness of each sample was calculated using the linear regression of the stiffness plot (Figure 11-6) corresponding to a 2μm/s strain rate and grouped per sample position. The topographical variations of tangential stiffness are presented with error bars showing one standard deviation either side of the mean.

The lack of a distinct relationship between physiological loading and stiffness in the young cartilage can be attributed to the effect of mechanical stimuli on the development of cartilage. The effect of mechanical stimuli has been determined to be an important factor in the final development of articular cartilage (Arokoski et al., 2000). These results for prenatal sheep tentatively concur with this statement.

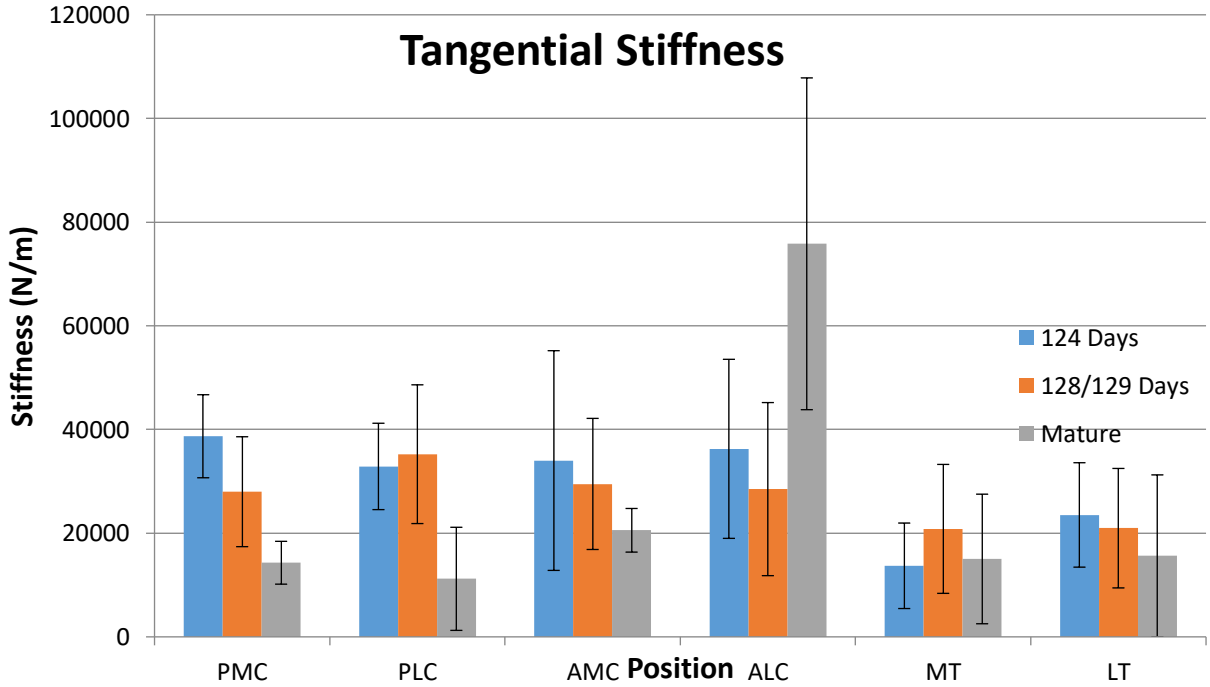

Figure 11-6: Topographical variation in tangential stiffness showing standard deviation in measurements

11.6.1 Equilibrium Modulus

The lack of a distinct relationship between physiological loading and stiffness in the young cartilage can be attributed to the effect of mechanical stimuli on the development of cartilage. The effect of mechanical stimuli has been determined to be an important factor in the final development of articular cartilage (Arokoski et al., 2000). These results for prenatal sheep tentatively concur with this statement. The compression appears to be linear at this strain rate.

During relaxation of articular cartilage due to the viscoelastic behaviour of the material (Figure 11-1), the gradient of the load with respect to time tends to zero, showing the achievement of a state of equilibrium in which the cartilage is no longer capable of distributing the applied load. The load at which this occurs is defined as the equilibrium load. This occurs due to the tissue reaching an even distribution of proteoglycans (Mow *et al*., 2005).

From Figure 11-2 it can be inferred that this material property is independent of strain rate, as the equilibrium load is equal for all rates of application. This implies that the equilibrium load is in fact a product of the structure, and shows the ability of the structure to withstand compressive loads. This property is defined as the equilibrium Young's modulus. The Equation used to determine the equilibrium Young's modulus is defined as:

$$E_{eq} = \frac{\sigma_{eq}}{\varepsilon} = \frac{4P_{eq}}{\varepsilon \pi D^2}$$

Where E_{eq} is the equilibrium Young's modulus of the system, σ_{eq} is the equilibrium stress of the cartilage, ε is the applied strain, P_{eq} is the equilibrium load and D is the diameter of the sample.

The effect of physiological loading capability on the equilibrium Young's modulus can be determined by studying the topographical variations across the stifle. Figure 11-7 shows the average equilibrium modulus for each sample site, with error bars showing one standard deviation either side of the mean.

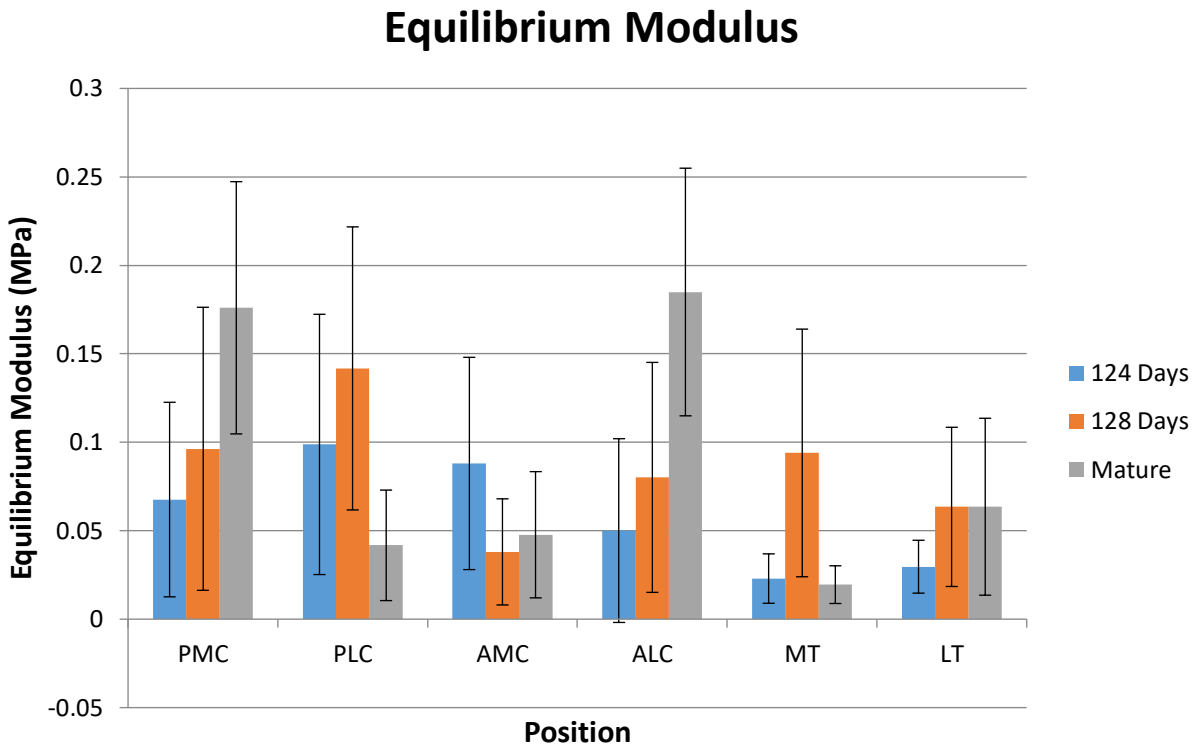

Figure 11-7: Topographical variation of the equilibrium modulus showing the standard deviation in the measurements

The lengths of the error bars show a large variation in the equilibrium modulus particularly for ALC and LT. Several extra samples were collected and measured. Instead of decreasing the variance, these added directly to the measured variation. Statistical analysis showed there was insufficient evidence to support the hypothesis that there was a real difference in equilibrium modulus across position and age.

Due to the presence of increased levels of collagen type II and proteoglycans in weight bearing regions and the extra viscous drag this would create during fluid flow, it was assumed that the redistribution of proteoglycans in the tissue during relaxation would be hindered, thus the residual load at equilibrium would be larger than in non-weight bearing regions. It was again concluded that an underlying tissue thickness was the real cause large variability.

11.7 Relaxation Time

Relaxation time can be considered as a measure of the porosity of the sample, as it proves how quickly the load can be redistributed before the equilibrium load is reached. It is calculated by measuring the time from the peak load of the sample during compression to the attainment of equilibrium. The relaxation times for the various sample positions are shown in Figure 11-8, with error bars showing one standard deviation either side of the mean.

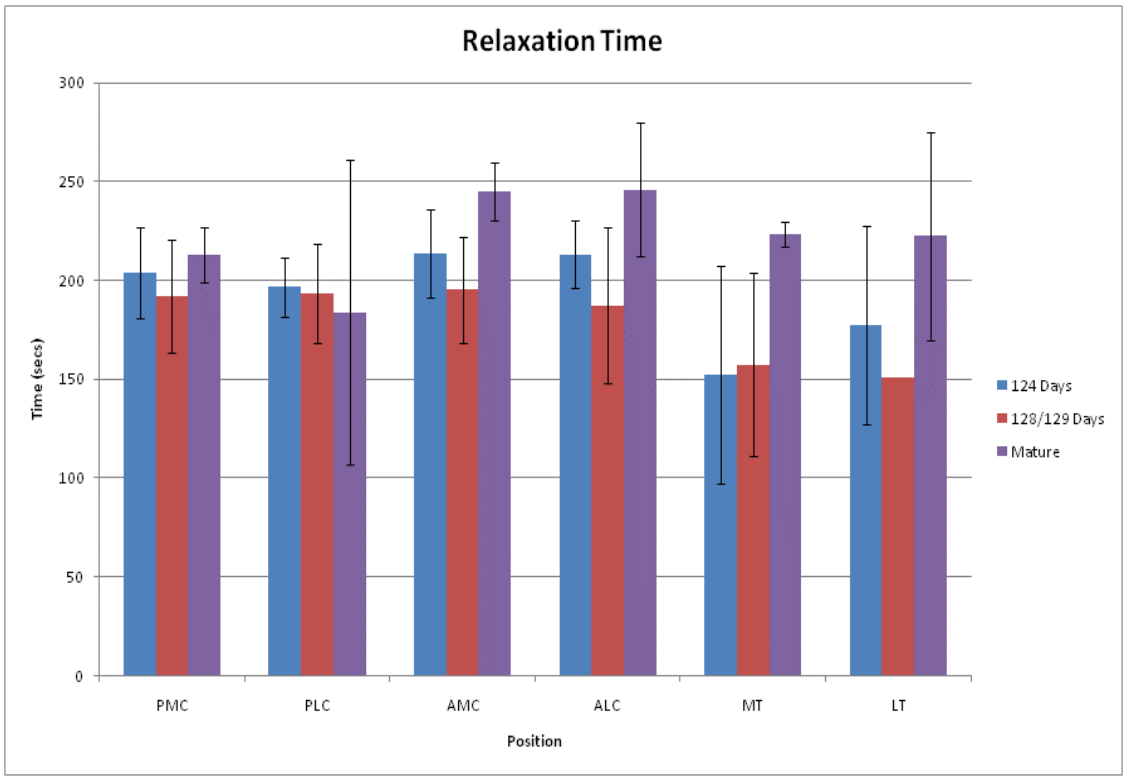

Figure 11-8: Average relaxation time showing standard deviation in measured timing.

It was expected that the relaxation time would be lower in load bearing regions compared to the non-load bearing regions. It has previously been noticed by studies that load bearing regions showing a larger equilibrium modulus can have a decreased relaxation time, despite the porosity of this cartilage being greater to inhibit fluid flow at higher pressures. This is because the peak load and equilibrium load are usually closer together due to this lack of porosity and so relaxation time also decreases. The trochlea regions were expected to have the lowest relaxation time, with the anterior regions having the largest relaxation times. This trend was seen in the Figure 11-8).

11.8 Study 3 Findings

From the study and analysis conducted, it can be concluded that:

1. Extended exposure to paraformaldehyde degrades the quality of images able to be acquired from a sample. This is most probably a result of the formaldehyde replacing the cross-links between collagen fibrils, causing them to become detached from the larger collagen fibres.

2. Type I and III collagen fibres are present in the upper regions of the developing ovine cartilage; however, the presence of the fibres were more difficult to determine in mature samples.

3. The lamina splendens were observed in mature samples on the condyles; however, the composition in terms of collagen fibres was not able to be determined due to the image clarity. A similar issue was found in determining the presence of the layer in prenatal samples.

4. Structural topography within samples from the condyles appeared as expected, with the load bearing regions showing decreased levels of type I and III collagen fibres in the developing samples, and showing thinner superficial zones than the low-load bearing regions in the mature cartilage.

5. Structural topography in the trochlea showed differing trends from the classical structure of mature cartilage, including chondrocyte distribution and thickness of the zones. It is assumed that this is the result of the different function of the cartilage from the trochlea compared to standard load bearing cartilage.

6. Articular cartilage displays a viscoelastic relationship under compressive loading. The strain rate dependent response affects the stiffness of the cartilage, while the equilibrium modulus appears to be independent of strain rate. Further testing is needed to decide the behaviour through the cross-over region between viscous and elastic behaviour.

7. There were no trends able to be inferred from the results of tangential stiffness across the sample locations due to the presence of abnormal variability in the mature samples. Again, this is thought to be age related rather than topological.

8. Results for the equilibrium modulus displayed extremely abnormal variability in all samples and so no trends can be predicted by topological position. The main differences were attributed the superficial zone thickness, which is a function of cartilage age.

9. Relaxation time was found to be the expected results to a reasonable level. The variability present in the tangential stiffness and equilibrium modulus was not as prevalent and so trends were found. The stiffer regions of cartilage showed lower relaxation times due to the larger equilibrium modulus usually associated with these regions. The trochleae had the lowest relaxation times, as it can be inferred that they have higher porosity due to the lack of need for large osmotic pressures to be contained. The low load bearing regions thus had the longest relaxation times.

Chapter 12 Study 4: Porcine Cartilage – Three to Six Month Pigs

This study was conducted over six months using pig samples as they became available.

12.1 Study Objectives

This was a topological study to measure any discernible differences in mechanical properties of juvenile porcine cartilage. The study also observed the effects of specimen fixation upon the quality of images. A total of 25 pigs were available for the study, giving fifty sample joints. Each joint was sampled with 3mm biopsy specimens taken from the eight sample positions shown in Figure 12-1.

12.2 Mechanical Testing - Young Pig Cartilage

This study was conducted with undergraduate students Michael Smith and Christopher Bird as part of their final year projects. The porcine samples were collected from the Large Animal Facility at UWA as part of waste animal utilisation program. Ethics approvals were varied dependent upon the principal researcher and our samples were all taken from waste materials. All pigs were aged between three and six months and were harvested over a four-month period. Each student conducted measurements on one hind leg from each euthanased animal.

Figure 12-2 shows the non-weight bearing regions (2, 6, 7 and 8) recording an equilibrium modulus that was typically lower than that recorded for regions subjected to higher anatomical compressive loading (1, 4 and 5). Only samples from position 3 appeared to oppose this. This apparent relationship was tested over all sampling positions, excluding position 3, and was confirmed for a confidence level of 95%, indicating the trend is highly probable.

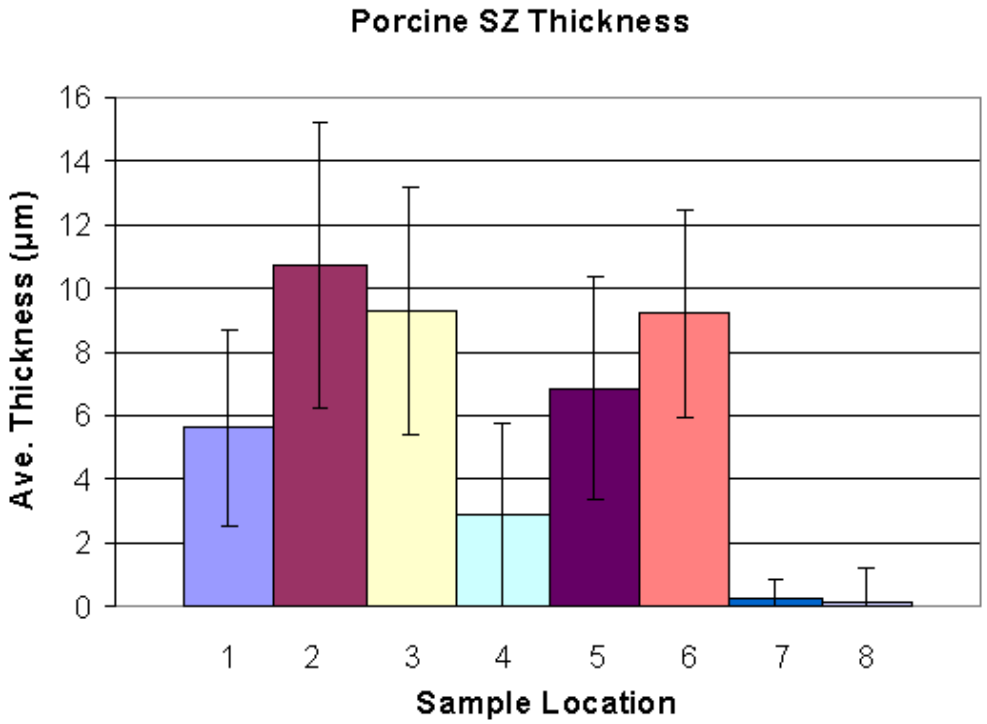

Figure 12-1:: Average thickness of porcine cartilage superficial zone showing standard deviation in thickness measurements.

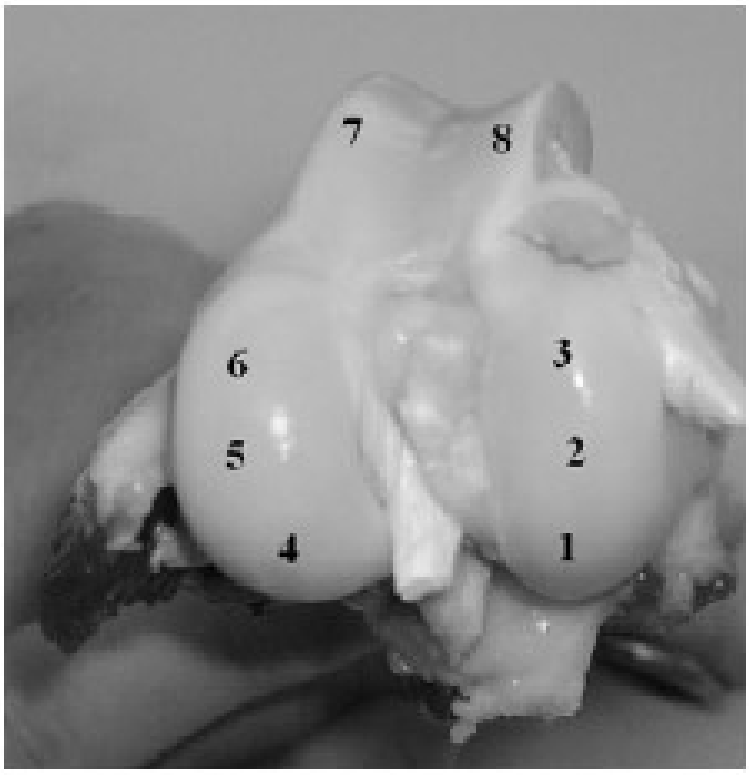

Figure 12-2: Sampling locations on the femoral condyle

Equilibrium modulus can be viewed as a measure for comparing the stiffness of AC after time dependent viscous activity has ceased. Therefore, expectations regarding these results would be that regions subjected to greater compressive loading should display a higher equilibrium modulus. This was confirmed by the results from porcine samples with the obvious exception of samples from region 3. The variation in sample site 3 is also likely that shear loading from the collateral ligament could result in increasing the relaxation modulus of the tissue at sampling position 3.

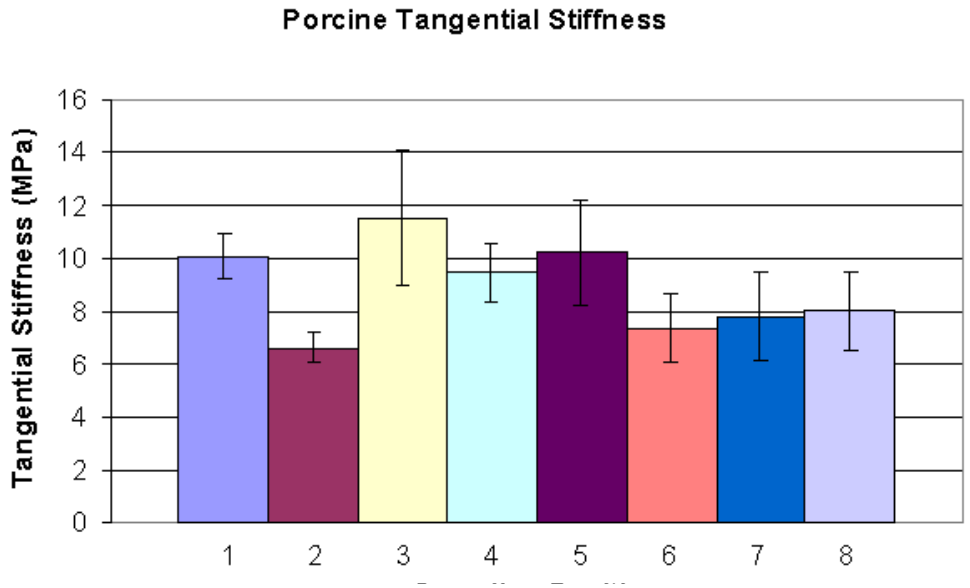

Figure 12-3: **Average tangential stiffness and standard deviation calculated for each site**

Figure 12-3 shows the typical anatomical compressive loading associated with each region. The predominant weight bearing areas of the condyles (positions 1, 4 and 5) seemed to produce higher stiffness measures than those from the regions on the femoral head that were subjected to lower compressive loading (positions 2, 6, 7 and 8). This hypothesis was tested across the sample sites and was confirmed on a confidence level of 95% with the only exception coming from position 3 where the confidence level was 90%.

The stiffness results from the porcine specimens can be accounted for by the role of chondrocytes within AC. Chondrocyte activity has been shown to increase with mechanical stimuli (Mow et al., 2005). Hence, regions that support a greater amount of compressive loading within the joint will have chondrocytes that synthesise more proteoglycans and collagen fibres.

Proteoglycans help form the resistance to compressive loading, so greater proteoglycan density results in increased stiffness of the tissue (Klein et al., 2007). An exception to the observed trend was seen at position 3, which could be the nearby presence of the collateral ligament, which provides shear loading in AC. Shear loading also stimulates chondrocyte activity, with resulting stiffer tissue being due to increased proteoglycan content (Klein et al., 2007)

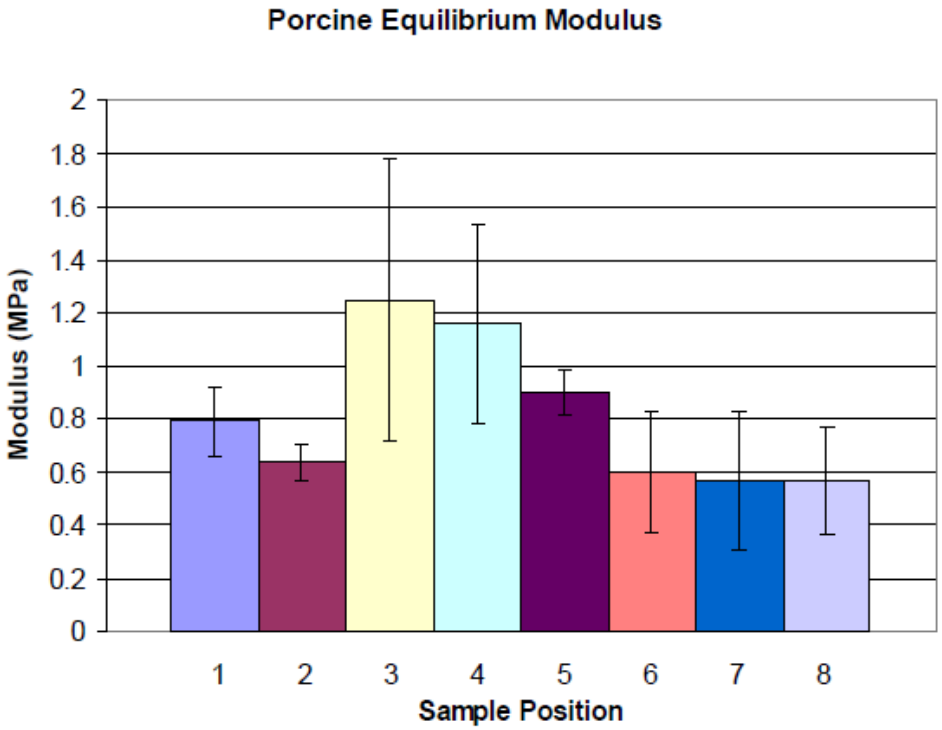

Figure 12-4: Porcine calculated equilibrium modulus with standard deviation

Figure 12-4 shows the non-weight bearing regions (2, 6, 7 and 8) recording an equilibrium modulus that was typically lower than that recorded for regions subjected to higher anatomical compressive loading (1, 4 and 5). Only samples from position 3 appeared to oppose this. This apparent relationship was tested over all sampling positions, excluding position 3, and was confirmed for a confidence level of 95%, indicating the trend is highly probable. This difference in equilibrium modulus is thought to be due to differences in cartilage thick which is cartilage age dependent.

Equilibrium modulus can be viewed as a measure for comparing the stiffness of AC after time dependent viscous activity has ceased. Therefore, expectations regarding these results would be that regions subjected to greater compressive loading or cartilage thickness should display a higher equilibrium modulus. This was confirmed by the results from porcine samples except for samples from region 3.

12.3 Study 4 Findings

1. Fresh AC samples provide the clearest LSCM images. Fixing specimens in paraformaldehyde for an extended period is appropriate for the study of chondrocyte cells but not for collagen structure.

2. Two separate types of collagen were identified in porcine samples. Research indicates these types of collagen to be type I and type III. Ovine samples displayed little observable collagen, indicating the superficial zone of three-year-old sheep is composed of type II collagen.

3. Superficial zone depth was observed to vary across the different topographical locations of the femoral head for both species. Across the condyles' sampling regions, porcine specimens displayed a thicker superficial layer than the ovine samples. A relationship between weight bearing and superficial zone depth was not fully characterised.

4. Depth and strain rate dependent stiffness properties were observed for porcine samples. A relationship between physiological compressive loading and tissue stiffness was indicated. Ovine samples displayed depth-dependent stiffness as in study 2.

5. Porcine and ovine samples displayed time dependent stress and strain properties. The response to stress relaxation and creep testing was typical of a viscoelastic material. Results inferred a relationship between relaxation modulus and weight bearing.

6. Ovine AC mechanical properties such as tangential stiffness and equilibrium relaxation modulus were typically slightly higher than those observed for porcine AC. Differences in age as well as species is the cause of this. AC is a complex biological material. By identifying the structure and mechanical properties of AC a greater understanding of the material will be developed. Increased knowledge of this tissue may lead to significant developments in identification of damaged tissue and cartilage repair techniques. Effective treatments for osteoarthritis are necessary due to the significant impact the disease has on society.

12.4 Relaxation Behaviour

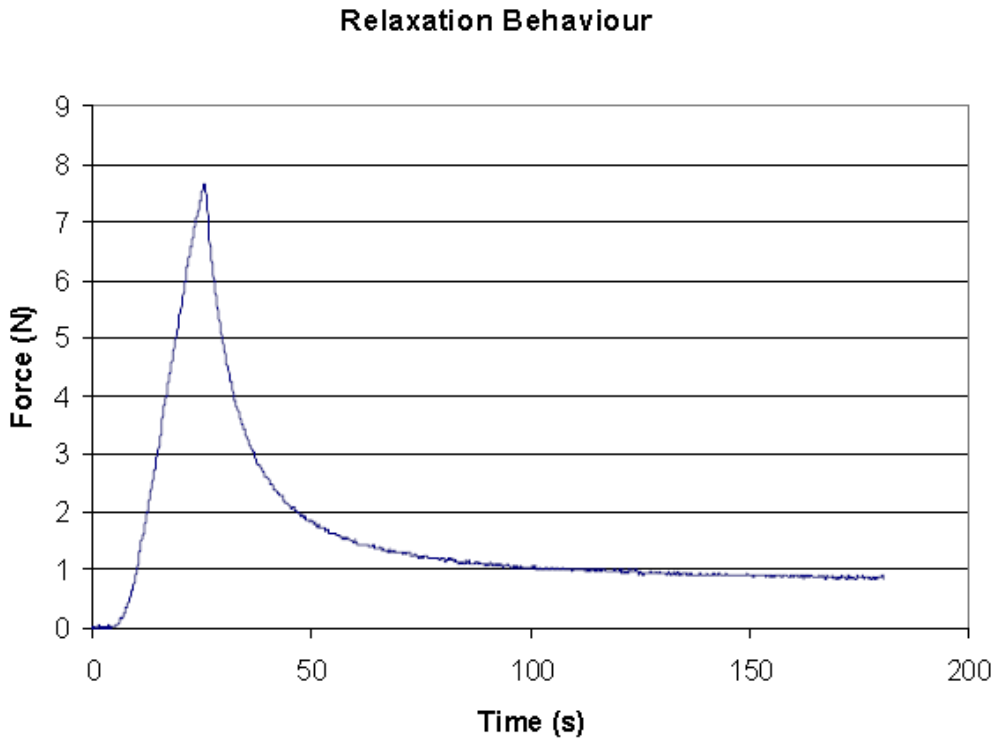

Figure 12-5: Typical stress/relaxation response of AC samples

AC has been observed to display viscoelastic relaxation properties (Wang et al., 2003). To test this relaxation ability, all samples were held at 15% compression (compressed at a rate of 10μm/s) for a period of 150 seconds. A typical response of the tissue is shown in Figure 12-5.

Relaxation was evident in all AC samples. After initial compression to 15% of thickness, AC displayed an ability to dissipate compressive force in the tissue over time. Eventually the specimens reached a point where it was completely relaxed (where the slope on the graph tended towards zero). Relaxation in AC cartilage is due to the flow of proteoglycans through the network of collagen fibres. Over time, the proteoglycans can evenly distribute throughout the tissue, causing AC to eventually reach a state of equilibrium (Mow et al., 2005).

12.5 Porcine Equilibrium Modulus

All porcine specimens displayed time-dependent deformation. Unlike the stress relaxation testing, these results typically showed samples not reaching an equilibrium displacement value. Therefore, as a comparative measure of creep behaviour, a creep modulus was calculated for when the samples had been held for 150 seconds. This behaviour is displayed in Figure 12-6.

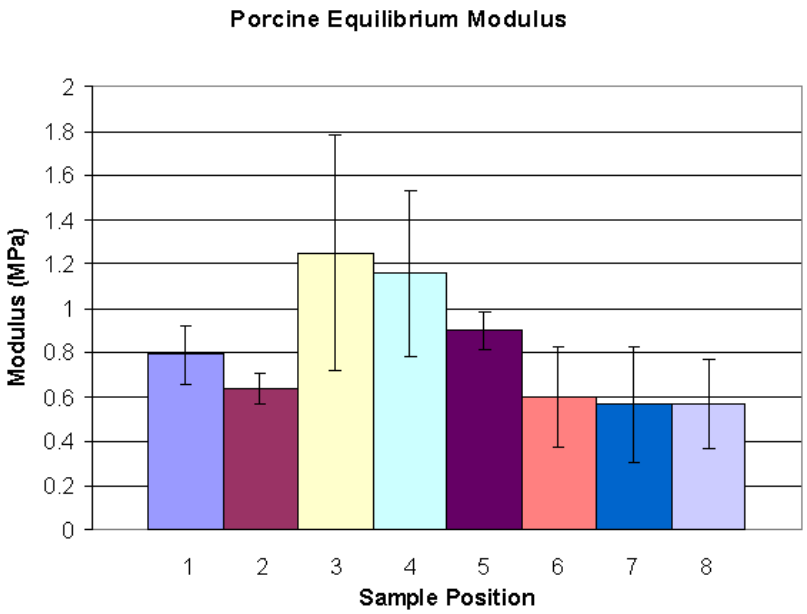

Figure 12-6: Equilibrium relaxation modulus with standard deviation for porcine samples (4 to 6 months)

12.6 Creep Modulus

Noteworthy features from Figure 12-7 are that the highest creep modulus was recorded at position 4 and the lowest observed creep modulus was recorded from a site located on the trochlea. Sample position 4 was confirmed to be the region with the highest creep modulus on a 97.5% confidence level. This is an indication that creep modulus is dependent on physiological compressive loading however this relationship could not be confirmed for all sampling sites across the femoral head.

Creep modulus can be understood as a measure of how a viscoelastic material responds to a constantly applied force. A higher comparative value of creep modulus will indicate that the material deforms less under this constant load. Therefore, stiffer viscoelastic materials should have a larger creep modulus under the same testing conditions. In keeping with the currently understood nature of AC, it would therefore be reasonable to assume that regions associated with larger compressive loading should maintain a higher creep modulus (Arokoski et al., 2000). This trend was observed in Figure 12-7. The highest creep modulus was recorded at position 4 and the lowest observed creep modulus was recorded from position 8 located on the trochlea. Sample position 4 was confirmed to be the region with the highest creep modulus on a 97.5% confidence level. This is an indication that creep modulus is dependent on physiological compressive loading. This trend was observed for chondrocyte activity is increased through mechanical stimuli (Mow et al., 2005).

Therefore, in regions subjected to larger compressive loading, greater amounts of proteoglycans will be synthesised. Increased proteoglycan content has been found to increase the stiffness of AC; hence regions of the femoral head that contain greater compressive loading would be expected to develop stiffer tissue (Klein et al., 2007).

This relationship was not as strongly indicated for the ovine specimens from study 2, with their equilibrium relaxation moduli showing a weak trend and their tangential stiffness measures appearing to be quite random. The reason for the sheep samples not displaying trends expected from previous work could be due to errors in sample preparation and small sample size.

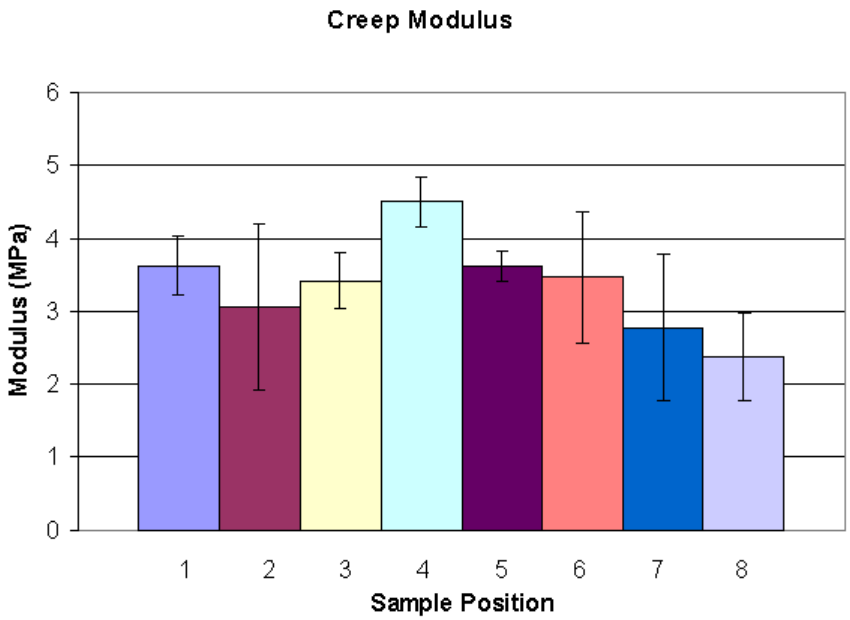

Figure 12-7: Average creep modulus and standard deviation for porcine samples

Porcine and ovine (study 2) AC specimens displayed similar stress relaxation and creep behaviour. Previous work conducted in this area has found AC displays viscoelastic properties; therefore, these results were expected (Wang et al., 2003). Although conducted under different testing conditions, the relaxation equilibrium modulus values displayed in this study were quite consistent with other research that has typically found the equilibrium modulus of AC from the femoral head to be between 0.5-1MPa (Arokoski et al., 2000).

This would indicate the validity of stress relaxation testing techniques conducted in this study.

Some of the porcine samples showed topological variation in their equilibrium modulus testing but it was not as strongly indicated as the results from the porcine stress relaxation testing. A possibility for this discrepancy is that the stress relaxation tests conducted in this study allowed the tissue to reach equilibrium conditions while creep testing did not. Another possibility for this observed difference is that the creep testing typically compressed the samples to 40% strain. AC has been observed to have depth dependent mechanical properties and hence testing at a much greater amount of compression would be likely to produce variations in behaviour across the topography of the femoral head (Guilak et al., 1995).

Creep testing that strained samples up to 40% would never be conducted *in vivo* due to the permanent damage that would be caused to the tissue. Therefore, these results can only be viewed as a comparative measure between samples and not as those produced from a possible future *in vivo* testing procedure.

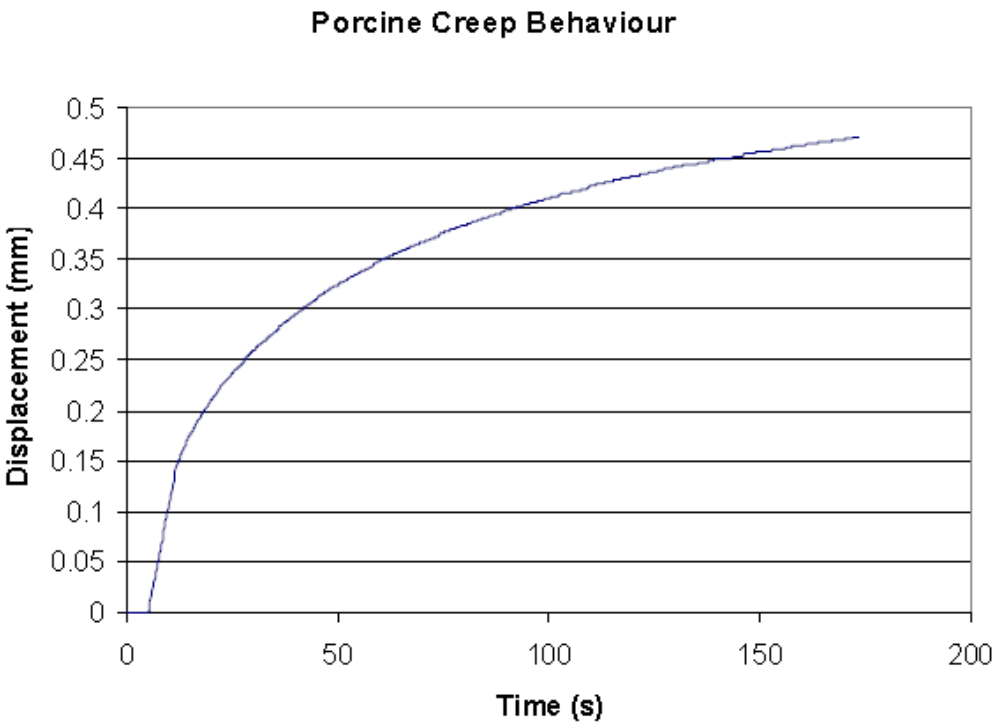

Figure 12-8: Typical porcine AC response to creep testing

Chapter 13 Study 5: Stiffness Testing of Neonatal Sheep

*This was a topological study to measure any discernible differences in mechanical properties of three-year old sheep cartilage. The study also observed the effects of specimen fixation upon the quality of image*s.

13.1 Study Objectives

A total of six sheep were available for the study giving twelve sample joints. Each joint was sampled with 3mm biopsy samples at the six sample positions shown in Figures 13-1 and 13-2.

This study was assisted by undergraduate student Tom Kierath.

Hyaline cartilage was sourced from the femoral heads of intact stifle (knee) joints from ovine specimens at four stages of maturity. Samples were harvested from foetuses at 123-124, 129-130 and 140-day gestation (average gestation period is 150 days) and seven-week post birth. All ovine samples were taken from waste material obtained from the Polglase research group, ethics approval number 07/100/565. In total, seventeen joints were collected, four joints per age group, with five joints from the 123/4-day gestation age group. Samples were harvested from subjects no later than two hours after being euthanized. The joints were disarticulated using a surgical scalpel to allow extraction of the hyaline cartilage lining the femoral head. Figures 13-1 and 13-2 show where the six cylindrical plugs were isolated from each joint using a 3mm diameter biopsy punch from lateral and medial condyles to encompass the posterior region, a physiologically load bearing region and the anterior region, a physiologically unloaded region and a centrally loaded. A 3mm punch was chosen to minimise sample curvature to facilitate confocal imaging and allow more uniform compression of cartilage specimens.

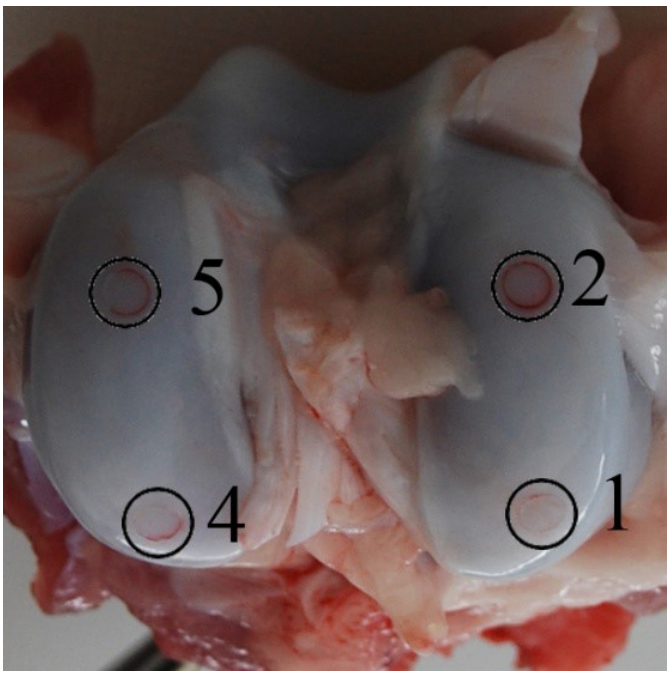

Figure 13-1: Distal view of femoral condyles showing sample sites 1, 2, 4 and 5

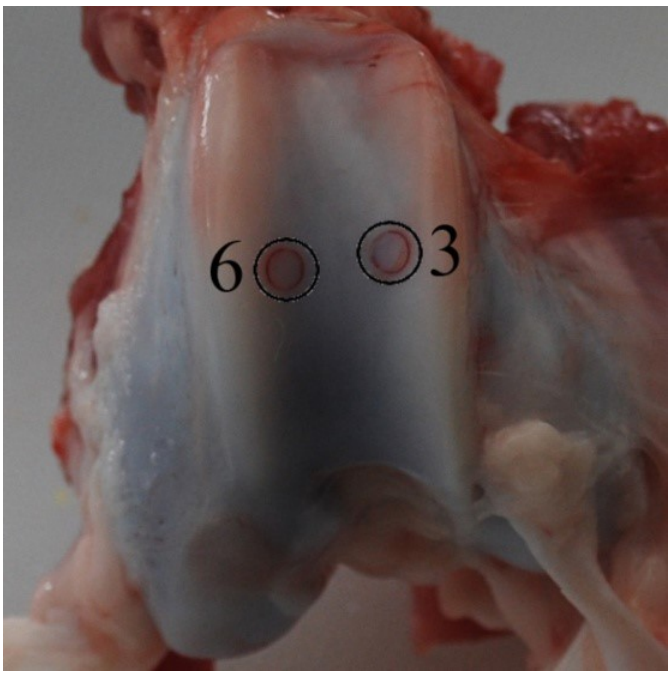

Figure 13-2: Anterior view of trochlea showing sample sites 3 and 6

13.2 Sample Images

The samples were imaged using an Optiscan F900e confocal microscope, operating in fluorescence mode with an excitation wavelength of 488nm. The laser power was set to 100% as this provided the clearest images. However, this introduced issues with photo bleaching, a process whereby contrast and hence image quality is reduced due to prolonged exposure to the excitation laser. An Olympus Plan Apo 60X oil immersion lens with a numerical aperture of 1.4 was also used. This lens gave lateral and axial resolutions of 0.23µm and 0.73µm, respectively, and a field of view of 100x100µm. This lens was chosen as it provided the highest resolution of the lenses available for use with the Optiscan F900e microscope.

The Optiscan F900e software was used for image acquisition. To reduce the level of noise in the images four scans were taken at each depth; consequently, each final image represented the average of the four scans. This was found to be optimal as a higher number of scans increased the rate of photo bleaching. To image the sample, the manual stage controls were used to focus on the AC surface. Images were recorded at 1µm depth increments, starting at the surface, and progressing deeper into the sample. Images were recorded as stacks of 50 image tiff files. If a significant fibrous component was seen in the last few images, a second image stack was recorded, starting at the end position of the previous stack. Representative images are shown below. The exhaustive data set is stored digitally.

Throughout the study several thousand individual images were recorded using the confocal microscope. As such it is impossible to present the entire data set collected within this thesis. For the purposes of the report, representative images from each age group and sample locations have been selected for presentation.

These images were chosen to reflect the structure of the cartilage structure within the specific sample set. For each sample location and age group shown, one image was taken from the surface of the cartilage sample, and a second taken from 20µm beneath the sample surface. These positions were chosen as they provide a visualisation of the cartilage surface as well as an image of the lower levels of the superficial zone. This study used an early version of the imaging software.

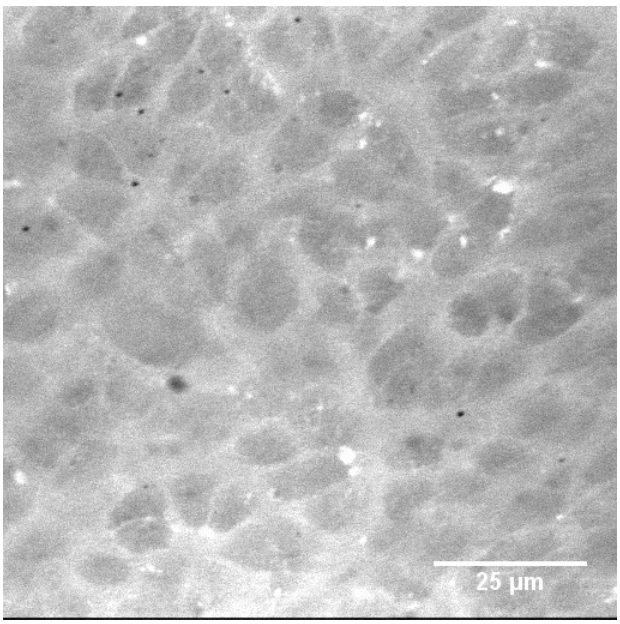

Image 13-1: 90 day, site 3 @ surface

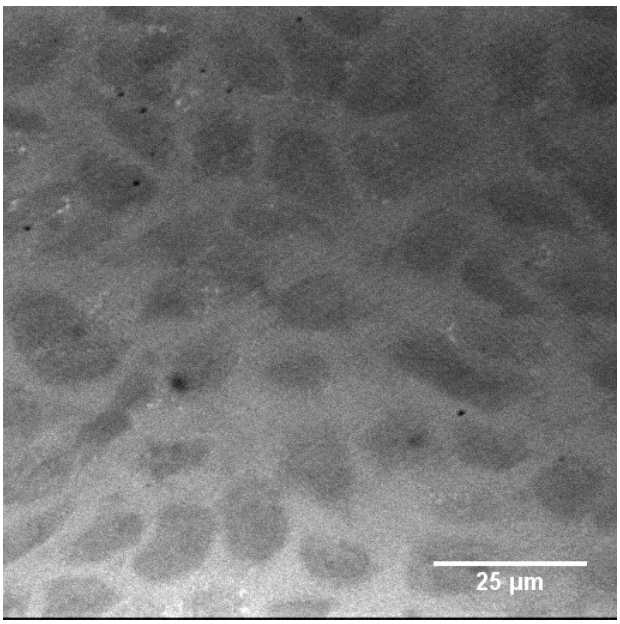

Image 13-2: 90 day gestation, site 3 @ 20 µm

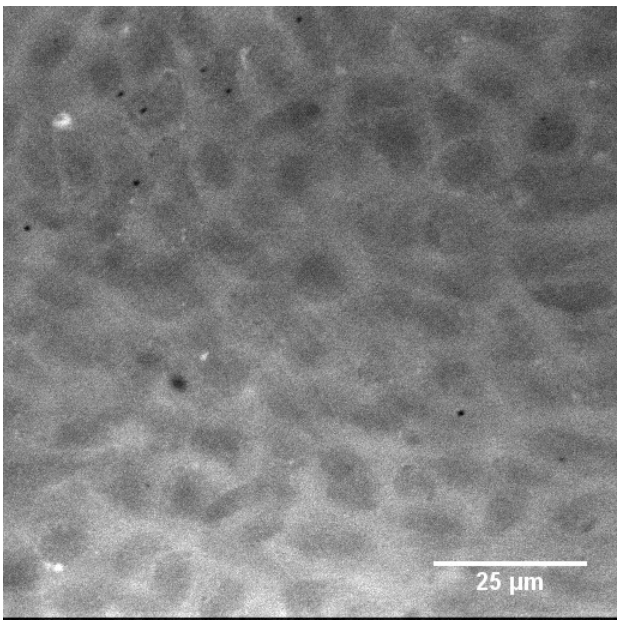

Image 13-3: 90 day, site 6 @ surface

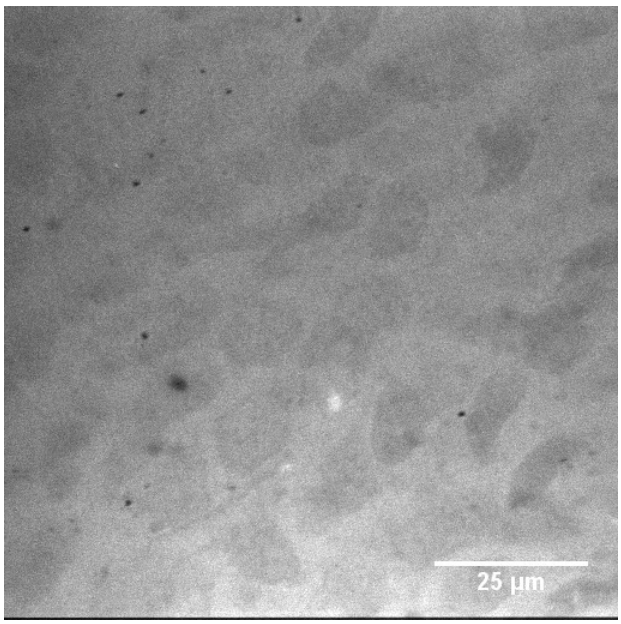

Image 13-4: 90 day, site 6 @ 20µm

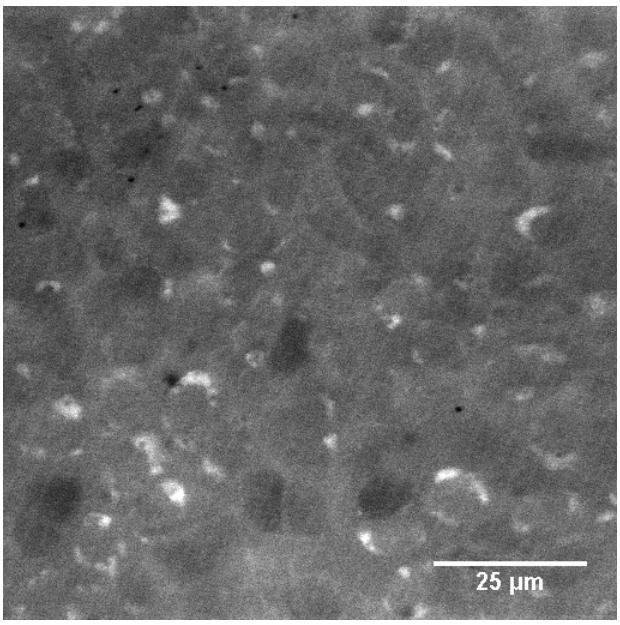

Image 13-5: 100 day, site 3 @ surface

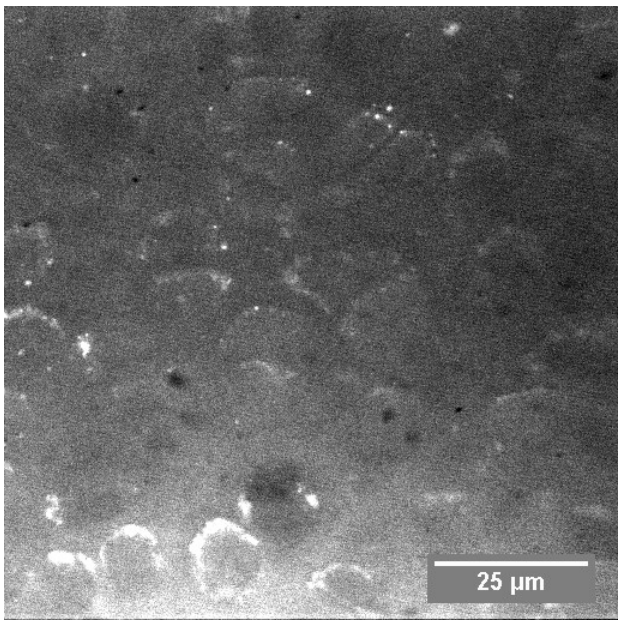

Image 13-6: 100 day, site 3 @20µm

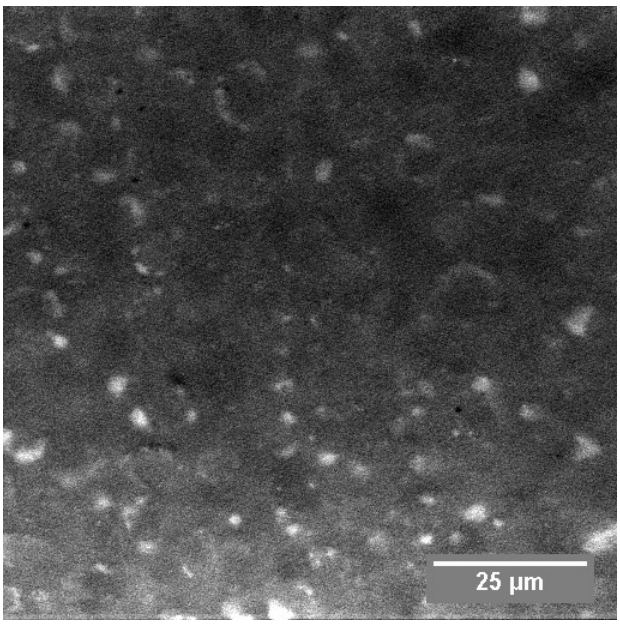

Image 13-7: 100 day, site 6 @ surface

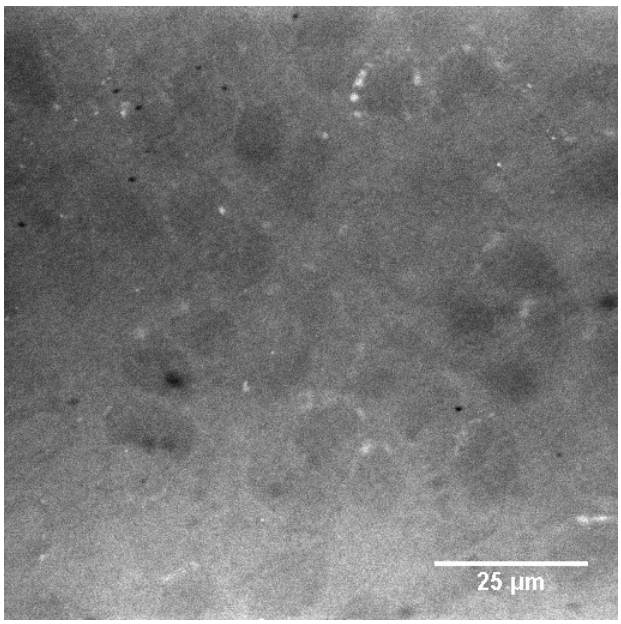

Image 13-8: 100 day, site 6 @ 20µm

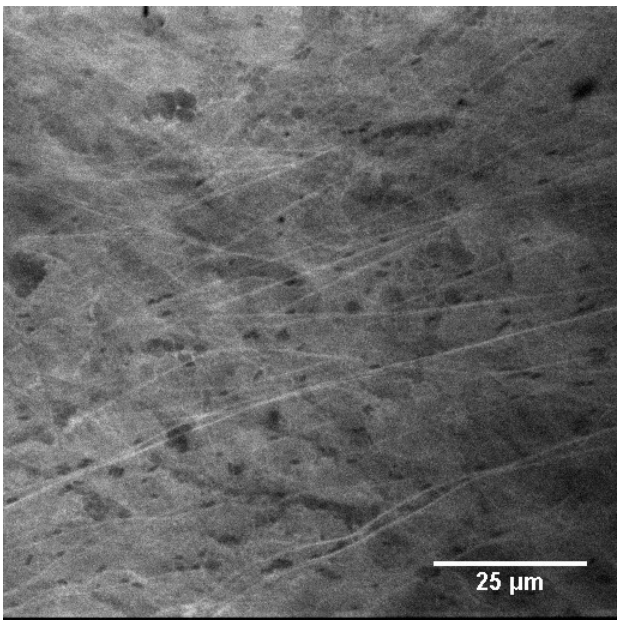

Image 13-9: 123 day, site 1 @ surface

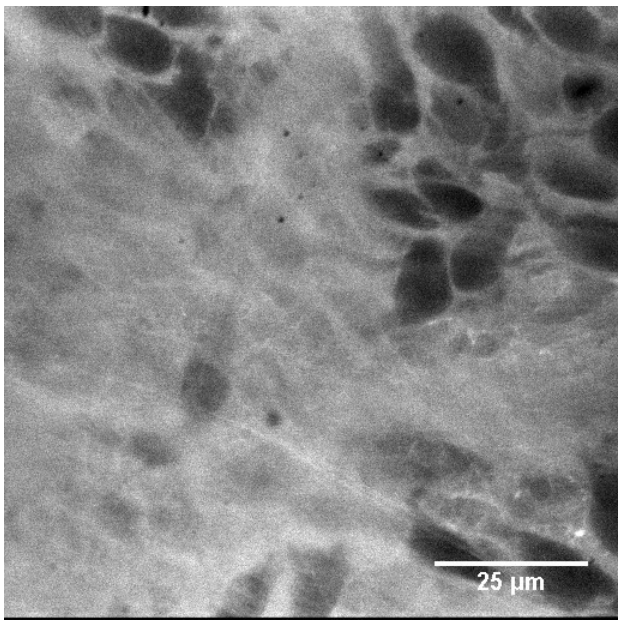

Image 13-10: 123 day, site 1 @ 20µm

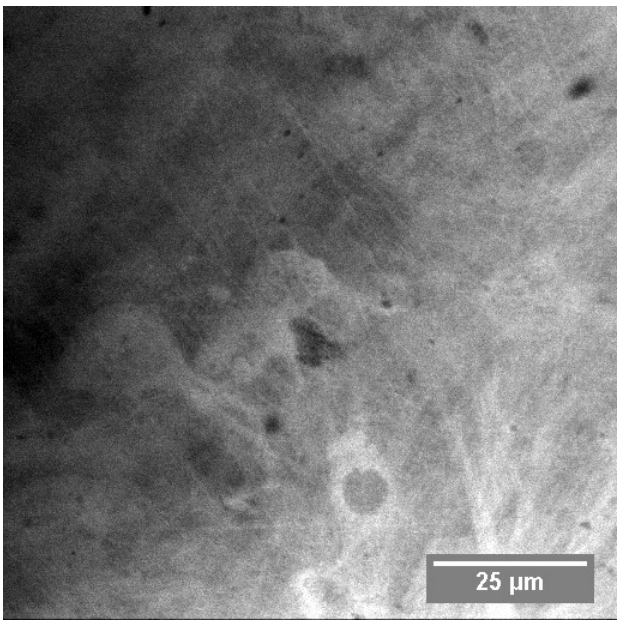

Image 13-11: 123 day, site 2 @ surface

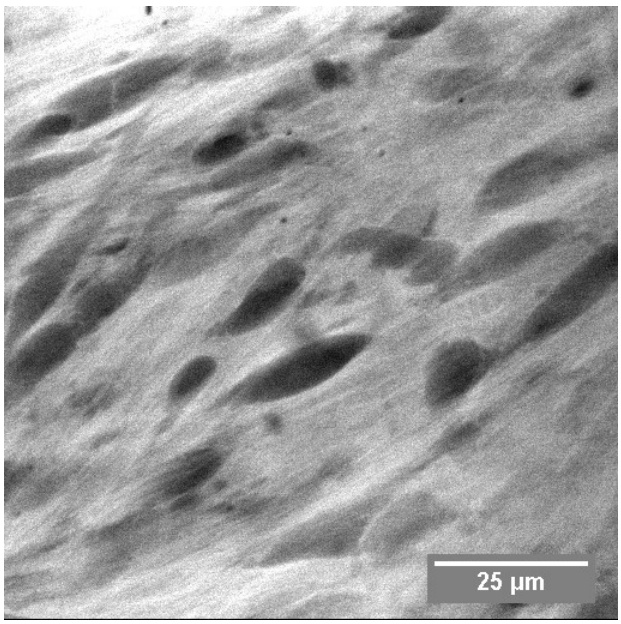

Image 13-12: 123 day, site 2 @ 20 µm

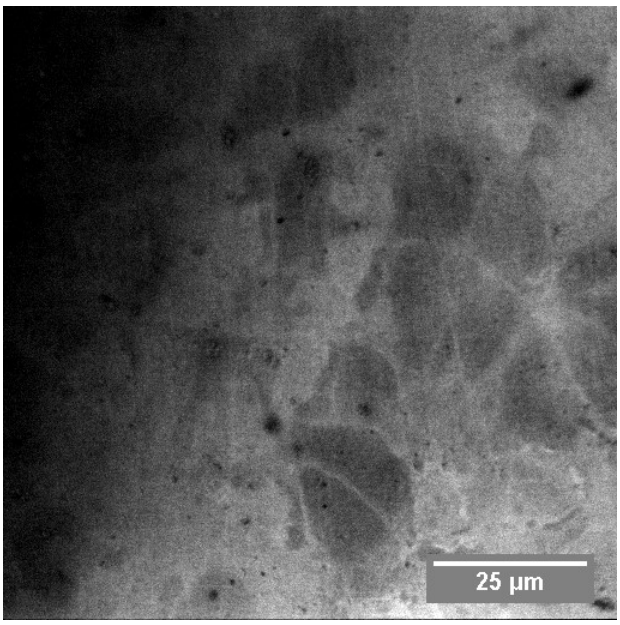

Image 13-13: 123 day, site 3 @ surface

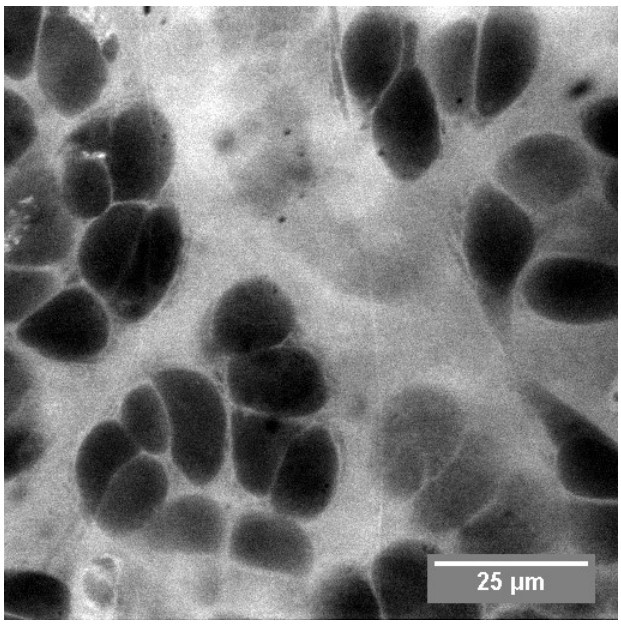

Image 13-14: 123 day, site 3 @ 20 µm

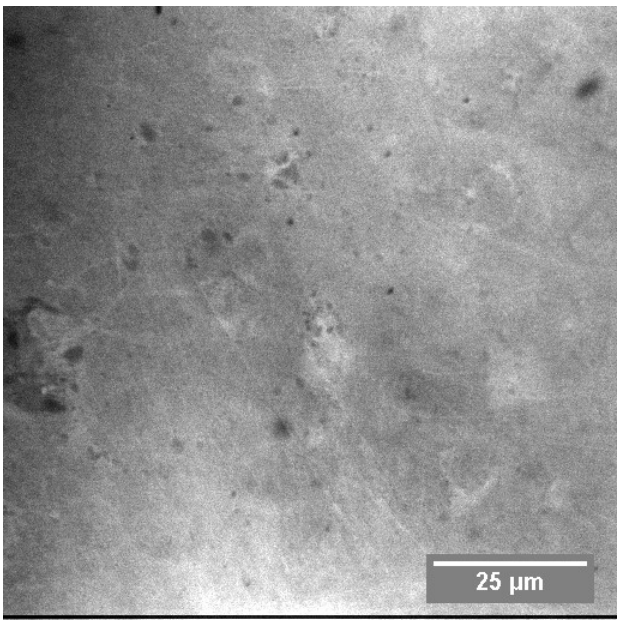

Image 13-15: 123 day, site 4 @ surface

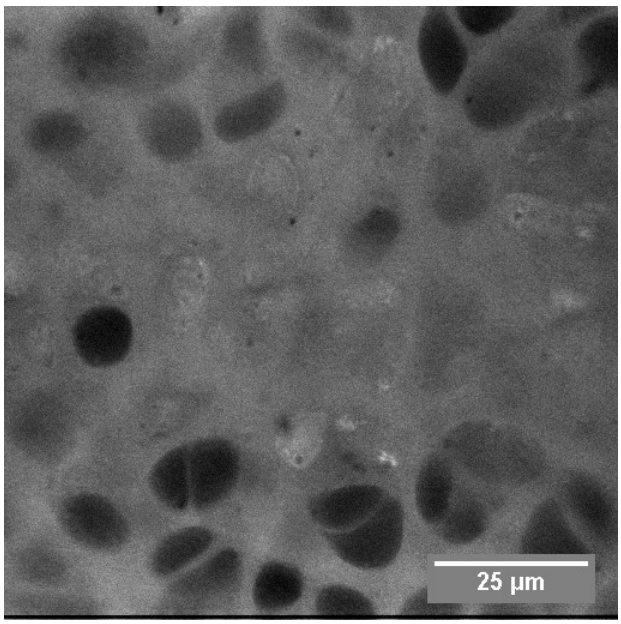

Image 13-16: 123 day, site 4 @ 20 µm

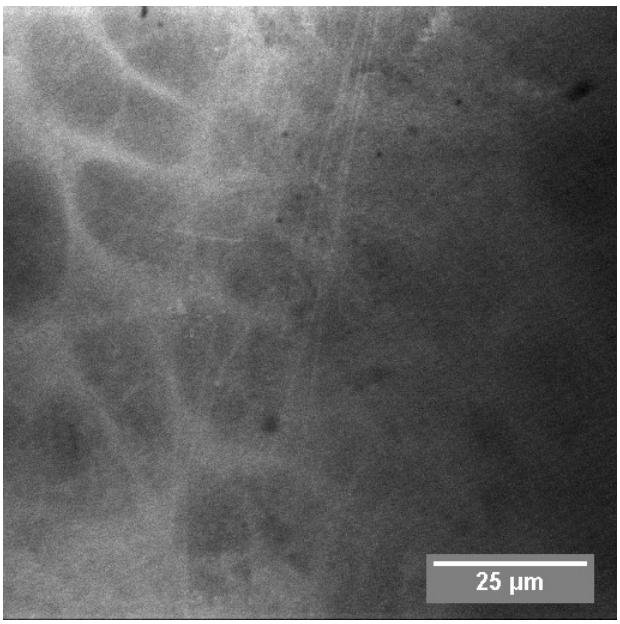

Image 13-17: 123 day, site 5 @ surface

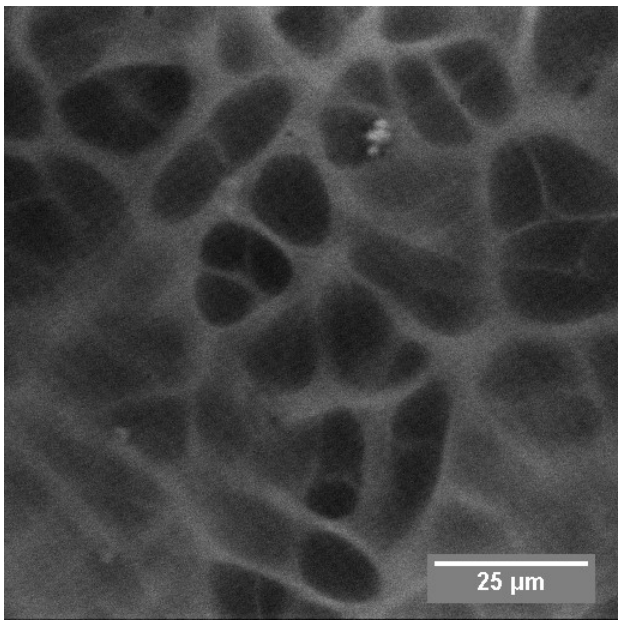

Image 13-18: 123 day, site 5 @ 20 µm

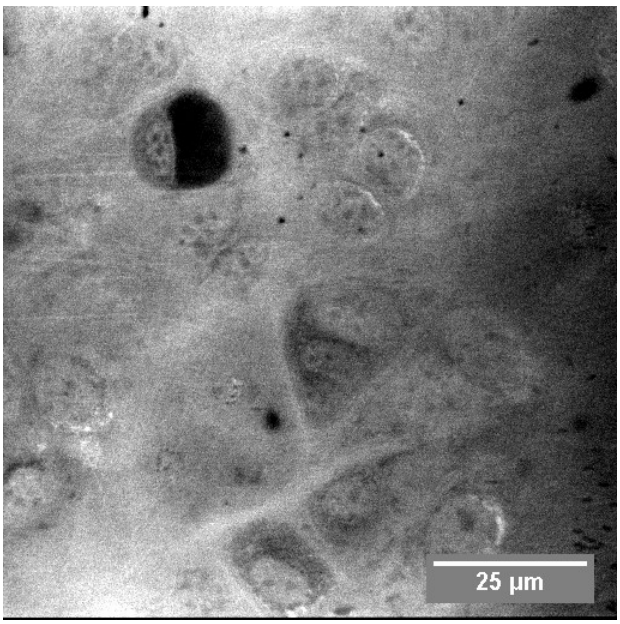

Image 13-19: 123 day, site 6 @ surface

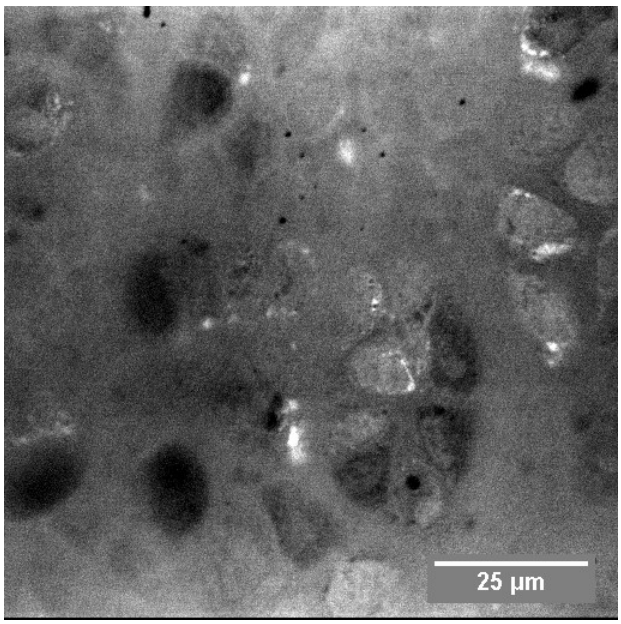

Image 13-20: 123 day, site 6 @ 20 µm

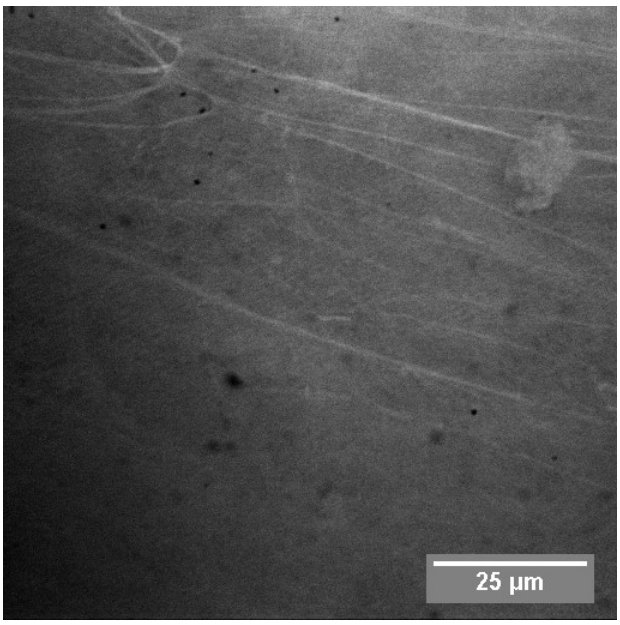

Image 13-21: 130 day, site 2 @ surface

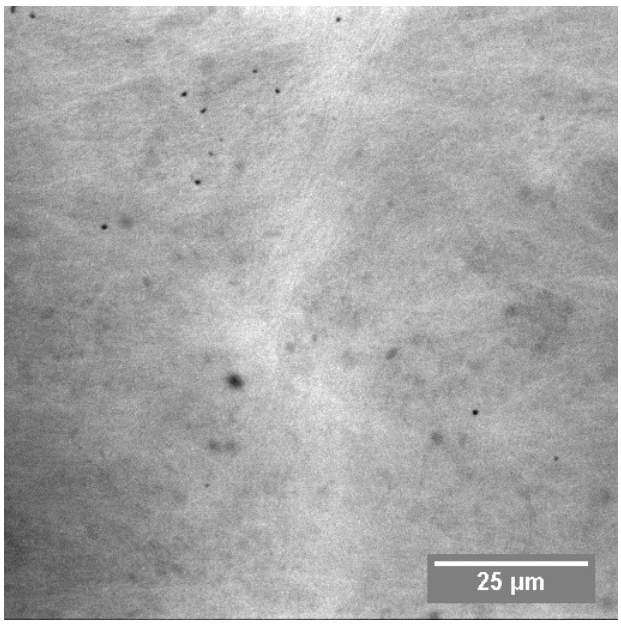

Image 13-22: 130 day, site 2 @ 20 µm

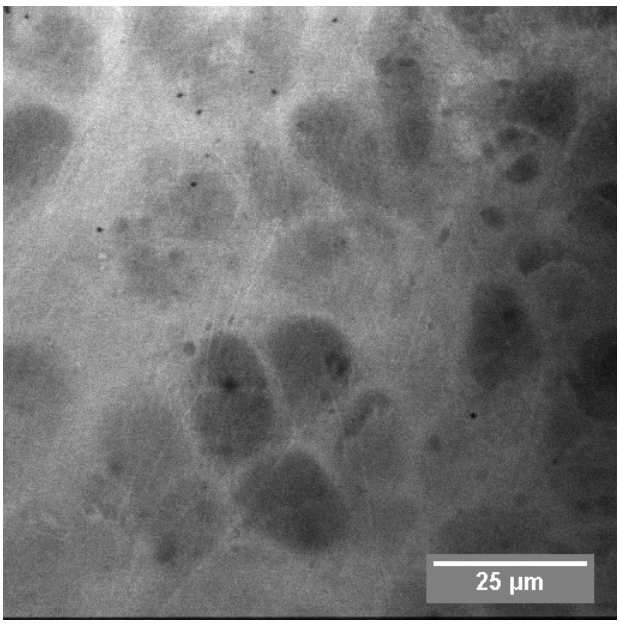

Image 13-23: 130 day, site 5 @ surface

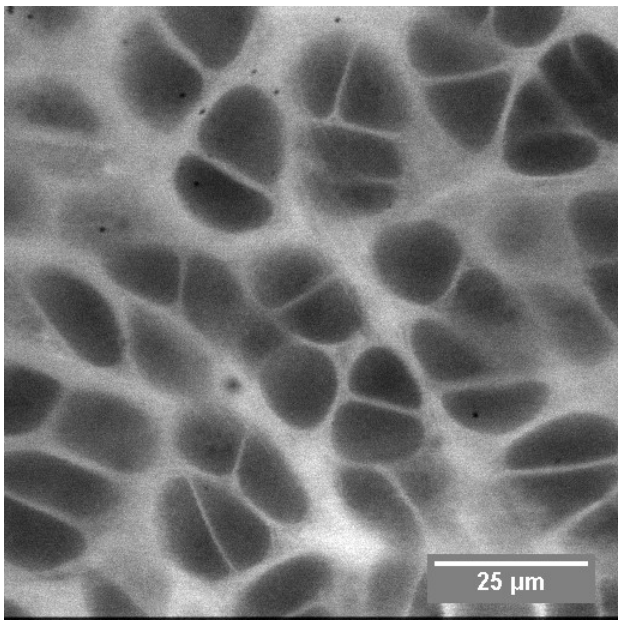

Image 13-24: 130 day, site 5 @ 20 µm

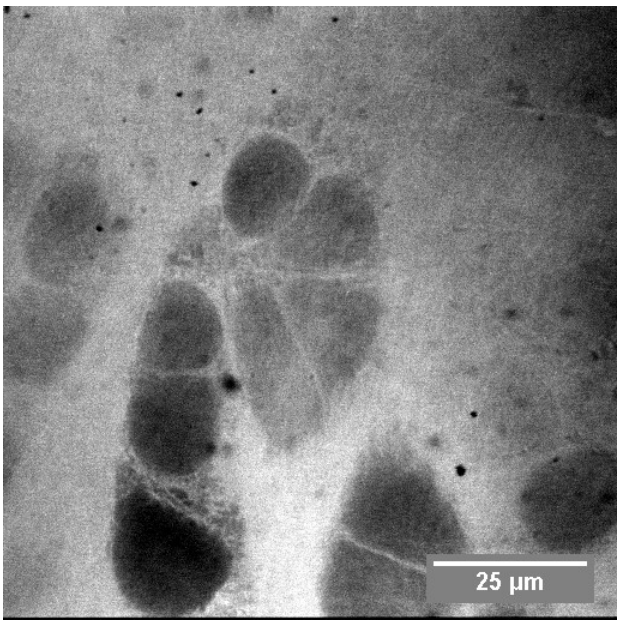

Image 13-25: 130 day, site 6 @ surface

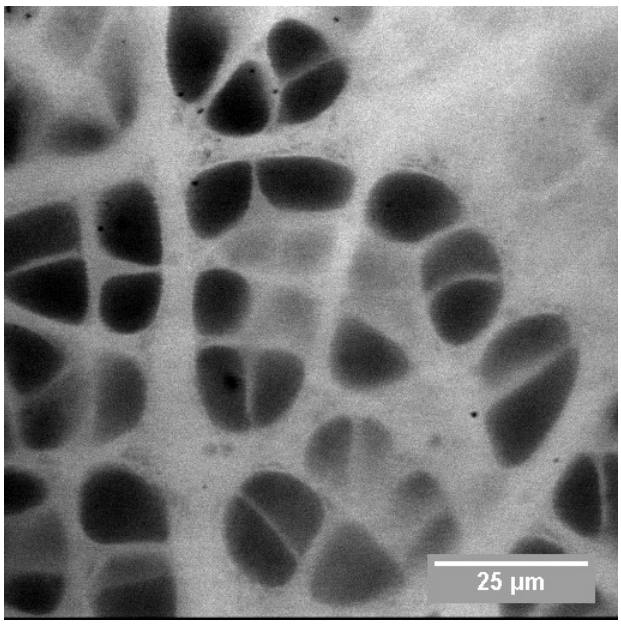

Image 13-26: 130 day, site 6 @ 20 µm

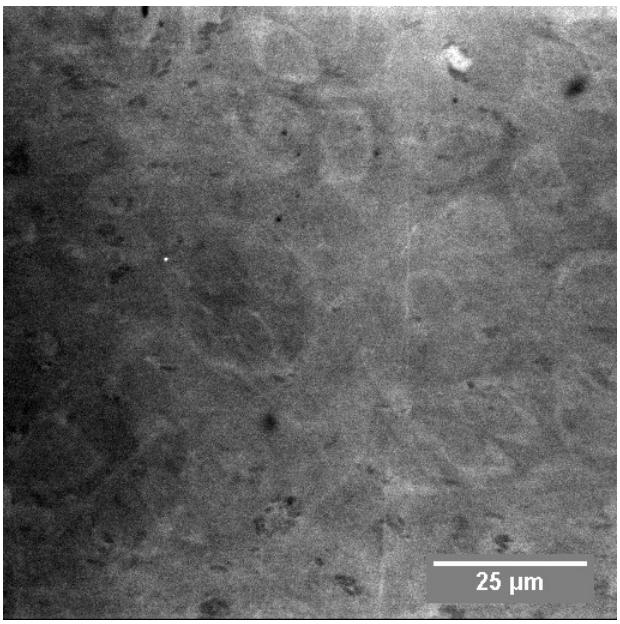

Image 13-27: 140 day, site 1 @ surface

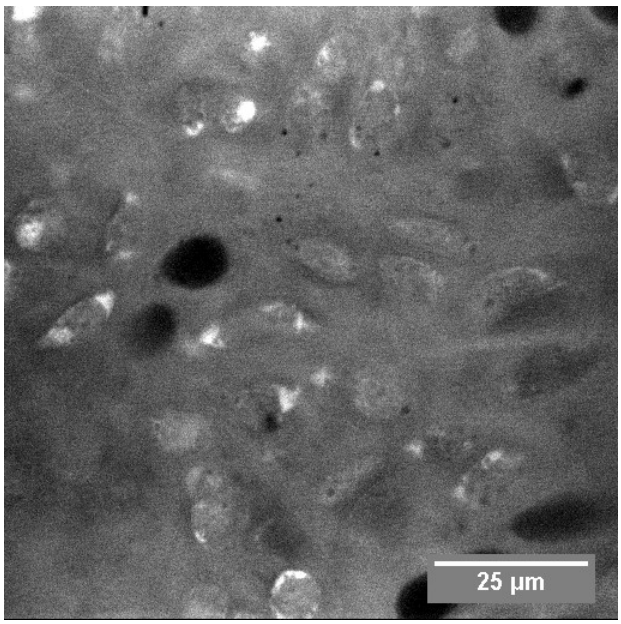

Image 13-28: 140 day, site 1 @ 20 µm

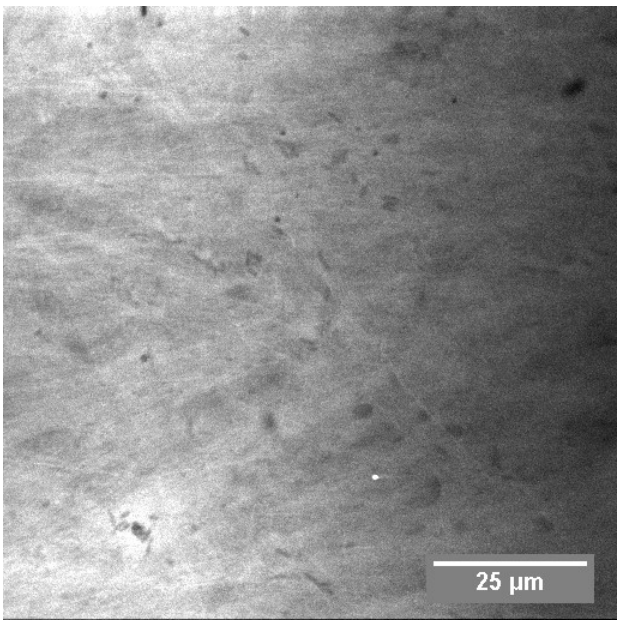

Image 13-29: 140 day, site 2 @ surface

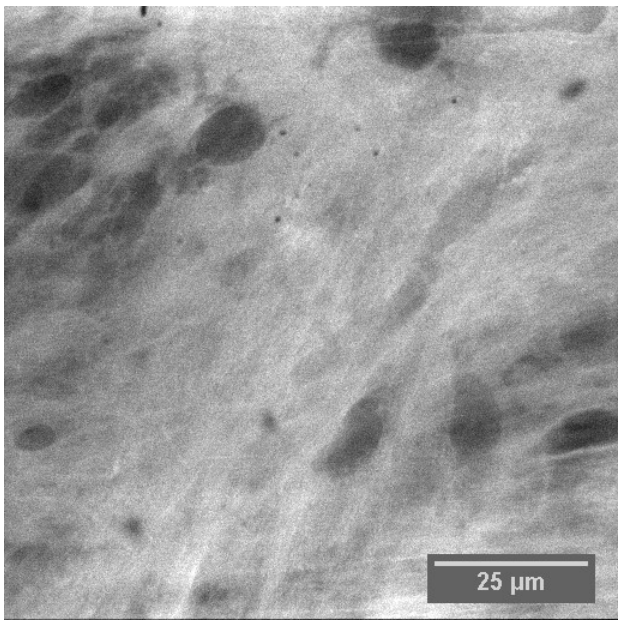

Image 13-30: 140 day, site 2 @ 20 µm

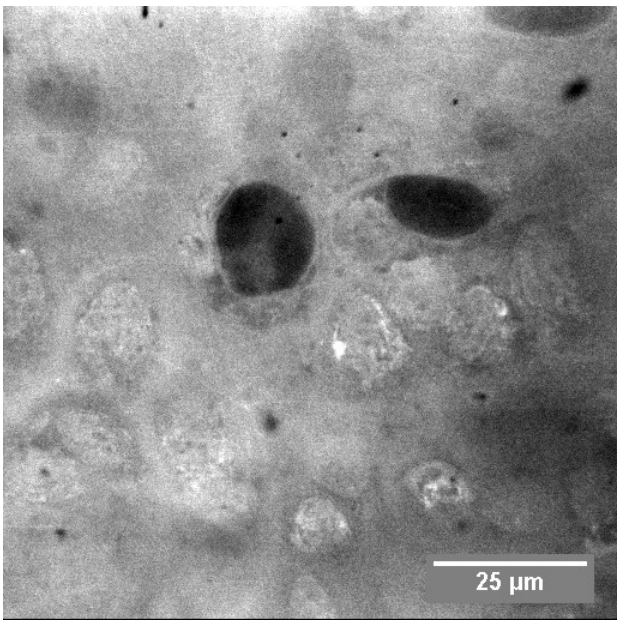

Image 13-31: 140 day, site 3 @ surface

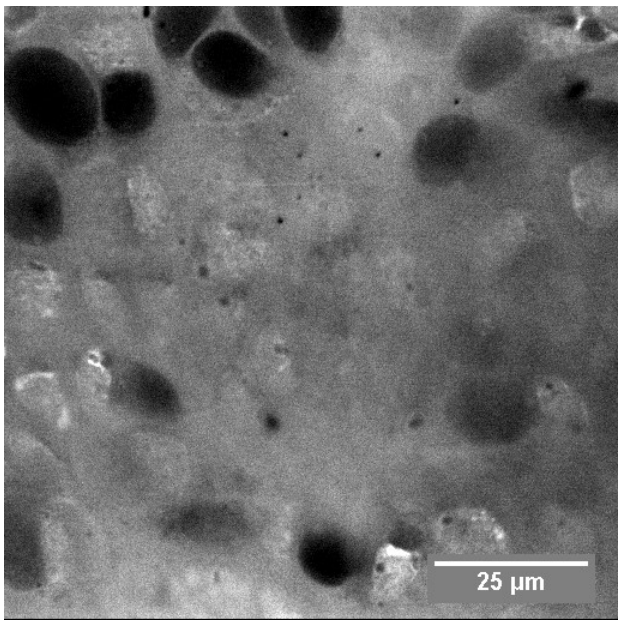

Image 13-32: 140 day, site 3 @ 20 µm

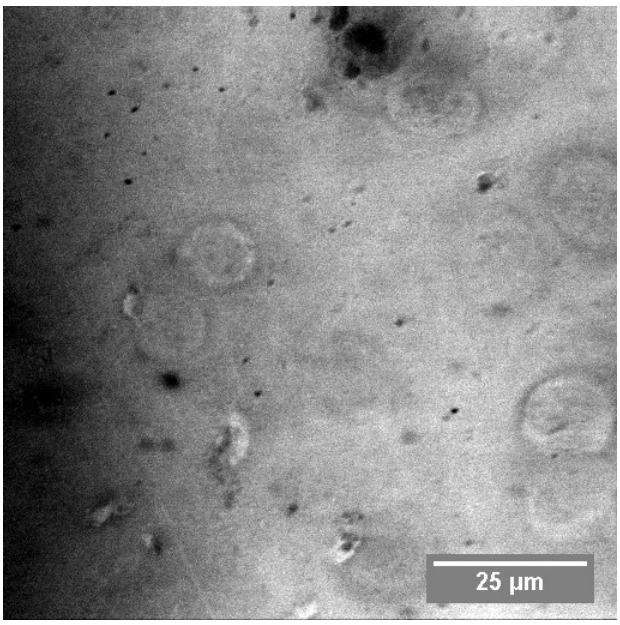

Image 13-33: 140 day, site 4 @ surface

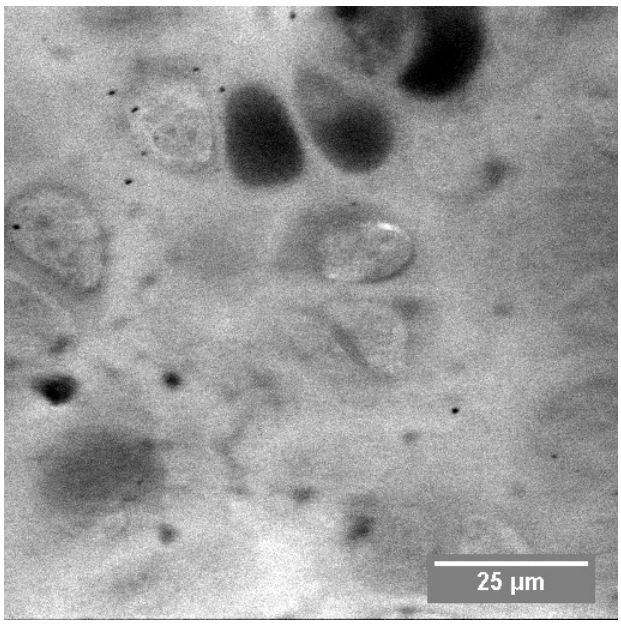

Image 13-34: 140 day, site 4 @ 20 µm

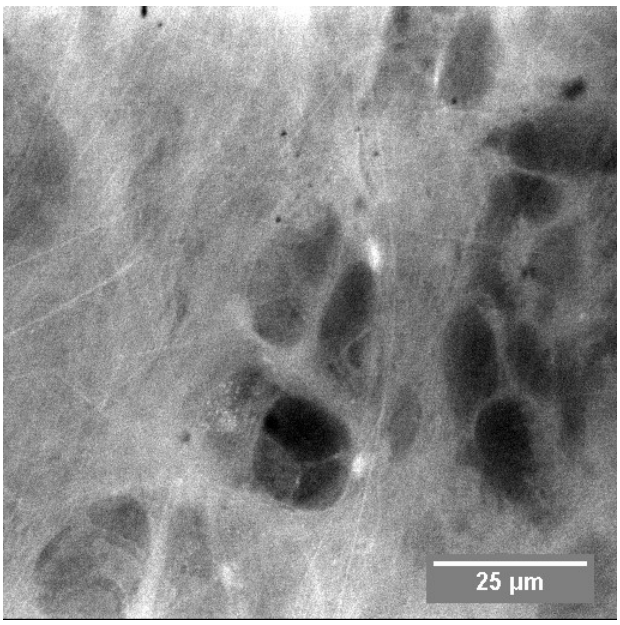

Image 13-35: 140 day, site 5 @ surface

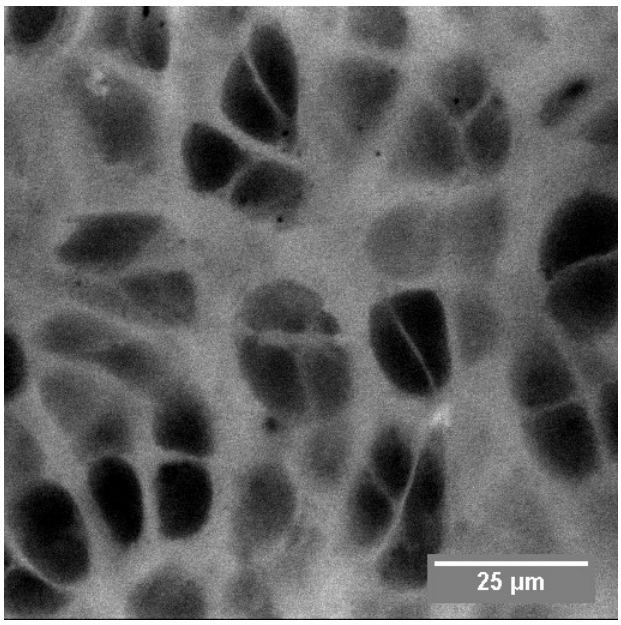

Image 13-36: 140 day, site 5 @ 20 µm

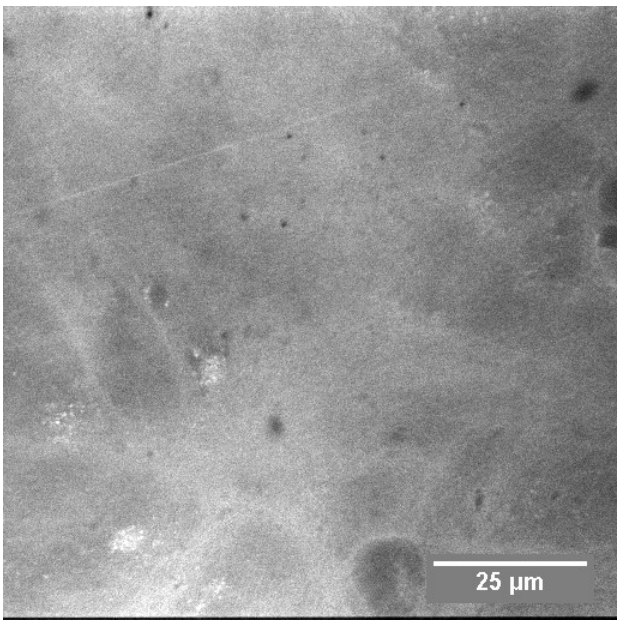

Image 13-37: 140 day, site 6 @ surface

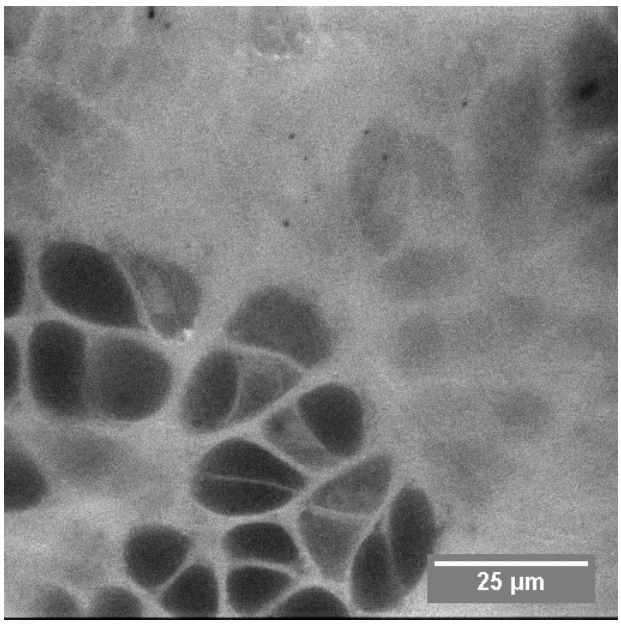

Image 13-38: 140 day, site 6 @ 20 µm

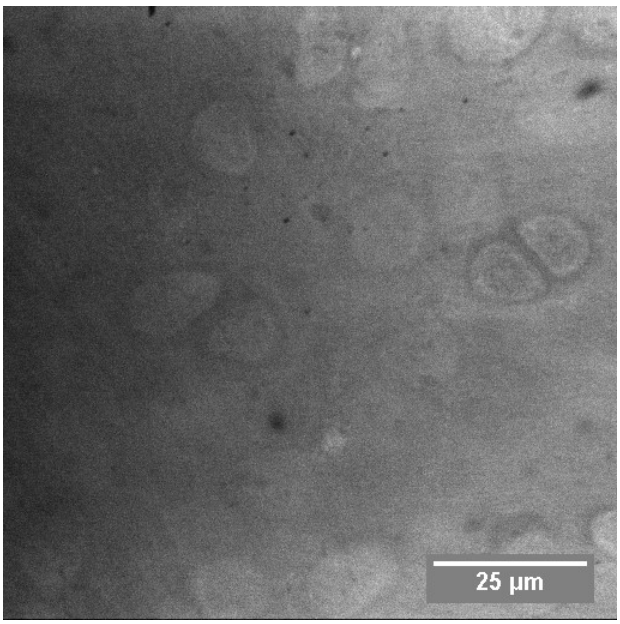

Image 13-39: 7 day postnatal, site 2 @ surface

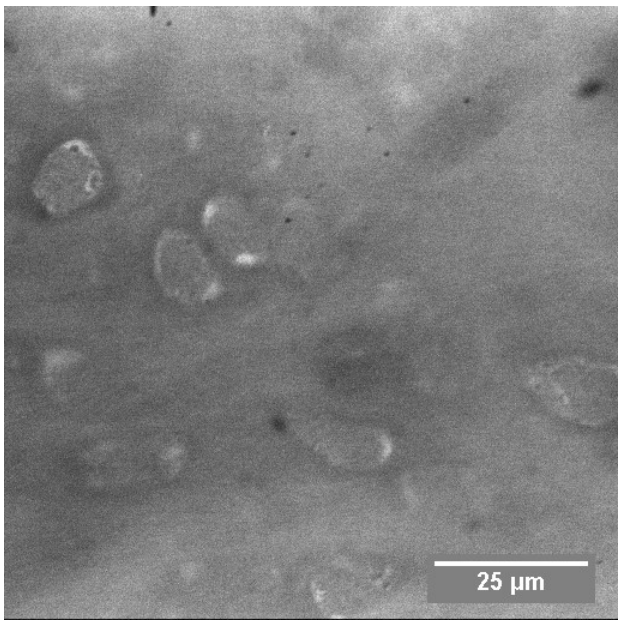

Image 13-40: 7 day postnatal, site 2 @ 20 µm

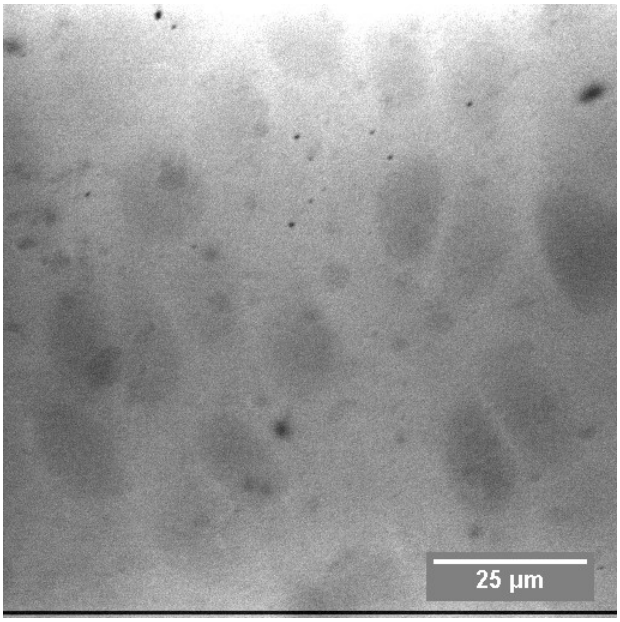

Image 13-41: 7 day postnatal, site 4 @ surface

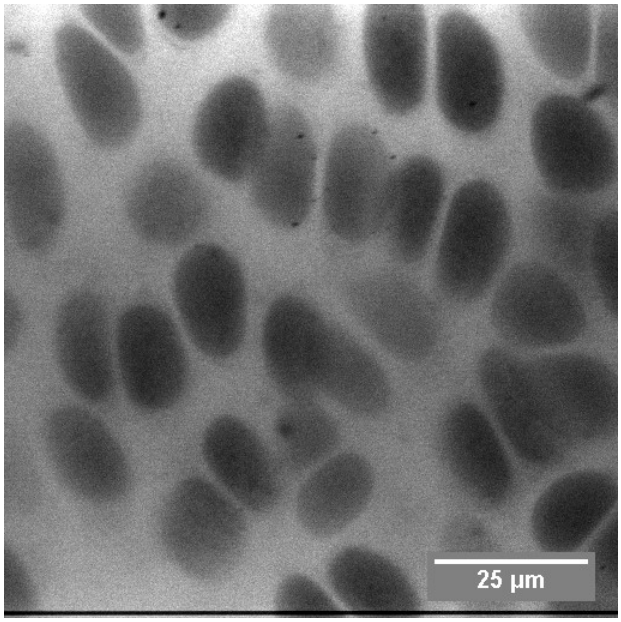

Image 13-42: 7 day postnatal, site 4 @ 20 µm

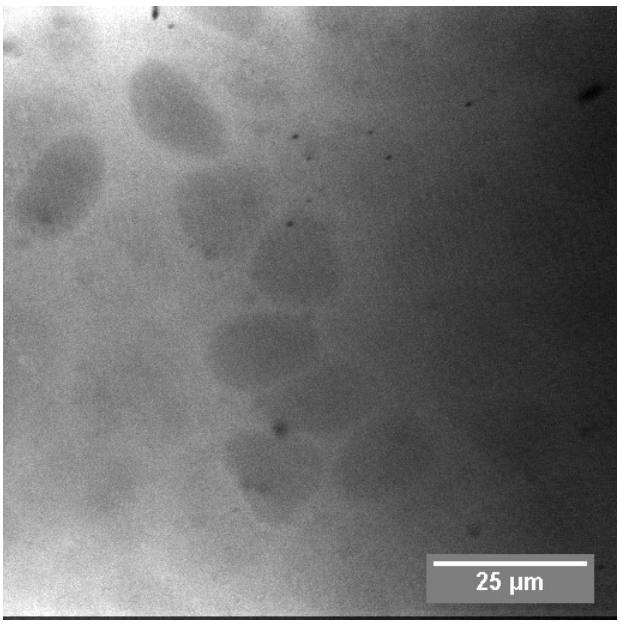

Image 13-43: 7 day postnatal, site 5 @ surface

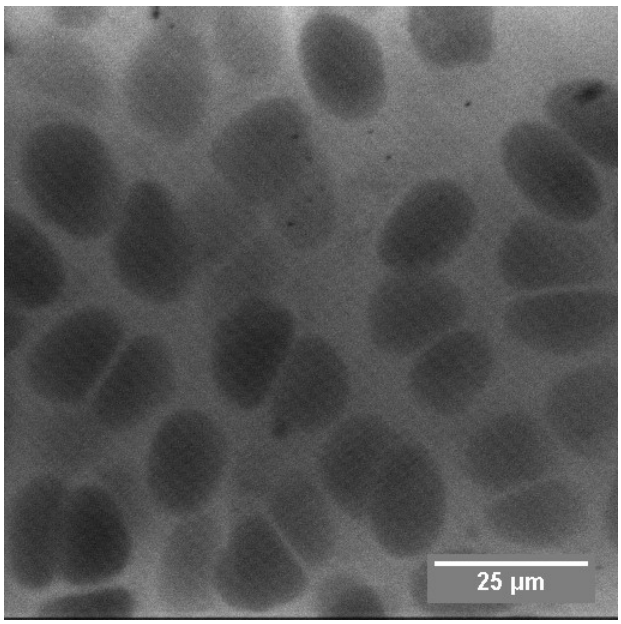

Image 13-44: 7 day postnatal, site 5 @ 20 µm

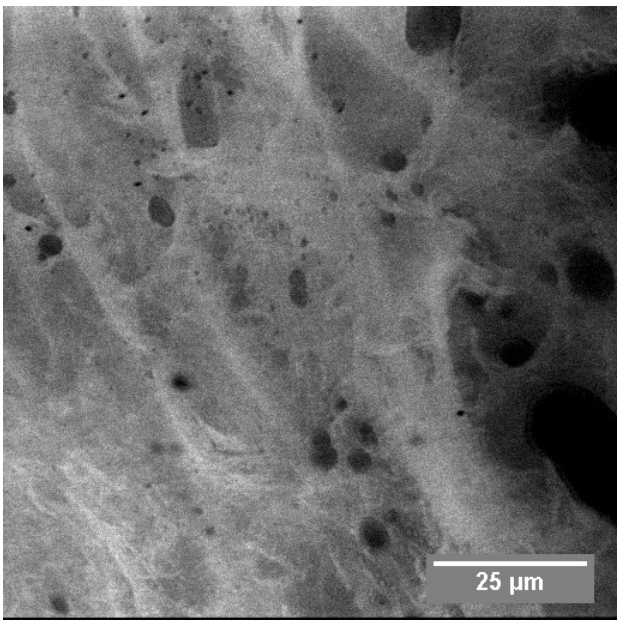

Image 13-45: 5 years old, site 2 @ surface

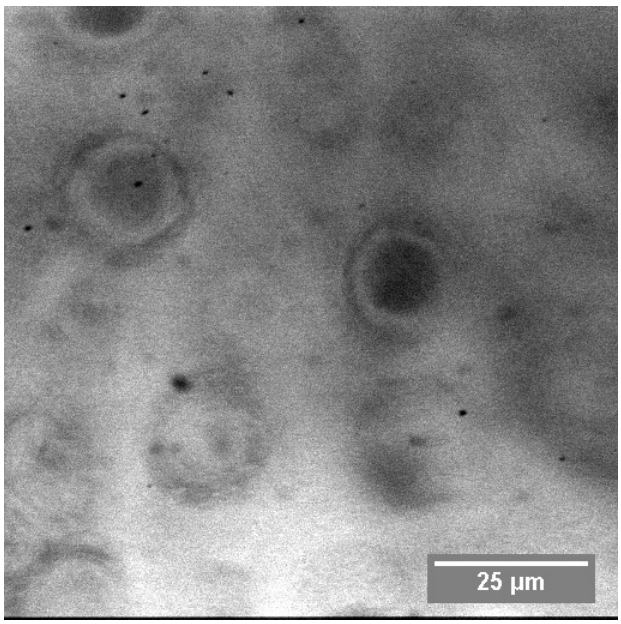

Image 13-46: 5 years old, site 2 @ 20 µm

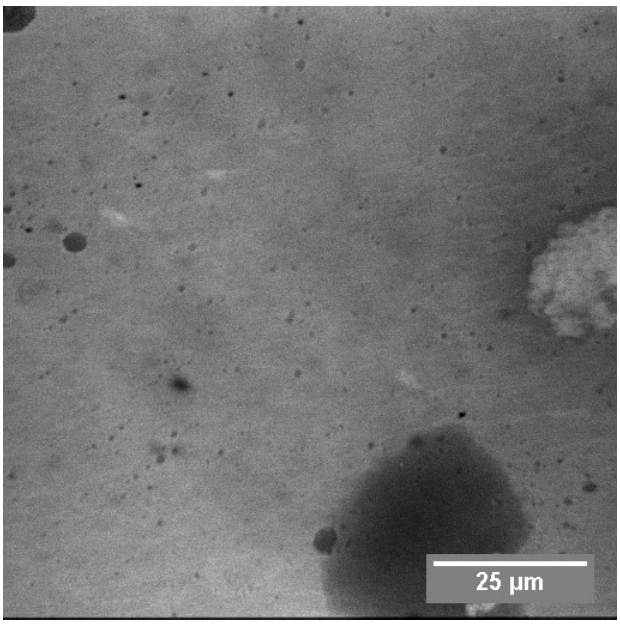

Image 13-47: 5 years old, site 6 @ surface

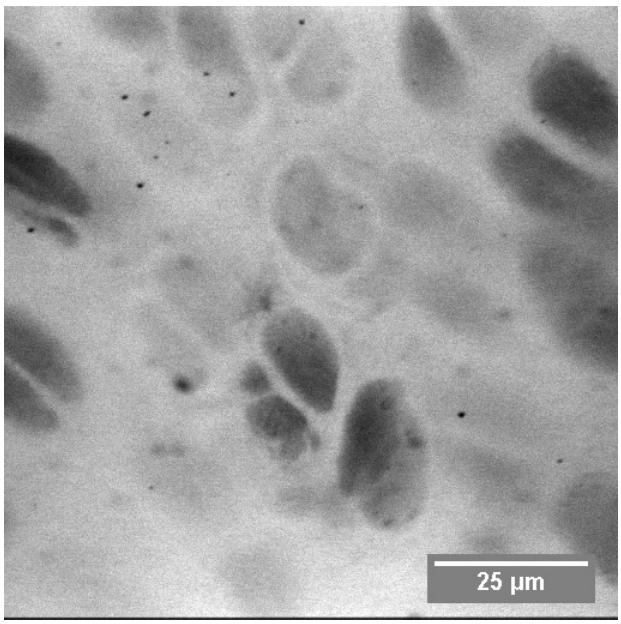

Image 13-48: 5 years old, site 6 @ 20 µm

Table 13-1: Summary of confocal microscope observations.

Position	1 PLC	2 ALC	3 LT	4 PMC	5 AMC	6 MT
90-day gestation	No fibres present	No fibres present	No fibres present	No fibres present	No fibres present	No fibres present
100-day gestation	No fibres present	No fibres present	No fibres present	No fibres present	No fibres present	No fibres present
123-day gestation	Surface fine fibres, Mesh type fibres present	Surface fine fibres, Mesh type fibres present	Fibre type difficult to determine Variation in fibre layer thickness	Thin fibrous layer present. Fibre type difficult to determine	Surface fine fibres, No mesh type fibres present	Surface fine fibres in 50%. No mesh type fibres present
130-day gestation	Surface fine fibres, mesh type fibres present	Surface fine fibres, mesh type fibres present	Very few Surface fine fibres, no mesh type fibres present	No surface fibres present	Surface fine fibres, mesh type fibres present	Surface fine fibres in 50%. No mesh type fibres present
140-day gestation	Surface fine fibres, Mesh type fibres present	Surface fine fibres, Mesh type fibres present	Few fine fibres on surface	Few fine fibres on surface, No mesh type fibres present	Surface fine fibres No mesh type fibres present	Surface fine fibres in 33%. No mesh type fibres present
7 weeks postnatal	Surface fine fibres. No mesh type fibres present	Surface fine fibres No mesh type fibres present	Few fine fibres on surface. No mesh type fibres present.	No surface fibres present	No surface fibres present	Few fine fibres on surface in 33%. No mesh type fibres present.
5 years postnatal	Surface fine fibres, no mesh type fibres present	Surface fine fibres, no mesh type fibres present	No surface fibres present	No surface fibres present	No surface fibres present	No surface fibres present

13.3 Study 5 Findings

The sheep used in the study ranged in age from 90-day gestation to five years postnatal. The amount of visible collagen was found to increase with age to a peak during foetal development and then at 140-day gestation decrease with cartilage maturity. The type and amount of collagen present was found to be dependent on the sample location within the joint.

Collagen type II fibre was present in all cases and increased with age and depth.

The fibrous layer was found to be significantly thicker on the lateral condyle than either the medial condyle or trochlea. The thickness of the layer increased towards 130-day gestation then decreased with maturity.

Fibre orientation appeared randomly distributed over all samples, except for sample 2, due to the close proximity towards the attachment of the lateral collateral ligament. Some of the thicker fibres may well be associated with the ligament anchor points.

Type I and type III collagen fibre development peaked at the 129/130-day gestation age group. After 130-day samples, the thickness of the fibre layer decreased with age. This thickness further decreased after birth, because of normal anatomical loads being applied during movement and standing. Note that due to staining with FTIC it was not possible to image elastin.

The mechanical use of the knee appears to strongly influence development of the fibrous zone in maturing sheep. In postnatal ovine cartilage sample the depth of the visible fibrous layer decreased with age. The depth thinning of the superficial layer is also observed in other studies of sheep aging from one to five years, harvested for observation of the superficial zone in adult sheep. It was also clear that the number of fibres in the very superficial zone increased with age. That is, the fibres appeared to be condensed into a thinner layer rather than depleted and removed from the samples. The presence of type I and type II collagen is integral with the development of mature cartilage.

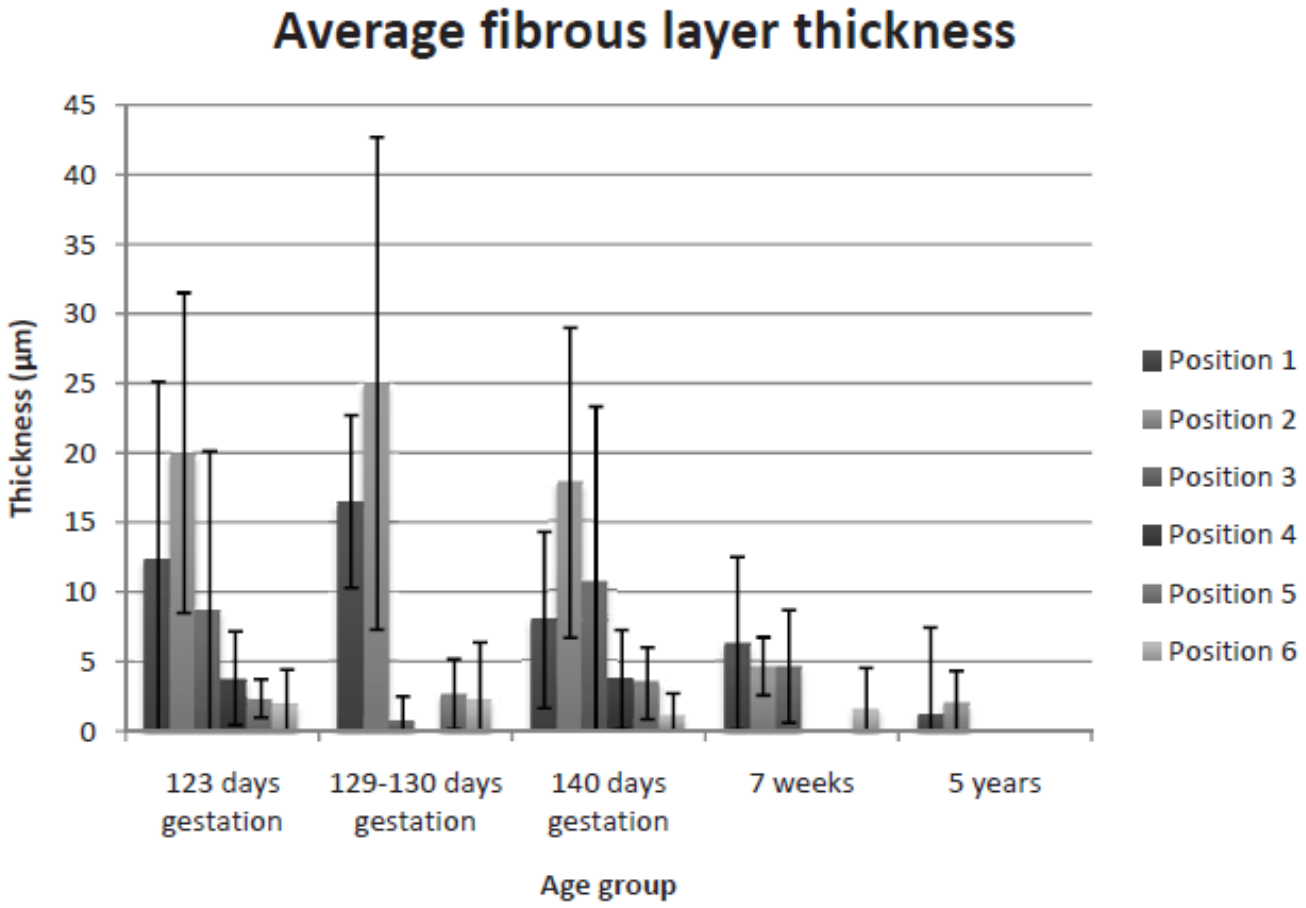

Figure 13-3: Summary of fibrous superficial layer thickness as a function of age and sampling position.

From Figure 13-3 the thickness of the fibre layer varies with both age and topological position across the femoral head of the knee joint. The standard deviation is high which implies that the depth of the fibre layer varies with topology. It is also apparent that the shape of the topological variation is similar across the age groups. These results are replotted in Figures 13-5 and 13-6.

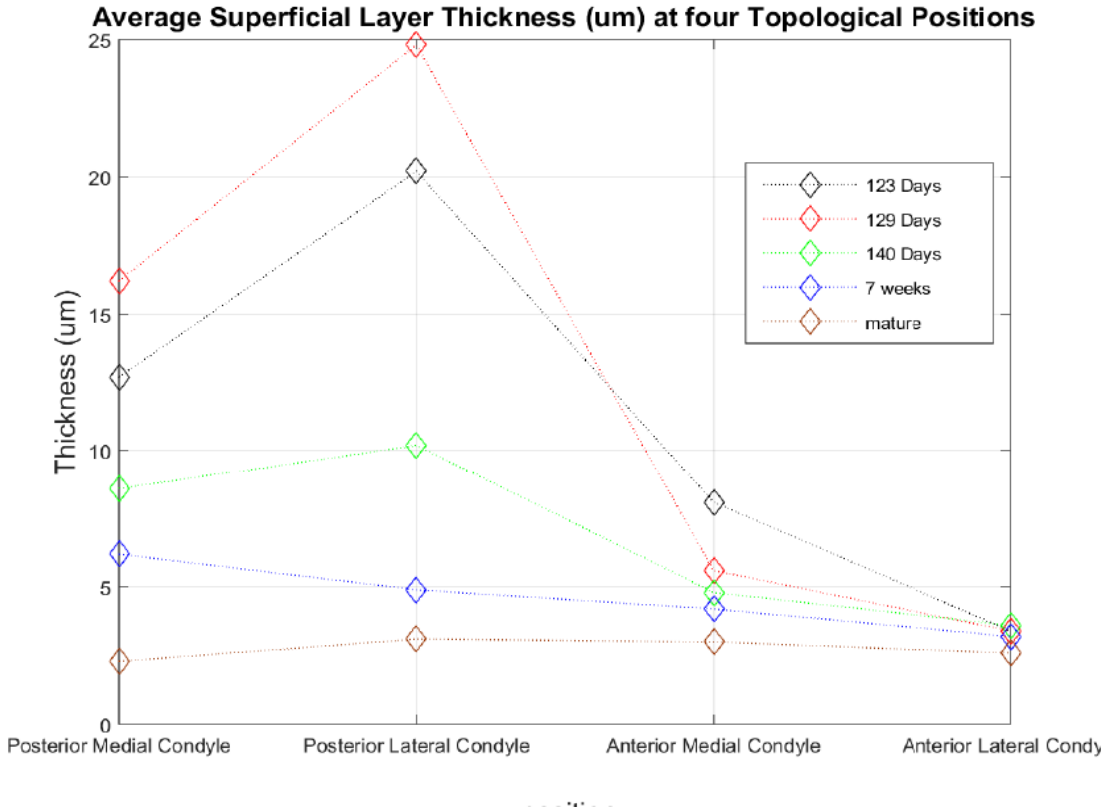

Figure 13-4: Superficial layer thickness as a function of sample position and age.

Figure 13-4 demonstrates that the superficial layer thickness is sample site dependent. Again, from Figure 13-3 there is a large variance between measurements at each point. This is due to the highly variable thickness across the sample site as well as within each site. Thickness is estimated from confocal stacks of 300µm square. More repetitive stacks would be required to give a statistically meaningful estimate of the true thickness. However it is clear that the site thickness also varies with age. Thickness reaches a maximum around 128/129-day gestation and decreases post birth. Interestingly, the superficial zone thickness becomes more uniform with age. This does not support the preconceived idea that the fibre zone thickness was dependent the notion of loaded and non-load bearing regions within the femoral head.

Figure 13-5 shows the age development in superficial fibre thickness. This gives a better idea of the growth in the superficial zone to about 128/129-day gestation. Thickness then decreases until birth. Following birth environment facts influence the collapse of the fibre bundles into layers due to the use of the joint in normal mobility.

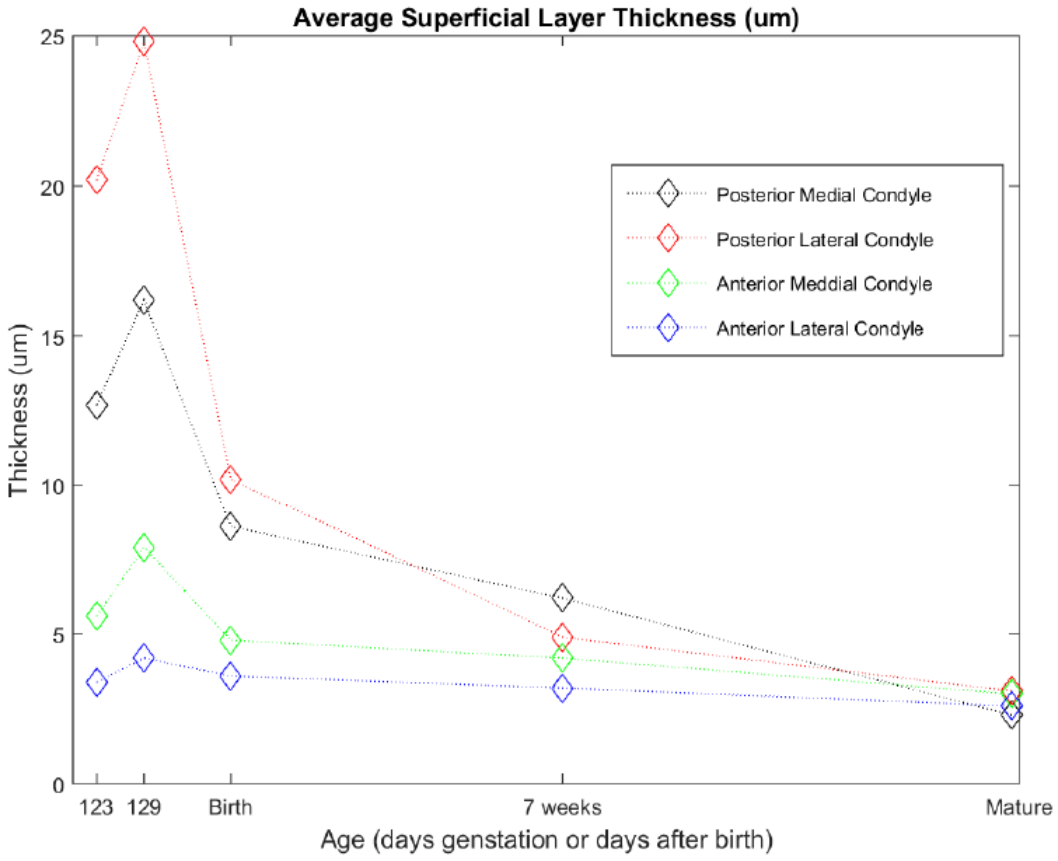

Figure 13-5: Superficial layer thickness as a function of age and sample position

Chapter 14 Study 6: Topological Variations in Ovine Cartilage Mechanical Properties Grouped by Age

This studied mechanical properties as a function of topological positions using prenatal, seven-week-old, and three-year-old sheep cartilage.

14.1 Study Objectives

This was a topological study to measure any discernible differences in the mechanical properties of three-year-old sheep cartilage. The study also observed the effects of specimen fixation upon the quality of images. A total of four sheep were available for the study giving twelve sample joints. Each joint was sampled with 3mm biopsy samples at the six sample positions shown in chapter 8.

This study was conducted with the assistance of final year undergraduate student Dan Spagnolo.

Samples were taken from the six locations across all age groups to perform a study of the topographical variation of the stiffness of AC as a function of tissue maturity. Final test specimens were obtained by isolating the top 1000 ± 200μm of the cartilage plug, ensuring the samples retained the superficial zone (including the laminar splendens). Only the upper 1000μm was retained as this was the approximate thickness of adult AC. This methodology ensured that the samples under investigation contained the same collagenous material and biochemical composition as that found in mature cartilage.

The typical thickness of cartilage plugs from foetal and 7-week-old specimens was in the range 4-7mm. During the developmental process cartilage at depths greater than 1-1.5mm is seen to calcify into subchondral bone.

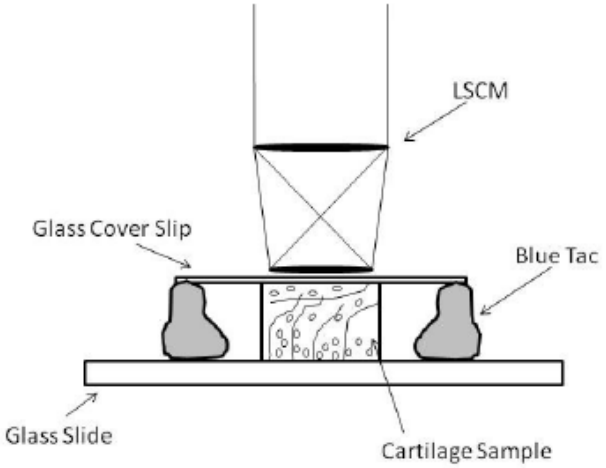

Figure 14-1: Schematic of test sample setup for LCSM to study 3D arrangement of collagen fibres

All AC specimens were subjected to unconfined compression testing. Samples were initially measured for their thickness using a micrometre and transferred to the centre of the cartilage stage. The sample was compressed through 15% of its original thickness to simulate physiological compression conditions at a rate of 2μm/s to obtain equilibrium compression conditions and imaged using the device shown in Figure 14-1. Cartilage displays depth dependent variations in its mechanical properties (Klein et al. 2007) and under compressive loads a non-uniform strain field is produced throughout the thickness of the sample (Mow et al. 2005).

From these unconfined compression tests of AC, three characteristic types of compression curves were generated that display depth dependent variations in stiffness (Figure 14-2).

The first compression curve (blue trace, Figure 14-2) indicates that there are two distinct regions of stiffness. This behaviour can be explained by the upper surface zone deforming at low loads, thus providing adequate conformation between articulating surfaces before most the compressive force is transmitted into stiffer tissue that deforms under higher loads. The second curve (red trace in Figure 14-2) indicates a constant rate of increase in tissue stiffness until a constant level was obtained. This response curve was that most frequently observed in confined compression of AC. The green trace shows a linear relationship between force and displacement due to compression,

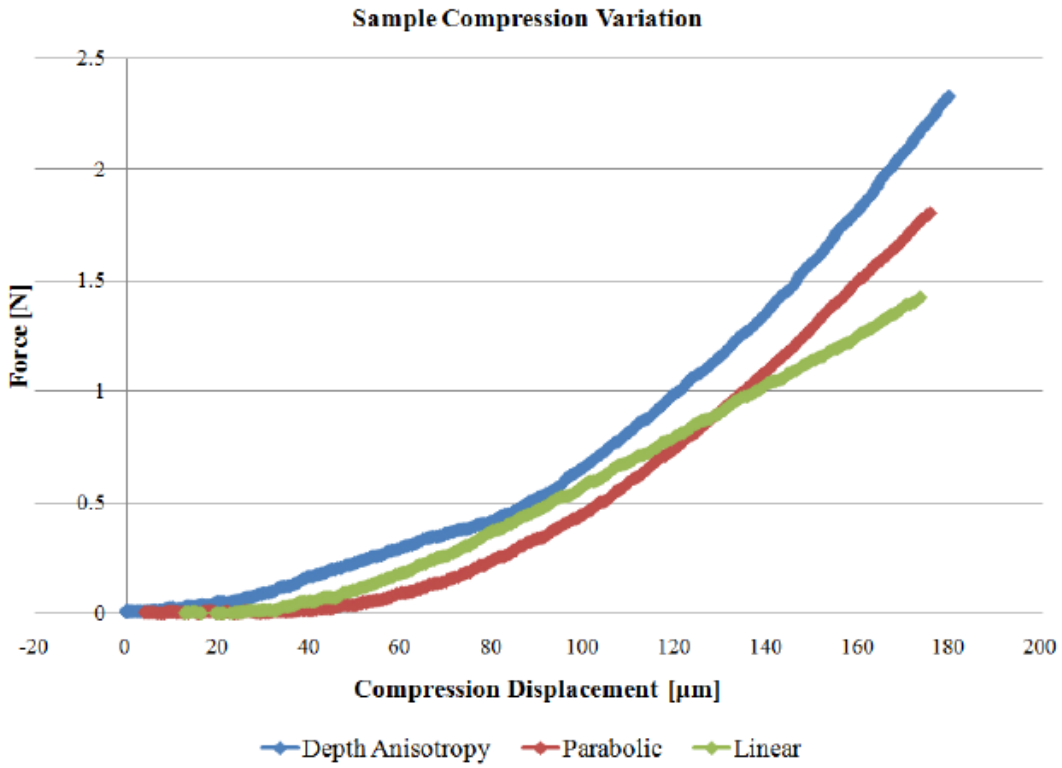

Figure 14-2: Three typical unconfined compression of articular cartilage showing depth dependent variation in the stiffness of the articular cartilage.

To compare the stiffness of AC across the condyles, both the upper and lower stiffness values were compared as a function of site-specific location and tissue maturity. The lower stiffness data could be determined on samples which displayed two distinct regions of stiffness (blue trace, Figure 14-2).

14.2 Deformation in Prenatal Ovine Articular Cartilage

The initial deformation of AC in response to compressive loads occurs in the upper surfaces of the tissue, allowing sufficient joint conformation to occur before most the compressive forces are transmitted through the tissue. This conformation serves two purposes. The first is to spread loads across the joint reducing the peak compressive stress to which the tissue is subjected. In the second, this conformation increases the surface area between the articulating surfaces thus forming a larger bearing surface and increasing the load capacity of the joint. The topographical variation in stiffness of the initial joint deformation as a function of tissue maturity is shown in Figure 14-3.

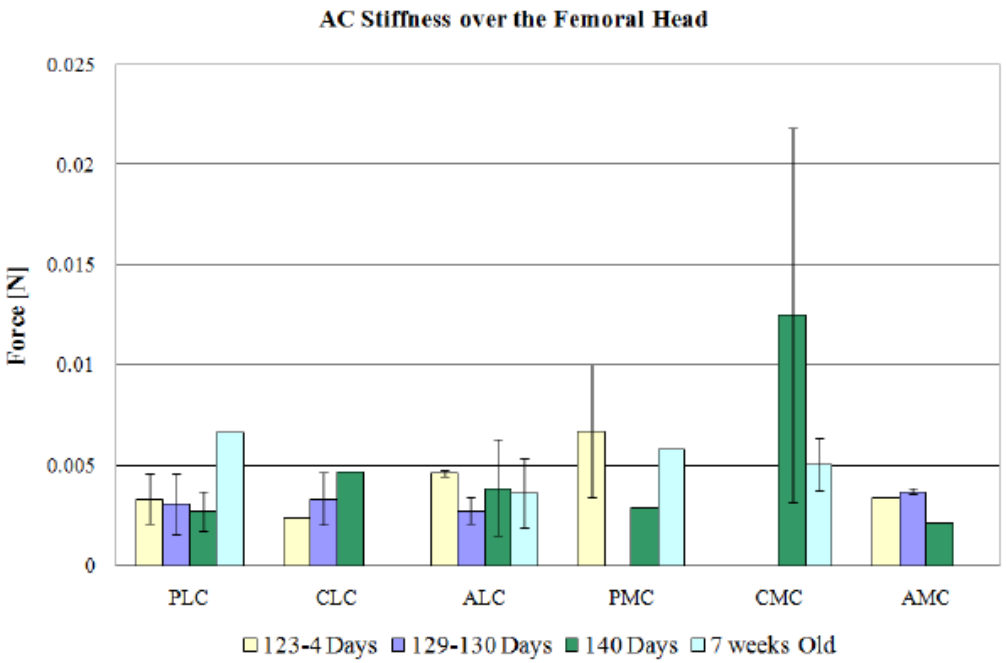

Figure 14-3: A plot of the AC stiffness and standard deviation from all six topographical sites across the femoral condyles over four stages of tissue maturity.

These results do not show any significant variation in the lower stiffness of AC samples across medial and lateral condyles as the tissue matures. The specimen from the CMC differs significantly (to one standard deviation) and should be regarded as an outlier, due to the proximity of ligaments to the harvest site. The data suggests that the surface layers appear to be mechanically independent from subjacent layers and that all specimens contained a laminar splendens. The existence of a lamina splendens on the outermost articulating surface has been previously reported (Teshima et al. 1995), and the lower stiffness value observed could be attributed to this.

Most the samples displayed a linear increase in tissue stiffness until a constant level was reached. Therefore, lower stiffness value could not be determined from the compression curves for many of the samples. Thus, the data should be regarded as indicating a general trend rather than providing conclusive experimental findings. To assess the topographical variations in stiffness in developing ovine AC, only the upper stiffness values were considered.

14.3 Secondary Deformation in Articular Cartilage

Once the upper layers of AC were deformed, compression required significantly additional force, i.e. the tissue sample acted as a stiffer material. The stiffness of the tissue was determined by linear regression of the upper compression curve and was seen to exhibit topographical variations (Figure 14-4).

In the predominantly weight bearing regions of the femoral heads, i.e. the posterior lateral and medial condyles, and the centrally loaded region of the medial condyle, the stiffness of AC samples was observed to increase as the tissue matured during foetal development. The stiffest AC samples were those of 7-week-old lambs from the regions subject to mechanical load. This observation accords well with the current understanding of AC, in that mechanical loads increase the metabolic rate of chondrocytes (Kiviranta et al. 1987; Mow et al. 2005).

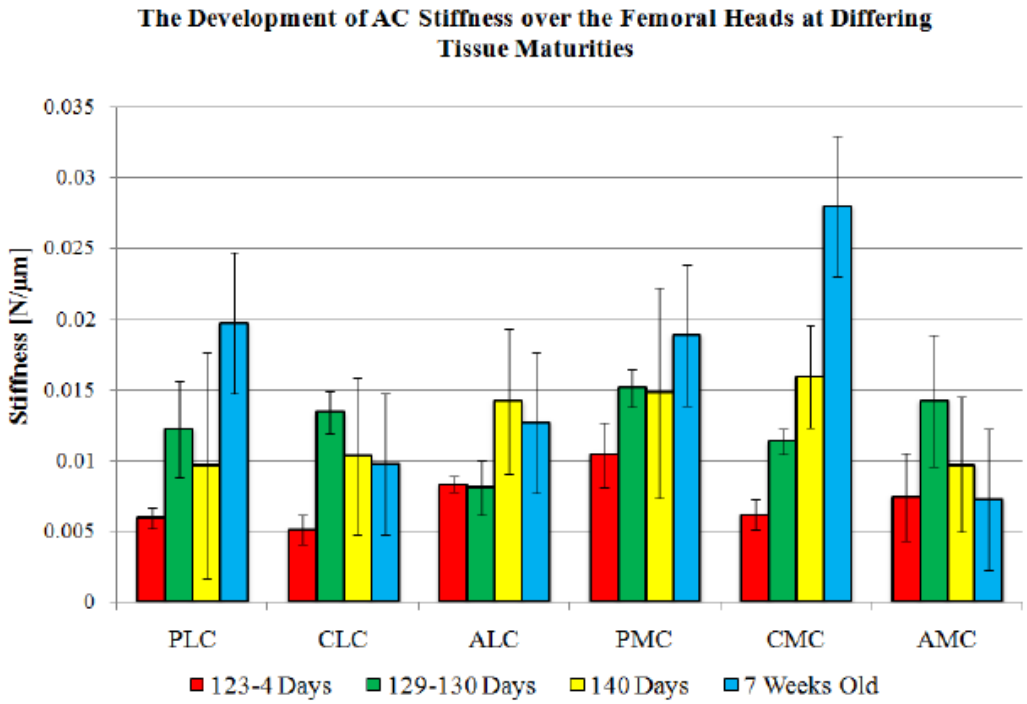

Figure 14-4: **Topographical variation in stiffness of AC over four stages of development showing the standard deviation for the measurements**

As chondrocytes are responsible for the synthesis of proteoglycans, samples from the weight bearing regions display the highest concentration of proteoglycans and can withstand the greatest compressive load.

In the non-weight bearing regions of the tissue, i.e. the AMC and the CLC, maximal AC stiffness occurred at 129/130-day gestation and thereafter decreased. As samples from these regions of the femoral head are not frequently subject to mechanical loads, the tissue is seen to be more elastic. It could be argued that as the anterior region of the lateral condyle is subject to minimal compressive loads, the AC cartilage here should display the greatest elasticity. However, as can be seen from Figure 14-4, the AC from this region is in fact stiffer than that of the centrally loaded zone of the lateral condyle. An explanation for this apparent paradox is that the chondrocytes in this zone are subject to shear loadings rather than compressive forces imparted by the adjacent ligamentous attachment. The net effect again would be increased synthesis of proteoglycans with a consequent increase in stiffness.

14.4 Stress-Relaxation Behaviour

As seen from the compression curves, AC is a biphasic tissue in which the outermost layers are seen to deform and are compacted at lower loads rather than at subjacent layers. Compression imparts a non-linear strain field in the tissue which over time, relaxes as fluid flows through the porous collagenous matrix into the upper surface layers, until a uniform strain field is generated throughout the tissue. Once the tissue has relaxed, the equilibrium Young's modulus can be calculated for the AC samples. The topographical variation in Young's modulus is presented in Figure 14-5 as a function of tissue maturity.

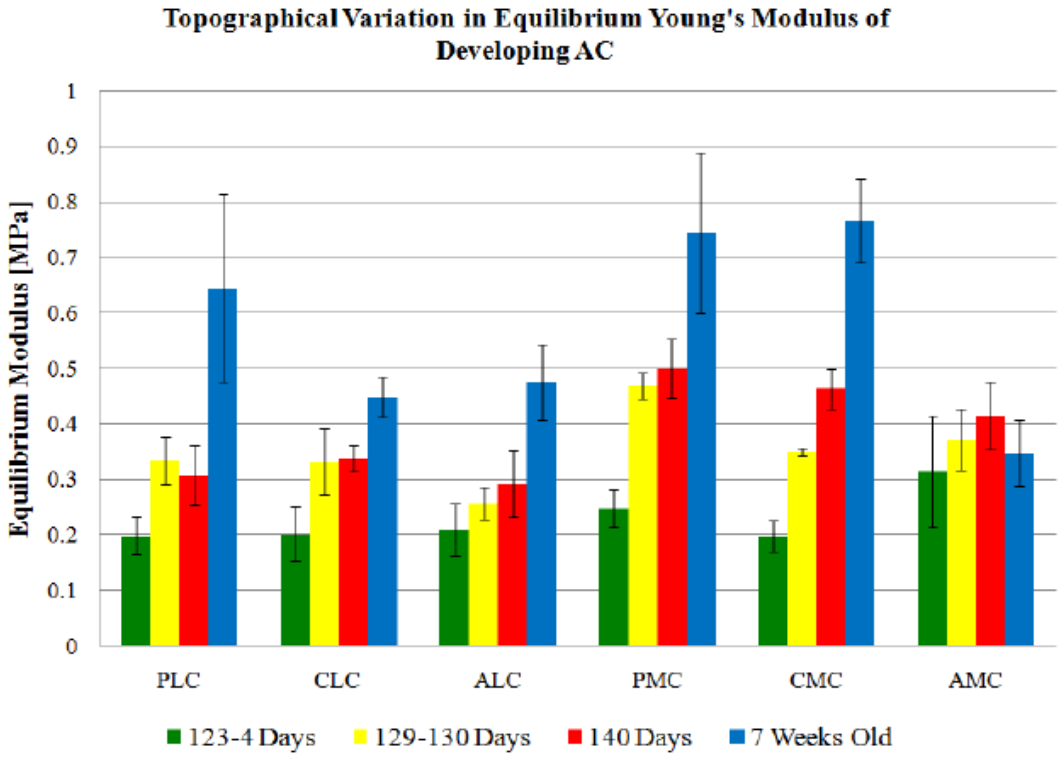

Figure 14-5: Topographical variation in Equilibrium Young's Modulus of AC including standard deviation of calculation as a function of tissue maturity

There is a complex structural relationship between the collagenous structure within the ECM and the proteoglycan component that affects the compressive mechanical properties within cartilage. The equilibrium modulus is indicative of the proteoglycan content of the tissue and its ability to withstand compressive loads. There is little, if any, topographical variation in the equilibrium Young's modulus of AC samples from 123/124-day gestation (Figure 14-6).

As the tissue matures to 140-day gestation, topographical variations across the condyles become apparent, with the medial condyle being coated in stiffer articular cartilage than the lateral condyle. The 7-week postnatal cartilage samples display different topographical variations in equilibrium modulus, the weight bearing regions of the condyles displaying the greatest stiffness. In contrast to the stiffness of AC during compression, there does not appear to be any significant variation in the equilibrium modulus of the non-weight bearing regions of the tissue, indicating that these regions have similar proteoglycan concentrations.

The time taken for the tissue to relax to an equilibrium stress can be interpreted as a measure of tissue porosity in the upper surface layers. The topographical variation in stress relaxation time as a function of tissue maturity can be seen in Figure 14-7.

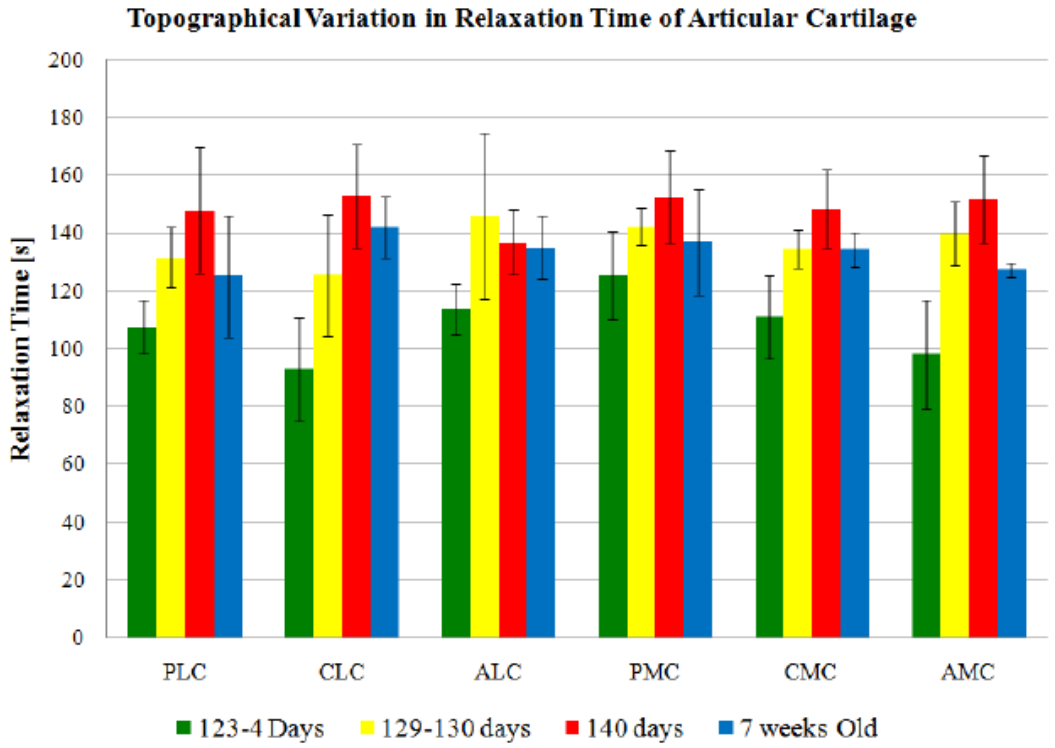

Figure 14-6: Topographical variation and standard deviation in relaxation time of AC as a function of tissue maturity

Like the variations in the Young's modulus of prenatal AC, the time taken for stress relaxation is seen to increase across all locations of the femoral head with age in prenatal tissues. Stress relaxation reaches a peak around birth and decreases as the cartilages ages towards seven-week-old.

Additionally, there does not appear to be any significant topographical variation in the relaxation time. These results indicate that the surface layers of AC are becoming less permeable and require longer time to equilibrate. Additionally, these observations indicate that the proteoglycan content of the tissue increases during the developmental stages as higher compressive loads can be sustained.

Samples from the 7-week postnatal sheep displayed a reduction in stress relaxation times compared to those of the 140-day gestation samples. Initially it was thought that the permeability of the collagen matrix had decreased in the early postnatal stages. However, the observed reduction in stress relaxation time can be attributed to the maintenance of higher equilibrium compressive stress by the mature tissue, compared to the immature tissue. As such, less time is required for the tissue to equilibrate to this stress.

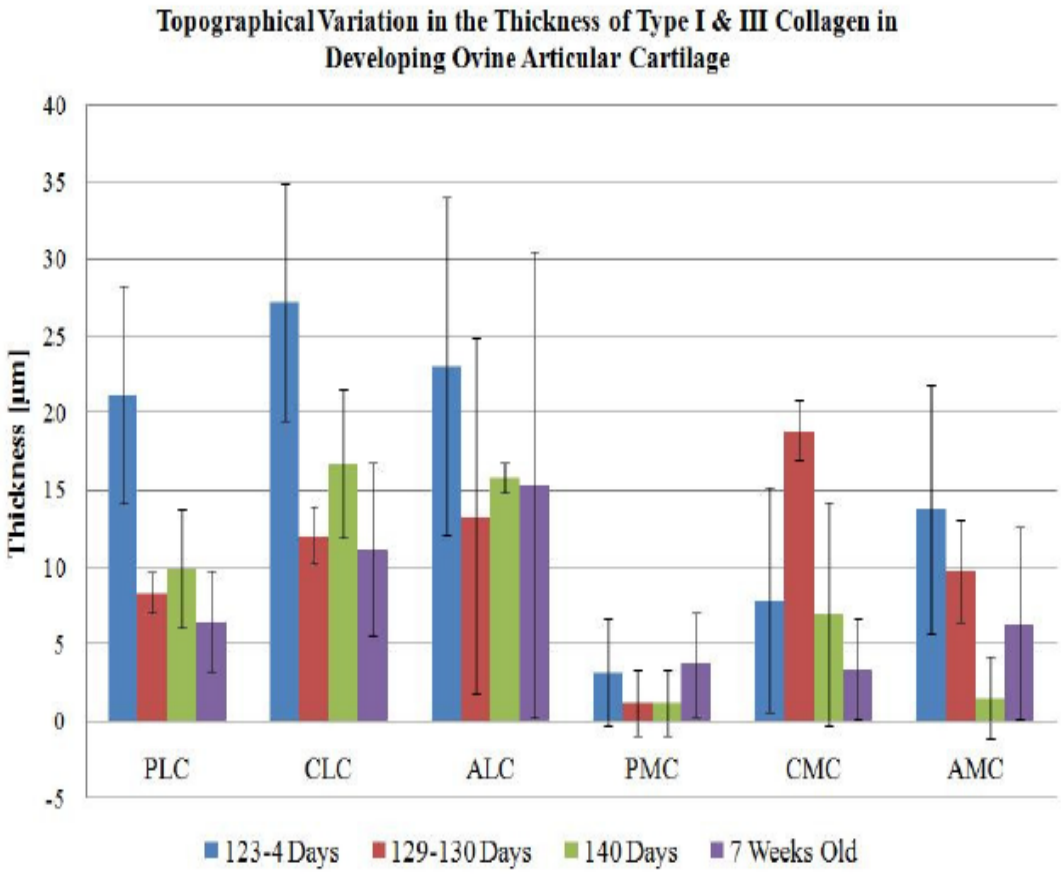

Figure 14-7: Topographical variation and standard deviation in the thickness of the observed collagen layer in developing ovine articular cartilage,

14.5 LSCM Observations

The following table summarises the depth and nature of the collagen fibres and chondrocytes in the superficial zone as a function of sample position and age. This experiment is the third repetition during this study.

Table 14-1: Summary of superficial zone at various ages of cartilage

Sample Site	123-124 Days Gestation	129 - 130 Days Gestation	140 Days Gestation	7-week post birth
PLC	• Highly cellular • Type I collagen in bands • Viable cells at depth	• Fine type I collagen throughout • Viable cells at depth • Bands of type I collagen	• Fine collagen I throughout • Viable cells at depth • Laminar splendens thickness decreases	• Sparse type I collagen on surface • Viable cells at depth
CLC	• Highly cellular • Viable cells at depth • Type I collagen in bands	• Fine collagen I throughout • Viable cells at depth • Bands of type I collagen	• Fine collagen I throughout • Viable cells at depth • Laminar splendens thickness decreases	• Sparse type I collagen on surface • Cells become spherical at depth
ALC	• Highly cellular • Type I collagen in bands • Viable cells at depth	• Fine type I collagen throughout • Viable cells at depth • Bands of type I collagen	• Fine collagen I throughout • Viable cells at depth • Laminar splendens thickness decreases	• Sparse type I collagen on surface • Viable cells at depth
PMC	• Sparse non-viable cells on surface • Viable cells at depth • Sparse collagen fibres on surface	• Sparse non-viable cells on surface • Viable cells at depth • Sparse collagen fibres on surface	• Sparse non-viable cells on surface • Viable cells at depth	• Sparse non-viable cells on surface • Viable cells at depth
CMC	• Non-viable cells on surface • Viable cells at depth • Sparse type I collagen throughout	• Few type I at surface • Viable cells at depth	• Few type I at surface • Viable cells at depth	• Sparse non-viable cells on surface • Viable cells at depth • Sparse type I collagen on surface
AMC	• Numerous type I collagen throughout • Viable cells at depth	• Few type I collagen at surface • Viable cells at depth • Non-viable cells at surface	• Few type I collagen at surface • Viable cells at depth • Non-viable cells at surface	• Thin layer of type I collagen • Viable cells at depth

14.6 Study 6 Findings

The outcomes of this study can be summarised as follows:

1. The fibrous layer was found to be significantly thicker on the lateral condyle than either the medial condyle or trochlea.
2. Fibre orientation appeared randomly distributed over all samples, except for sample 2 due to the proximity towards the attachment of the lateral collateral ligament. Some of the thicker fibres may well be associated with the ligament anchor points.
3. Type I and type III collagen fibre development peaked at 129/130-day gestation age group. After 130-day the thickness of the fibre layer decreased with age. This thickness further decreased after birth because of normal anatomical loads being applied during movement and standing. This was also observed in studies 3 and 5.
4. Type II collagen fibre grows quickly at birth. This is associated with the growth in proteoglycans. The increase in type II density is visible as the background cloud of bright light. Again, this relationship agrees with studies 3 and 5.

Chapter 15 Study 7: Additional Prenatal Sheep Data

This was a topological study to measure the equilibrium modulus neonatal sheep cartilage.

15.1 Study Objectives

A total of four sheep were available for the study, giving twelve sample joints. Each joint was sampled with 3mm biopsy specimens taken at the three sample positions shown in Figure 15-1.

A small project to redesign the test rig and modify it to act as a large-scale indentation compression testing rig was carried out in 2010 by final year engineering undergraduate student Mohamad Asrul Ayob. The new control routine for the rig was written by me and I assisted in construction of the rig. During testing with rubber samples the rig operated satisfactorily and so several 126-day gestation sheep samples were also tested. At the time the results showed that the cartilage sample responded in a linear fashion, and the results were put aside until they could be analysed further. The main purpose of the test was to confirm the operation of the rebuilt rig. A set of twelve samples were tested, all of which showed linear relationships between measured force and displacement. The results were initially discarded as over compressed and not re-examined until this thesis was written up, and the decision made not to delete the data set. The linear response was unexpected and significant. A sample of the raw data is shown below.

These results were scaled to plot relative displacement against applied force. This gave more consistent results but the spread of the measured slopes of the samples suggested that the samples need to be averaged to estimate the actual Young's modulus for prenatal sheep cartilage.

These results were also removed from the initial compression motion on the new test rig and the final over compression of the samples. These samples were very thin and unintentionally over compressed but the linear deformation was extensive, comprising at least 60% of the total compression travel.

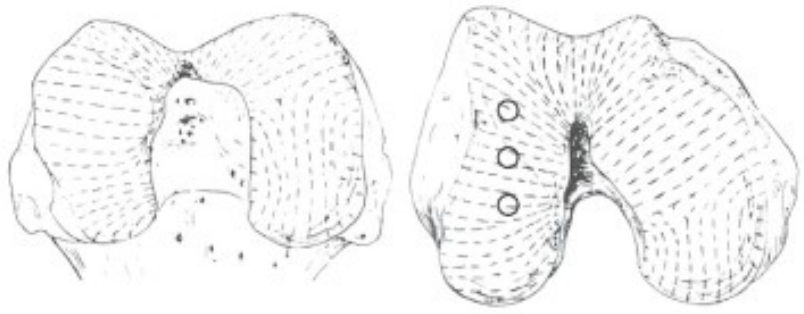

Figure 15-1: Sample sites from medial condyle of neonatal sheep used for testing the newly modified compression rig.

In prenatal sheep, the cartilage layer is too thin, hard to harvest and its mechanical properties differ from that of older cartilage. , the depth of the superficial layer represents most of the cartilage sampled in the prenatal sheep foetuses. It was observed that the prenatal cartilage had a linear response to compression testing, whereas older cartilage samples gave the normal viscous-elastic response expected in mature cartilage. This is indicative of a larger proportion of elastic (elastin) fibres with respect to collagen fibres, in combination with proteoglycans found in these samples. The samples were soft and pliable as the femoral head had not mineralised at this stage, and hence the bone was composed almost entirely of cartilage.

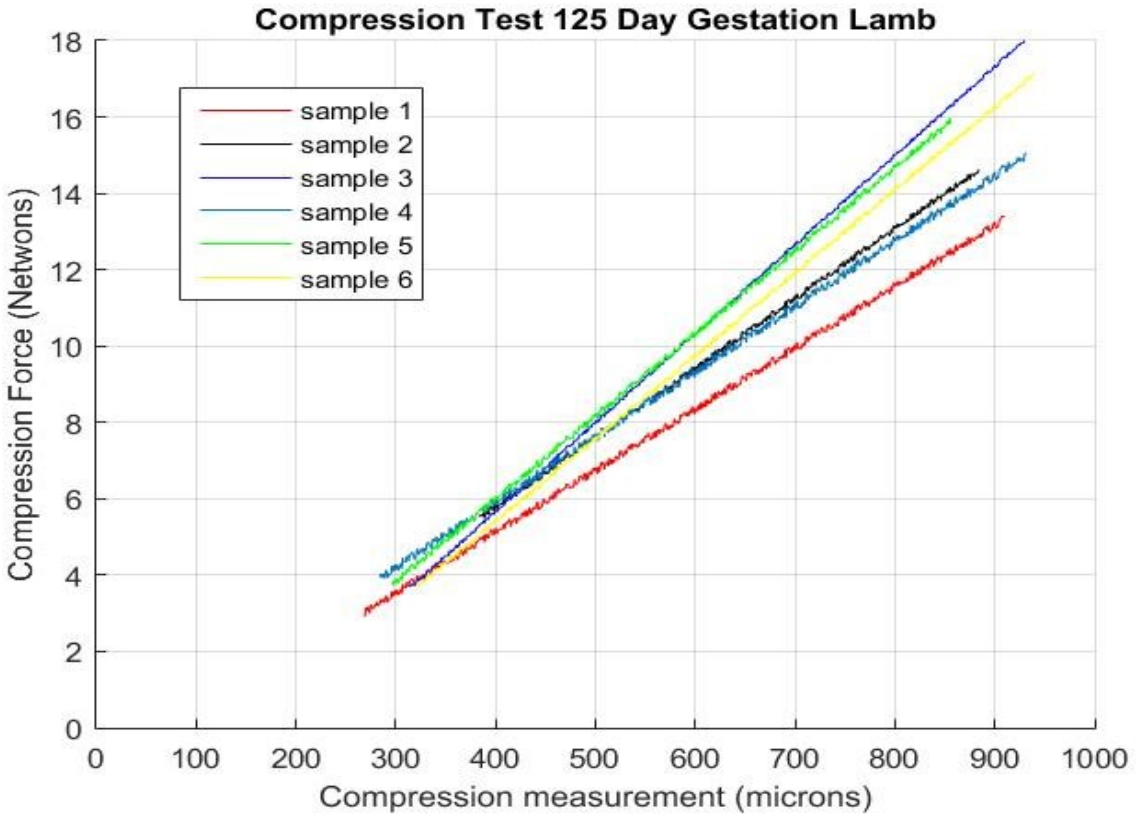

Figure 15-2: Raw compression force vs displacement for 125 day gestation sheep cartilage

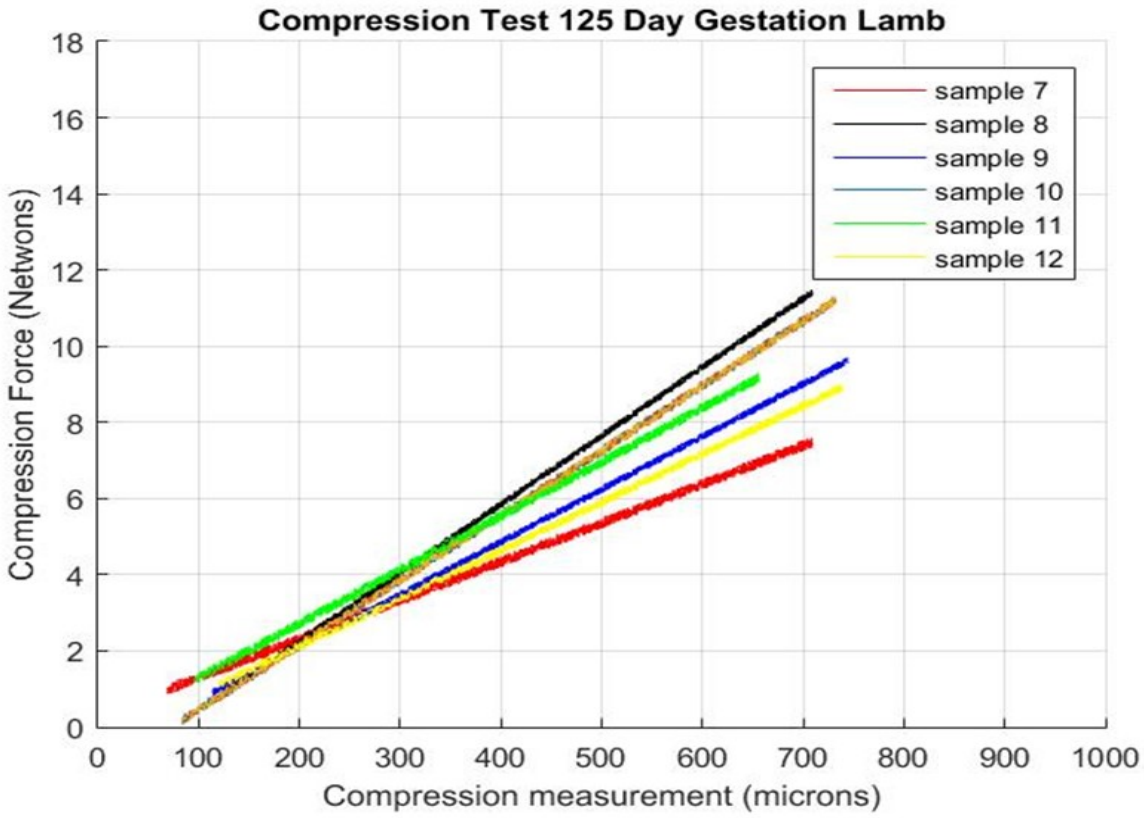

Figure 15-3 Raw compression force vs displacement for 125-day gestation sheep cartilage.

Table 15-1: Stiffness of prenatal (125-day gestation) sheep articular cartilage

Sample No	Δ Force (N)	Δ Displacement (um)	Stiffness (MPa)
1	10.109	640	0.5587
2	9.168	500	0.6471
3	14.765	630	0.8274
4	10.834	645	0.5934
5	11.213	520	0.7638
6	12.561	600	0.7390
7	6.438	640	0.6754
8	11.186	625	0.6330
9	8.731	630	0.5269
10	11.170	648	0.6082
11	8.080	560	0.5446
12	8.102	618	0.5340

15.2 Study 7 Findings

This study confirmed the linear stress-strain relationship for neonatal sheep as seen in other studies with age. The linear relationship changes from linear to a more familiar visco-elastic response or parabolic curve in older sheep tested. The reason for this is not understood in terms of proteoglycan, which has not developed to a dominant position by this age, but rapidly increases along with collagen II postnatal.

The role of elastin is unknown as elastin was not visible (or considered) with FTIC staining. Elastin has become more visible after this study through the work of He Bo in the research group. Elastin presence through staining with acridine orange or immuno-chemical staining and two photon auto fluorescence of cartilage would be the next logical step in this progression to determine the growth behaviour of cartilage.

Chapter 16 Discussion from Study Findings

This section summarises the results of the study: software development; and animal studies involving articular cartilage.

16.1 Image Analysis Program

There are significant differences between natural images and biological images. Biological images are not readily understood from a casual glance and often require some experience to interpret the meaning of areas of interest within the image. Biological imaging is formed from within the specimen at the scale from which it was constructed. The objects of interest make up the entire imaging region, which comes from within the sample, whereas with natural vision images are formed external to the observer and the objects appear as part of the scene. A biological image is viewed from the samples' inside so that no spaces exist between the viewer and the region of interest: all objects within the image appear to be continuous so that the information surrounds the viewer. In making the visualisation of small scale biological images clear, it is necessary to process the entire image as a single 3D image, composed of many smaller 3D objects embedded in noise.

Three dimensional objects are synthesised from a stack of 2D planes arranged vertically, one above another. Objects that extend outside of a 2D stack element are often mistaken as noise or are incorrectly represented from one frame to its adjacent neighbour. A true 3D approach to signal filtering has eliminated most of the short-comings of this 2D system. This 3D approach permitted the various cartilage components, used in this study, to be segmented and separated from one another, with the ability to artificially colour objects and form new images from the component parts. These are clearer with the final 3D image showing the spatial relationship between each of the component objects. The unbalanced axial view intrinsic with the non-isotropic confocal microscope resolution has been replaced by space equalisation to give better interactive views.

A number of approaches were investigated for extending the phase symmetry algorithm approach to 3D. Monogenic filters were found to provide the best results and the lowest computation time. It was found that image compression due to non-isotropic confocal microscope resolution could be compensated by scaling the distance vectors used to construct the filter set. Intensity based image normalisation prior to image processing was found to improve the performance of the phase symmetry algorithm. The monogenic filters were developed from a scale space model of the image.

The main issue with biological images at the scale studied (1 to 10 microns in size) is that these images are not readily recognisable as 3D objects in the same way as a building or room interior are recognised. The image processing software was developed without pre-assumptions of the objects detected or the presence of defining features such as sharp edges or corners. This means that the system could be used for any 3D biological image. The software has been used successfully with CAT scans to improve image quality. The software was developed to also be used in a batch processing mode so that objects are segmented according to size criteria as defined by the aperture of a series of band-passed filters. These filters must be tuned to give good performance for component segregation. These components are stored separately and may then be further processed and/or recombined into artificially coloured images. The component parts are available to be reprocessed using standard ImageJ processes to give length, area, and volume measurements.

The software developed can adjust the illumination intensity; rearrange the component voxels into a regular pattern by sub-voxel interpolation; reject noise and give clear images that can be easily and readily measured using a standard ImageJ processing environment. Objects of interest are identified using phase symmetry and phase congruency processing techniques.

The software is modular and has been run in an interactive Matlab environment. The use of voxel equalisation and intensity adjustment produced a standard image file that uses the same scale in all three dimensions. This format can be used to support 3D smoothing filters recursively as these filters produce a new standard image file. The decision to use ImageJ as the display process made it more attractive to write the Matlab code in Java to run directly under the ImageJ processing engine as a series of filters.

Thus, the recursive mode of the filters may be exploited to selectively display more items of interest, of very different sizes, using tuned band-passed filters upon either the raw data or a raw data file with the segregated object subtracted from the raw image. As the output images are of the same format, ImageJ is used to add these together compose composite images from the separated objects. Furthermore, the separated objects can be recursively reprocessed to allow for additional segmentation or to adjust their image properties using ImageJ.

As part of documenting and release of the software, a display back end filter is being designed to use transparent images added into a composite image for the ImageJ environment. Each component image can be coloured individually (i.e. assigned a base colour or hue), using the grey scale forming the image as the degree of colour saturation in a hue, saturation, transparency (HSV) format rather than the usual RGB colour format used here. The transparency indicated by the strength of the grey scale will make small values transparent and higher values more opaque. When HSV formatted images are added together to produce colour images of varying transparency giving a much clearer visualisation of the processed samples by allowing the 3D image to appear transparent with included opaque structures coloured by the type of object found.

The software has been successfully used with other images such as CT scans and MRI images. The general noise reduction was acceptable. CT scan artefact reduction due to metallic hardware introduced into the body was likewise successful.

16.2 Small Scale Studies

The mechanical use of the knee appears to strongly influence development of the fibrous zone in maturing sheep. In postnatal ovine cartilage samples the depth of the visible fibrous layer decreased with age. The thinning of the depth superficial layer is also observed in other studies of sheep ageing from birth to five years. It was clear that the number of fibres in the very superficial zone increased with age. That is, the fibres appeared to be condensed into a thinner layer rather than depleted and removed from the samples. The presence of type I and type II collagen is integral with the development of mature cartilage.

The relationship between superficial zone depth and comparative weight bearing was investigated for ovine and porcine specimens. Both species gave very similar results and both pigs and sheep but displayed counterintuitive trends with regards to the superficial zone thickness. The trochlea had the thinnest superficial zones, however, on the condyles the predominant weight bearing regions appeared to have thinner surface layers than those found on less weight bearing areas. Therefore, a conclusive relationship could not be formed, indicating that the superficial zone reaches a steady state thickness with age that is not strongly dependent upon the loading of cartilage across the femoral head. Additional study is required to better understand the complex nature of AC and its uppermost layer.

Superficial zone depth was observed to vary across the different topographical locations of the femoral head for both species. Across the condyles' sampling regions, porcine specimens displayed a thicker superficial layer than the ovine samples. A relationship between weight bearing and superficial zone depth was not fully characterised. The main reason for the topological variation appeared to be age of the animal and the stage of growth development. In mature animals, the superficial zone thickness plateaued to something roughly uniform (within 2 to 3 microns) across the femoral condyle. The superficial zone thickness increased to the age of 128 to 130-day gestation and then decreased rapidly, especially from after birth (nominally 140-day gestation). This is strong evidence that environmental factors played a larger role in the formation of mature aged cartilage. The growth of early age cartilage and its effects upon the mechanical properties of the cartilage have been identified as important. The development of the cartilage with age requires additional study.

The fibrous layer was found to be thicker on the lateral condyle than either the medial condyle or trochlea. The fibre orientation appeared randomly distributed over all samples, except for samples with a proximity towards the attachment of the lateral collateral ligament. Some of the thicker fibres may well be associated with the ligament anchor points.

Type I and type III collagen fibre development peaked at the 129/130-day gestation age group. After 130 days of gestation the thickness of the fibre layer decreased with age and further decreased after birth because of normal anatomical loads being applied during movement and standing. This was also observed in studies 3, 5 and 6. Type II collagen fibre grows quickly at birth. This is associated with the growth in proteoglycans. The increase in type II density is visible as the background cloud of bright light. Again, this relationship agrees with studies 3, 5 and 6.

The density of chondrocytes near the surface of samples taken from the 124-day gestation sheep was low, increasing dramatically with depth until the density reached a plateau at 18μm into the sample. In comparison, the size of the cells decreased significantly with depth, starting at 20-25μm in diameter near the surface compared to the 5-10μm encountered at the lower depths. The classical structure of horizontal, elongated sheets of chondrocytes near the surface and spherical, randomly arranged chondrocytes in the middle layer also appears to be developing in the younger sheep. Evidence of mitosis was visible in the chondrocytes indicating the developmental stage of the cartilage. Few non-viable cells were evident, most due also to the developmental stage of the cartilage.

Despite the small age difference between samples, the 128/129-day gestation samples demonstrated a marked difference in chondrocyte structure. Cells near the surface were smaller at 10-15μm and decreasing with depth to 5-10μm. Cell density near the surface had significantly decreased, then increasing slowly until a density similar to that for the 124-day gestation sheep was reached at a depth of around 35μm. Chondrocytes in the middle region appeared to resemble those found in the younger sheep.

Observational results for the fibre layer thickness and composition was similar across studies1, 3, 5 and 6 and are summarised in Tables 9-1, 11-2, 13-1 and 14-1.

The linearity of the prenatal cartilage will need to be further studied to identify the presence of elastin fibres in the growth modes of cartilage.

The process of superficial fibre development has direct implications upon the repair of damaged cartilage. Current repair techniques rely upon the production of new hyaline cartilage from autologous chondrocytes in mature adult knees (Zheng M H, Willers C, Kirilak L, Yates P, Xu J, Wood D and Shimmin A 2007). It has been previously stated that the integrity of the superficial layer of cartilage is necessary for the normal function of the articular surface (Poole 2003) and that without the superficial layer the low friction and wear resistant properties of articular cartilage are lost (Stachowiak GW, Batchelor AW and Griffiths LJ 1994).

If this trend is also shown in human cartilage histology then the presence of tightly bundled collagen fibres across the articulating surface due to environmental effects postnatal, give rise to the strength and stability of the adult cartilage. These conclusions are consistent with findings in the literature (Bo He, Wu JP, Chen H, Kirk TB and Xu 2013), (Bo He, Wu JP, Chim SM, Xu J and Kirk TB 2013) and that the inability to repair the superficial layer may well affect the long term effectiveness of autologous cartilage replacement.

References

AFWA Australia, Arthritis Foundation of Western Australia. 1999. "http:/www.arthritiswa.org.au." Accessed May 1, 2009.

Alford J and Cole B. 2005. "Cartilage restoration, part 1 - Basic science, historical perspetive, patient evaluation and treatment options." *American Journal of Sports Medicine* 33: 295-306.

American Academy of Orthopaedic Surgeons, AAOS. 2010. *Information on Osteoarthritis.* Accessed January 27, 2016. http://www.orthoinfo.aaos.com.

Appleyard C and Swain V. 2003. "Topological analysis of the structural, biochemical and dynamic biomechanical properties of cartilage in an ovine model of osteoarthritis." *Osteoarthritis and Cartilage* 11 (65).

Arokoski JP, Jurvelin J, Vaatainen U and Helminen H. 2000. "Normal and pathological adaptations of articular cartilage." *Scandanavian Journal of Medicine and Science in Sports* 10: 186-198.

Ateshian GA, Warden WH Kim JJ et al. 1997. "Finite deformation biphasic material properties of bovine articular cartilage from confimed compression experiments." *Journal of Biomechanics* 30: 551-558.

Ayob, MA. 2008. *Design of a creep testng apparatus to investgate the mechanical properties of articulr cartilage.* Undergrauate final year project, Perth: School of Mecanical Engineering, University of Western Australia.

Bae WC, Lewis CW, Levenston ME and Sah RL. 2006. "Indentation testing of human articular cartilage: Effects of probe tip geometry and indentation depth on intro-tissue strain." *Journal of Biomechanics* 39 (6): 1039-1047.

Bank R, Bayliss MT, Lafeber FP, Maroudas A and Tekoppele JMI. 1998. "Ageing and zonal variation in post-translational modification of collagen in normal human articular cartilage." *Biochemical Journal* 330: 345-351.

Behrens P, Bitter T, Kurz B and Russlies M. 2006. "Matrix-associated autologous chondrocyte transplantation/implantation (MACT/MACI) - 5 year follow up." *The Knee* 13 (3): 194-202.

Below S, Arnoczky SP, Dodds J, Kooima C and Walter N. 2002. "The split-line pattern of the distal femur." *Arthroscopy* 18 (613).

Bennink H E et al. 2007. "A Novel 3D Multi-Scale Lineness Filter for Vessel Detection." *Medical Image Compuing and Computer-Assisted Intervention* 4792: 436-443.

Bird, C. 2010. *Studying the role of the most superficial layer of articular cartilage on the mechanical and physiological function of the tissue.* Final year project report, Perth: School of Mechanical Engineering, University of Western Australia.

Bo He, Wu JP, Chen H, Kirk TB and Xu. 2013. “Elastin fibres display a versatile microfibril network in articular cartilage depending on the mechanical microenvironments.” *Journal of Orthopaedic Research* 3 (9): 1345-1353.

Bo He, Wu JP, Chim SM, Xu J and Kirk TB. 2013. “Microstructural analysis of collagen and elastin fibres in the kangaroo articular cartilage reveals a structural divergence depending on its local mechanical loading.” *Journal of Osteoarthritis and Cartliage* (21): 237-246.

Bo He, Wu JP, Xu J, Day RE and Kirk TB. 2013. “Microstructural and Compositional Features of the Fibrous and Hyaline Cartilage on the Medial Tibial Plateau Imply a Unique Role for the Hopping Locomotion of Kangaroo.” *PLOS ONE* 9 (8).

Broom N and Poole C. 1983. “Articular Cartilage Collagen and Proteoglycans - Their Funcional Interdependency.” *Arthritis and Rematism* 26: 1111-1119.

Broom, N. 1984. “Further insights into the structural principles governing the function of articular cartilage.” *Journal of Anatomy* 139 (2): 275.

Buckwater JA, Rosenburg LA and Hunziker EB. 1990. *Articular Cartilage and Knee Joint Function: Basic Science and Arthroscopy.* New York: Raven Press.

Callister, WD. 2007. *Materials Science and Engineering. An Introduction, Seventh Edtion.* John Wiley and Sons.

Chen FH, Rousche KT and Tuan RS. 2006. “Technical insight: adult stem cells in cartilage regeneration and tissue engineering.” *National Clinical Practical Rheumatology* (2): 373-382.

Clark JM, Norman AG, Auml BM, Ouml and Tzli HP. 1999. “The surface contour cartiage in an intact, loaded joint.” *Journal of Anatomy* (195): 45-56.

Clarke, I. 1971. “Articular Cartilage: A Review and Scanning Electron Microscope Study.” *Journal of Bone and Joint Surgery* 53: 732-750.

Crockett R, Dora C, Troxler H, Grubelni A, Born W and Roos S. 2007. “Biochemical composition of the superficial layer of articular cartilage.” *Journal of Biomedical Materials Research. Part A* 82a: 958-964.

Darling EM, Hu JCY and Athanasiou KA. 2004. “Zonal and topographical differences in articular cartiage gene expression.” *Journal of Orthopaedic Research* 22: 1182.

Davies, DV. 1945. “Anatomy and Physiology of Diarthodial Joint.” *Annual Rheumatism Disclosure* (5): 29-35.

Eyre, D. 2002. “Collagen of Articular Cartilage.” *Arthritis Research* 4: 30-35.

Felsberg M and Sommer G. 2000. “A New Extension of Linear Signal Processing for Estimating Local Properties and Detecting Features.” *22 DAGM Symposium Mustererkennung.* Keil.

Felsberg M and Sommer G. 2004. “The mongenic scale-space: A uniying approach to phase-based image processing in scale-space.” *Journal of Mathematical Imaging and Vision* 21: 5-26.

Felsberg M and Sommer G. 2001. “The monogenic signal.” *IEEE Transactions on Signal Processing* 49: 3136-3144.

—. 2002. *The Structure Multivector.* Birkhauser Boston: Cambridge.

Ficklin, T., Thomas, G., Barthel, J. C., Asanbaeva, A., Thonar, E. J., Masuda, K., Chen, A. C., Sah, R. L.,. 2007. “Articular cartilage mechanical and biochemical property relations before and after in vitro growth.” *Journal of Biomechanics* 40 (16): 3607-3014.

Field, D. 1987. “Relations between the statistics of natural images and the response properties of cortical cells.” *Journal of the Optical Society of America A* 4: 2379-2394.

Fox AJS, Bedi A and Rodeo SA. 2009. “The Basic Science of Articular Cartilage: Structure, Composition, and Function.” *Sports Health* 6 (1).

Franz T et al. 2001. “In situ compressive stiffness, biochemical composition and structural integity of articular cartilage of the human knee joint.” *Osteoarthritis and Cartilage* 9: 582-592.

Gardner D et al. 1997. “Advances in the Microscopy of Osteoarthritis.” *Microscopy Research and Tecnique* 37: 245-270.

Grodzinsky, A. 2011. *Force, Fields and Flows in Biological Systems.* Garland Science.

Guilak F, Ratcliffe A and Mow VC. 1995. “Chondrocyte deformation and local tissue strain in articular cartilage: A confocal microscope study.” *Journal of Orthopaedic research* 13 (3): 410-421.

Hayes, A. 2009. *Studying the role of the most superficial layer of articular cartilage on the mechanical and physiological function of the tissue .* Final year project report, Perth: School of Mechanical Engineering University of Western Australia.

Hollander A et al. 1995. “Damage to type II collagen in ageing and osteoarthritis starts at the articular surface, originates around chondrocyes and extends into the cartilage with progressive degeneration.” *Journal of Clinical Investigation* 96: 2859-2869.

ImageJ Development Team. 2009. “ImageJ Documentation.” *National Institute of Health.* Accessed January 25, 2016. http://rsbwb.hih.gov/ij/.

Jadin K et al. 2007. “Three-dimensional (3-D) imaging of chondrocytes in articular cartilage: Growth-associated changes in cell organsation.” *Biomaterials* 28: 230-239.

Jadin K, Bae W, Sah R and Schumachr B. 2007. “Three-dimensional (3D) imaging of chondrocytes in articular carilage: growth-associated changes in cell organisation.” *Biomaterials* 28: 230-239.

Jeffery et al. 1991. “Three Dimensional Collagen Arcitecture in Bovine Articular Cartilage.” *Journal of Bone and Joint Sugery* 73: 795-801.

Jones C et al. 2007. “Laser scanning confocal arthroscopy of a fresh cadaveric knee joint.” *Osteoarthritis and Cartilage* 15: 1388-1396.

Jones C W, Smolinski D, Keogh A, Kirk T B, Zeng M H. 2005. “Confocal laser scanning microscopy in orthopaedic research.” *Progress in Histochemistry and Cytochemistry* 40: 1-7.

Jones CW, Willers C, Keogh A, Smolinski D, Fick D, Yates PJ, Kirk TB and Zeng MH. 2008. “Matrix-induced autologous chondrocyte implantation in sheep: objective assessments including confocal arthroscopy.” *Journal of Orthopaedic Research* 26 (3): 292-303.

Jurvelin JS, Arokoski JPA, Hunziker EB and Helminen HJ. 2000. “Topological variation of the elastic properties of articular cartilage in the canine knee.” *Journal of Biomechanics* 33 (6): 669-675.

Kierath, T. 2008. *The development of collagen structure in the superficial zone of ovine articular cartliage: A study using confocal microscopy.* Final year project report, Perth: School of Mechanical Engineering, Univerity of Western Australia.

Kiernan, J. 2000. “Formaldehyde, formalin, paraformaldehyde and glutaraldehyde: What are they and what do they do.” *Miscoscope Today* 1: 8-12.

Kirk, TB. 1992. *Wear in Synovial Joints.* PhD Thesis, Perth: School of Mechanical Engineering, University of Western Australia.

Klein et al. 2007. “Depth-dependent biomechanical and biochemical properties of foetal, newborn and tissue-engineered articular cartilage.” *Journal of Biomechanics* 40: 182-190.

Knee Joint Surgery. 2009. “Articular Cartilage: Applied Anatomy.” Accessed Septmber 14, 2014. http:/www.kneejointsurgery.com/hml/articular_cartilage/anatomy.html.

Korhonen R et al. 2002. “Comparison of the equilibrium response of articular cartilage in unconfirmed compression, confined compression and indentation.” *Journal of Biomechanics* 35: 903-999.

Korhonen R et al. 2003. “Fibril reinforced poroelastic model predicts specifically mechanical behaviour of normal, proteoglycan depleted and collegan degraded articular cartilage.” *Journal of Biomechanics* 36: 1373-1379.

Kovesi, P. 1999. “Image features from Phase Congruency.” *Videre: Journal of Computer Vision Research* 1 (3).

Kovesi, P. 1996. *Invariant Measures of Image Features from Phase Information.* PhD Thesis, Perth: Department of Psychology, University of Western Australia.

—. 2006. “Matlab and Octave Functions for Computer Vision and Image Processing.” *Department of Computer Science and Computer Engineering.* Accessed November 3, 2008. http:/www.csse.uwa.edu.au/~pk/Research/MtlabFns.

—. 2003. “Phase Congruency Detects Corners and Edges.” *The Australian Pattern Recognition Society Conference: DICTA 2003.* Sydney: Australian Pattern Recognition Society. 309-318.

Kovesi, P. 2007. *Phase: An Important Low-Level Image Invariant.* Lecture Topic, Perth: School of Computer Science and Sofware Engineering, University of Western Australia.

—. 1997. “Symmetry and Asymmetry From Local Phase.” *AI' 97.* Sydney: Australian Joint Conference on Artificial Intelligence. 185-190.

Kühn K and Glanville R. 1980. “Molecular Structure and Higher Organisation of Different Collagen Types.” In *Biology of Collagen*, by Viidik A and Vuust J, 1-15. London: Academic Press Inc.

Luitjens, P. 2009. *Development of a 3D Phase Symmetry Program for Study of Articular Cartilage.* Final year project report, Perth: School of Mechanical Enginering, University of Western Australia.

Maroudas A, Bayliss MT and Venn MF. 1980. “Further studies on the composition of human femoral head cartilage.” *Annual Rheumatism Discussion* (39): 514-523.

Maroudas, A. 1979. “Physiochemical properties of articular cartilage.” In *Adult Articular Cartilage*, by Freeman MAR, 215-290. Kent: Cambridge University Ppress.

Meachim D and Stokwell RA. 1973. “'The Matrix' .” In *Adult Articular Cartilage*, by MAR Feeman, 1-50. London: Pitman Medical.

Michalek J, Capek M, Mao XW and Kubinova L. 2010. “Application of Morpholgy Filters to Compensation of Lateral Illumination Inhomogeneities in Cofocal Microscope Images.” *Biosignal 2010.* Paris: Biomedical Image Analysis 2010. 49-54.

Misiti M, Misiti Y, Oppenheim G Poggi J-M. 2009. “Wavelet Toolbox 4 User's Guide.” *The Math Works Inc.* Accessed August 30, 2011. http:/www.mathsworks.com.au/helpdesk/help/toolbox/wavelet/.

Montes GS and Junqueria LCU. 1988. “Histochemical localisation of collagen and of proteoglycans in tissues.” In *Collagen - Volume II: Biochemistry and Biomechanics*, by Mini ME, 41-73. London: CRC Press.

Morlet J, Arens G, Fourgeau E and Giard D. 1982. “Wave propagation and sampling theory - Part II: Sampling theory and complex waves.” *Geophysics* 47: 222-236.

Morrone M and Owens R. 1987. “Feature Detection from Local Energy.” *Pattern Recognition Letters* 6: 303-313.

Mow et al. 1992. “Cartilage and diarthroidial joints as paradigms for hierarchical materials and structures.” *Biomaterials* 67-97.

Mow V, Gu W, and Chen F. 2005. *Structure and Function of Articular Cartilage and Meniscus.* 3rd. Lippincott, Williams & Wilkins.

Mow VC and Guo XE. 2002. “Mechanoelectromechanical properties of articular cartilage: their homogeneities and anisotropes.” *Annual Review of Biomedical Engneering* 4: 175-209.

Mow VC, Wenbo Z and Ratcliffe A. 1991. “Structure and Function of Articular Catilage and Meniscus.” In *Basic Orthopaedic Biomechanics*, by Mow VC and Hayes WC, 143-243. London: Raven press Ltd.

Muir, H. 1983. “Proteoglycans as organisers of the extracellular matrix.” *Bioochemistry Society Transactions* 11: 613-622.

Muir, H. 1980. “The chemistry of the ground substance of joint cartilage.” In *The Joints and Synovial Fluid*, by L Sokoloff, 2-27. New York: Academic Press.

Nievergel, Y. 1999. *Wavelets Made Easy.* Boston: Birkhausr.

Poole, A R. 2003. “What type of cartilage repair are we attempting to attain?” *Journal of Bone and Joint Surgery* 85: 40-44.

Quin T and Morel V. 2007. “Microstructural modelling of collagen network mechanics and interactions with proteoglycan gel in articular cartilage.” *Biomechanics and Modelling in Mechano-Biology* 6: 73-82.

Richardson, B. 2010. *Development of a 3D Phase Congruency program for the Study of Articular Cartilage.* Undergraduate Project, Perth: School of Electrical, Electronic and Computer Engineering, University of Western Australia.

Robbins S, Abbas N, Kumar V and Cotran R. 2005. “Bones Joints and Soft Tissue Tumors.” In *Pathologic Basis of Disease*, by Robbins and Cotran, 1303-1305. Saunders.

Robbins, B. 1996. *The detection of 2D image features using local energy.* PhD Thesis, Perth: Department of Computer Science, University of Western Australia.

Robins, J. 1999. *Local Energy Feature Tracing in Digital Images and Volumes.* PhD Thesis, Perth: Department of Computer Science university of Western Australia.

Shoulders M and Raines R. 2009. “Collagen Structure and Stability.” *Annual Review of Biochemistry* (78): 929-958.

Smith, M. 2008. *The physiological importance of the superficial layer in articular cartilage.* Final year project report, Perth: School of Mechanical Engineering, University of Western Australia.

Smolinski D, Wu JP, Jones CW, Zheng MH, O'Hara LJ, Miller KS and Kirk TB. 2003. “The confocal arthroscope as a cartilage optical biopsy tool.” *Osteoarthritis and Cartilage* (supplement A) (11): 111-112.

Spagnolo, D. 2008. *Topographical changes in the mechanical properties and 3D arrangement of collagen fibres in developing ovine cartilage.* Final year project report, Perth: School of Mechanical Engineering Univerity of Western Australia.

Stachowiak GW, Batchelor AW and Griffiths LJ. 1994. “Friction and wear changes in synovial joints.” *Wear* 171: 135-142.

Stockwell, RA. 1979. *Biology of Cartilage Cells.* Cambridge: Cambridge University Press.

Tam HK, Srivastava A, Colwell CW and D'Lima DD. 2007. “In vitro model of full-thickness cartilage defect healing.” *Journal of Orthopaedic Research* 25: 1136-1144.

Tam HK, Srivastava A, Colwell CW and D'Lima DD. 2008. “In vitro model of full-thickness cartilage defect healing.” *Journal of Orthopaedic Research* (25): 1136-1144.

Teshima R et al. 1995. “Structure of the Most Superficial Layer of Articular Cartilage.” *Journal of Bone and Joint Surgery* 77B: 460-464.

Teshima R, Ono M, Yamashita Y, Hirakawa H, Nawata K and Morio Y. 2004. “Immunohistochemical collagen analysis of the most superficial layer in adult articular cartilage.” *Journal of Orthopaedic Science* 9: 270-273.

Van De Graff, KM and Fox, SI. 1986. *Concepts of Human Anatomy and Physiology.* New York: Brown Publishers.

Venkatesh S and Owens R. 1989. “An Energy Feature Detection Scheme.” *The International Conference on Image Processing.* Singapore. 553-557.

Weiss C, Rosenberg L and Helfet R. 1968. “An Ultrastructural Study of Normal Young Adult Human Articular Cartilage.” *Jornal of Bone and Joint Surgery* 50: 663-674.

Widuchowski W, Widuchowski J and Trzaska T. 2007. “Articular cartilage defects: study of 25,124 knee arthroscopies.” *The Knee* 14: 177.

Williamson A, Thonar E, Chen A, Sah R and Masuda K. 2003. “Tensile mechanical properties of bovine articular cartilage: Variations with growth and relationships to collagen network components.” *Journal of Orthopeadic Research* 21: 872-880.

Wu J P and Hezog W. 2002. “Elastic antiscope of articular cartilage is associated with the microstructures of collagen fibres and chondrocytes.” *Journal of Biomechanics* 35: 931-942.

Wu J P, Kirk T B, and Zheng M H. 2004. “Assessment of three-dimensional architecture of collagen fibre in the superficial zone of bovine articular cartilage.” *Journal of Musculoskeletal Research* 8 (4): 167-179.

Wu JP, Kirk TB and Zheng MH. 2008. “Study of the collagen structure in the superficial zone.” *Journal of Orthopeadic Surgery and Research* 3: 29-40.

Wu, JP. 2005. *Development of Microscopic Techniques for Study of the 3D Collagen Stucture in the Superficial Zone and its Relationship to the Degeneration of Articular Cartliage.* PhD Thesis, Perth: The School of Mechanical Engineering, University of Western Australia.

Yasui N and Nimni ME. 1988. “Cartilage Collagen.” In *Collagen - Volume 1 Biochemistry*, by Nimni ME, 225-243. CRC Press.

Young RD, Vaughan-Thomas C, Wardale RJ and Duance VC. 2002. “Type II collagen deposition in cruciate ligament preceded osteoarthritis in the guinea pig knee.” *Osteoarthtitis and Cartilage* 10: 420-428.

Zhang M, Zheng YP and Mak AFT. 1997. “Estimating the effective Young's Modulus of soft tissue from indentation tests - nonlinear finite element analysis of effects of friction and large deformation.” *Medical Engineering Physics* 19 (6): 512-517.

Zheng M H, Willers C, Kirilak L, Yates P, Xu J, Wood D and Shimmin A. 2007. “Marix Induced Autologous Chondrocyte Implantation (MACI®):Biological and Histological Assessment.” *Tissue Engineering* 13: 737-746.

Appendix A Excitation / Fluorescence Wavelength of Fluorescein (nm)